Green synthesis and structural control of metal and mineral nanostructures

Engelbrekt, Christian

Publication date:
2014

Document Version
Publisher's PDF, also known as Version of record

Technical University of Denmark

Green synthesis and structural control of metal and mineral nanostructures

Christian Engelbrekt

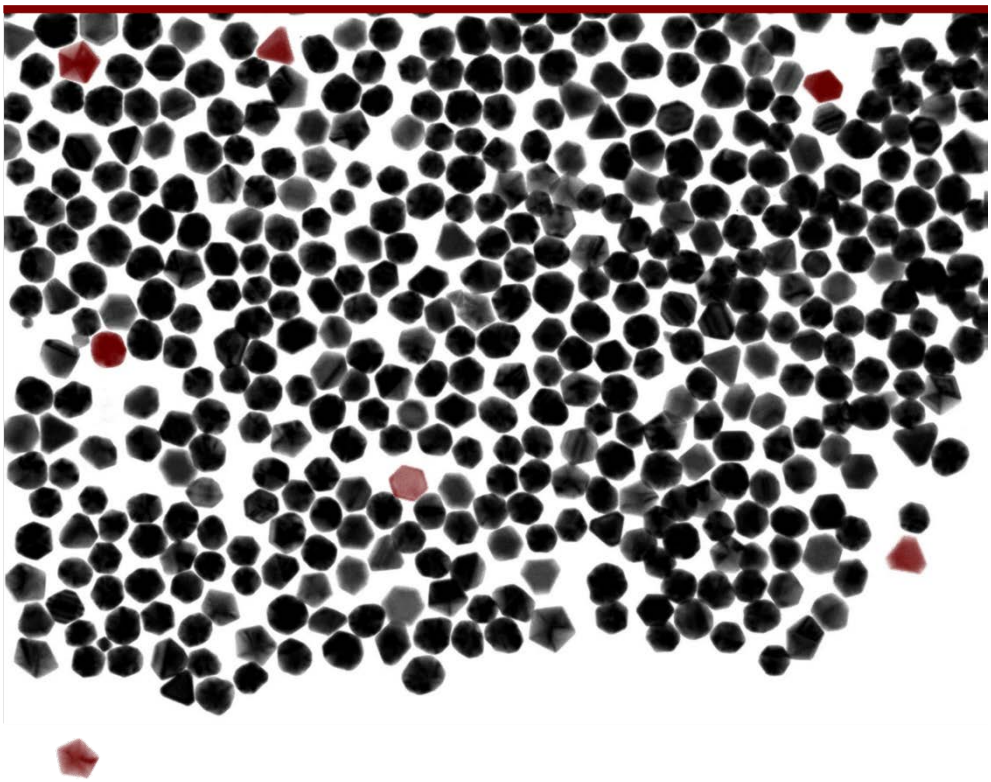

PhD Thesis

September 2014

DTU Chemistry
Department of Chemistry

"That which is not sustainable, will not be sustained"

Herb Stein

Chairman of the US President's
Council of Economic Advisors

Preface and Acknowledgements

This dissertation is submitted to the Technical University of Denmark (DTU) in partial fulfilment of the requirements for the degree of Ph.D. The work was carried out at DTU Chemistry in the NanoChemistry Group with Jingdong Zhang and Jens Ulstrup as main and co-supervisor, respectively. Financial support from the Lundbeck Foundation and DTU Chemistry for the PhD programme as well as support from the Knud Højgaards Foundation, EU FP7 IRSES programme *ELECTRONANOMAT* and Otto Mønsted Foundation for external research and conference participation are acknowledged.

My thanks go first and foremost to Jingdong Zhang. She has been more than a good supervisor. She supported me in all my ideas and worked hard to give me the best possible starting point for my own research career and the opportunity to take active part in the research community at international conferences. My current professional ambitions have grown from her motivation ever since my first hands-on experience with research as a bachelor student. Our cooperation has been efficient and I am convinced it will continue to be fruitful in the future.

I appreciate greatly the strong support the NanoChemistry group has provided. In particular, Jens Ulstrup and Palle Skovhus Jensen were consistently available for guidance during my project and I have learned many things from them. I have been fortunate to work in a group with many great people and scientists. They have contributed to an environment of high academic level and social coherence. It is important to prioritize events for the group as whole with a social element, even with the extreme time constraints of modern academia. On a related note, I have had the support of a good network of students from DTU Chemistry resulting in both successfully published collaborations and a dynamic and pleasant working environment. I would like to thank especially PhD students Phillip Malcho, Jonas Andersen, Raju Poreddy and Nedjeljko Seselj for our common fruitful scientific collaboration.

The Center for Electron Nanoscopy (CEN) at DTU has been crucial for my work and I have benefitted from the guidance and assistance of a number of experts at the center. I would like to thank in particular Wilhelmus Huyzer and Jacob Birkedal Wagner for their support regarding technical challenges, training and fundamental insight for data analysis.

I appreciate the successful collaborations with Professor Katrin Kneipp from DTU Physics, Professor Janina Kneipp and PhD student Virginia Joseph from Humboldt University Berlin; Professor Anders Baun and postdoc Nanna I. B. Hartmann from DTU Environment;

and Associate Professor Søren Kegnæs and PhD student Jerrik Mielby from DTU Chemistry.

I thank also guest PhD student Shiyu Gan; Professor Li Bin from Shanghai Institute of Applied Physics (SINAP) and her students Na Wu and Youjie Fan for hosting my visit to SINAP and assistance with AFM and experiments at the Shanghai Synchrotron Radiation Facility (SSRF); Professor Lijuan Zhang for organizing the experiments at the SSRF; Associate professor Wei Yan and professor Liyi Shi for organizing my stay at Shanghai University (SHU) and their students Xiang Wang, Ling Wang, Fan Zhang, Zhongju Tao, Wenjuan Yu, Ruien Hou and others for tremendous assistance with experiments and stimulating scientific discussions; Associate professor Pengchao Si from Shandong University (SDU) and their students Xinxin Xiao, Liangliang Peng, Li Hui and especially Wenxin Wang for organizing my stay at SDU and help with running and evaluating experiments.

Last but not least, I thank my family and friends for support and understanding, especially during the intense final part of the PhD project.

September 2014, Kgs. Lyngby

Christian Engelbrekt

Abstract

Nanomaterials are widely used in modern technology, especially as catalysts in energy technology. Nanocatalysts are often prepared from expensive elements that constitute a large part of the total device cost. A critical component in the successful implementation of sustainable energy technology is efficiency which in large part comes down to the efficiency of the catalyst. Global issues arising from the use and reliance on fossil fuels urges the transition to sustainable alternatives and the development of new highly efficient nanomaterials. The efficiency depends on structure so controlling size, shape and composition at the atomic level is essential. To this adds low cost if massive use is anticipated.

In this work, nanostructures of gold, platinum/gold, platinum/palladium, clinoatacamite ($Cu_2(OH)_3Cl$), cupric oxide and gold/titanium dioxide were synthesized and broadly characterized, their formation mechanisms studied, and their application as catalysts in relevant systems tested.

Solution synthesis of nanomaterials offers large-scale, mild production but control of size, shape and composition is often challenging. This may be improved by expanding the understanding of the complex processes of nanoparticle formation which, however, entails the development of new methods.

Two approaches to the advancement of solution synthesis of gold nanomaterials for energy technology were exploited, namely the development of techniques to study nanoparticle formation and the synthesis of active, composite nanomaterials.

In the first approach, time-resolved chronopotentiometry, pH, conductivity and turbidity, and ultraviolet-visible light spectroscopy were employed to follow the green synthesis of gold nanoparticles. Several distinct phases were observed with all techniques providing a broad picture of the complex processes. Strong indications of sequential reduction were found and details about ligands and surface immobilized molecules disclosed. This platform is a widely available alternative to traditionally used synchrotron techniques.

In the second approach, systematic efforts toward size and shape control of gold nanostructures provided controlled synthesis of not only spherical gold nanoparticles of 8-80 nm but also graphene oxide templated preparation of flat, ring-shaped gold nanostructures up to 1 μm in diameter mainly exposing (111) facets.

Increased efficiency of new platinum nanocatalysts was attempted by two parallel strategies. One entailed avoiding inactive bulk platinum using a gold core and leaving only

an atomically thin platinum shell. The specific catalytic activity of this nanocomposite will be studied in the future. The other strategy was to alloy platinum with a cheaper element, i.e. palladium, while retaining high activity. Supported PdPt alloy nanoparticles were successfully prepared and showed promising performance as catalysts in direct methanol and formic acid fuel cells.

Catalysts made from earth-abundant elements may provide other low-cost anternatives to traditional, scarce and expensive catalysts. This may be achieved through niche applications and nanoscale engineering. Copper mineral nanoparticles were prepared and studied for this purpose. A buffered synthesis offering the preparation of phase-pure clinoatacamite $Cu_2(OH)_3Cl$ and tenorite CuO by controlling pH was developed. Detailed crystallographic characterization was obtained by combining X-ray diffraction and infrared spectroscopy. The synthesis of CuO was further optimized and the flat, rod-shaped nanostructures applied as heterogeneous catalysts for oxidative dehydrogenation reactions. High activity and good reusability was found and the potential of this noble metal-free system will be explored further.

Solar energy is appealing as a plentiful and free energy source. A plasmonic photoelectrocatalytic system was prepared to utilize visible light by incorporating gold nanoparticles in titanium dioxide. The composite material showed improved optical properties compared to pure titanium dioxide and preliminary catalytic tests were promising.

Danish summary

Nanomaterialer er bredt anvendt i moderne teknologi, særligt som katalysatorer i energiteknologi. Nanokatalysatorer er ofte fremstillet af dyre grundstoffer, som udgør en stor del af apparatets samlede omkostninger. Effektivitet er en kritisk del af succesfuld indføring af vedvarende energiteknologi, hvilket i høj grad afhænger af katalysatorens effektivitet. Globale problemstillinger med rod i brugen og afhængigheden af fossile brændsler tilskynder omstillingen til vedvarende alternativer og udvikling af nye højeffektive nanomaterialer. Effektiviteten afhænger af nanomaterialets struktur, så styring af størrelse, form og sammensætning på atomart niveau er essentiel.

I det foreliggende projekt er nanostrukturer af guld, platin/guld, platin/palladium, clinoatacamit ($Cu_2(OH)_3Cl$), kobberoxid og guld/titandioxid syntetiseret og bredt karakteriseret, deres dannelsesprocessor studeret og nanostrukturerne anvendt som katalysatorer i relevante systemer.

Væskesyntese af nanomaterialer muliggør produktion i store mængder under milde betingelser, men styring af størrelse, form og sammensætning er ofte en udfordring. Dette kan forbedres ved at udvide forståelsen af selve de komplekse processer, som indgår i nanopartikeldannelse, hvilket imidlertid kræver udvikling af nye metoder til at studere dem.

To tilgange til at videreudvikle væskesyntese af nanomaterialer til energiteknologi er undersøgt, fokuseret på udvikling af teknikker til at studere nanopartikeldannelse og syntese af aktive, sammensatte nanomaterialer.

I den ene tilgang anvendes tidsopløst kronopotentiometri, pH, ledningsevne og turbiditet, samt ultraviolet-synligt lys spektroskopi til at følge grøn syntese af guldnanopartikler. Adskillige distinkte faser kunne observeres i alle teknikker, hvilket dannede et bredt billede af de komplekse processer. Stærke indikationer af sekventiel reduktion blev fundet og detaljer omkring ligander og overfladeimmobiliserede molekyler klarlagt. Denne platform er et bredt anveldeligt alternativ til traditionelt anvendte synkrotronteknikker.

I den anden tilgang førte arbejde imod størrelses- og formkontrol af guldnanostrukturer til kontrolleret syntese af ikke blot sfæriske 8-80 nm guldnanopartikler, men også fremstilling af flade, ringformede guldnanostrukturer 1 µm i diameter med hovedsageligt (111) facetter eksponeret ved brug af grafenoxid som skabelon.

Øget effektivitet af platinnanokatalysatorer blev forsøgt ved to parallelle strategier. Den ene indebar begrænsning af inaktivt bulk-platin ved at bruge en guldkerne omgivet af en kun atomtynd platinskal. Dette kompositmateriales specifikke katalytiske aktivitet vil blive

studeret i fremtiden. Den anden strategi var at legere platin med et billigere grundstof, i.e. palladium, med høj aktivitet bibeholdt. PdPt legeringsnanopartikler på bæremateriale var fremstillet og udviste lovende ydedygtighed som katalysatorer i metanol- og myresyrebrændselsceller.

Katalysatorer fremstillet af hyppigt forekommende grundstoffer kan repræsentere andre billige alternativer til traditionelle, knappe og dyre katalysatorer. Dette kan opnås gennem nicheanvendelser og nanoskalakonstruering. Kobbermineralnanopartikler blev fremstillet og studeret til dette formål. En pufferkontrolleret syntese til fremstilling af faseren clinoatacamit $Cu_2(OH)_3Cl$ og tenorit CuO ved at kontrollere pH blev således udviklet. Detaljeret krystallografisk karakterisering blev opnået ved at kombinere Røntgenspredning og infrarødspektroskopi. Syntesen af CuO blev yderligere optimeret og de flade, stavformede nanostrukturer anvendt som heterogene katalysatorer til oxidative dehydrogeneringsreaktioner. Dette ædelmetalfri system viste høj aktivitet og god genanvendelighed og vil blive yderlige udforsket.

Solenergi er attraktiv da denne energiform er i overflod og gratis. Et plasmonisk fotoelektrokatalytisk system blev fremstillet ved at inkorporere guldnanopartikler i titandioxid for at udnytte synligt lys. Det kompositte materiale udviste forbedrede optiske egenskaber sammenlignet med ren titandioxid og foreløbige katalyse tests var lovende.

Motivation and project objectives

Project objectives

In order to facilitate a transition to sustainable energy and out-compete fossil fuels, sustainable technologies must improve in terms of cost and efficiency. Sustainable technologies have seen major advances which can be largely attributed to the utilization of nanotechnology and -materials. Very often nanoparticles (NPs) play the critical role of catalyst in energy-conversion, e.g. solar energy to electricity, fuel to electricity and solar to chemical energy. Precise engineering of the nanomaterials is thus a central parameter in the success of these technologies.[1-3]

My PhD work covered two strategies for advancing the field of nanomaterial synthesis, especially relating to energy technology: (1) Disclosing the complex processes of nanoparticle synthesis to control their formation and (2) developing mild, easy and cheap syntheses of novel nanomaterials.

Motivation

Society is facing a global energy challenge relating to the use of and reliance on fossil fuels. This challenge (or crisis) has many aspects, advocated by a wide spectrum of interest groups, politicians, scientific communities, government and non-governmental organizations (NGOs), grassroots movements, multinational corporations etc. Some of these aspects are:

1. Climate (global warming, greenhouse gas (GHG) emissions, climate change, pollution)
2. Limited resources ("Peak Oil", rising prices)
3. Politics (reliance on supply from politically unstable regions, conflicts over control of supply, prices controlled by supplying nations)
4. Population growth (link between gross domestic product (GDP) and energy consumption, emerging economies, BRIC nations (Brazil, Russia, India, China))

Many of these topics are complex and many groups (some very powerful) have a lot at stake. This leads to an overwhelming amount of contradicting information and bias ultimately obscuring the situation. However, a few things are certain: The GHG emissions from human activities are affecting the climate[4,5], conventional fossil fuels are being depleted[6,7] and the growth in population and wealth of emerging economies lead to

increased energy consumption[8], Figure 1. So, regardless of which point one's concerns relate to, new technologies are needed.

A large part of new technology supported by multinational industrial players focuses on non-conventional oil (NCO) and gas, such as bitumen (a solid/highly viscous petroleum form in rock, e.g. oil sands in Canada), tight oil and gas (oil and gas contained in low-permeable rock systems, i.e. shale oil and gas) and extra-heavy oil (density greater than 1 g/cm^2).[9] These highly advanced drilling and extraction techniques are accompanied by the risk of severe environmental impact and are expensive. The efficiency of energy technologies is often evaluated by the energy return on investment (EROI). This number gives the ratio between the output energy of a given technology and the energy consumed in the process of acquiring that output. The EROI of conventional oil has dropped drastically since the discovery of the "black gold". Reports vary but the EROI of current conventional oil production is in the order of 10-20. NCO technologies have much lower EROI than conventional oil. The EROI of oil sands is below 10 and shale oil as low as 1.5 meaning that a significant amount (or most) of the energy contained in the resource is used to extract it.[8] In comparison, the EROI of hydropower is an order of magnitude higher than conventional oil, photovoltaics around 9 and wind power above 20.[10,11] Nevertheless, the NCO technologies are being employed on a large scale and expanding exponentially, effectively postponing the point of decline in fossil fuel production.

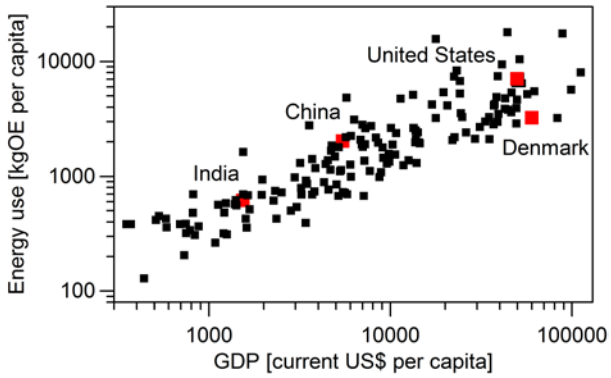

Figure 1.Energy consumption vs. GDP. Data from the World Bank, average of 2007-2011.[12]

Thesis structure

The thesis is structured in five chapters. **Chapter 1** introduces concepts, theory and methodology for the discussion of results in the following chapters. **Chapter 2** describes the efforts towards understanding and controlling the synthesis of nanostructures using gold as a model element. Gold nanoparticle (AuNP) formation, size control and flat gold nanostructure synthesis are the main topics of this chapter. Work on reducing the need for platinum in catalytic systems with bimetallic structures is summarized in **Chapter 3**. Two approaches to limit platinum consumption were taken; core-shell geometry with gold as the core element, and alloying with palladium. Efforts to limit the reliance on noble metals are described in **Chapter 4**. Earth-abundant elements such as copper and titanium are utilized in their oxidized forms. The present work includes controlled synthesis of copper minerals, their employment in catalytic oxidation of alcohols and composite nanomaterials of AuNPs and titanium dioxide for photocatalysis. **Chapter 5** summarizes the conclusions of the project, reflections on the outcomes and perspectives for future work.

Acronyms and instructional note

A293: UV peak at 293 nm

A366: UV peak at 366 nm

ATR-FTIR: Attenuated total reflectance Fourier transform infrared spectroscopy

AuNP: Gold nanoparticle

BF: Bright field

BPG: Basal-plane graphite

BRIC: Brazil, Russia, India, China

CAPS: *N*-cyclohexyl-3-aminopropanesulfonic acid

CB: Carbon black

CCD: Charge-coupled device

CE: Counter electrode

CEN: Center for Electron Nanoscopy

CV: Cyclic voltammetry

DF: Dark field

DFAFC: Direct formic acid fuel cell

DFT: Density functional theory

DLS: Dynamic light scattering

DLVO: Derjaguin, Landau, Verwey, Overbeek

DMFC: Direct methanol fuel cell

DMSO: Dimethyl sulfoxide

DTU: Technical University of Denmark

EC: Electrochemistry

EDX: Energy-dispersive X-ray spectroscopy

EROI: Energy return on investment

ESI: Electrospray ionisation

EXAFS: Extended X-ray absorption fine structure

FCC: Face-centered cubic

FWHM: Full width at half maximum

GC: Gas chromatography

G-CB: Graphitized carbon black

GCE: Glassy carbon electrode

GDP: Gross domestic product

GHG: Greenhouse gas

GO: Graphene oxide

HEPES: 4-(2-hydroxyethyl)piperazin-1-ethanesulfonic acid

HR: High resolution

HWP: Half-wave potential

HAADF: High angle annular dark field

LSPR: Localized surface plasmon resonance

$LSPR_{long}$: Longitudinal mode of the localized surface plasmon resonance

$LSPR_{trans}$: Transverse mode of the localized surface plasmon resonance

MB: Methylene blue

MEA: Membrane electrode assembly

MES: 2-(*N*-morpholino)ethanesulfonic acid

MOS: MES-optimized synthesis

MS: Mass spectrometry

MSE: Mercury/mercury sulfate electrode

MSMS: Tandem mass spectrometry

NCFF: Non-conventional fossil fuels

NCO: Non-conventional oil

NF: Nanoflower

NGO: Non-governmental organization

NIR: Near-infrared

NP: Nanoparticle

NPG: Nanoporous gold

NTA: Nanoparticle tracking analysis

NTU: Nephelometric turbidity units

OBS: Only buffer synthesis

OCP: Open-circuit potentiometry

ORR: Oxygen reduction reaction

PB: Phosphate buffer

PDA: Photodiode array

PdNP: Palladium nanoparticle

PTFE: Polytetrafluoroethylene

PtNP: Platinum nanoparticle

r.t.: Room temperature

RDE: Rotating disc electrode

RE: Reference electrode

RHE: Reversible hydrogen electrode

rpm: Revolutions per minute

SAED: Selected area electron diffraction

SAMENS: Saccharide-based approach to metallic nanostructure synthesis

SAXS: Small-angle X-ray scattering

SCE: Saturated calomel electrode

SD: Standard deviation

SDU: Shandong University

SEM: Scanning electron microscopy

SHU: Shanghai University

SINAP: Shanghai Institute of Applied Physics

SSRF: Shanghai Synchrotron Radiation Facility

STEM: Scanning transmission electron microscopy

STM: Scanning tunneling microscope

STXM: Scanning transmission X-ray microscopy

TEM: Transmission electron microscopy

UHV: Ultra-high vacuum

UPLC: Ultra-high pressure liquid chromatography

UV-vis: Ultraviolet-visible

WAXS: Wide-angle X-ray scattering

WE: Working electrode

XAFS: X-ray absorption fine structure

XANES: X-ray absorption near-edge structure

XRPD: X-ray powder diffraction

Instructional note

Acronyms of terms ending in microscopy, -chemistry, voltammetry and spectrometry are also used to refer to microscope, -chemical, voltammogram and spectrum/spectrometer, respectively. Abbreviations are used in plural form by adding “s” except for spectrum/spectra where the same abbreviation is used.

Figures and tables in appendices are labelled “App. Fig.“ and “App. Table”, respectively.

In part, the current work builds on results obtained prior to the PhD programme. Prior data are presented when necessary for coherence and indicated in the figure text with **[Prior data]**.

Table of Content

Preface and Acknowledgements iii

Abstract v

Danish summary vii

Motivation and project objectives ix

Acronyms and instructional note xii

Table of Content xiv

Chapter 1 Gold, nanoparticles and their synthesis 1

1.1 The golden standard ... 1

1.1.1 The importance of gold in history and modern society ... 1

1.1.2 Gold - The element 79 ... 3

1.2 Nanoparticles and nanomaterials ... 4

1.2.1 Solution synthesis and NP formation ... 5

1.2.2 Nanoparticle stability ... 8

1.3 Characterization and functionality ... 9

1.3.1 Ultraviolet-visible spectroscopy ... 10

1.3.2 Nanoparticle tracking analysis ... 11

1.3.3 Transmission electron microscopy ... 13

1.3.4 Electrochemical techniques ... 16

1.3.5 X-ray techniques ... 18

1.3.6 Other optical techniques ... 20

Chapter 2 Control of gold nanostructure synthesis 23

2.1 Mechanisms of gold nanoparticle formation ... 23

2.1.1 The AuNP synthesis method ... 25

2.1.2 Solution potential dynamics ... 27

2.1.3 Conductivity and pH dynamics ... 34

2.1.4 Dynamics of optical properties ... 37

2.1.5 Formation mechanism ... 40

2.2 Controlling the size of AuNPs in solution synthesis....42
2.2.1 Size and optical properties....45
2.2.2 Development of nanoparticle morphology....48
2.2.3 Concluding remarks on size control....50
2.3 Size is not everything, shape control....51
2.4 Flat gold nanostructure synthesis....52
2.4.1 Controlled reduction of tetrachloroaurate....53
2.4.2 Graphene oxide templated synthesis....59
2.4.3 Concluding remarks on flat gold nanostructure synthesis....65
2.5 Unidentified UV peaks....66
2.5.1 Formation kinetics and UV sensitivity of A366....66
2.5.2 Isolation of UV active compound....68
2.5.3 Fluorescence of the UV active compound....71
2.5.4 Mass spectrometry and electron microscopy....72
2.5.5 A general phenomenon?....75

Chapter 3 Better utilization of platinum in catalysis 78
3.1 The scarcity of platinum....78
3.2 Au-Pt core-shell nanoparticles....79
3.2.1 Synthesis of Pt monolayer shells on AuNPs....80
3.2.2 Electrochemical characterization....85
3.2.3 Towards catalytic application of AuPt core-shell NPs....89
3.3 Using palladium with platinum....92
3.4 Palladium-platinum nanostructures....93
3.4.1 Palladium nanoparticles....93
3.4.2 Synthesis of Pd/Pt nanostructures....96
3.5 Application of PdPt nanostructures in fuel cells....98
3.5.1 Initial fuel cell tests....99
3.5.2 Synthesis of PdPt NP catalyst at Shandong University....102
3.5.3 Electrochemical characterization of PdPt catalyst....103
3.5.4 Cathode preparation, DMFC assembly and fuel cell test....105

Chapter 4 Minerals and hybrids with metal NPs 108
4.1 Earth-abundant solutions....108

4.2 Selective synthesis of $Cu_2(OH)_3Cl$ and CuO 108
4.2.1 pH effect on product phase 109
4.2.2 Scale-up and product identification 115
4.2.3 Formation mechanisms 122
4.3 Benzyl alcohol oxidation by CuO 124
4.4 Plasmonic photocatalysis 130
4.4.1 Materials preparation 132
4.4.2 Photoelectrode fabrication 136
4.4.3 Photoelectrocatalytic activity tests 141

Chapter 5 Conclusions 149

Bibliography 153

Appendix A Publications and dissemination I

Appendix B Supplementary data IV

Chapter 1

Gold, nanoparticles and their synthesis

1.1 The golden standard

Nanostructured gold has intriguing properties that can be utilized for catalysis and sensing. This very stable metal also has value as support or carrier for other active materials, e.g. metals or proteins. The chemistry of gold is well-defined and gold nanoparticles serve as an ideal model system for studying nanoparticle synthesis. Gold is the key element and directly or indirectly related to all topics covered in the thesis. An introduction to this special element is therefore given in the following sections.

1.1.1 The importance of gold in history and modern society

Gold is found in nature in its pure elemental form and has been utilized for more than 5000 years. The intense yellow colour, the lustrous metal surface, the malleability and scarcity of gold have always attracted people's attention and made this element synonymous with wealth. The ancient Egyptian and Asian cultures acquired great skill in applying gold in art, sculptures and religious artefacts. One of the most well-known examples is the funeral mask of the pharaoh Tutankhamun, Figure 2A. Not only the Egyptians but the elite of any society in history accumulated great riches in the form of gold coins and artefacts, i.e. hoards, and gold has become a universal symbol of treasure.

The obsession with gold was a central topic of the European medieval alchemists that paved the way for modern chemistry. Sophisticated chemical operations were undertaken with great skill in attempts to synthesize gold from an array of starting materials, e.g. lead and urine. Figure 2B shows a famous late 18th century painting of the German alchemist Hennig Brand successfully discovering phosphorous obtained from phosphate in urine.[13,14] He believed phosphorous to be the *philosopher's stone* - a substance able to turn common metals into gold. Seeking fortunes through gold took a new meaning in the 19th century where gold mining was the cause of mass migrations of workers around the world; the so-

called *gold rushes*. This intensive search for gold coined phrases like “gold fever” and “gold digger”.

Figure 2. Examples of historical significance of gold. (A) The exquisite gold funeral mask of Tutankhamun.[15] (B) “The alchemist discovering phosphorous” (1771) painting by Joseph Wright.[14] (C) The Roman Lycurgus cup showing its green colour by scattered light (left) and red colour by transmitted light (right).[16]

Gold coins have been used for monetary exchange since the 6th century BC and still today gold bars are used to store and represent monetary value. Gold is also used figuratively to a great extent in our modern culture; first place is awarded the gold medal, the gold standard is something excellent to which other things are compared, a golden opportunity is a very advantageous situation etc. Myths have incorporated gold as a special element; King Midas from the Greek mythology turned everything he touched into gold and the leprechauns of the Irish mythology are said to hide a pot of gold at the end of the rainbow.

Despite the young age of nanotechnology, the special properties of gold in the nanometer range (10^{-7} - 10^{-9} m) have been utilized for 600 years. The incorporation of AuNPs in glass provided a ruby red colour that can be seen in decorative glass such as church glass mosaics. The most referenced object in this respect is the Roman Lycurgus cup from the 4th century, Figure 2C.[16] However, the Lycurgus cup actually does not contain AuNPs but 50-100 nm gold-silver alloy NPs (an alloy known as electrum) in a Au/Ag ratio of 70/30.[17] It was shown that the scarlet red colour of the cup (rather than the ruby red colour of AuNPs) stems from a blue-shift of the absorption caused by the silver content.[18]

Gold still finds many uses in modern society. Indeed, the 5000 year long tradition of using gold for decoration and to represent value still exists today. More modern versions of this usage includes the addition of shimmering gold flakes to luxury goods such as champagne, ice cream, chocolate, cheese etc. Even nanoscale gold has entered luxury consumer goods to allegedly improve the function of the products. Most of these are beauty products, e.g. lotions for “anti breast sagging”[19], but also a wide variety of dietary supplements with claims ranging from increasing people’s intelligence by the particle’s “electromagnetic

frequencies"[20] to strengthening the libido and curing obesity by "harmonizing the nervous system"[21]. All these are non-scientific but a testament to the enduring fascination of gold and the sensational value of "nano" in today's society - not only in academia.

Gold is also applied in more scientifically documented areas. Gold complexes, e.g. auranofins[22], got a lot of attention in the 1980s for treatment of rheumatoid arthritis.[23] More recently, AuNPs have been utilized for many medicinal and therapeutic purposes. The large variety of different possible surface coatings can be exploited to target different aspects of the organism; drug delivery, cholesterol binding, small-molecule detection etc.[24] The special optical properties combined with the flexibility in surface modifications have enabled the use of AuNPs in targeted cancer therapy, so-called photothermal therapy.[25] The AuNPs are coated with molecular anchors that bind specifically to cancer cells. The tissue is then irradiated with a near-infrared (NIR) laser that excites the surface plasmons of the AuNPs (see section 1.3.1 for details of this effect) resulting in a localized increase in temperature that destroys the cancerous tissue. AuNPs have been employed in a number of sensing devices based on their sensitive optical properties. "Antenna" molecules that bind specific analytes are attached to the surface. Analyte binding causes a slight change in the local refractive index inducing a change in the optical properties of the AuNPs.[26] This effect can be detected, quantified and enhanced by controlling the AuNP assemblies, i.e. dimers[27] or 3D structures[28]. Catalysis is a hot topic within applied research on AuNPs. The catalytic oxidation of CO initialized this research area which now includes a multifariousness of chemical reactions.[29] Since the early 2000s, increasing attention has been put on the significance of the support and support/AuNP interface for catalysis[30,31] and size-dependence of the AuNP activity is well documented.[32-35]

1.1.2 Gold - The element 79

Gold (together with silver and copper) belongs to group 11 in the periodic table of elements with platinum and mercury as neighbours. It is as scarce as the notoriously scarce element platinum with each kg of earth crust containing on average 4 µg of gold.[36] Yet gold is cheaper[i] than platinum because it is more accessible as a resource leading to a much larger supply. The world gold production has been stable around 2500 t/year since 1997 but increased steadily the past 5 years to above 3000 t in 2013 - 16 times higher than that of platinum[ii, 37] - with another 1400 t being recycled.[38] China is by far the biggest supplier with almost 15 % of the world production.[39] Gold is mined both in open pit mines and underground mines. Large ores can be sent directly for purification while small particulate

[i] Special conditions in the global economic environment have historically led to limited periods where gold was more expensive than platinum.
[ii] The world platinum supply has been stable around 200 ton per year during the last decade and almost exclusively come from South Africa.

gold is leached from rock with alkali cyanide. Previously, gold was extracted by chemical precipitation but today the precious metal is physisorbed on carbon black.[40,41]

The specific surface and crystalline structure are essential when dealing with NPs, especially with regards to catalytic activity and function. Gold belongs to the face-centered cubic (FCC) system. The FCC is the closest packing of solid spheres and common among metals. Atoms are positioned in each corner (red spheres in Figure 3A) and face-centre (orange spheres in Figure 3A) of the cubic unit cell, thus containing a total of 4 atoms (8·⅛+6·½). The cubic crystal structure is defined by one lattice parameter, α, describing the side length which is 4.08 Å for gold. 3 types of low-index facets belonging to the crystal plane families {111}, {100} and {110} are mainly found on gold crystals. Higher index facets are unstable but can be prepared and used. However, these can be viewed as one of the main facets with a highly stepped structure as illustrated in Figure 3B, where a (410) surface can be regarded as a highly stepped (100) surface.

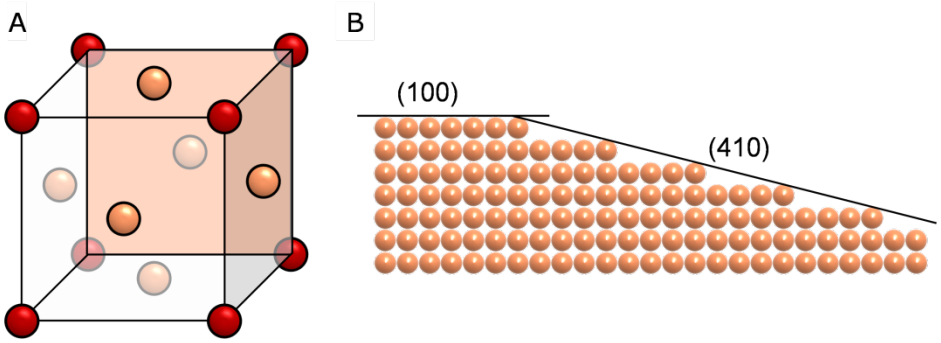

Figure 3. (A) The unit cell of the FCC crystal structure of gold. Corner atoms are red and face-centered atoms orange. (B) A gold surface showing the relation between the (100) and (410) surfaces. The latter can be regarded as a series of short (100) steps.

1.2 Nanoparticles and nanomaterials

The term *nanotechnology* emerged around the early 1980s though the science of colloidal chemistry was more than 100 years old at the time.[iii] An important milestone in the dawn of nanotechnology was the famous talk "There's plenty of room at the bottom" by physicist Richard Feynman in 1959 starting the bottom-up concept of building structures atom by atom.[42] The development of microscopes able to "see" nanomaterials at the nanoscale and image individual atoms was crucial for nanoscience. This was achieved by Ernst Ruska (who constructed the first electron microscope in the 1930s), Gerd Binnig and Heinrich

[iii] A colloid is a suspension of particles in a medium, e.g. solid particles in liquid (sol), liquid particles in liquid (emulsion) or particles in gas (aerosol).

Rohrer (who developed the scanning tunnelling microscope (STM) in the late 1970s/early 1980s[43]) and they shared the 1986 Nobel Prize in physics for these efforts.[44]

Despite the fact that nanotechnology has been around for roughly 30 years, the European Commission only adopted an official recommendation for the definition of nanomaterials in 2011[45]:

> *"A natural, incidental or manufactured material containing particles, in an unbound state or as an aggregate or as an agglomerate and where, for 50 % or more of the particles in the number size distribution, one or more external dimensions is in the size range 1 nm - 100 nm."*

NPs are in principle particles of any material in the nanometer range. On the one hand, this very fine division of a material drastically increases its specific surface area which is critical for many applications. On the other hand, the specific domain of the nanoscale imparts exotic new properties to well-known bulk materials. This size domain bridges the regimes of single molecules and bulk materials. Nanoparticle properties can sometimes be regarded as one or the other, and other times as something completely different. This is where the real power of nanoscale materials lie - even more so because the nanoscale properties are not fixed but tunable.

The following sections will briefly describe concepts related to nanomaterials that make up a necessary foundation for the work presented.

1.2.1 Solution synthesis and NP formation

A range of approaches to the fabrication of NPs have been developed. These can be divided into top-down approaches, where bulk materials are divided into continuously smaller parts (e.g. mechanical grinding and etching), and bottom-up approaches, where NPs are built from smaller constituents such as molecules or atoms. Examples of bottom-up approaches are gas-phase reactions or high-vacuum methods (i.e. chemical vapour deposition, cluster sources, laser ablation, sputtering) or formation from dissolved chemicals in solution. The latter is often referred to as chemical synthesis, solution synthesis or "wet" synthesis of NPs and is the method employed in the current work.

Solution synthesis of NPs has drawbacks and advantages compared to other approaches. It is disadvantageous because 1) purification is challenging, 2) NPs in solution easily aggregate and 3) the simultaneous existence of a large number of chemical species and the complex mixture of chemical and physical processes make these systems very complicated and difficult to characterize and control. Solution synthesis can therefore appear less concrete and are teasingly referred to as art. Meanwhile, major advantages make it worth tackling these obstacles, such as 1) the use of traditional facilities and equipment well-established within chemistry, 2) the scalability of the syntheses, 3) the low requirements for

the input of external energy, 4) no requirement for surface immobilization, 5) the possibilities of post-formation particle modifications in situ, 6) high throughput compared to vacuum-based methods etc.

The current understanding of the solution synthesis process has its foundation in the studies of an analogues system by Gibbs. Gibbs described the thermodynamics of liquid particle formation in gaseous media providing a seed for the classical nucleation theory developed in the first half of the 20th century. The free energy of the bulk of the generated solid particles decreases with particle size while increasing high-energy solid-liquid interface has the opposite effect. The sum of surface and bulk considerations leads to an energy barrier corresponding to intermediate-sized particles that are energetically unfavourable.[46,47]

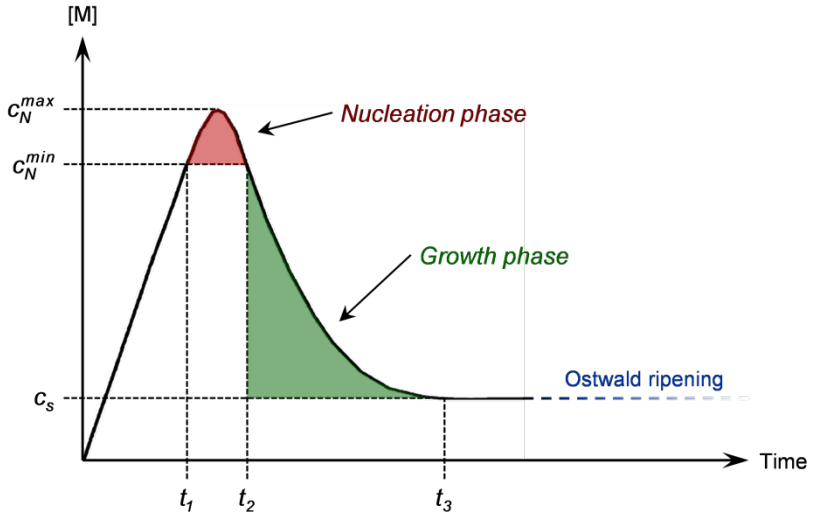

Figure 4. The LaMer diagram describing the formation of NPs in solution by the monomer concentration vs time. The nucleation phase (red) occurs between t_1 and t_2 during which the monomer concentration is above the critical nucleation limit, c_N^{min}. The growth phase (green) follows and ends at t_3 when the concentration reaches the solubility of monomer.[46,48]

LaMer and Dinegar published their complementary theory on hydrosol[iv] formation in 1950.[48] It is now widely accepted and has become the foundation of most experimental work on nanoparticle formation.[46,49-51] They studied the mechanisms leading to mono-dispersity in the formation of sulphur particles in ethanol but the model describes formation of solid particles in liquid in general. A non-soluble species is generated through chemical reactions or changes in solubility, i.e. a soluble *precursor* (e.g. $[AuCl_4]^-$) becomes an

[iv] A sol is a colloidal suspension of solid particles in a liquid medium. If the medium is water the suspension is a hydrosols. Today these systems are more commonly referred to as nanoparticle suspensions.

insoluble *monomer* (e.g. Au^0). Because the monomer is insoluble there is a potential to form a solid phase but due to the energy barrier described above this does not happen at concentrations immediately above the solubility of the monomer. Instead, the solution is supersaturated with monomer until a critical point where the high density of monomers enables the formation of nuclei large enough to cross the energy barrier. The limit is called the critical nucleation limit (c_N^{min}, Figure 4). The nucleation is a dramatic process which rapidly consumes monomer causing a decrease in concentration. Eventually, the concentration drops below c_N^{min} and no new nuclei are formed. The period during which nucleation occurs (t_1 to t_2, Figure 4) is called the nucleation phase. At the end of the nucleation phase, the solution is still supersaturated with monomer but no new nuclei can form. The remaining supersaturation is depleted by transfer of solvated monomer to the surface of existing solid particles during the growth phase.

The timing of the nucleation and growth phases is what governs mean particle size and dispersity. In broad terms, the particle concentration is determined in the nucleation phase where it grows from 0 to the final concentration, while the size is determined in the growth phase where concentration is constant but the size increases. The growth phase is dependent on the nucleation because the total growth depends on the amount of monomer left after nucleation. Reducing the nucleation phase leads to fewer particles that will grow bigger while increasing the phase results in more particles being formed with a smaller size. Meanwhile, nucleation is governed by the initial precursor concentration and the rate of monomer production, the latter of which can be controlled by the choice of reagents and reaction temperature. On the one hand, fast reactions provide a dominating nucleation phase and small particles. On the other hand, a dominating growth phase tends to produce monodisperse NPs as small NPs grow faster than larger ones. High concentrations of precursor can result in continued rapid supply of monomer and prolonged nucleation. In this case, nucleation and growth are not separate events and occur simultaneously. The size of a given particle then relates to the time of its nucleation. The nuclei formed early in the synthesis experience a longer growth phase and grow bigger than nuclei formed later leading to polydispersity.

The NP size distribution continues to develop even after the monomer concentration goes below the solubility limit in a process called Ostwald ripening. Adsorbed monomers are still in equilibrium with dissolved ones even if this is shifted very much towards the adsorbed state. The under-coordinated monomers on high-curvature surfaces of small NPs are higher in energy than ones on more flat large NPs, serving as a driving force for preferential adsorption of dissolved monomer on large NPs. As a consequence, the smallest of the NPs tend to shrink and dissolve (even completely) while the largest ones grow, and the size distribution shifts to larger sizes and narrows.

1.2.2 Nanoparticle stability

A widely used theory of colloidal stability was derived independently by and named after B. Derjaguin and L. Landau in Moscow[52] and E. Verwey and J. Overbeek in Eindhoven[53] in the 1940s, i.e. the DLVO theory. It describes the stability of colloidal systems as a balance between attractive and repulsive forces. Nanoscale metallic surfaces are inherently unstable due to the high interfacial energy of the metal-solvent interface. This effect is extremely pronounced for nanoparticles that contain high energy facets, edges and corners. There is a high driving force to eliminate these interfaces by aggregation. The attraction between the metal surfaces leads to instability of the nanoparticle suspension. Adding repulsion between the nanoparticles counters the attraction and is generally obtained through two different strategies of surface coating, i.e. electrostatic and steric stabilization. DLVO theory only deals with electrostatic stabilization but the way of evaluating colloid stability can also be applied to steric stabilization. Adding charged molecules to the metal surface creates an electric field around the particles and electrostatic repulsion between them. Two particles approaching each other will at the same time experience an increasing attraction between the metal surfaces and an increasing repulsion of the charged coating layers. The balance between these forces will dictate whether the suspension is stable or unstable, Figure 5.

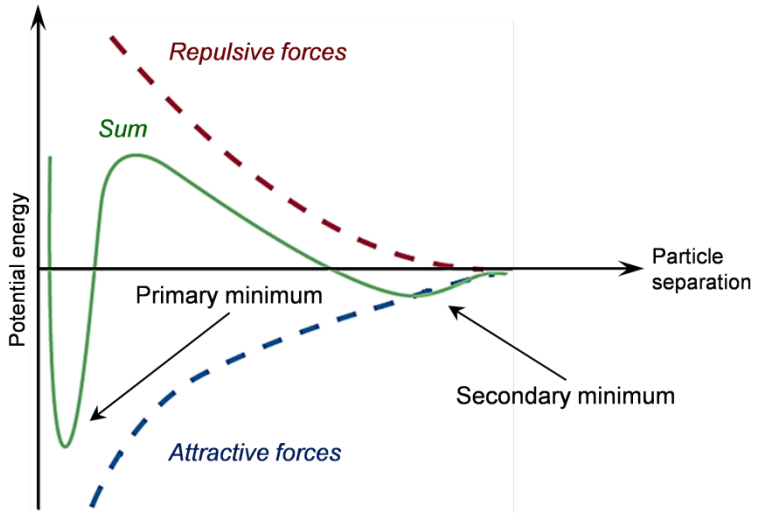

Figure 5. A representative DLVO diagram of particle stability showing potential energy as function of particle separation. The sum (green) of repulsive (red) and attractive (blue) forces reveal minima in the potential energy corresponding to aggregation (primary) and flocculation (secondary).[54]

The attraction increases with interparticle distance more drastically than the repulsion. This means that approaching particles will eventually experience a net attractive force no matter the repulsion. However, the repulsive forces may dominate at greater distances where the

attractive forces are weak. The interplay between attraction and repulsion results in a barrier of net repulsive force that needs to be overcome for particles to approach each other and aggregate. Many factors will influence this balance. Charged species in the solution, i.e. the ionic strength, contribute to a shielding of the electrostatic field around the particles effectively lowering the energy barrier for aggregation. This is an important effect to keep in mind when working with electrostatically stabilized nanoparticles. The kinetic energy of the particles determines the probability that two approaching particles can overcome the energy barrier. Increasing the temperature and thus the kinetic energy decreases the stability of the suspension.

An alternative stabilization strategy is to stabilize the suspension by steric rather than electrostatic effects. The NPs are coated with large, bulky polymers that generate a physical barrier between two approaching particles. Compression of the polymer coatings is not favourable in terms of sterics and entropy leading to NP stabilization. In contrast to electrostatic stabilization, sterically stabilized suspensions are not sensitive to ionic strength. However, this does not apply to particular polymer coatings where charged side groups add to the stability in which case ionic strength will have an effect.

1.3 Characterization and functionality

Three techniques have played a central part in all studies of nanomaterial preparation and characterization in this project; Ultraviolet-visible (UV-vis) spectroscopy, nanoparticle tracking analysis (NTA) and transmission electron microscopy (TEM). They provide crucial information on precursor conversion, formation kinetics NP size and shape.

However, the present work involves a broad range of techniques for the evaluation of syntheses and characterization of dynamics, structure, morphology and properties of synthesized nanomaterials. These include **electrochemical techniques**, i.e. cyclic voltammetry (CV), chronopotentiometry (open-curcuit potentiometry, OCP), time-resolved pH and time-resolved conductivity, **microscopies**, i.e. scanning electron microscopy (SEM) and scanning transmission X-ray microscopy (STXM), **spectrometries**, i.e. attenuated total reflectance Fourier transform infrared spectrometry (ATR-FTIR), fluorescence spectrometry, X-ray absorption spectrometry and mass spectrometry (MS), **diffraction/scattering**, i.e. X-ray powder diffraction (XRPD) and nephelometry, and **chromatographies**, i.e. ultra-high pressure liquid chromatography (UPLC), gas chromatography (GC).

1.3.1 Ultraviolet-visible spectroscopy

UV-vis spectroscopy is a must-have when working with solution synthesis of nanomaterials. Light is passed through a cuvette (most often quarts) containing a solution to be characterized. The amount of light that is transmitted on the other side of the cuvette is measured and converted to absorbance as a function of wavelength (or energy). Spectrometers generally come in two different modes of operation. One mode uses a monochromator placed just after the light source exposing the sample to a fixed wavelength. The wavelength can then be scanned to cover the desired spectrum range. In the other mode, the sample is irradiated with white light, an optical grating behind the sample splits the light, and all wavelengths are recorded simultaneously by a photodiode array (PDA) detector. In principle, the scanning system is a bit slower but more precise than the PDA system. However, for most general nanoparticle characterization uses, both are suitable.

The optical behaviour of nanoparticle suspensions provides information very fast. It reflects reaction yield, nanoparticle size and shape, aggregation and band gap.

Light consists of electromagnetic waves from which an oscillating electric field emanates. When these waves hit a metallic surface, the electric field interacts with the “sea of electrons” among the atomic nuclei. This generates plasmons (oscillations of electrons) that propagate along the surface. Certain conditions relating to wavelength and optical properties of the metal lead to resonance. Nanoparticles as opposed to bulk metals have a finite extension of the surface which localizes the plasmons on the particle. At resonance, excitation of the plasmons results in very high light absorbance. The phenomenon is known as localized surface plasmon resonance (LSPR), Figure 6, and cause a peak in the UV-vis spectrum, the LSPR peak. The electronic properties of the nanoparticles are strongly correlated with shape, size, surface morphology, surface composition, surface ligands, aggregation and particles in close proximity. Thus, the structure and position of the LSPR peak can provide detailed information about the nanoparticles. As illustrated in Figure 6, surface plasmons of anisotropic structures (e.g. rods or platelets) exhibit resonance at more than one condition. Nanorods, for example, can be polarized while being oriented with the long axis along the beam direction which is similar to the isotropic case; transverse LSPR ($LSPR_{trans}$). They can also be polarized with the short axis along the beam direction which requires less energy giving rise to a peak at longer wavelengths than the $LSPR_{trans}$; longitudinal LSPR ($LSPR_{long}$).

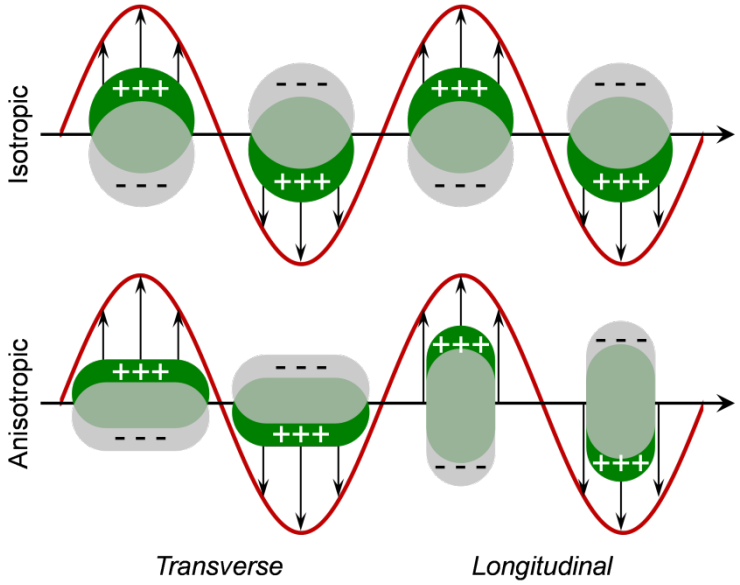

Figure 6. Illustration of localized surface plasmon resonance (LSPR). The alternating direction of the electric field emanating from the electromagnetic radiation excites surface plasmons of the metallic NP. Anisotropic NPs give rise to several resonance conditions depending on their orientation relative to the light beam.[55,56]

NP suspensions often exhibit very strong absorption and scattering (collectively describes as extinction) and must be diluted for UV-vis measurements. In the current work, the dilution factor is often multiplied to the measured data to represent the conditions in the samples and allow for comparison between data and systems. In such cases, a dilution factor of *X* is given in the figure legend as "*(dil: X)*".

1.3.2 Nanoparticle tracking analysis

NTA is a laser-based nanoparticle sizing technique developed by Nanosight (now part of Malvern Instruments Ltd., Malvern UK). Similar to dynamic light scattering (DLS), NTA is based on Brownian motion of nanoparticles suspended in liquid. Brownian motion is the random movement of particles caused by collisions with the molecules of the medium. The sample is injected into a laser block as a thin film between two quarts plates. A narrowly focused laser beam is scattered off of the suspended particles. The scattered light is magnified by a microscope and recorded by a charge-coupled device (CCD) camera, Figure 7. The recorded video is subsequently processed during which the NTA software tracks every individual particle from frame to frame thus determining their speed.

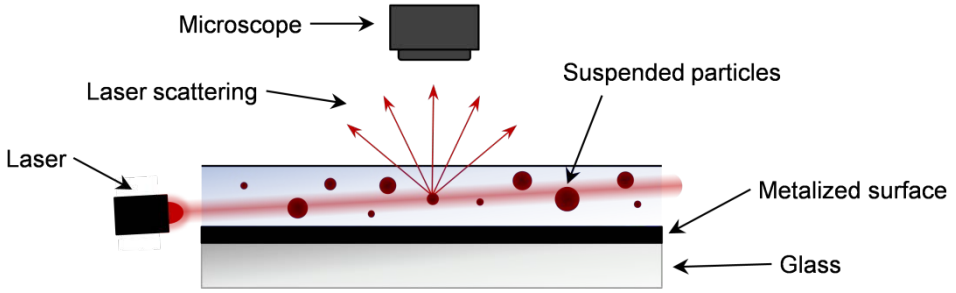

Figure 7. Scheme of the NTA technique. A narrow laser beam is scattered by NPs in suspension and the scattered light recorded through a microscope.[57]

The distance travelled over time is directly correlated with the hydrodynamic diameter by Eq. (1.1) derived from the Stokes-Einstein equation.[58]

$$\overline{(x,y)^2} = \frac{4k_B T}{3d_h \pi \eta} \qquad (1.1)$$

where $\overline{(x,y)^2}$ is the mean-squared speed of a particle with hydrodynamic diameter d_h moving under Brownian motion in a medium with viscosity η at temperature T. k_B is the Boltzmann constant. The hydrodynamic diameter is the diameter of a hypothetical sphere diffusing with the same speed as the particle being measured. Regarding colloids, this number is affected by the nanoparticle core, coating shell, adsorbed ions, hydration and the electric double layer. The d_h is therefore larger than the measured size of the metal (or metal-based) nanoparticles from electron microscopy, where often only the dense core is observed. Charged particles have a significant electric double layer around them and the d_h can be affected by ionic strength. The starch-coated particles presented in this work are sterically stabilized and largely neutral, so ionic species of the medium moving with the particles do not contribute significantly to the measured size. The d_h of our starch-coated nanoparticles can be regarded roughly as the core plus the hydrated coating layer.

In this work, NTA data are presented in composite plots. A histogram shows the raw data of all measured particles while an overlaid, filled curve presents the derived “true” size distribution produced by the NTA 3.0 software. An inset provides an intensity plot, which is a key feature of NTA data. The intensity of each measured particle is plotted against its size generating a scatter plot of intensity populations. This extra information is very helpful in evaluating the data and distinguishing different materials. Two nanoparticle populations of different materials might be indistinguishable by size, but show different relative intensities.

1.3.3 Transmission electron microscopy

The transmission electron microscope (TEM) was a key factor in the boom in nanotechnology during the last century by offering the ability to *see* at the nanoscale. The interactions of a beam of electrons with a nanosized sample are utilized to create images in the TEM in much the same way as the interactions of light with an overhead slide create an image on a screen.

According to de Broglie, electrons behave like both particles and waves. Their wavelength, λ_e, is related to their velocity which in the TEM depends on the accelerating voltage giving the following expression[59]:

$$\lambda_e = \frac{h}{\sqrt{2m_e eV}} \tag{1.2}$$

where h is Planck's constant, m_e electron mass, e the elementary charge and V the accelerating voltage. The electrons in the TEM however travel at speeds approaching the speed of light and relativistic effects have to be considered resulting in a de Broglie wavelength of about 2-3 pm. This is one of the key factors to the high resolution of TEM.

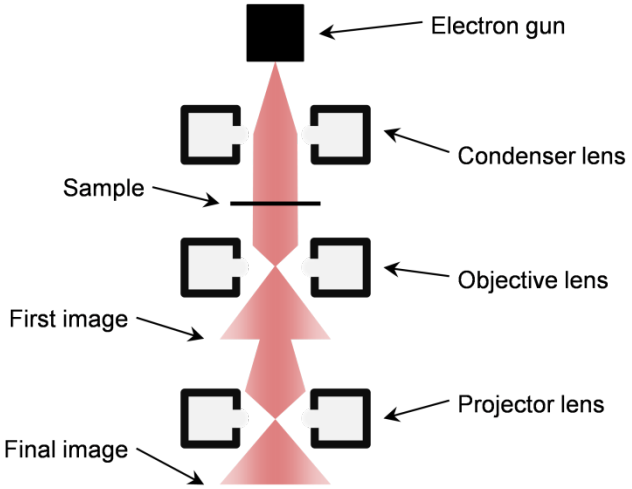

Figure 8. Simple schematic representation of the TEM. The electrons are extracted and accelerated from the source (gun) and the beam (red) passed through a series of lenses manipulating the electron beam.

A simple representation of the TEM is shown in Figure 8. An electron beam is generated at the source (gun) at the top of the microscope. This can be a thermionic gun in which electron are extracted from a hot filament (LaB_6 or W) or a field emission gun where the source tip is especially engineered for electron extraction. The electrons are generally accelerated by an accelerating voltage of 120-300 kV. The beam is manipulated by a series

of electromagnetic lenses and apertures as it passes through the column and the sample. The beam finally reaches a luminescent screen for direct viewing or a camera for digital acquisition of data. Everything is carried out at ultra-high vacuum (UHV) conditions.

The complicated interactions of electrons with matter can be exploited to perform a range of measurements relating to microscopy, spectroscopy and scattering/diffraction at the same time. The most commonly used technique apart from standard imaging is energy-dispersive X-ray spectroscopy (EDX or EDS). When the high-energy electrons pass through the sample, they can “kick out” core electrons of the sample atoms. Outer shell electrons will relax into the created hole and emit X-rays with characteristic energies corresponding to the energy difference between the outer shell and the core. These discrete energy levels are element specific and can be used to identify the element from which the X-rays were emitted. X-rays can be collected during TEM studies to identify which elements are present in the electron beam illuminated area and are presented as EDX spectra with X-ray counts vs X-ray energy. Because the interactions of electron with matter are complex, a number of effects need to be considered when evaluating EDX spectra. Secondary X-rays are generated outside the illuminated area, e.g. by X-ray initiated ejection of core electrons or scattered electrons. Consequently, background signals from elements present in high amounts will always be present in the spectra. This mainly relates to the TEM grid material (which is Cu in the present work) but also other components of the TEM.

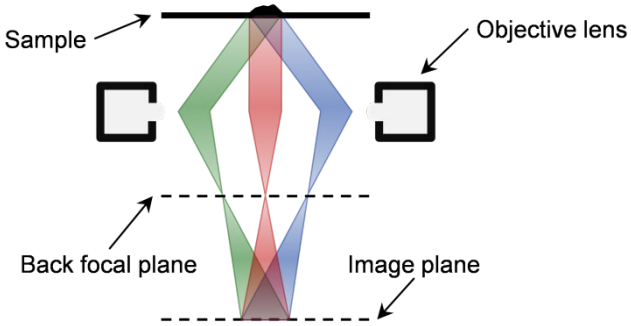

Figure 9. The positions of the back focal and image planes below the sample in the TEM. The image plane is put in focus for imaging and the back focal plane for diffraction experiments.

The electron wave also experiences diffraction when it passes through the sample giving rise to interference effects. If a material consists of a regularly repeating pattern of diffraction points (atoms in a crystal lattice), spots will appear in the back focal plane of the microscope, Figure 9. The distance between equivalent points in the lattice determines the angle of diffraction and the distance of the spots from the center of the diffraction image - the larger the distance in the lattice the shorter the distance from the center in the diffraction image. In this way, diffraction represents the crystal structure in so-called reciprocal space.

The collection of many diffraction spots, the diffraction pattern, is an image of part of the reciprocal space and contains information on the crystal structure from which they arise. This phenomenon is used in TEM and the technique known as selected area electron diffraction (SAED). A selected area aperture is placed after the sample selecting only diffraction from a small section of the sample. The back focal plane is placed in focus and the diffraction pattern recorded. The positions of the spots in the diffraction pattern provide information about plane spacings in the crystals within the selected area and the orientations of the corresponding crystals. This is useful for identifying crystalline material and NP facets.

As seen from Figure 9, both diffracted and transmitted electrons make up the image in standard imaging mode. The contrast of the image can be enhanced by using an objective aperture to block diffracted electrons, Figure 10 left, known as a bright field (BF) image.

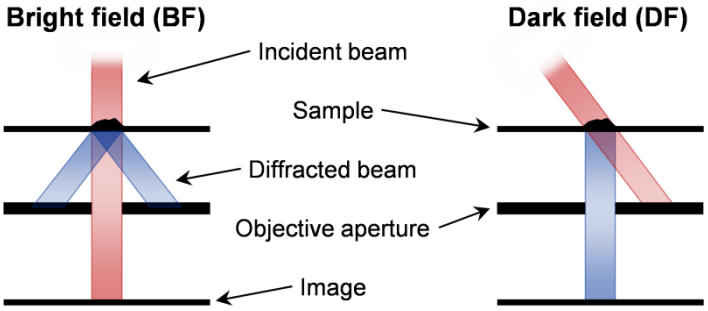

Figure 10. Illustration of BF and DF imaging where the objective aperture selects the direct (not diffracted) beam or diffracted beam, respectively.

A related technique, dark field (DF), utilizes only specific diffracted electrons rather than transmitted electron for imaging. In so-called on-axis DF, the incident beam is tilted to make the diffracted beam parallel to the column, Figure 10 right. The beam is tilted in diffraction mode to place a specific spot in the centre of the screen. The objective aperture is placed around the spot blocking the transmitted beam and other diffracted beams. Now intensity in imaging mode only comes from areas of the sample able to diffract electrons in the specific direction of the chosen diffraction spot. This generates an image with a dark background and bright areas of certain crystalline structure and orientation. Such images are very useful for highlighting the location of certain crystalline elements in complex nanomaterials.

The last TEM technique employed in the present work is scanning TEM (STEM). The electron beam is focused into a small probe which is raster scanned across the sample to generate an image by the use of a high angle annular dark field (HAADF) detector. This is a ring-shaped detector placed below the sample detecting electrons diffracted at high angles. The intensity of each point in the STEM image represents the counts on the HAADF

detector from that area. High angle diffraction is highly dependent on atomic number so STEM provides high Z contrast relative to standard TEM making it useful for distinguishing materials of different atomic number. STEM also gives very sharp images of metal NPs on carbon-based materials due to the large difference in atomic number.

All treatment of TEM data was done with ImageJ 1.46r.[60] Particle size was analysed by hand or by an automated procedure. The latter was done with the *analyse particles* in ImageJ. A high contrast (black and white) image is generated to make particles black on a white background. The area of each particle is then measured automatically using two parameters, i.e. range and circularity. Range defines an area range outside which particles are not being counted. This is optimized to exclude noise (mainly single black pixels) in the lower end and aggregates in the higher. Circularity defines a requirement for particles to appear circular. This is optimized to exclude touching particles and aggregates. Range and circularity parameters are given in the legends of size distributions obtained through this method. Finally, area is converted to diameter by assuming sphericity.

1.3.4 Electrochemical techniques

A number of electrochemical (EC) techniques were used. Chronopotentiometry as well as time-resolved pH and conductivity measurements were used to monitor the formation of AuNPs. Figure 11 shows the two-electrode setup employed for chronopotentiometry where the potential of the working electrode (WE) relative to the reference electrode (RE) is recorded as function of time. No counter electrode (CE) was used and no current passed during measurement. This particular chronopotentiometric method is called open circuit potentiometry (OCP). A Ag/AgCl or reversible hydrogen electrode (RHE) was used as RE and a polished basal-plane graphite (BPG) electrode as WE.

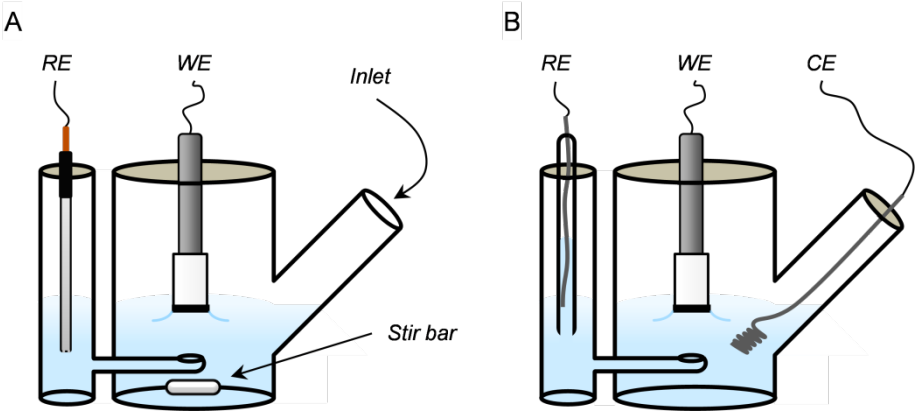

Figure 11. Schematic of the setups used for (A) chronopotentiometry and (B) cyclic voltammetry.

The BPG surface was considered inert so changes in potential as a result of surface changes on the BPG was neglected. Thus, any observed changes in potential reflected changes to the redox species in solution. The experiments were carried out with magnetic stirring.General electrochemical characterization of synthesized nanomaterials was done with cyclic voltammetry (CV), a broadly applicable and powerful tool in EC. This is a 3-electrode method in which current between WE and CE is recorded as function of potential controlled relative to the RE, Figure 11B. The potential is scanned linearly from the starting potential, E_{st}, to the lower vertex potential, E_{LV}, where the direction is reversed and the potential scanned to the upper vertex potential, E_{UV}, before again changing scan direction to end at the end potential, E_{end}, Figure 12A. This constitutes one of several cycles being recorded for a CV measurement. The data is presented as cyclic voltammograms with current vs potential as in Figure 12B.

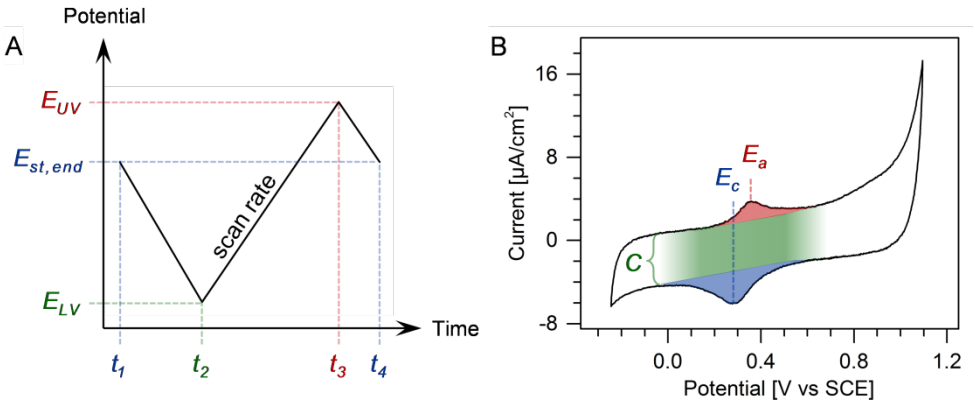

Figure 12. (A) The applied potential changes during one cycle of a CV measurement. The potential is scanned at a constant scan rate between the upper lower vertex potentials and generally several cycles are recorded. (B) A representative CV showing a redox signal. An anodic peak (red), cathodic peak (blue) and capacitance (green) is indicated on the figure.

The start and end potentials are often chosen close to the OCP, where the WE is not significantly polarized. The vertex potentials depend on the specific system being investigated and define the “potential window” through which the system is observed. The last configurable parameter for standard measurements is the potential scan rate indicated by the slope on the curve in Figure 12A. Depending on the system and purpose of the measurement this can range from a few mV/s to many V/s. The scan rate was 10 or 50 mV/s for the CV studies in the current project.

Scanning the potential away from the OCP polarizes the electrode surface which leads to oxidation and reduction of redox active chemical species at sufficient polarizations. Redox reactions give rise to a current increase and the appearance of anodic (red, Figure 12B) and

cathodic (blue, Figure 12B) peaks for oxidation and reduction, respectively. For a given redox couple, oxidation happens at the anodic peak potential, E_a, reduction at the cathodic peak potential, E_c, and their standard reduction potential is the average of the two. The area under the peaks represents the total charge being transferred in the process and can in some cases be used to calculate the exact number of redox units or molecules that are on the surface if the redox process is known. The redox peaks in Figure 12B arise from functional groups on the BPG. The electrode polishing process preceding every EC measurement produces a small number of "dangling bonds" that are oxidized to produce redox active functional groups during scanning above roughly 600 mV vs saturated calomel electrode (SCE). Non-faradaic current contributions from charge being accumulated on the surface give rise to capacitive signals in CVs (green, Figure 12B).

The equilibrium potential of a given redox couple is described by the Nernst equation and depends on the number of electrons involved in the redox process *n*, the standard reduction potential of the couple E^0 and the chemical activity of the reduced and oxidized forms. In dilute systems the chemical activity can be regarded as equal to concentration.

$$E = E^0 - \frac{RT}{nF} \ln\left(\frac{[Red]}{[Ox]}\right) \tag{1.3}$$

where R is the gas constant, T temperature and F Faraday's constant.

Time-resolved pH was measured using a glass pH electrode calibrated with standard solutions at pH 4.01, 7.00 and 10.01 (DIN 19266, NIST)[v] and conductivity with a conductivity probe calibrated with prepared standards of KCl and NaCl. Both sensors were from Vernier Software and Technology (Beaverton Oregon, USA).

1.3.5 X-ray techniques

X-rays are electromagnetic radiation with wavelengths ranging from pico- to nanometers and energies from 100 eV to 100 keV. The high energy end of the range has wavelengths on the atomic scale making them useful for diffraction experiments. At the same time, X-rays cover the energy range of core-level ionization of many elements which is exploited in X-ray spectroscopic techniques.

The principle of X-ray diffraction is very similar to electron diffraction described in section 1.3.3. SAED is extremely local providing information on the nanoscale while X-ray diffraction can be used to study mg-sized samples. Bragg's law describes the conditions leading to constructive interference of the diffracted X-rays:

[v] DIN and NIST refer to the national standardization bodies *Deutsche Institut für Normung* (Germany) and *National Institute of Standards and Technology* (USA), respectively.

$$\lambda = 2\,d_{hkl}\sin(\theta) \tag{1.4}$$

where λ is the X-ray wavelength, d_{hkl} the distance of (hkl) planes and θ half the angle of observed constructive interference. In the present work, X-ray powder diffraction (XRPD) is used to study crystal structures of nanomaterial powders. A large number of randomly oriented crystallites are present in the powder sample and all possible Bragg conditions are fulfilled. The powder diffraction patterns in reality consist of many diffraction rings but are represented as Fourier transform spectra. Rietveld refinement is a technique in which powder patterns are fitted using already known crystal structures. In the present work, this method was used to extract crystallite sizes and relative content of different phases in mixed samples. The refinements presented in this work were carried out in close cooperation with PhD student Jonas Andersen at DTU Chemistry. XRPD patterns were obtained using a Huber (Rimsting, Germany) G670 Guinier imaging plate camera and Cu$K\alpha_1$ radiation. Powder is pressed into a thin disk in the hole of a copper ring and suspended between two pieces of Scotch tape. The samples were mounted at 45 ° relative to the X-ray beam and rotated during data collection.

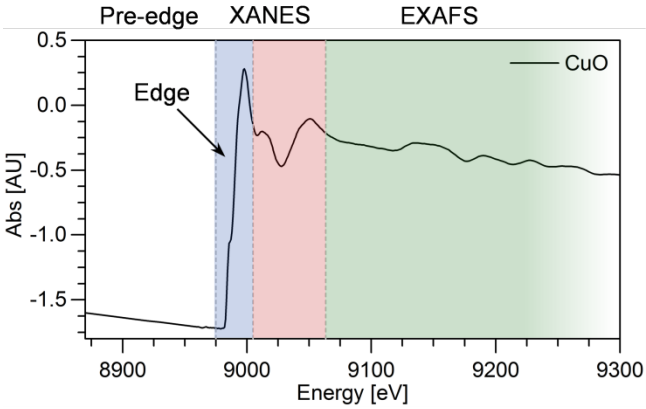

Figure 13. X-ray absorption spectrum of CuO K-edge highlighting the range of XANES covering the edge (blue) and near-edge fine structure (red) and EXAFS dealing with extended fine structure region (green). The shown spectrum is obtained from the CARS database from the University of Chicago.[61]

In an X-ray absorption spectroscopy experiment, a sample is irradiated with monochromatic X-rays and transmission recorded to measure absorbance. The energy of the incident X-rays is scanned to cover an energy spectrum of interest. X-rays of sufficient energy can be absorbed by core electrons of the sample and excite them to a continuum state generating so-called photoelectrons. This happens at well-defined energies due to the discrete energy levels of electrons of specific elements. As a consequence strong absorbance by a given element is observed at certain X-ray energies characteristic for that element and an *edge* appears in the spectrum. The absorption spectrum is generally divided

into X-ray absorption near-edge spectroscopy (XANES) providing information about coordination and oxidation state and extended X-ray absorption fine structure (EXAFS) that holds information about the structure of the local environment around the atom.

During the work at SINAP in 2012, two days of experiments were conducted at the Shanghai Synchrotron Radiation Facility (SSRF). Simply put, a synchrotron is a particle accelerator. Electrons are accelerated and injected into a large storage ring where the constant bending of the electron path causes emission of X-rays in a very broad energy range (so-called “white light”). Workstations are set up around the perimeter of the ring to utilize these X-rays in an array of techniques some of which use hard (high energy) X-rays and others soft (low energy). The experiments presented in this work were carried out at two such workstations at the SSRF; the hard X-ray micro-focus beamline (BL15U1) and soft X-ray spectromicroscopy beamline (BL08U1A). The work at BL15U1 included X-ray absorption spectroscopy and diffraction experiments.

X-rays of 250-2000 eV are available at BL08U1A and generally used to image biological material. The beam is focused to a small probe which is scanned across the surface while the transmitted X-rays are being detected. A 2-dimensional image of transmitted X-ray intensity is generated similar to the principle of STEM. The spatial resolution of the maps is governed by the probe and was 30 nm at BL08U1A. The energy of the X-rays can be tuned very precisely enabling spectroscopic information in 2-dimensions. Two STXM techniques were utilized; stack imaging and dual-energy contrast imaging. In stack imaging, many STXM images are recorded at different energies covering an energy range of interest. Combining (*stacking*) all these images provides local X-ray absorption information in the covered energy range in 2-dimensions. The result is a map of the spatial distribution of chemical species. Dual-energy imaging is an alternative technique and can be used if the position of the X-ray absorption spectral feature is known. Two images are recorded at energies just below and on top of an absorption edge of a given element. Areas of the image where this element is present will exhibit a large difference in intensity while the difference in areas with other elements will be small. The contrast difference in the two images therefor maps the distribution of that specific element.

1.3.6 Other optical techniques

A broad range of interactions occur between electromagnetic radiation and matter which can be used in a range of techniques to study structure and properties of materials. Several techniques were utilized in the present work, i.e. infrared spectroscopy, fluorescence and nephelometry as well as UV-vis and X-ray techniques already described.

The infrared spectrum follows the visible spectrum at lower energies. For historical reasons, infrared radiation is described by wavenumbers (cm^{-1}) rather than wavelength or energy and spectra are often presented going from high to low wavenumbers from left to

right. The infrared spectrum ranges from about 12500 cm^{-1} (800 nm) to 200 cm^{-1} (50 µm) and is divided in a near-, mid- and far-infrared. Mid-infrared is the most widely used covering 4000-200 cm^{-1}. The energy of infrared light can excite vibrational modes of molecules and minerals, e.g. bond stretching, bending, rocking, twisting and wagging. The specific positions of excited vibrational modes can be used for structure identification.

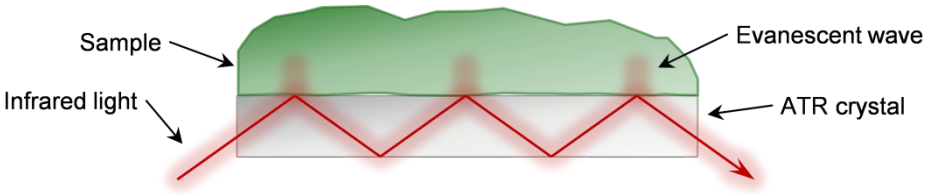

Figure 14. Illustration of the ATR-FTIR setup in which the infrared light (red) is reflected off of the interface between ATR crystal (grey) and sample (green) giving rise to evanescent waves.

An attenuated total reflectance Fourier transform infrared spectroscopy (ATR-FTIR) setup was used in the present project allowing for measurement directly on solid samples. A dense layer of solid sample is pressed on top of an ATR crystal transparent to infrared radiation. The crystal is illuminated from below at an angle and the light is reflected at the interface between crystal and sample followed by detection. A so-called evanescent wave is created at the interface giving rise to interaction with the sample over a few microns.

Another type of excitation is studied with fluorescence spectroscopy. An electron is excited by absorbing a photon of specific energy corresponding to the difference in ground state and excited state. The excited state decays partially by vibrational relaxation followed by radiative relaxation from a lower level back to the ground state. The final relaxation is accompanied by the emission of a photon with lower energy (higher wavelength) than the exciting photon. The fluorescence spectrometer measures the absorbed light (in the same way as a UV-vis spectrometer) by comparing the incident and transmitted light. Fluorescent emission is monitored through a detector placed at 90 ° relative to the incident light. In practice, either emission or excitation is kept at a fixed value while a spectrum of the other is recorded.

Finally, turbidity was employed to study NP formation. Turbidity is a measure of the scattering ability of a medium and is traditionally used to evaluate water quality by the content of particles. A nephelometer measures the turbidity of a solution by measuring the amount of scattered light from a NIR diode at 90 °. The measurements from the turbidity sensor employed here however were not simple. The presence of scatterers in the solution increases the intensity of light reaching the detector as expected but the opposite occurred for absorbers. Careful study of the setup determined that in all cases light from the diode is

reflected at the interface between the glass vial and solution. Solution that absorbs light at the diode wavelength decreases the amount of reflected light leading to negative turbidity relative to ultrapure water which is defined as '0'. Consequently, the "turbidity" measurement is in reality a combination of absorption and scattering contributions with opposite effect.

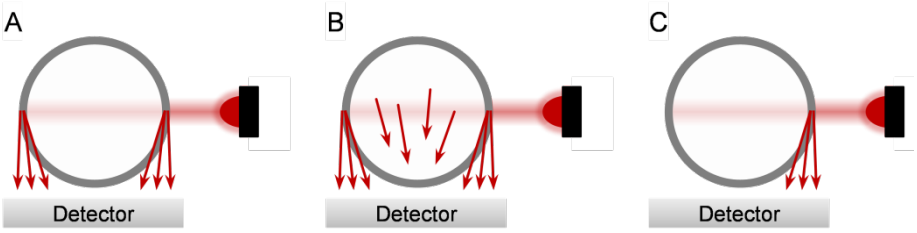

Figure 15. The principle of turbidity measured with the nephelometer. (A) Reflected light from the glass-solution interface is defined as 0 nephelometric turbidity units (NTU), (B) scattering solution leads to positive turbidity while (C) absorbing solution leads to negative turbidity.

Chapter 2

Control of gold nanostructure synthesis

2.1 Mechanisms of gold nanoparticle formation

Modern technology relies increasingly on nanomaterials as catalysts. Nanomaterial properties depend on size, shape and composition. Control of these parameters is therefore vital and can only come from a deep understanding of the processes involved. Efforts towards disclosing the complex formation of NPs in solution were taken in the present work using AuNPs as a model system.

The study of particle formation by LaMer and Dinegar[48] (described in section 1.2.1) provides a foundation for understanding solution synthesis of NPs but only in very broad terms. Modern NP syntheses are complex and employ capping and structure directing agents allowing for the preparation of an endless number of NP morphologies and sizes. This variety cannot be explained in terms of the LaMer model. Since the 1950s, few advances have been made to the understanding of NP formation. The "organizer" scheme was proposed by Turkevich et al.[62] in which a polydentate "organizer molecule" builds up a network cluster of metal ions and organizer. When the cluster reaches a size needed for a stable nucleus, the organizer (also acting as reducing agent) reduces the metal ions to form a metal nucleus. The organizer employed was citrate and their synthesis became one of the most studied and reliable methods for AuNP formation still widely used today and known as the Turkevich or citrate method. A mechanism involving autocatalysis was proposed by Watzky and Finke[63] (the first advance in 45 years) and their model was later shown to describe the observations of Turkevich very accurately.[64] Their model was based on growth of the nuclei through surface catalyzed reduction rather than reduction in solution followed by monomer diffusion to the NP surfaces.

Watzky and Finke monitored the formation of Ir nuclei indirectly by measuring hydrogenation of cyclohexene catalyzed by the nuclei. Direct in situ methods has only been used since the late 2000s, Table 1.

Table 1. Summary of reports on situ study of AuNP formation. Techniques in bold refer to the use of synchrotron radiation.

	Authors	Technique	Time-resolution	Year
1	B. Pong et al.[65]	UV-vis, TEM	5 s [a]	2007
2	X. Ji et al.[66]	UV-vis, TEM	10 s	2007
3	B. Abécassis et al.[67]	UV-vis, **SAXS**, **WAXS**	3 , 130, 800 ms	2007
4	B. Abécassis et al.[68]	**SAXS**, **WAXS**	130 ms	2010
5	J. Polte et al.[69]	**SAXS**, **XANES**	≈ 3 min [a]	2010
6	J. G. Parsons et al.[70]	**XAFS**	15 min [a]	2010
7	J. Polte et al.[71]	SAXS	100 ms	2010
8	Y. Fong et al.[72]	**XPS**	60 s	2011
9	T. Tanaka et al.[73]	**XAFS**	100 ms	2012
10	J. Ma et al.[74]	**XAFS**	> 30 min	2013
11	M. A. Uppal et al.[75]	UV-vis	70 s	2013
12	Present work[76]	OCP	100 ms	2013
		Turb., cond., pH	500 ms	
		UV-vis	20 s	

[a] Sampling frequency is not given directly in the reference.

These studies solely utilize UV-vis or X-ray techniques such as small-angle (SAXS) or wide-angle X-ray scattering (WAXS), XANES and X-ray absorption fine-structure (XAFS) supported by ex situ TEM. UV-vis spectroscopy is good due to its wide availability, fast data acquisition and sensitivity but has limitations. It is often necessary to take out aliquots and dilute these for measurement, something modern instruments are tackling with the use of optical probes (in situ) and high-absorbance capabilities (for concentrated samples). The main problem with UV-vis spectroscopy for studying NP formation is that many species present in the reaction medium absorb light in the same UV-vis range and themselves change during formation. This leads to limitations in data interpretation and UV-vis spectroscopy cannot be used on its own. The X-ray based techniques are excellent as they directly provide information about coordination around the metal, metal oxidation state, cluster size and cluster concentration. The downside is that the fast processes of NP formation demands rapid sampling and the use of synchrotron radiation to obtain a high enough signal on a millisecond timescale, Table 1. Less than 50 synchrotrons exist in the world (less than 20 in Europe)[77] and availability is limited and access/experiments time consuming. Polte et al. overcame the need for synchrotron radiation by employing a continuous-flow mixing setup, entry 7 Table 1. SAXS was measured on the flow at

different distances from the point of mixing. This corresponded to measuring the reaction at different times. Continuous supply of fresh mixture (all at the same stage of formation) made it possible to collect data long enough (several minutes) for analysis with an in-house SAXS instrument and still with a 100 ms time-resolution.

Despite the advances no clear understanding of the NP formation processes exists mainly due to limitations in techniques able to follow them.[64,73,78] The present work explores the potential of readily available EC and optical techniques for in situ monitoring of NP formation. Preliminary studies were done prior to the PhD project during which deeper investigation was undertaken.

2.1.1 The AuNP synthesis method

A green synthesis protocol for the preparation of AuNPs was developed in the group in 2009[79] based on vegetable extract from potato, onion, carrot and seaweed inspired by a report by Liu et al.[80] Starch and glucose were identified as possible capping and reducing agents present in all tested vegetables and the refined procedure based on these reagents in buffered media was successful. This method proved to be versatile and applicable for the synthesis of many different metal and bimetallic nanostructures. The term *saccharide-based approach to metallic nanostructure synthesis* (SAMENS) was used to encompass all these syntheses. The SAMENS AuNP synthesis is similar to a method developed by Raveendran et al. with the defining difference being the use of buffered media to control reaction conditions. Different buffers were tested. Reaction was especially fast in 2-(*N*-morpholino)ethanesulfonic acid (MES) because MES itself reduced the Au precursor at a higher rate than glucose.

Scheme 1. Components of the MOS synthesis (1-4) and the OBS synthesis (1-2).

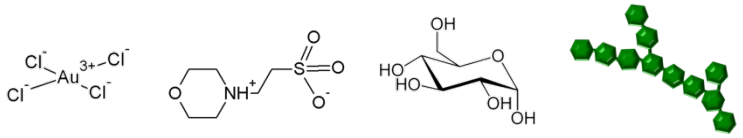

(A) $[AuCl_4]^-$ (B) MES (C) Glucose (D) Starch

Two different syntheses were chosen for the study of NP formation, Scheme 1; (1) *the MES-optimized synthesis* (MOS) with standard conditions incl. starch, glucose and MES and (2) *the only buffer synthesis* (OBS) where focus was on the reaction between buffer as reducing agent and precursor, and no other components were used. The Au precursor reacts with the aldehyde of glucose to form gluconic acid, Scheme 2A, and with the amine of MES to form an N-oxide (MES_{OX}), Scheme 2B.

Scheme 2. Total reactions between the Au precursor and (A) glucose or (B) MES. Only the aldehyde/acid of the glucose/gluconic acid molecules is shown. R_2 = ethanesulfonic acid.

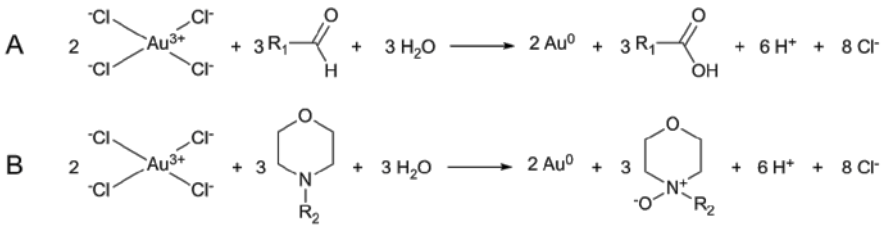

The precursor dissociates completely under conditions relevant here and exist mainly as $[AuCl_4]^-$ but the reactive species is $[AuCl_3OH]^-$. The latter is formed by ligand substitution with water and subsequent deprotonation, Scheme 3A.[81-83] The increased rate of reaction for MES is considered to be related to a formation of an intermediate where the ring-O of the morpholine moiety coordinates to $[AuCl_4]^-$ or $[AuCl_3OH]^-$ perpendicular to the plane making a pentacoordinate complex. This positions the N in a position favourable for attack by a hydroxo ligand. Similar intermediates have been reported for related reaction with Au^{3+}.[82,84]

Scheme 3. (A) Activation of Au precursor through ligand substitution. (B) Complete reduction of the Au precursor. (C-D) Stepwise reduction of the Au precursor via a Au^+ intermediate.

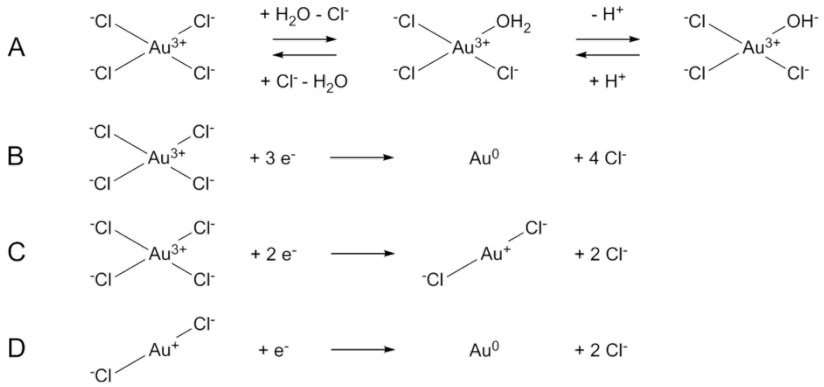

The Au precursor can be reduced to metallic gold in one step by acquiring 3 electrons, Scheme 3B, or in two steps via $[AuCl_2]^-$, Scheme 3C-D. The standard reduction potentials for (B-D) are 1.00, 0.929 and 1.154 V vs SHE, respectively,[85] which is strongly reflected in the time evolution of the equilibrium potential during AuNP formation, cf. next section.

2.1.2 Solution potential dynamics

The main technique for providing information of AuNP formation dynamics was OCP. The OCP is a measure of the changes in solution potential over time and can be monitored with high sampling rate (10 s^{-1}). This type of measurement has not been reported before but the reproducible data with distinct features potentially holds valuable information.

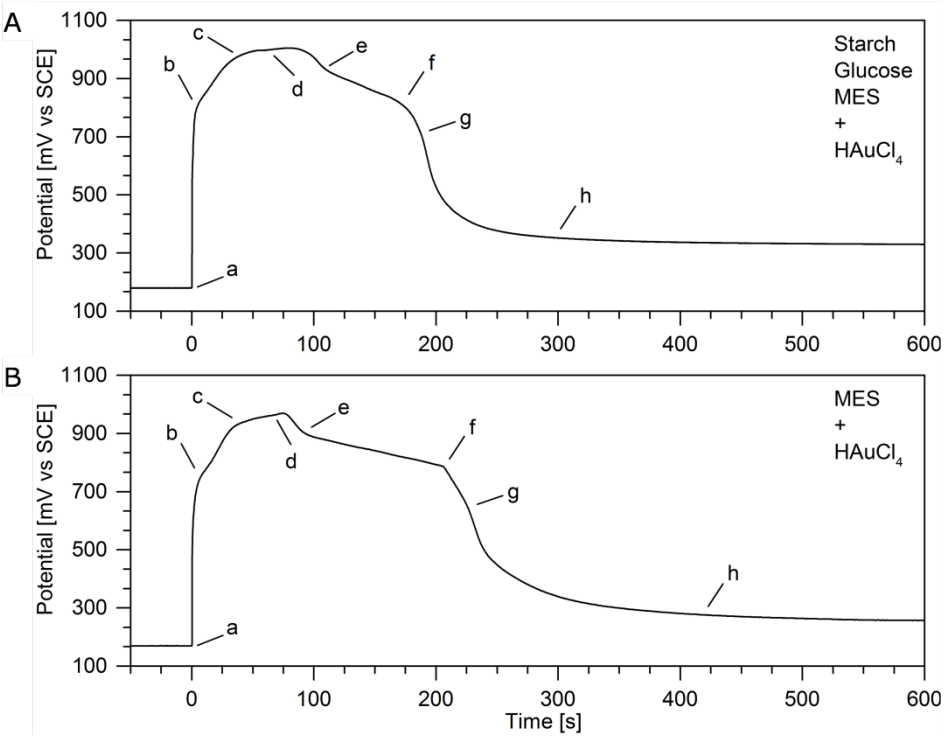

Figure 16. Potential dynamics of addition of 2 mL 20 mM precursor (t = 0) to 18 mL solution containing (A) starch, glucose and MES, the MOS synthesis, and (B) MES, the OBS synthesis at r.t. Final conc. of $HAuCl_2$, MES, glucose and starch were 2 mM, 10 mM, 10 mM and 0.6 wt%, respectively. Phase features are indicated with lower case letters. WE = BPG, CE = Pt wire, RE = RHE. **[Prior data]**

The first measurements were done by letting the freshly cleaned BPG electrode equilibrate in a solution containing starch, glucose and MES for the MOS synthesis and just MES for the OBS synthesis. After ≈ 100 s, 2 mL 20 mM precursor solution was injected into the cell. This corresponds to point 'a' in Figure 16. The two syntheses provided a similar potential development with a 3-step increase ('a' to 'c') and a 4-step decrease ('c' to 'h'). The solution lost its colour before 'd' at which point it started to turn black so already this gave an indication that nucleation and NP formation happened during the decrease in potential.

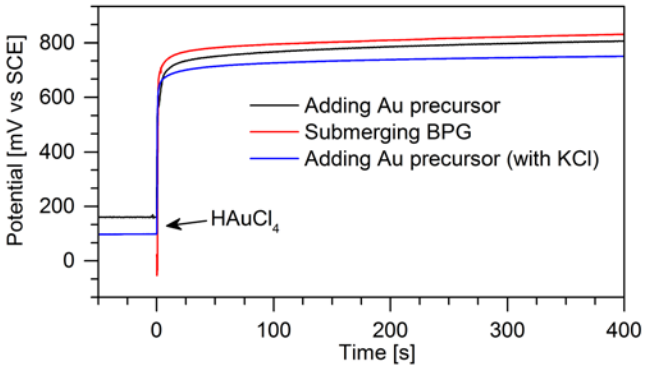

Figure 17. Potential dynamics for equilibration to addition of 2 mL 20 mM precursor. At t = 0 $HAuCl_4$ precursor was added to 18 mL ultrapure water (black), the BPG was dipped into aqueous solution of the $HAuCl_4$ precursor (red) or $HAuCl_4$ precursor was added to electrolyte solution of KCl (blue). Final concentrations of $HAuCl_4$ precursor and KCl were 2 and 10 mM, respectively. WE = BPG, CE = Pt wire, RE = SCE.

The increase phase is potentially a convolution of mixing/diffusion of precursor in the solution, equilibration of the electrode and chemical reactions. A set of reference experiments was undertaken to clarify the origin of the steps of potential increase. The Au precursor was injected to ultrapure water to measure the mixing of precursor, black curve Figure 17. The potential shot up to around 670 mV within 5 s followed by a logarithmic increase of an additional 150 mV over 900 s. Another experiment was carried out in order to decouple the mixing of the precursor with the equilibration around the electrode surface. First, the BPG was dipped into water to wet the surface and lifted out again. Then, Au precursor was added to the solution and allowed to homogenize before reinserting the electrode, red curve Figure 17. This resulted in an almost identical potential development as the previous case and the observed stabilization dynamics must relate to equilibration of the interface between electrolyte and electrode. The EC cell contains a Luggin capillary that serves to create a close contact between RE and WE. The capillary is normally filled with electrolyte and for standard EC measurements (short experiment duration and studying surface reactions) the conditions herein can be regarded as constant. The measurements of AuNP formation, however, take up to 30 min and the capillary is filled with low conducting solution (ultrapure water, starch, glucose and MES). An experiment was done where the EC cell and Luggin capillary were filled with 10 mM KCl before addition of precursor. The initial jump in potential was unaffected but the system stabilized faster for the subsequent phase. There might be an effect of diffusion through the Luggin capillary but it is small relative to the AuNP formation dynamics.

Scheme 3A shows that $[AuCl_4]^-$ exists in equilibrium with aqua- and hydroxo-substituted analogues sensitive to pH. Adding precursor to water as in the previous reference

experiments only change pH as a result of dilution (1 pH point for the 10-fold dilution), while the pH change experienced by the precursor in the actual AuNP synthesis is affected by the buffer. It is therefore possible that the development in potential is a result of a shift in the ligand exchange equilibria when mixed with the buffered, neutral media assuming that the ligands significantly change the reduction potential. Measurements were carried out in unreactive buffers instead of MES; phosphate buffer (PB) and ammonium acetate (NH_4Ac) Figure 18. Similar dynamics to those in Figure 17 were obtained but the potential increased roughly 200 mV more. This may relate to the presence of reducing agent, glucose, already initiating the reduction of the precursor, albeit at a very slow rate.

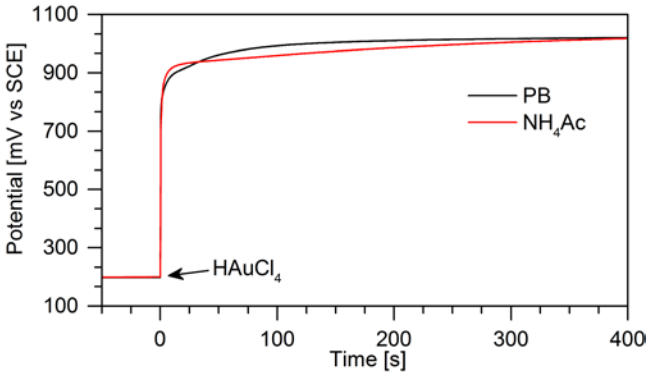

Figure 18. Potential dynamics of addition of 2 mL 20 mM precursor to 18 mL phosphate buffered (black) and ammonium acetate buffered (red) reaction mixture. Final concentrations: 2 mM $HAuCl_4$, 0.6 wt% starch, 10 mM glucose and 10 mM buffer (pH 7). WE = BPG, CE = Pt wire, RE = RHE. **[Prior data]**

Finally, the reaction was carried out in unbuffered medium to study initiation of reduction at low pH, Figure 19. A potential development identical to the buffered synthesis mixtures was observed. UV-vis measurements taken over the course of a week after the experiment showed that the reduction and AuNP formation do occur under these conditions, inset in Figure 19. It is clear that the features observed during AuNP formation are neither caused by equilibration of the system nor ligand substitution of the Au precursor and must be related to its reduction. The first rapid jump (‘a’ to ‘b’) fits with the fast equilibration that also occurred in the reference experiments but the next increase phases (‘b’ to ‘c’ and ‘c’ to ‘d’) suggest a two-step reduction mechanism. The potential dynamics could be proof of a stable Au(I) intermediate that builds up before any Au(0) is formed.

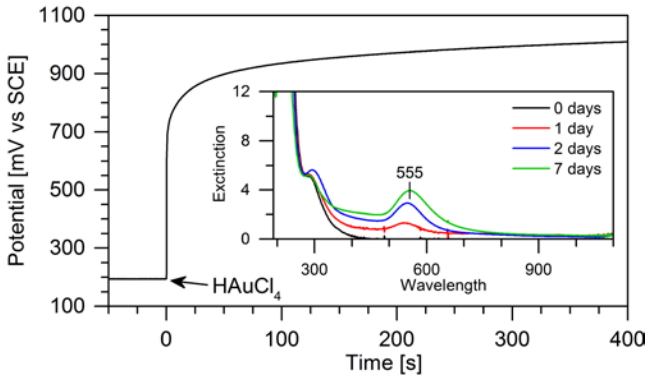

Figure 19. Potential dynamics of addition of 2 mL 20 mM precursor (2 mM) to 18 mL unbuffered starch (0.6 wt%) and glucose (10 mM) at r.t. Conc. in parenthesis are final conc. WE = BPG, CE = Pt wire, RE = RHE. Inset shows UV-vis spectra recorded after EC measurement (black) and at 1 (red), 2 (blue) and 7 (green) days (dil: 10). **[Prior data]**

A measurement with OBS conditions was done where the MES had been homogeneously distributed in the cell to make sure the concentration was the same in the main chamber, the Luggin capillary and the reference chamber. The initial potential development was as expected but the process stopped between 'e' and 'f' and the steep decrease never appeared, black curve in Figure 20.

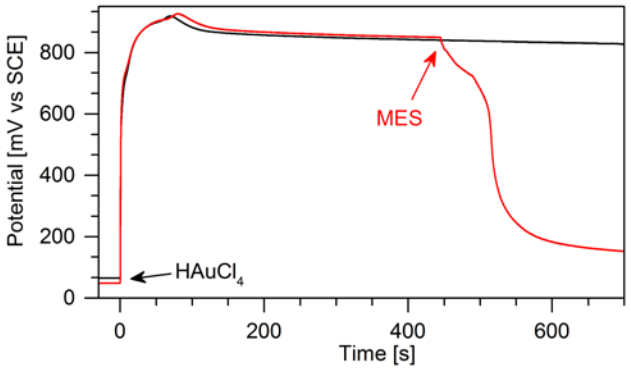

Figure 20. Potential dynamics of AuNP formation by addition of 2 mL 20 mM precursor (2 mM) to 18 mL MES (10 mM, pH 7) solution. Conc. in parenthesis are final conc. MES was homogeneously distributed in the cell incl. reference chamber and Luggin capillary before addition of precursor. Additional MES was added for the red curve indicated with the arrow. WE = BPG, CE = Pt wire, RE = SCE.

Initially, this was thought to be caused by an error in the preparation and the experiment was repeated with the same result, red curve in Figure 20. Additional MES solution was added after 440 s and instantly the potential dropped in a course similar to 'e-h' in original

measurements. Clearly MES is involved in the processes occurring after ‘e’. MES must be present in close to equivalent amounts for these processes under standard conditions. The homogenization in the EC cell led to a “loss” of MES outside the main chamber and a MES deficiency. The concentrations of precursor and MES are 2 and 10 mM, respectively.

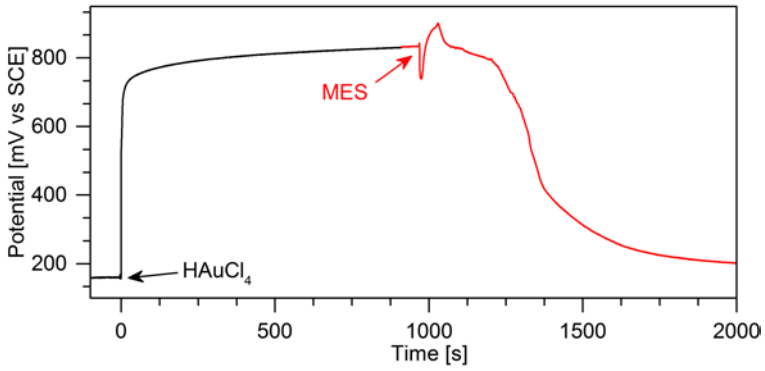

Figure 21. Potential dynamics of addition of 2 mL 20 mM precursor (2 mM) to 16 mL ultrapure water (black arrow) followed AuNP formation by addition of 2 mL 0.1 M MES (10 mM, pH 7) (red arrow). Conc. in parenthesis are final conc. The graph is “stiched” together by two consecutive data collections (black and red curve). WE = BPG, CE = Pt wire, RE = SCE.

According to Scheme 2B, they react in a 2:3 ratio and consequently MES is in excess by more than 3 equivalents. Not enough MES would be “lost” due to homogenization to account for MES deficiency based on the simple redox reaction and the role of MES is more complex than initially assumed. The previous AuNP synthesis measurements entailed stabilization of the electrode to the reducing agent and then addition of precursor. The potential changes are then a convolution of the potential adjusting to the presence of strongly oxidizing $[AuCl_4]^-$ and redox reactions. Reversing the sequence of precursor and reducing agent addition allows for the electrode to stabilize to the precursor as the redox dominating compound. The potential changes can then be expected to largely reflect chemical reactions. Such an experiment is shown in Figure 21 where the precursor is first added to ultrapure water and the system given time to stabilize. The reducing agent MES was added after about 970 s giving rise to a sudden drop of almost 100 mV before starting a potential course similar to ‘b’-‘h’ in Figure 16B. This suggests are point ‘b’ has a physical meaning and is not an artefact of the convolution.

The standard reduction potentials reported by J. J. Lingane[85] provide some insight. He reported that reduction of $[AuCl_4]^-$ involves three redox couples, $[AuCl_4]^-/Au^0$, $[AuCl_4]^-/[AuCl_2]^-$ and $[AuCl_2]^-/Au^0$, Scheme 4. It is believed that with only $[AuCl_4]^-$, as in Figure 21, the potential is dominated by the $[AuCl_4]^-/Au^0$ couple. The $[AuCl_4]^-/[AuCl_2]^-$ instantly

takes over when reduction starts and the potential drops as indicated by the difference in E^0 of about 80 mV. This corresponds to point 'b' in Figure 16. The potential quickly increases again as a substantial amount of $[AuCl_2]^-$ builds up and the third redox couple with the highest E^0 dominates. This is the phase from 'b' to 'c'. In fact, a similar potential increase during reduction was observed by Lingane[86] reporting that the $[AuCl_2]^-/Au^0$ was potential determining in the reaction and $[AuCl_4]^-$ reduced in a stepwise manner.

Scheme 4. The EC reactions and standard redox potentials involved in the potential increase phase.

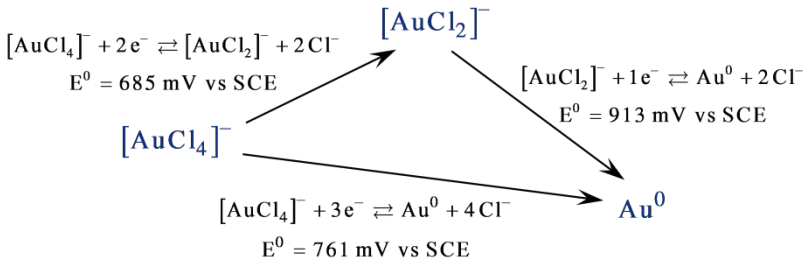

Around 'c' the concentration of intermediate $[AuCl_2]^-$ is highest and the potential tails off towards 'd' as Au^0 begin to form. A fourth redox couple may play a role in the reaction, namely the disproportionation of $[AuCl_2]^-$. This process is slow at r.t. and negligible within the time-frame of the reduction in our syntheses.[87] However, disproportionation is catalyzed by gold surfaces.[87] These are generated during the AuNP formation which adds to the complexity of the process. The influence of the presence of AuNPs was studied by running a second synthesis after AuNP formation in the same pot, Figure 22.

Scheme 5. Disproportionation of $[AuCl_2]^-$ to $[AuCl_4]^-$ and metallic gold.

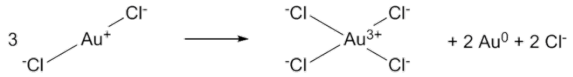

A second portion of Au precursor similar to the standard amount, 2 mL 20 mM, was injected after AuNP formation. The potential shot to over 800 mV vs SCE as had been observed before. The presence of AuNPs did thus not affect the potential measurement of the Au precursor. Surprisingly, no indication of reduction was found when the second amount of precursor was added despite the fact that MES was in excess for the initial AuNP synthesis. It is believed that excess MES is immobilized on the high energy, fresh gold surfaces during nucleation resulting in a negligible concentration in solution. Further evidence of this is presented in section 2.1.3. A "draining" of MES in solution by the AuNP surfaces may also explain the deficiency observed in Figure 20.

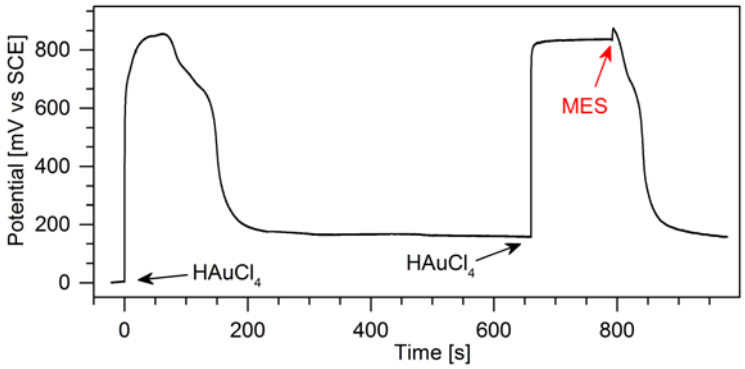

Figure 22. Potential dynamics of AuNP formation by addition of 2 mL 20 mM precursor (2 mM) to 18 mL solution containing starch (0.6 wt%), glucose (10 mM) and MES (10 mM, pH 7). Conc. in parenthesis are final conc. Additional precursor was added after complete reaction (black arrow) followed by MES (10 mM, red arrow). WE = BPG, CE = Pt wire, RE = SCE.

Addition of MES to the solution containing AuNPs and additional precursor led to reduction of the precursor causing the potential to drop to 160 mV vs SCE which is identical to the baseline after the initial AuNP formation, Figure 22. Interestingly, the potential drop was much faster the second time suggesting a catalytic effect of the already formed AuNPs. This was studied in a bit more detail in a similar experiment.

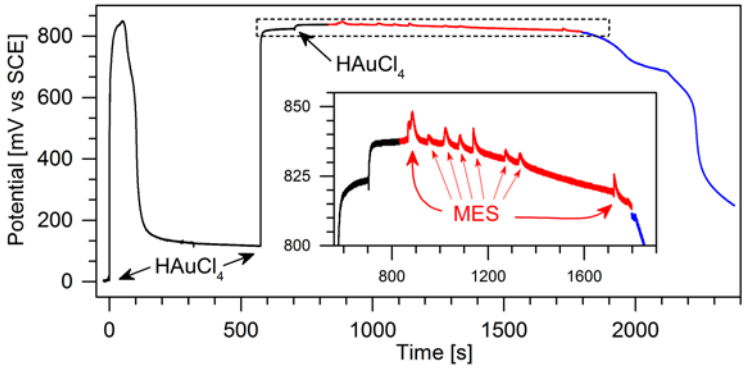

Figure 23. Potential dynamics of AuNP formation by addition of 2 mL 20 mM precursor (2 mM) to 18 mL solution containing starch (0.6 wt%), glucose (10 mM) and MES (10 mM, pH 7). Conc. in parenthesis are final conc. Additional precursor was added twice (black arrows) followed by addition of small amounts of MES (red arrows). The inset shows a close view of the section enclosed by the dashed rectangle. The graph is “stiched” together by three consecutive data collections (black, red and blue curve). WE = BPG, CE = Pt wire, RE = SCE.

This time the second portion of Au precursor is added in two steps of 1 mL 20 mM each, Figure 23. No indication of reduction was found for either case. The second addition provided a small increase which was expected from the logarithmic dependence of potential on concentration set by the Nernst equation (Eq. (1.3) section 1.3.4). The second amount of MES (2 mL 0.1 M) was added in small volumes each giving rise to a sharp spike in the potential that returned to a steadily decreasing baseline, inset Figure 23. Shortly after addition of the final portion of MES, the potential dropped in a manner identical to what was generally observed for the AuNP synthesis. The role of MES is not straight-forward and it seems that a critical concentration of MES exists. The SAMENS method utilizes a concentration close to this value.

2.1.3 Conductivity and pH dynamics

Further investigation of the AuNP formation was undertaken using time-resolved studies of conductivity and pH. Considering the reactions in Scheme 2 and Scheme 3, the liberation of chloride ions and production of H^+ must be detectable in these measurements.

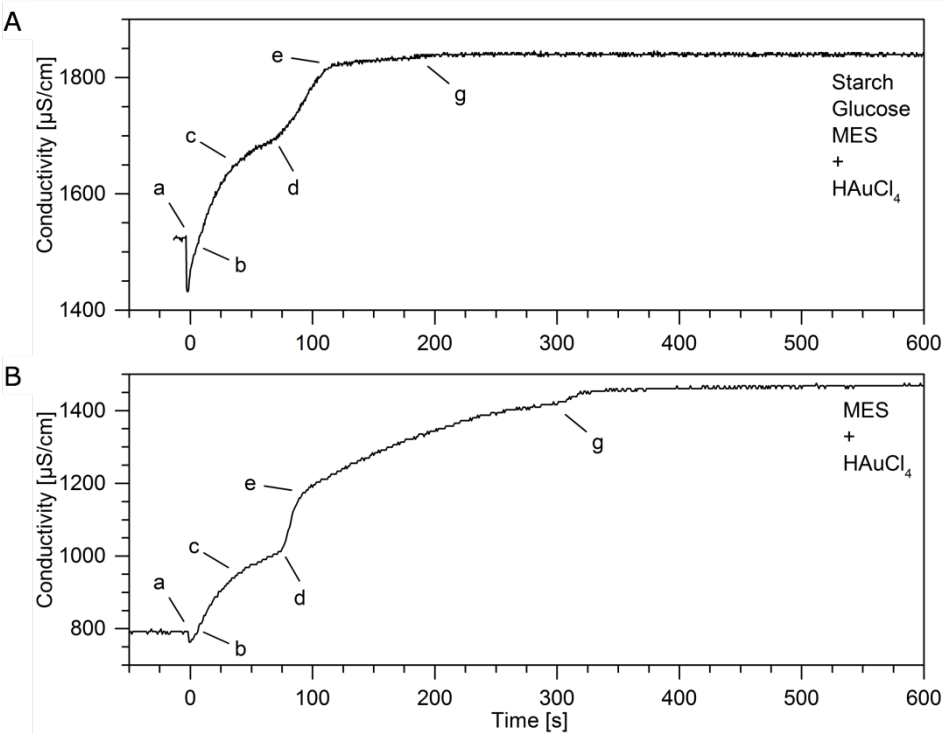

Figure 24. Conductivity dynamics of addition of 2 mL 20 mM precursor (t = 0) to 18 mL solution containing (A) starch, glucose and MES, the MOS synthesis, and (B) MES, the OBS synthesis at r.t. Final conc. of $HAuCl_2$, MES, glucose and starch were 2 mM, 10 mM, 10 mM and 0.6 wt%, respectively. **[Prior data]**

Other ions involved are deprotonated MES, monovalent gold complexes, gluconate and K^+. K^+ is merely a spectator providing a constant conductivity contribution. The remaining ions are significantly larger than chloride which is expected to dominate the conductivity dynamics. Features were found on the conductivity (Figure 24) and pH (Figure 25) dynamics curves at similar time-markers as with potential dynamics. Stabilization to the addition of precursor also took a few seconds ('a' to 'b') with these systems. A roughly 200 µS/cm conductivity jump and a pH decrease from ≈ 6.2 to 5.5 occurred from 'b' to 'c' which accords with the assumption that this phase represents partial reduction to $[AuCl_2]^-$, Scheme 3C. The second phase, believed to be the second reduction step and build-up of monomer, was accompanied by moderate conductivity and pH changes.

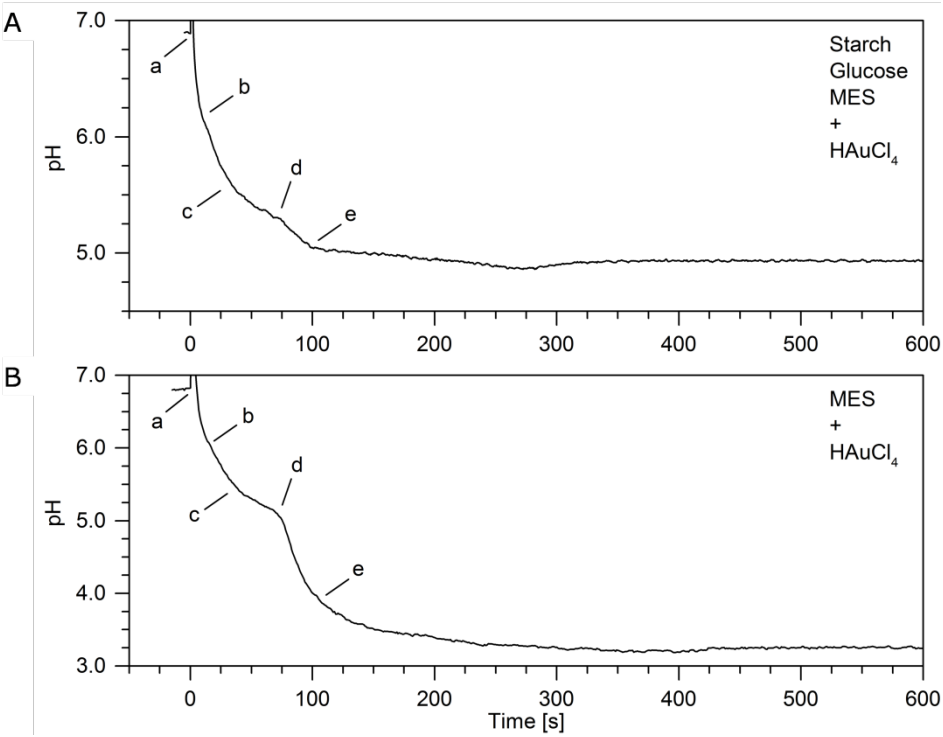

Figure 25. pH dynamics of addition of 2 mL 20 mM precursor (t = 0) to 18 mL solution containing (A) starch, glucose and MES, the MOS synthesis, and (B) MES, the OBS synthesis at r.t. Final conc. of $HAuCl_2$, MES, glucose and starch were 2 mM, 10 mM, 10 mM and 0.6 wt%, respectively. **[Prior data]**

Up until point 'd' there was little difference in the dynamics of the MOS and OBS syntheses, supporting that 'a' to 'd' mainly involves redox chemistry in which glucose and starch do not take part. The conductivity is, however, shifted to higher values when starch and glucose is present. This contribution comes mainly from starch and is believed to arise from inorganic traces in the as purchased chemical. The nucleation phase is assumed to take

place from ‘d’ to ‘e’ during which drastic shifts in conductivity and pH appeared. Chloride ions may still be coordinated to the freshly formed monomer and only released as nucleation occurs. Furthermore, the autocatalysis that sets in after the formation of gold surface, speeds up the decomposition of $[AuCl_2]^-$ and completion of precursor reduction. Consistent with potential observations, the nucleation occurs earlier in the OBS and the subsequent slow phase is longer than the MOS. The development of pH showed a large difference for the two syntheses in the drop following nucleation. The final pH was 4.93 and 3.25 in MOS and OBS, respectively. The large drop in OBS is explained by MES immobilization on the surface of the AuNPs as discussed earlier. MES in the immobilized state is not active as a buffer and the buffer capacity of the solution effectively drops as MES covers the freshly formed surfaces. Starch may adsorb more strongly than MES preventing the loss of buffer capacity in the MOS.

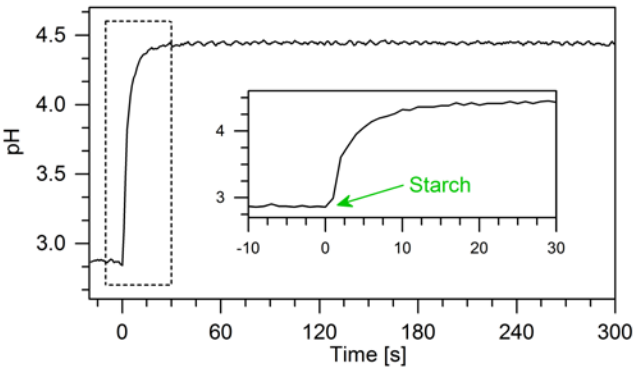

Figure 26. pH dynamics of starch (2 mL 2 wt%) addition to OBS AuNP solution (20 mL). Inset shows a close view of the area enclosed by the dashed square.

An experiment was done to test this hypothesis, Figure 26. Time-resolved pH measurements were carried out on the OBS AuNP solution (after AuNP formation). Addition of starch caused pH to jump towards the level of the MOS AuNP solution within 10 seconds. This cannot be explained by dilution effects or any basicity of the starch solution, but is a clear indication that the immobilized MES was exchanged by starch releasing the buffer back to the solution and increasing pH. There are subtle features late in the pH dynamics. Plotting the same data as the proton concentration vs time makes them more visible, Figure 27. It is interesting to note that a stable signal is found at the same time-markers as for the potential measurements.

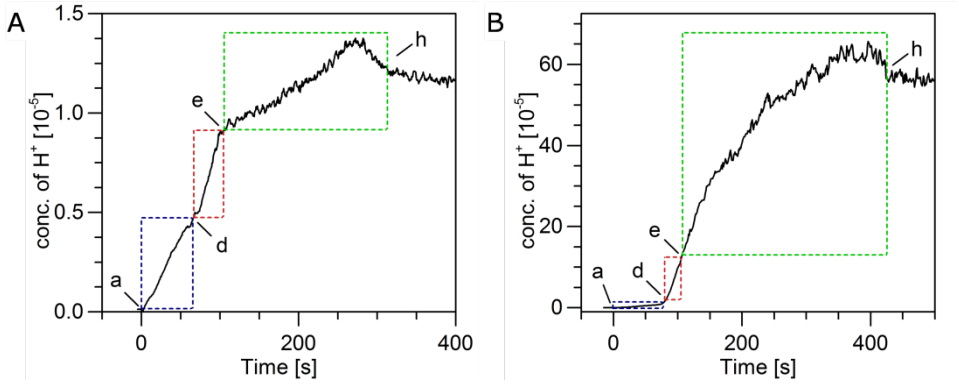

Figure 27. H^+ concentration dynamics of AuNP formation by the (A) MOS and (B) OBS syntheses. Same data as Figure 26 but the ordinates are converted to proton concentration by $[H^+] = 10^{-pH}$.

2.1.4 Dynamics of optical properties

The turbidity dynamics of AuNP formation were measured with a nephelometer (section 1.3.6). Addition of precursor required opening of the sample compartment that excludes ambient light giving a very large spike in the time course. The turbidity is a measure of scattering and absorbance of light from the diode (890 nm). None of the components or involved gold complexes interact with light at this wavelength. As a result, no changes were seen for the reduction phases. The turbidity started to decrease at the end of the reduction phase and at 'd' a drastic drop occurred signifying a strong absorbance at 890 nm, Figure 28. This was expected as this was believed to be the nucleation phase and that to some extend NPs absorb light in the entire visible range. Supporting optical characterization was obtained with UV-vis spectrometry. The available instrument entailed the use of cuvettes and so a fresh cuvette with diluted solution had to be prepared for each measurement. Disposable plastic cuvettes were used rather than quarts to ensure fast sampling. Unfortunately, the behaviour of the plastic cuvettes was not very uniform so the baseline was shifting between measurements. The measurement was further complicated by the "sticky" nature of the poorly stabilized AuNPs in the OBS synthesis resulting in attachment of AuNPs to the cuvette walls. Because of the dilution of the samples prior to each measurement the actual timing should be attributed an uncertainty of up to 5 s.

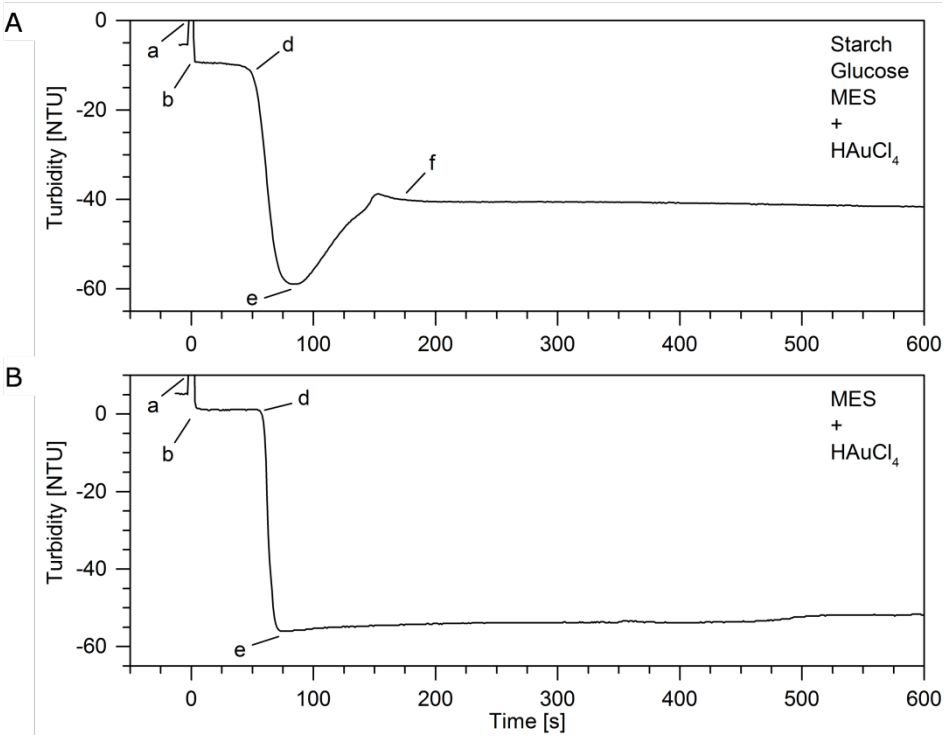

Figure 28. Turbidity dynamics of addition of 2 mL 20 mM precursor (t = 0) to 18 mL solution containing (A) starch, glucose and MES, the MOS synthesis, and (B) MES, the OBS synthesis at r.t. Final conc. of $HAuCl_2$, MES, glucose and starch were 2 mM, 10 mM, 10 mM and 0.6 wt%, respectively. **[Prior data]**

UV-vis spectra recorded at stages of the AuNP formation in the MOS and OBS syntheses are shown in Figure 29A and -B, respectively. The absorbance of the $[AuCl_4]^-$ almost completely disappeared before 60 s in both syntheses supporting the sequential reduction and intermediate $[AuCl_2]^-$ (I in Figure 29). The first indication of a LSPR was found during the nucleation phase at 85 and 70 s for the MOS and OBS, respectively. The LSPR grew in intensity and was red-shifted up to about 220 s. The final LSPR of the MOS AuNPs was narrow with $LSPR_{max}$ at 521, indicative of spherical AuNPs. The $LSPR_{max}$ of the OBS AuNPs was at 524 nm hinting at larger particles than in the MOS synthesis and the appearance of a dominant shoulder around 700 nm, which could be caused by anisotropic particles or slight agglomeration.

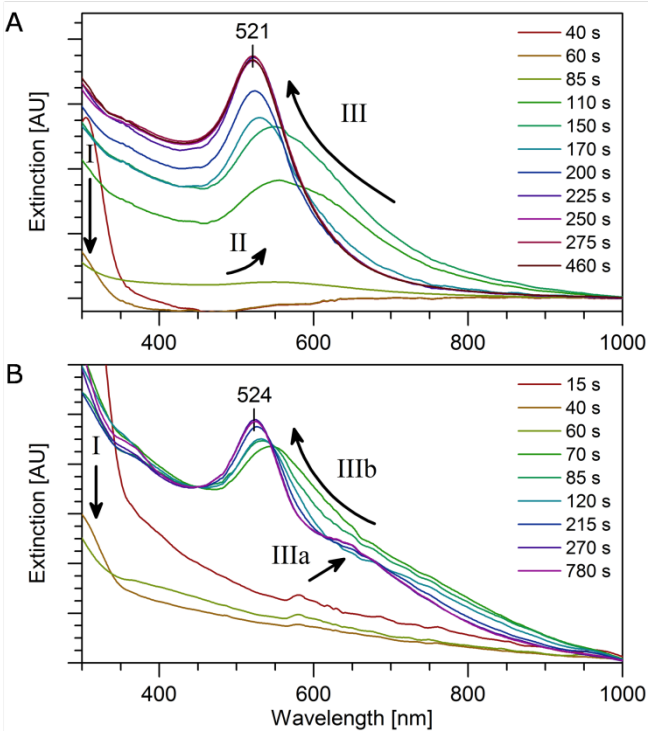

Figure 29. UV-vis spectra at different stages of AuNP formation in the (A) MOS and (B) OBS syntheses. Numbers in legends refer to seconds after precursor addition. The disposable cuvettes gave rise to an unstable signal. The individual spectra are normalized to comparable extinction so the ordinates are relative. (A) = **[Prior data]**

The optical characterization was substantiated by TEM of the AuNP products from the MOS and OBS, Figure 30. Uniform, spherical AuNPs around 8 nm were produced in the MOS while larger spherical AuNPs, nanosheets and -rods were found in the OBS product. A tendency to form aggregates on the TEM grid was seen for the OBS AuNPs while the MOS product was well-dispersed.

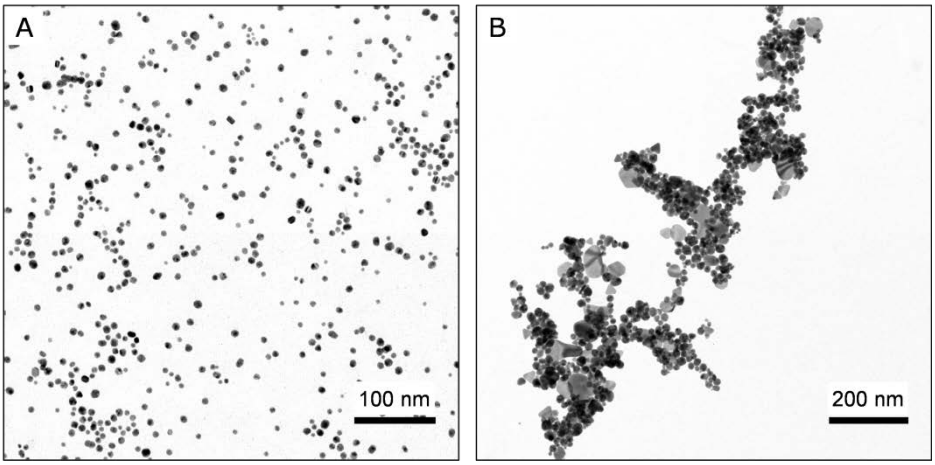

Figure 30. Representative TEM images of AuNPs formed in the (A) MOS and (B) OBS syntheses. Uniform, spherical, well-dispersed AuNPs are found in the MOS sample while the OBS synthesis produced a mixture of spherical AuNPs, rods and sheets being poorly dispersed on the TEM grid.

2.1.5 Formation mechanism

The major advantage of the current approach to the study of AuNP formation is the use of well-established EC instruments that are often present within one laboratory and operate at high time-resolutions. The availability enables combining a series of techniques offering insight into different aspects of the complex processes and a broad overall picture.

The approach also has drawbacks and significant challenges. Mainly, the lack of previous literature to aid or support the data analysis due to the non-traditional use of these well-known techniques. The measured signals in all of the time-resolved techniques employed presently are compound signals with contributions from several species. This makes data analysis complex and less concrete than the X-ray spectroscopies.

Each of the time-resolved signals was generated and measured independently. The response time of the sensors and appearance of features relative to the processes causing them is different for each measurement. The time-markers can therefore vary between techniques with at least a few seconds. In terms of the OBS AuNP formation, the synthesized NPs were poorly stabilized and had a tendency to attach to the equipment. The reproducible time-course measurements showed that this effect did not influence the shape and features of the observed signals. It did, however, influence the timing of features occurring after nucleation making it difficult to place time-markers of the late features exactly.

The signal-changes during the different phases were drastically different. Looking at the derivative makes it easier to identify and compare phases between measurements. Examples of differentiated signals are shown in Figure 31 normalized to span 1 unit on the

ordinate axis and centered on 0. Signal jumps and drops will give rise to positive and negative peaks, respectively.

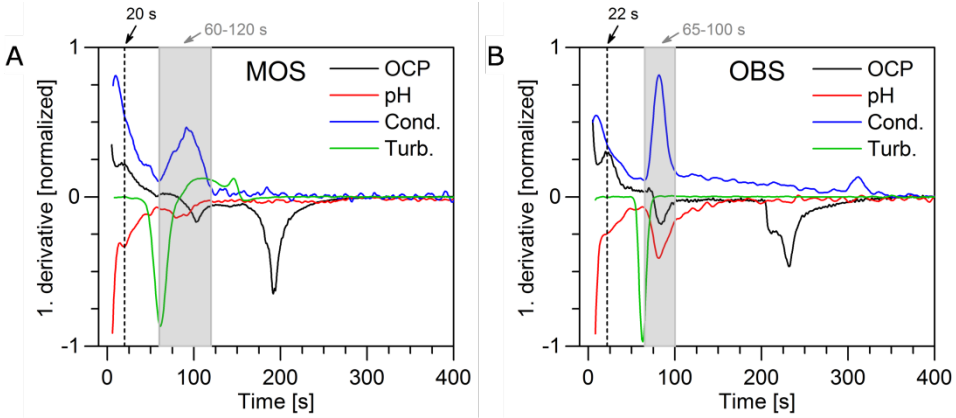

Figure 31. First derivatives of all time-resolved measurements of AuNP formation in the (A) MOS and (B) OBS syntheses. The curves are normalized to an ordinate axis range of 1 and end at 0 at 400 s. The nucleation phase is highlighted with a grey square and the peak of the first reduction step with a dashed line.

Especially the nucleation phase becomes very evident (marked in grey in Figure 31) being clearly visible in all measurements. The nucleation event is expected to be very rapid and constitute the beginning of the phase from 'd' to 'e' which would also include coalescence of the nuclei to form polycrystalline NPs. The data from all the dynamics experiments are summarized in Table 2 and the following mechanism for AuNP formation is proposed. The Au precursor, $[AuCl_4]^-$, is reduced to $[AuCl_2]^-$ within the first half minute ('b' to 'c') leading to a jump in potential and liberation of chloride ions and protons. In a separate step, a second reduction occurs and metallic gold starts to form ('c' to 'd'). This again entails liberation of protons but a large part of the chloride ions from the $[AuCl_2]^-$ complex remain coordinated to the monomer form of Au^0. The bound chloride ions are liberated in the next phase, the nucleation phase ('d' to 'e'). Nuclei of solid gold are generated in a very rapid process and MES and/or starch cover the high energy surfaces. In the absence of starch, MES is immobilized significantly decreasing its bulk concentration and pH. The solution turns black, the turbidity plummets and indications of a LSPR band appear. Nucleation also marks the onset of decreasing potential. After nucleation a growth phase ensues ('e' to 'h') during which the pH and conductivity do not change significantly. The potential exhibits a drastic drop and major changes to the LSPR are observed.

Table 2. Summary of time-resolved experiments. Arrows indicate increase or decrease in the dynamics measurements. "n.c." = no change. "n.o." = not observed, indicates that phase separation was not observed. In cases where observations in the MOS and OBS differed, the MOS data are written in green and OBS data in red.

Phase	a-b	b-c	c-d	d-e	e-f	f-g	g-h
	Eq.	$Au^{3+} \rightarrow Au^{+}$	$Au^{+} \rightarrow Au^{0}$	Nucl.	---------- *Growth* ----------		
Time (s)	0-5	5-25 5-35	25-60 35-65	60-120 65-100	120-175 100-200	175-190 200-225	190-300 225-400
OCP	↑↑↑	↑↑	↑	↓↓	↓	↓↓	↓↓
pH	↓↓↓	↓↓	↓	↓ ↓↓↓	(↓)	n.o.	n.o.
Cond.	n.c.	↑↑	↑	↑↑	(↑)	n.o.	n.c. ↑
Turb.	n.c.	n.c.	↓↓↓	↓↑ ↓	↑↑ (↑)	(↓)	n.c. n.o.

The ability to observe and distinguish phases in all measurements make the present approach promising as a widely accessible alternative to studying NP formation and other NP related processes that is complementary to synchrotron studies. Disclosing the exact timing of specific events, e.g. nucleation, within the complexity of solution synthesis of NPs is important for gaining control of the system and direct formation. Timing is especially critical for composite systems such as core-shell NPs, nanoalloys and bifunctional nanostructures. Further development and support from theoretical considerations of the generated signals are needed to unlock the full potential of this approach.

2.2 Controlling the size of AuNPs in solution synthesis

The properties and especially catalytic activity of NPs strongly depend on their size.[88-90] This is largely related to the specific surface area of the NPs. This is especially important for nanoparticles applied in catalysis. The catalytic activity of nanoparticles occurs at the surface by reactant adsorption and activation, intermediate stabilization, and product desorption. In this sense, bulk atoms are not utilized, which is an important aspect as many nanoparticle catalysts are of expensive and rare metals. Small NPs are very active and have a strong tendency to aggregate, making them more unstable as catalysts than larger ones. Regarding NPs as drug carriers or therapeutic agents, their size affects their ability to penetrate tissue, enter interstitial space and therefore the biodistribution.[91,92] The optical properties of AuNPs (among others, e.g. Ag NPs, Cu NPs and semiconductor quantum dots

such as CdSe) depend strongly on size and affect their efficiency in photovoltaics and photocatalysis. Controlling the size of NPs is an important aspect of wet synthesis of NPs.

An approach to the synthesis of AuNPs with controlled size based on seeded growth inspired by a report by Bastús et al.[93] was used. They prepared AuNPs in the range of 8-180 nm using the Turkevich method with sequential reduction of $HAuCl_4$ by sodium citrate. They diluted the sample after every third step and kept a constant addition of precursor and reductant for each step. Our protocol consisted of sequential reduction and growth using similar conditions to the MOS procedure (MES pH 7, starch and glucose). The sample was also diluted after every third step by removing a sample fraction (12 of 40 mL) and adding starch, glucose and MES keeping those at constant concentration. The fractions are shown in Figure 32. The crucial point of seeded growth is to keep the monomer concentration below the critical nucleation limit at all times. This is controlled by reaction rate (reducing agent and temperature) and precursor addition (concentration and frequency). We kept the rate of reaction roughly stable by running at constant temperature and having an approximately constant addition of precursor. The temperature was maintained at 60 °C, which is lower than the standard MOS procedure, to decrease the rate of monomer formation and facilitate growth. Controlling the redox reaction rate only ensures a constant production of monomer. If the depletion of monomer from solution through growth of seeds by adsorption on the surface is not controlled, the monomer concentration might increase and cause further nucleation. The amount of precursor added at each step was thus adjusted to obtain a steady but small increase in added monomer units per existing surface area of AuNP seeds per step. The slight increase is allowed as the AuNP concentration slowly decreases during the experiment. The details of the experiment are given in Table 3. Volume fractions were taken out after 0 (seeds), 3, 6, 9, 12, 15, 18, 21, 24 and 27 steps and characterized with UV-vis spectroscopy, NTA and TEM.

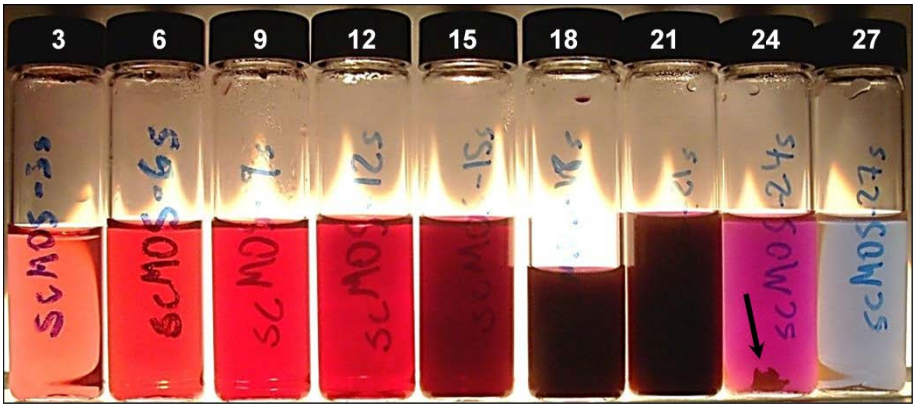

Figure 32. Photograph of fractions from the size control experiment. The number of steps preceding the fraction is indicated on the photo. Large agglomerate observed after step 24 is highlighted with an arrow.

Table 3. Reaction scheme for the size control experiment. The temperature was kept at 60 °C and stirring maintained throughout the experiment. The given component conc. disregarding any change due to reactions and refer only to the amount that has been added.

Step	[MES] [a] (mM)	[Starch] (wt%)	[Glucose] (mM)	[$HAuCl_4$] (mM)	[AuNP] [b] #/mL	Time
0 [c]	10.0	0.60	10.0	2.00 [d]	$7.63 \cdot 10^{13}$	28 min
1	7.76	0.47	7.76	0.08	$1.54 \cdot 10^{12}$	31 min
2	7.74	0.46	7.74	0.15	$1.54 \cdot 10^{12}$	39 min
3 [c]	7.70	0.46	7.70	0.25	$1.54 \cdot 10^{12}$	31 min
4	8.02	0.48	8.02	0.28	$1.08 \cdot 10^{12}$	17 min
5	7.97	0.48	7.97	0.42	$1.08 \cdot 10^{12}$	37 min
6 [c]	7.89	0.47	7.89	0.60	$1.08 \cdot 10^{12}$	33 min
7	8.24	0.49	8.24	0.61	$7.54 \cdot 10^{11}$	29 min
8	8.14	0.49	8.14	0.84	$7.54 \cdot 10^{11}$	31 min
9 [c]	8.02	0.48	8.02	1.12	$7.54 \cdot 10^{11}$	23 min
10	8.40	0.50	8.40	1.07	$5.28 \cdot 10^{11}$	*overnight*
11	8.27	0.50	8.27	1.36	$5.28 \cdot 10^{11}$	36 min
12 [c]	8.12	0.49	8.12	1.70	$5.28 \cdot 10^{11}$	22 min
13	8.51	0.51	8.51	1.55	$3.69 \cdot 10^{11}$	30 min
14	8.35	0.50	8.35	1.88	$3.69 \cdot 10^{11}$	38 min
15 [c]	8.18	0.49	8.18	2.26	$3.69 \cdot 10^{11}$	59 min
16	8.59	0.52	8.59	1.99	$2.59 \cdot 10^{11}$	86 min
17	8.41	0.50	8.41	2.35	$2.59 \cdot 10^{11}$	48 min
18 [c]	8.23	0.49	8.23	2.74	$2.59 \cdot 10^{11}$	*overnight*
19	8.64	0.52	8.64	2.38	$1.81 \cdot 10^{11}$	35 min
20	8.46	0.51	8.46	2.75	$1.81 \cdot 10^{11}$	26 min
21 [c]	8.26	0.50	8.26	3.15	$1.81 \cdot 10^{11}$	52 min
22	8.67	0.52	8.67	2.69	$1.27 \cdot 10^{11}$	26 min
23	8.48	0.51	8.48	3.06	$1.27 \cdot 10^{11}$	87 min
24 [c]	8.28	0.50	8.28	3.46	$1.27 \cdot 10^{11}$	66 min
25	8.69	0.52	8.69	2.91	$8.87 \cdot 10^{10}$	55 min
26	8.50	0.51	8.50	3.29	$8.87 \cdot 10^{10}$	35 min
27 [c]	8.30	0.50	8.30	3.68	$8.87 \cdot 10^{10}$	24 min

[a] The MES stock solution was adjusted to pH 7. [b] AuNP concentrations are calculated based on the seed size and concentration, assuming that all precursor is used for growth of spherical monodisperse NPs. [c] After reduction of gold at these steps, a fraction was taken out and the remaining sample diluted with ultrapure water and synthesis components. [d] This is the [$HAuCl_4$] in the seed solution. The remaining numbers refer to added precursor after from step 1 to 27.

2.2.1 Size and optical properties

Already the colour of the volume fractions as shown in Figure 32 (and App. fig. 1) indicates significant changes to the nanoparticle size. The corresponding UV-vis spectra are presented in Figure 33 as a 3D plot where the extinction is represented by the colour scale and the steps on the y-axis. The individual spectra are also shown in App. fig. 2. Several features worth noting are present in the 3D plot. In the seed solution (Step 0) a peak just above 350 nm (a) was observed. This phenomenon is discussed in detail in section 2.5. A shoulder around 270 nm grew from about 6 steps to be most pronounced at 12-15 steps after which it slowly disappeared again. In the very last fraction (Step 27) a small amount of the gold precursor was still left in solution giving peaks at 222 and 305 nm. The spectra were normalized at the peak maximum of the LSPR ($LSPR_{max}$) to 10 giving rise to the blue vertical line in Figure 33. It shows that the LSPR narrowed from 0 to 12 steps without any significant shift in $LSPR_{max}$ (519 to 528 nm). After 12 steps the LSPR again broadened and was red-shifted to 592 nm for step 27. The LSPR is responsible for the characteristic colour of the AuNP suspensions and the red-shift of the $LSPR_{max}$ is clearly visible in the photograph, Figure 32, where the colour is shifted from red to blue. This agrees well with the data from Bastús et al. where significant red-shifts occurred at sizes above 40 nm.[93]

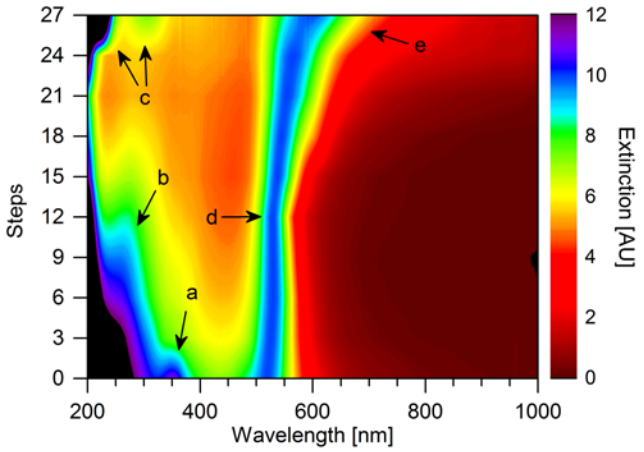

Figure 33. 3D plot of UV-vis spectra of fractions from different stages of the size control experiment. Absorbance is normalized to 10 at the $LSPR_{max}$ and shown with the colour scale. Specific features are highlighted; Peaks at (a) 350, (b) 270, (c) 222 and 305 nm, (d) point of most narrow LSPR and (e) red-shift and broadening of the LSPR.

Fractions 0 and 3 were below the detection limit of the NTA and fraction 6 close to it. Very fast moving and dim particles were seen in the video of step 6 and some were not separable from the background. The size distributions of the remaining fractions are shown in Figure 34 with frequency in % presented by the colour scale. A clear steady increase in size as

function of number of steps is seen as expected. The hydrodynamic size increased from 27 nm at step 6 to 83 nm at step 21. After this point, the AuNP suspensions became unstable. Large agglomerates appeared in the solution and the size distributions became very broad.

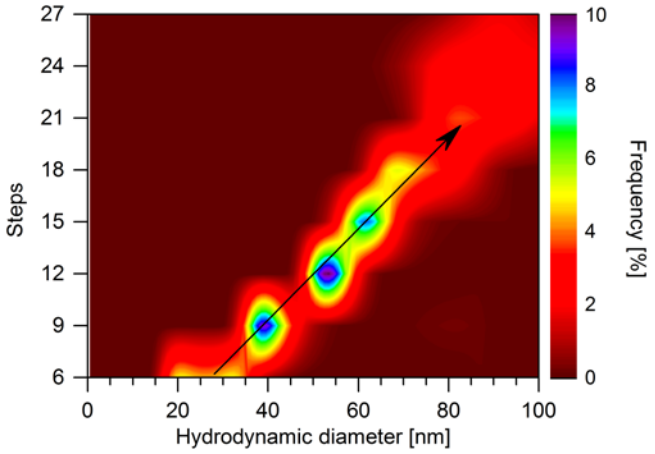

Figure 34. 3D plot of NTA measurements of fractions from different stages (y-axis) of the size control experiment. The colour scale shows the relative distribution within each fraction.

Overlaid size distributions are shown in App. fig. 3 and normalized to ideally represent the same number of particles. It is here clear that AuNPs are agglomerating to macrosize and not being measured by NTA in fractions at step 24 and 27. NTA provides information about size and particle concentration simultaneously. The concentration measurement is much less reliable than the sizing and takes a lot of effort to be used quantitatively. However, the concentrations from NTA are close to the expected concentrations used for designing the synthesis scheme, Table 3, supporting the notion that most of the gold content is indeed detected with NTA. The NTA concentration values are given in the summary presented in Table 4, section 2.2.3.

Images from TEM showed monodisperse AuNPs of increasing size with increasing number of steps in good agreement with NTA, Figure 36 and Figure 35. 26-332 particles were measured for the each fraction to determine the size, App. fig. 6. Few particles were measured in the last three fractions due to aggregation and significantly non-spherical particle shapes (section 2.2.2). The size increased from the seeds of 8 ± 2 nm (standard MOS AuNPs) to 80 ± 10 nm after 21 steps.

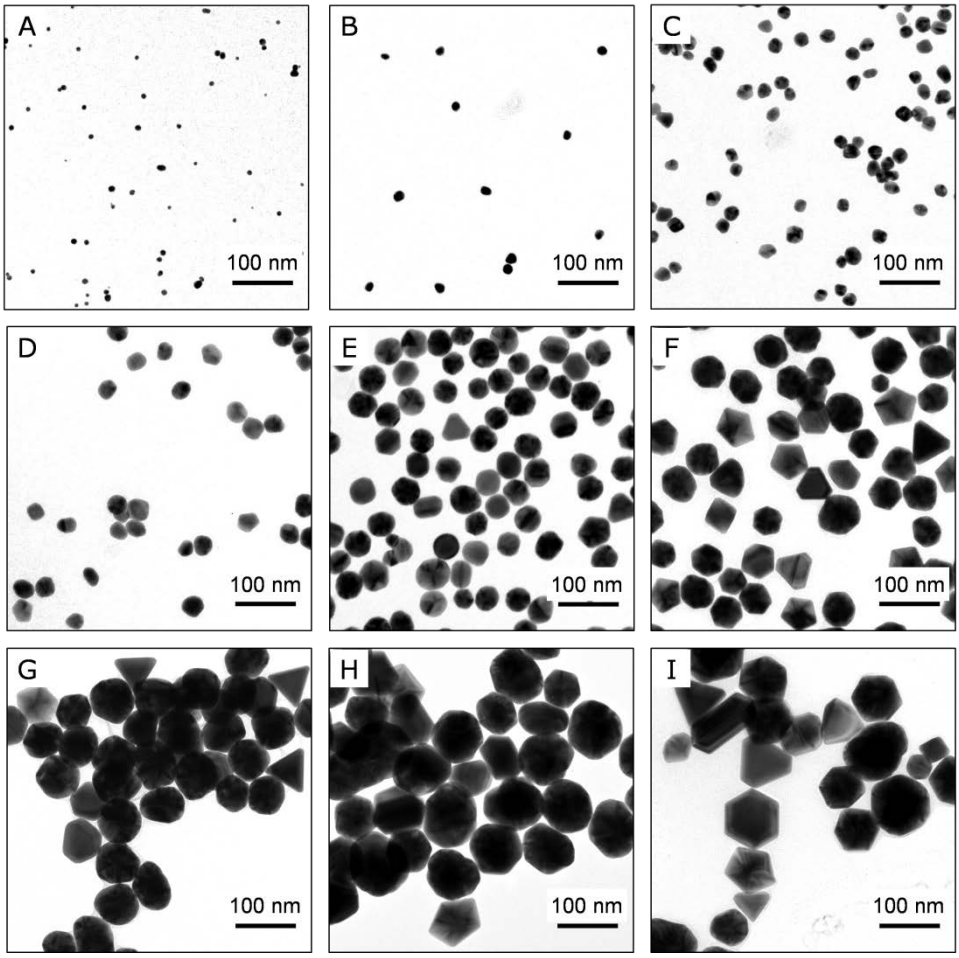

Figure 35. TEM images of fractions from the size control experiments. (A) shows the initial seeds and (B) to (I) show samples after every three steps from 3 to 24, respectively. All images are given in the same scale.

Aggregates of particles are not counted by the ImageJ automated particle sizing method and only "primary" particles are measured. This is not the case for NTA where aggregates are measured as large particles. A few large aggregates greatly affect the statistical mean and standard deviation (SD) from the NTA measurement. The size from TEM is therefore better compared to the mode in the NTA size distribution where the standard deviation can be defined from the full width at half maximum (FWHM) of the main peak[94]:

$$\mathrm{FWHM} = 2\sqrt{2\ln 2}\,\sigma \Rightarrow \sigma \approx \frac{\mathrm{FWHM}}{2.355} \tag{2.1}$$

where σ is the standard deviation of a Gaussian distribution.

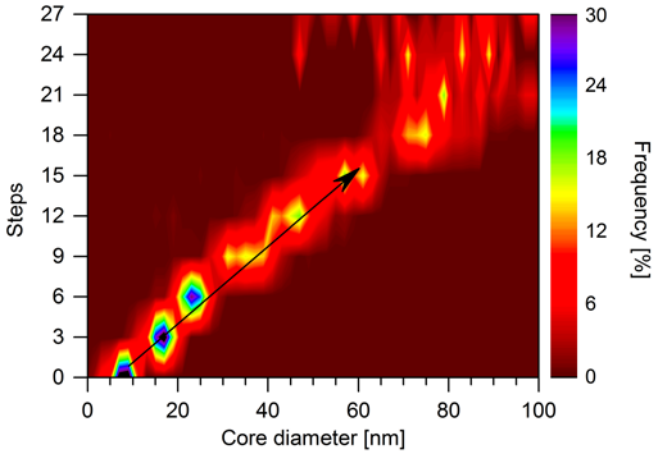

Figure 36. 3D plot of size distributions from TEM measurements of fractions from different stages (y-axis) of the size control experiment. The colour scale shows the relative distribution within each fraction.

The TEM mean and NTA mode agree very well in the stable region (0-21 steps) where NTA generally gives a slightly bigger size of 4-8 nm. This is in the order of the SD so much significance cannot be attributed. In addition, it fits well with the expectations of the coating layer being a few nm thick.

2.2.2 Development of nanoparticle morphology

Several morphologically different structures appeared after 12 steps and became more well-defined for later fractions. Flat structures being hexagonal, triangular or truncated triangular were found, Figure 35F-I and Figure 37A-B. This is a very common phenomenon in the solution synthesis of nanocrystals of FCC materials. These have often been explained by single crystals growing preferentially in the [100] and [110] directions.[95,96] Lofton and Sigmund proposed an alternative mechanism in 2008 where twinning in early stages of nanoparticle formation guided the subsequent growth.[97] Twinning along (111) facets creates twin boundaries that have a higher growth rate than the crystal facets resulting in two-dimensional growth.

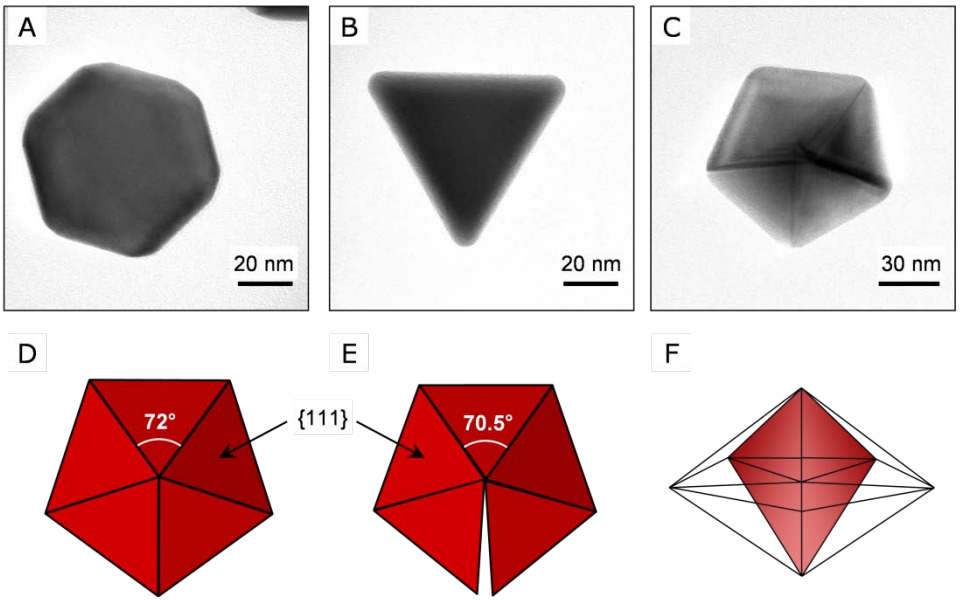

Figure 37. (A) to (C) TEMs of individual faceted AuNPs prepared after 18 steps of the size control experiment. The hexagon in (A) and triangle in (B) are single crystals (or twinned crystals) whereas the decahedron in (C) consists of five tetrahedral crystallites. (D) Schematic top view of the gold decahedron. (E) Assembly of five tetrahedral with ideal angles revealing a gap of 7.5 °. (F) Schematic side view of the gold decahedron with one tetrahedral crystallite highlighted.

Apart from the faceted crystals with hexagonal geometry an equally abundant structure with 5-fold symmetry had formed, Figure 35F-I and Figure 37C. This decahedral structure consists of five crystallites with tetrahedral shape and four {111} faces, Figure 37D. The decahedron exposes exclusively {111} facets, the most densely packed of the FCC facets, making it energetically favoured.[97,98] An ideal {111} tetrahedron in this arrangement would cover 70.5 ° when viewed along the 5-fold axis, Figure 37E, and not 1/5 of 360 ° (72 °) as observed for the decahedra. This mismatch in the decahedral structure costs energy due to induced strain but the energy gain of exposing low-energy facets is higher.[98] The faceted nanoparticles can be seen as exaggerations of twinning in the original seed solution and so twinned polycrystals as well as single crystals must be present in the standard MOS AuNPs. A large area TEM of the uniform faceted nanoparticles in the fraction after 15 steps is shown in App. fig. 4. Agglomeration was beginning after 21 steps.

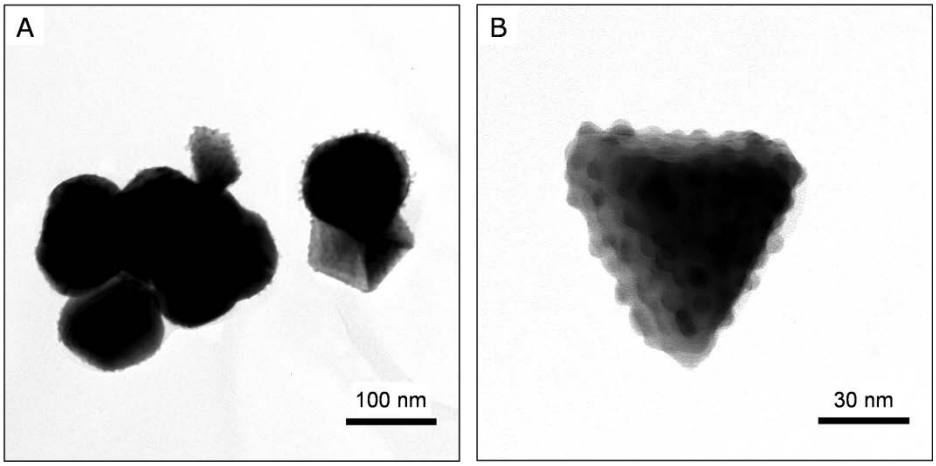

Figure 38. TEM images of seed decorated AuNPs found after 27 steps of the size control experiment.

This resulted in a lower concentration of nanoparticles in solution and a decrease in surface area available for growth by monomer addition. Consequently, a rise in monomer concentration above the nucleation limit occurred and new seeds were formed. The seeds attached to the poorly stabilized AuNPs giving them a lumpy surface, Figure 38. The "lumps" were between 3 and 5 nm and evenly distributed on most of the AuNPs. A selection of individual lumpy AuNPs is presented in App. fig. 5. Sedimentation was observed for some fractions where the solution in the top of the vial was colourless as particles settled towards the bottom of the vial. Gravitation acts on the particles forcing them to settle, but is counteracted by Brownian motion acting to redisperse them. If particles are sufficiently small, the Brownian motion is fast enough to overcome gravitation and the suspensions will not settle. The critical limit for these AuNPs seems to be around 40 nm above which sedimentation is observed within the time-frame of this project. A photograph of the fractions having had time to settle is shown in App. fig. 1. Fractions at 0-21 steps are still stable now after more than 2½ years while fractions after 24 and 27 steps had completely agglomerated in a few weeks leaving a colourless solution and brownish sediment.

2.2.3 Concluding remarks on size control

The seeded growth procedure was successful for the preparation of AuNPs in the size range 8-80 nm. The systematic growth could be followed by NTA, TEM and UV-vis. The starch coating did not hinder the growth of the AuNP seeds. Above the size of 80 nm the starch coating was not sufficient to stabilize the NPs but increasing the starch concentration may solve this. Highly faceted platelets and penta-twinned decahedra were found, especially

above 70 nm, indicating that a part of the seed NPs were polycrystalline. Key figures from NTA, TEM and UV-vis are summarized in Table 4.

Table 4. Key figures from UV-vis spectra, TEM and NTA characterization of the fractions from the size control experiment. UV-vis spectra and size distributions from NTA and TEM are shown in App. fig. 2, App. fig. 3 and App. fig. 6, respectively.

Step	UV-vis $LSPR_{max}$ [nm]	Target size [a] [nm]	TEM Mean ± SD [nm]	NTA Mean ± SD [nm]	NTA Mode ± σ [nm]	NTA NP conc. [mL^{-1}]
0	519	8	7.6 ± 2.2	-	-	-
3	525	14.6	16 ± 2.5	-	-	-
6	529	22.2	23 ± 2.7	28 ± 10	27 ± 8.5 [c]	$5.93 \cdot 10^{11}$
9	528	30.7	35 ± 4.7	47 ± 37	39 ± 3.8	$1.35 \cdot 10^{12}$
12	528	39.8	45 ± 6.6	66 ± 57	53 ± 3.8	$7.51 \cdot 10^{11}$
15	538	49.2	56 ± 5.9	66 ± 23	62 ± 4.6	$7.04 \cdot 10^{11}$
18	544	59.2	74 ± 8.4 [b]	74 ± 13	69 ± 8.0	$7.04 \cdot 10^{11}$
21	555	69.8	83 ± 10 [b]	94 ± 29	83 ± 11	$5.64 \cdot 10^{11}$
24	564	81.1	77 ± 12 [b]	93 ± 15	93 ± 17	$9.20 \cdot 10^{10}$
27	592	93.2	81 ± 19 [b]	114 ± 26	108 ± 24 [c]	$5.22 \cdot 10^{10}$

[a] The theoretical size assuming ideal spherical growth of monodisperse particles and gold concentrations as given in Table 3. [b] Highly faceted particles makes it difficult to report size by a single number. Aggregation in the final fractions complicates particle sizing further. [c] Two maxima of almost equivalent intensity was present, the reported mode is the average of the two.

2.3 Size is not everything, shape control

A large focus is often put on particle size in the field of nanoparticle catalysis when in fact this parameter alone does not determine the performance. Even for the examples given in section 2.2, size is not the core parameter. Rather, the ratio between active and inactive atoms determines the specific activity. It is true that by reducing size, the surface-to-volume ratio increases, which often means an increase in active-to-inactive atoms. However, to evaluate this we need to take a closer look at which atoms are active. The catalytic activity of AuNPs, for example, often arises from under-coordinated edge and corner atoms and not "facet" atoms on the surface. Small-sized spherical particles will contain a much higher degree of active edge and corner atoms than inactive facet and bulk atoms and thus have a greatly increased activity.[88-90,99] In fact, multi-scale simulations have shown that the chemical reactivity of AuNPs is dominated by atoms with six or less coordinating neighbours corresponding to corner atoms and defect sites.[100] An increase in under-coordinated atoms could also be obtained by having a very anisotropic particle with a very rough surface. In this case, the particles do not necessarily need to be extremely small. In

fact, if a porous network of rough and twisting ligaments is created, materials with nanoscale functionality can be made in the cm range. Nanoporous gold (NPG) is an example of such a material. NPG consist of a bicontinuous network of nm-sized gold ligaments and nanopores and is commonly prepared by de-alloying of elements less noble than gold (i.e. silver or copper).[101] This special structure gives rise to increased strain and a very high density of under-coordinated surface atoms on the twisting ligaments. The latter is stabilized by residual silver and responsible for high catalytic activity.[102,103]

Certain catalytic systems involving platinum rely on reactions on terraces rather than edges and corners.[104,105] Decreasing the size of spherical particles is therefore advantageous due to reduction of bulk atoms but a disadvantage due to reduction of facet atoms and a larger portion of edge and corner atoms. Better solutions for these systems are flat sheet-like structures or thin Pt shells on cheaper cores where the amount of bulk Pt is small and facet atoms are abundant. This is the basis for the studies described in the following sections. Shape control of gold is attempted for the preparation of sheets for future work on flat, core-shell nanostructures.

2.4 Flat gold nanostructure synthesis

The interaction of a range of buffers relevant for biochemical research with single-crystal gold surfaces was studied previously. It was found that certain buffers, namely 4-(2-hydroxyethyl)piperazin-1-ethanesulfonic acid (HEPES) and MES, adsorb strongly and facet specifically on gold surfaces. MES adsorbs very selectively on Au(111) resulting in 4 times current increase during its electrooxidation on Au(111) relative to Au(100) which in turn was an order of magnitude higher than on Au(110).[79]

This observation was used as the basis for designing a synthesis of flat gold nanostructures. Adsorption of MES on the Au(111) facets of the freshly synthesized AuNPs may “block” these surfaces facilitating selective growth of Au(100) and Au(110) to form flat structures. This hypothesis is supported by the presence of both flat and rod-shaped structures in the OBS samples. Facet “blocking” is expected to have an effect only during the growth phase of the formation and not the nucleation. Limited nucleation was therefore pursued to focus on slow and controlled growth allowing for MES to adsorb and direct it. The following sections describe two approaches to synthesizing flat gold nanostructures; (1) slow growth by controlling the rate of precursor reduction, samples GS-1 to -3, (2) a template-based approach using graphene oxide as a 2-dimensional template, samples GOsGS-1 to -4 (graphene oxide (GO) supported gold sheets).

2.4.1 Controlled reduction of tetrachloroaurate

The controlled reduction of Au precursor was done in one case by stepwise addition and another by reducing the reduction rate with temperature or choice of reducing agent.

Table 5. Experimental conditions for gold sheet syntheses. Numbers in parentheses after buffer names refer to the pH of the buffer stock solution.

Sample ID	A	B	C	D	Temp.	Time	Stir.
GS-1	$HAuCl_4$ 1 mM	MES (7) 5 mM	Starch 0.3 wt%	Glucose 5 mM	r.t.		Yes
GS-2	$HAuCl_4$ 2 mM	PB (7) 10 mM	Starch 0.6 wt%	Glucose 10 mM	r.t.		Yes
GS-3	$HAuCl_4$ 2 mM	MES (7) 10 mM	Starch 0.6 wt%	Glucose 10 mM	<3 °C	90 min	Yes

For the first approach, the MOS synthesis was carried out at half the standard concentrations at r.t. and the gold precursor, 1 mL 10 mM, was added stepwise with 0.1 mL every 30 min, roughly. This sample is referenced as "GS-1". The dark red colour of the prepared sol indicated that mainly spherical AuNPs were formed which was supported by the UV-vis spectrum and a LSPR max at 525 nm, Figure 39A. No shoulder on the low-energy side of the peak to indicate anisotropic NPs was present. Formation of spherical particles was confirmed by TEM, Figure 39B.

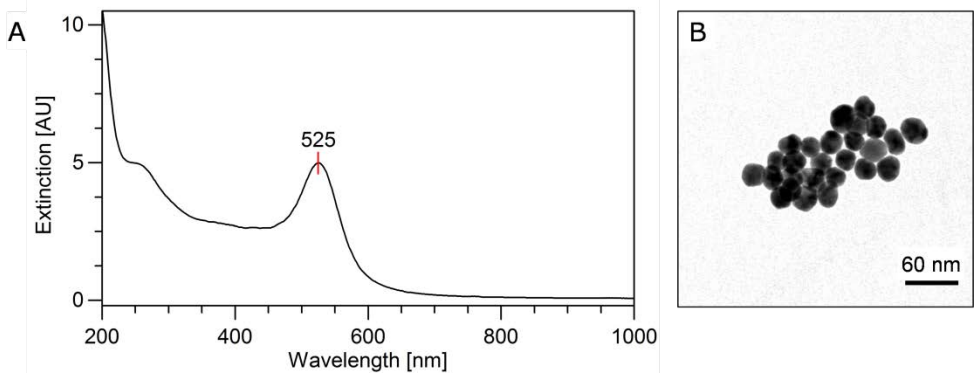

Figure 39. (A) UV-vis spectrum (dil: 10) and (B) TEM of AuNPs synthesized under MOS conditions at 95 °C with slow addition of gold precursor. Only spherical particles were obtained.

Only spherical AuNPs with the size of 27 ± 3 nm (App. fig. 7) were observed. The results are in perfect agreement with predictions based on LaMer theory stating that less nucleation and more growth leads to few, large and monodisperse particles. However, these conditions did not support the formation of flat nanostructures.

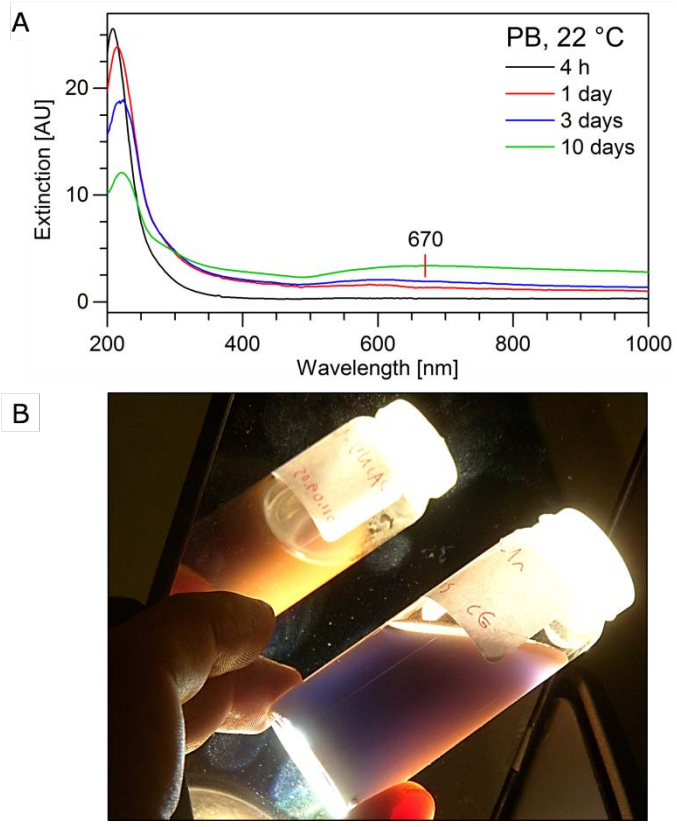

Figure 40. (A) UV-vis spectra of GS-2, gold precursor reduced in PB at r.t. Spectra are recorded from 4 h to 10 days after synthesis initiation (dil: 10, 10, 5, 10 from 4h to 10 days, respectively). (B) Photograph of GS-2 after two weeks. The highly opaque sol looked brown under scattered light, seen by the reflection in the mirror at top of the photo, and blue/purple under transmission. Both effects give rise to the broad extinction band in the UV-vis spectrum.

One issue with the stepwise reduction might be the irregular production of monomer. A slow and steady monomer formation may be more appropriate for controlling the growth process. Such slow formation was achieved in one case by changing the reducing agent (sample denoted “GS-2”) and another by lowering the temperature (“GS-3”). Switching from MES buffer to PB entailed that the gold precursor would be reduced by glucose which is a significantly slower process than reduction by MES. From previous projects, it is known that spherical AuNPs of 13 ± 2 nm are formed in PB at ≈ 90 °C. The synthesis for flat structures was run at r.t. to slow down the reduction further and obtain anisotropy. The UV-vis characterization of the synthesis mixture revealed that the gold precursor was indeed reduced very slowly, Figure 40. The absorption peak around 220 nm from $[AuCl_4]^-$ was still clearly visible after 10 days.

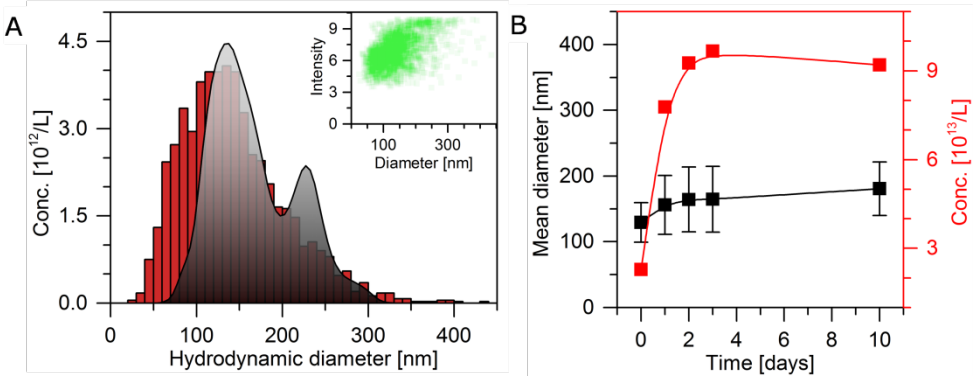

Figure 41. NTA measurements of GS-2. (A) The measured size distribution 2 days after synthesis initiation. (B) The time evolution of the mean hydrodynamic diameter (black) and the concentration (red) measured by NTA. Bars indicate ±SD.

A very broad LSPR band around 670 nm appeared after a few days indicating that non-spherical particles were formed. The presence of large nanoparticles was confirmed by NTA, Figure 41. The concentration of particles grew significantly within the first 2 days to almost 10^4 particles per L after which it stabilized and slightly decreased due to aggregation/precipitation. The size increased with a similar trend from 130 ± 30 nm to 160 ± 50 nm over 2 days. The size distribution at day 2 is shown in Figure 41A.

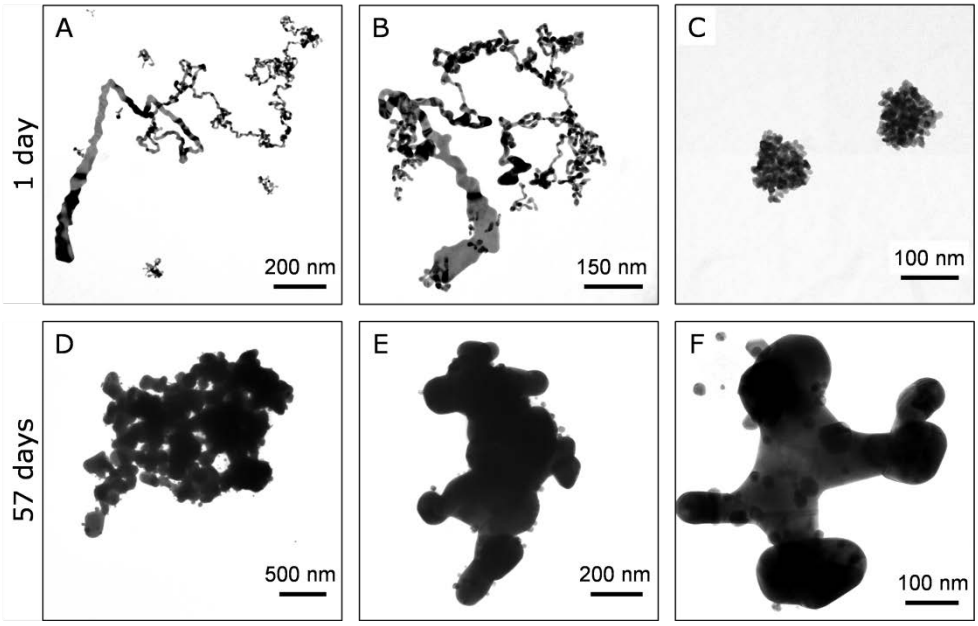

Figure 42. TEM images of GS-2 after (A-C) 1 day and (D-F) 57 days. Initially, many "spaghetti-like" structures and spherical nanoporous aggregates were observed. After about two months mainly large anisotropic sintered aggregates were found.

TEM samples were prepared early in the process (1 day) and after almost 2 months. The first sample contained a mixture of highly anisotropic, porous gold structures with a largely spherical shape and string-like flat structures. The strings seemed to have one end with large, flat areas with single-crystal appearance and another which is more randomly oriented. It is possible that the anisotropic structures grew in solution to form the porous structures and strings. However, most of the Au precursor was not reduced after 1 day as evidenced by the peak at 210 nm in the UV-vis spectra. $[AuCl_4]^-$ reacts with the metallic copper mesh of the TEM grid which may contribute to the observed structures, especially the flat ends of the strings. The sample was investigated with SEM after 20 days, Figure 43. The SEM sample support is carbon, which is inert against oxidation by the $[AuCl_4]^-$ ion. Large crystals of the remaining synthesis components and anisotropic, porous gold structures were found in high concentration.

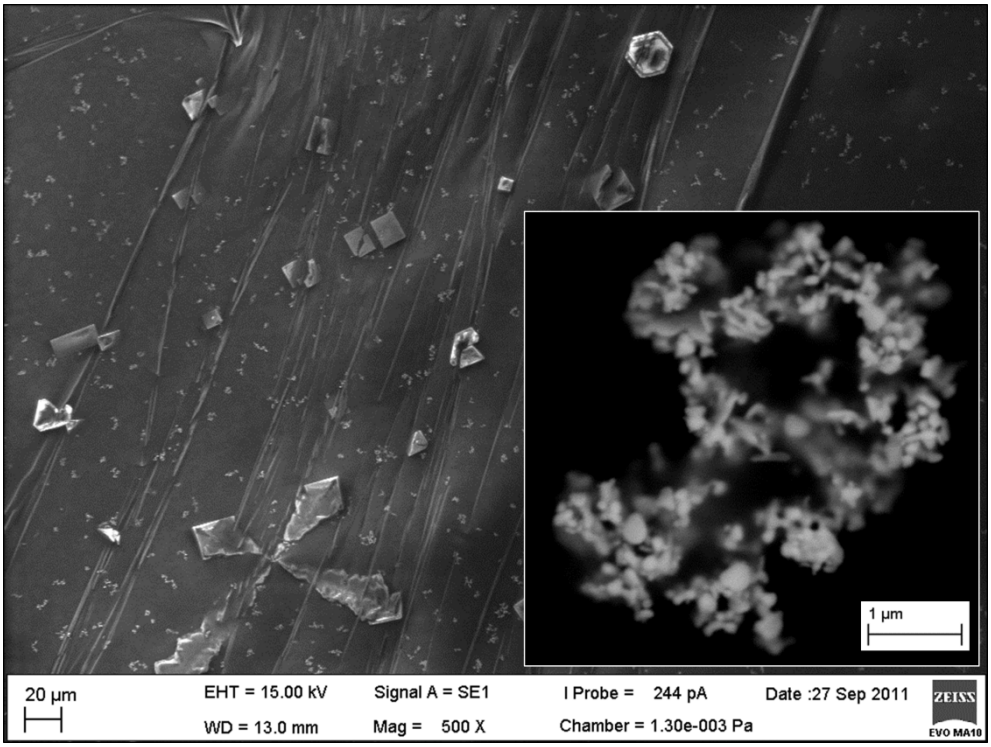

Figure 43. SEM images of GS-2 after 20 days. The low magnification image shows many large crystals of KCl, glucose, phosphate and starch leftover from the synthesis. Scale bar = 20 µm. EDX showed that gold was only found in the smaller, evenly distributed, anisotropic features. A magnified image of the gold structures is shown in the inset. Scale bar = 1 µm. This was recorded using the backscatter detector. The intensity from this type of detector increases with atomic number thus providing improved contrast for gold relative to organic structures.

A backscatter image of one of these structures is shown in the inset in Figure 43. After two months µm-sized anisotropic structures had formed. Interestingly, spherical particles of 10-30 nm were also present and in many cases decorated the large structures, Figure 42. The large anisotropic structures are believed to have formed through growth, aggregation and sintering of the initially formed smaller anisotropic particles. The presence of spherical nanoparticles implies that nucleation still occurred late in the synthesis in a similar way as observed for the seeded growth experiments. It is unclear what gave rise to this behaviour since nucleation only occurs in the early stages of formation when no additional precursor is added later. The reduction of $[AuCl_4]^-$ with glucose in PB at r.t. did induce anisotropic growth but with insufficient control resulting in porous, string-like structures rather than sheets.

The lack of control over the crystal growth direction may be due a lack of facet specific adsorption of starch/glucose on the freshly formed gold surfaces. Switching back to a MES based system will improve this, but also increase the reduction rate due the fast reaction between $[AuCl_4]^-$ and MES. The reaction was instead slowed down by reducing the temperature, i.e. running the reaction in an ice bath. Apart from the reduced temperature, the synthesis was run under standard MOS conditions.

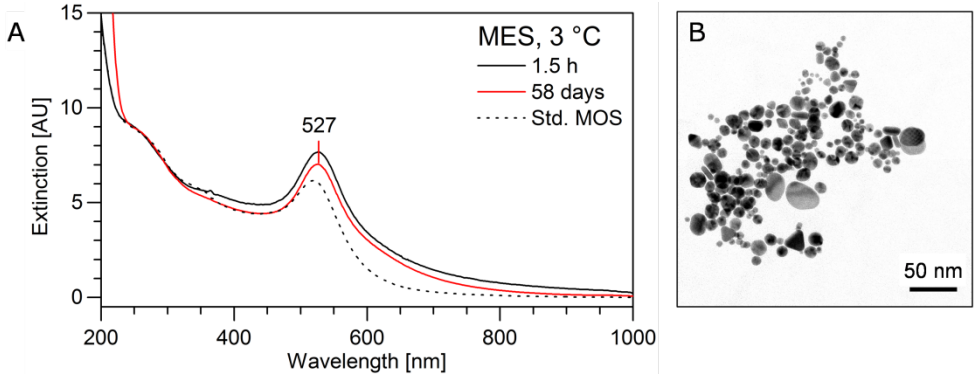

Figure 44. (A) UV-vis spectra of GS-3 after complete reduction (black) and 58 days (red) (dil: 10). A spectrum of MOS AuNPs formed at 90 °C is shown for comparison (dotted line). (B) TEM of GS-3 particles showing spherical, rod-shaped and flat nanoparticles. The TEM sample was prepared 1 day after synthesis.

The reaction time was increased from about 5 min at r.t. to 20 min at 2-4 °C. At this point a dark red sol had formed, which looked similar to the standard MOS AuNP solution. The UV-vis spectrum was stable from 1.5 h and revealed some slight deviations from the extinction spectra of standard MOS AuNPs synthesized at 90 °C, Figure 44A. The LSPR peak was red-shifted ca. 10 nm and the intensity increased. This suggests the presence of AuNPs larger than those formed at 90 °C. Additionally, a tail was present between 600 and 800 nm indicating anisotropic structure formation and/or agglomeration.

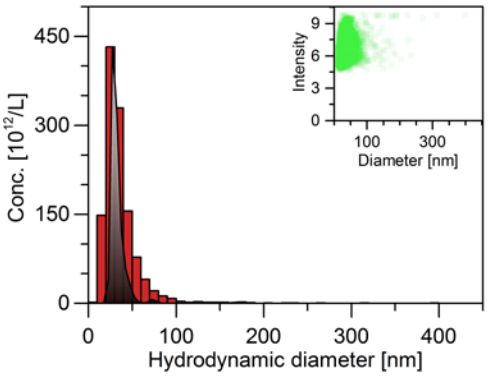

Figure 45. NTA measurement of GS-3 1.5 h after precursor addition. Monodisperse particles are found on the edge of the size detection limit. The size from NTA was 30 ± 20 nm and the concentration $1.0 \cdot 10^{15}$/L.

The observations from the optical properties were supported by NTA showing monodisperse particles around 30 nm, Figure 45. However, the distribution covers a size range close to the detection limit of NTA. TEM imaging showed a mixture of spherical particles in a broad size range and the presence of anisotropic structures, i.e. sheets and rods, Figure 44B, correlating with the tail in the extinction spectrum. The TEM sample was prepared 1 day after synthesis and revealed many cubic CuO features indicating that ionic gold was present in the solution, App. fig. 8. Based on UV-vis spectroscopy, no $[AuCl_4]^-$ was however left in solution. A small remainder of ionic gold may be adsorbed on the surface of the nanoparticles and reduced very slowly in solution but react with the Cu grid during TEM sample preparation. After about two months the main change in the extinction spectra was an increased absorbance below 220 nm, Figure 44A. Both MES and starch absorbs in this range and the observations might relate to changes in adsorbed molecules on the nanoparticles.

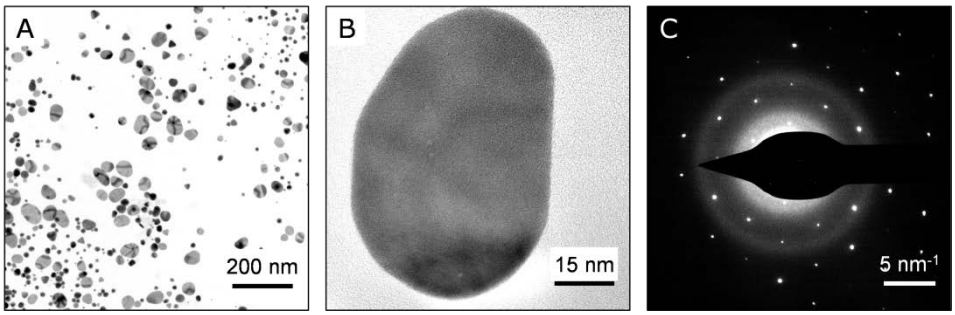

Figure 46. TEM images of GS-3 57 days after precursor addition. (A) Areas with many small nanosheets were seen. HR-TEM (B) and SAED (C) of single sheets revealed single-crystal structure with the large facet being (111).

TEM did not show any oxidized copper at this point. Interestingly, areas with a large amount of small nanosheets were found several places on the sample. Other areas were dominated by spherical particles, App. fig. 9. The large facet of the sheets was determined by electron diffraction and HR-TEM to be (111), Figure 46B-C. The diffraction pattern fits with a [111] zone axis[vi] and the HR-TEM images shows 3 sets of fringes with equal spacing and at 60 ° angles confirming {111} lattice planes, App. fig. 10.

In conclusion, the slow reduction approach worked well for the formation of anisotropic structures. However, it proved challenging to limit the growth to two dimensions. Cooling the reaction mixture during synthesis by the MOS method was most suitable for the growth of nanosheets presumably due to the interaction of MES molecules with and blocking of the (111) surface.

2.4.2 Graphene oxide templated synthesis

An entirely different approach utilizing the atomically thin graphene oxide as template for growth of the gold sheets was also taken. GO is the oxidized form of graphene and contains many functional groups on the surfaces and edges, such as acid, alcohol, aldehyde and epoxide groups. These increase stability and hydrophilicity and are also able to bind cations.[106,107] It was expected that the gold precursor would adsorb on the GO either directly by coordination of the trivalent gold ion or through electrostatic interaction between the $[AuCl_4]^-$ ion and adsorbed K^+.

Table 6. Experimental conditions for GO templated gold sheet syntheses. Numbers in parentheses after buffer names refer to pH of the buffer stock solution.

Sample ID	A	B	C	Temp.	Time	Stir.
GOsGS-1	$HAuCl_4$ 2 mM	MES (7) 10 mM	GO [a] 100 mg/L	<3 °C	90 min	Yes
GOsGS-2	$HAuCl_4$ 2 mM	MES (7) 10 mM	GO [a] 100 mg/L	<3 °C	60 min	Yes
GOsGS-3	$HAuCl_4$ 1 mM	MES (7) 5 mM	GO [a] 100 mg/L	<3 °C	60 min	Yes
GOsGS-4	$HAuCl_4$ 1 mM	MES (7) 5 mM	GO [a] 50 mg/L	<3 °C	60 min	Yes

[a] 2 g/L stock solution of graphene oxide made by Shiyu Gan in the group.

[vi] In this report, zone axis refers to the axis of the electron beam which can be considered the "viewing direction". The zone axis is normal to the crystal plane of the same index for cubic crystal system such as Au. The crystal facet which is normal to the beam will therefore have the same index as the zone axis, i.e. (111) for a [111] zone axis.

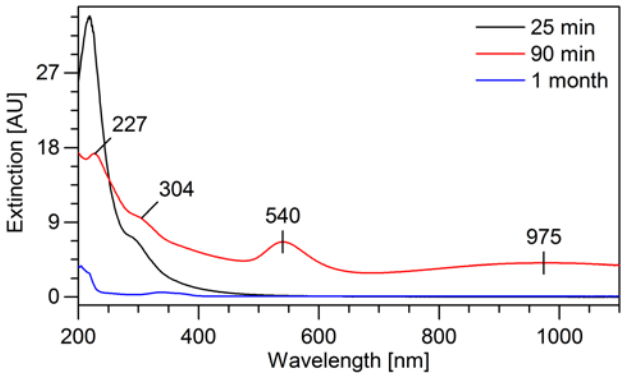

Figure 47. UV-vis spectra of GOsGS-1 25 min (black, dil: 10), 90 min (red, dil: 10) and 1 month (blue, dil: 1) after precursor addition. After 1 month at r.t. the sample had completely aggregated and the UV-vis spectrum of the supernatant was measured.

GO was prepared in the group by guest PhD student Shiyu Gan from Changchun Institute of Applied Chemistry, Chinese Academy of Sciences, China, in 2012.[108] No capping agent was used since stabilisation of particles in solution was not desired. Due to the positive effects observed for GS-3, ice bath was again utilized. The gold precursor was added dropwise over 10 min. A 20 mL batch of 2 g/L purified GO was used as stock solution. Gold precursor and MES buffer concentrations were kept at standard conditions (2 and 10 mM, respectively) for the initial test (GOsGS-1) and GO was added to obtain a concentration of 100 mg/L. The reaction was slow and after 25 min still no LSPR peak was present in the UV-vis spectrum, Figure 47. Only a strong absorbance from the gold precursor and the spectrum of the GO was observed. The precursor was not detectable after 90 min. Instead, two peaks associated with LSPR appeared. This resembles the behaviour of gold nanorods where two modes, transverse ($LSPR_{trans}$, high energy) and longitudinal ($LSPR_{long}$, low energy) modes, arise from different orientations of the rods relative to the direction of the light. $LSPR_{long}$ is red-shifted with aspect ratio and can occur well above 1 µm for high aspect ratio gold nanorods.[109] The notation of $LSPR_{trans}$ and $LSPR_{long}$ is adapted for the current data. The extinction of the sample suggests that anisotropic gold nanostructures had formed. Absorbance from GO was still present in the UV range with a peak and shoulder at 230 and 300 nm, respectively. Reduction of GO brings a red-shift of the main peak to 270 nm which was not observed.[110-112] NTA showed a broad size distribution of 60 ± 30 nm with a mode at 48 nm, App. fig. 11A. A TEM sample was prepared a few hours after precursor addition and revealed some exciting structures. Ring-shaped gold nanostructures dominated the sample. Approximately round gold sheets with holes in the middle had formed, often stacked on top of each other, Figure 48.

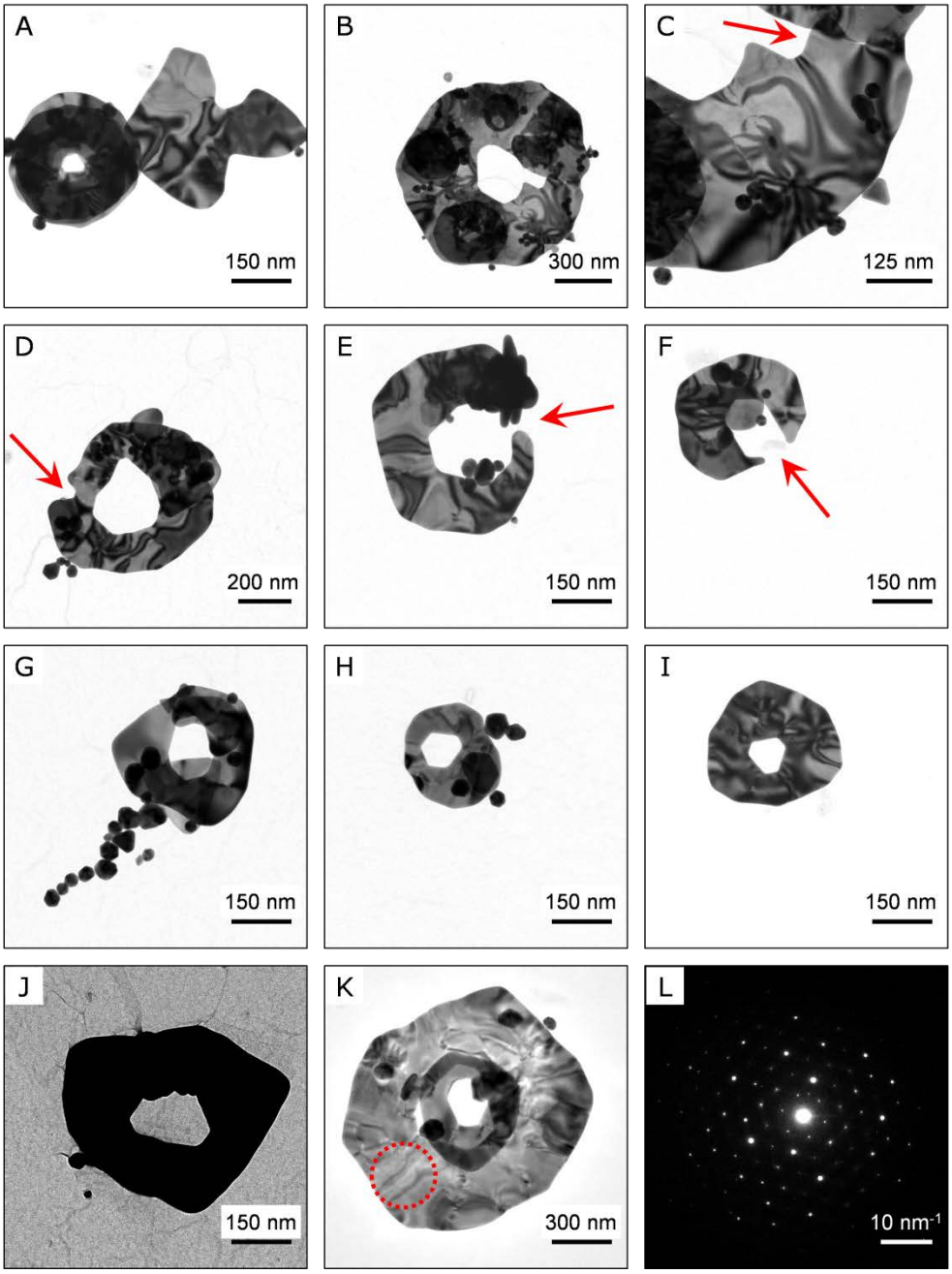

Figure 48. TEM images of gold nanorings synthesized on GO. Red arrows indicate where rings are in the process of closing. (L) shows the SAED of the circled area in (K). Sample was prepared within a few hours of precursor addition.

The nanorings ranged from 200 nm to more than 1 µm in diameter and had a single hole close to the centre. The size of the holes varied but they were often faceted with a hexagonal shape indicating {111} sides. It is believed that metallic gold nucleated on the GO and grew laterally in two directions creating a curved ribbon. Eventually the two ends met and the ring was closed. This is supported by a large number of rings being incomplete. Nanorings in different stages of closing are indicated by red arrows in Figure 48 and App. fig. 12. A magnified view of the semi-joined ring in Figure 48B is shown in Figure 48C. The ring has fused on the right side of the joint but on the left side the two ends overlap. Gold monomers may freely diffuse on the surface of the GO facilitating growth of a single crystal rather than formation of new nuclei.

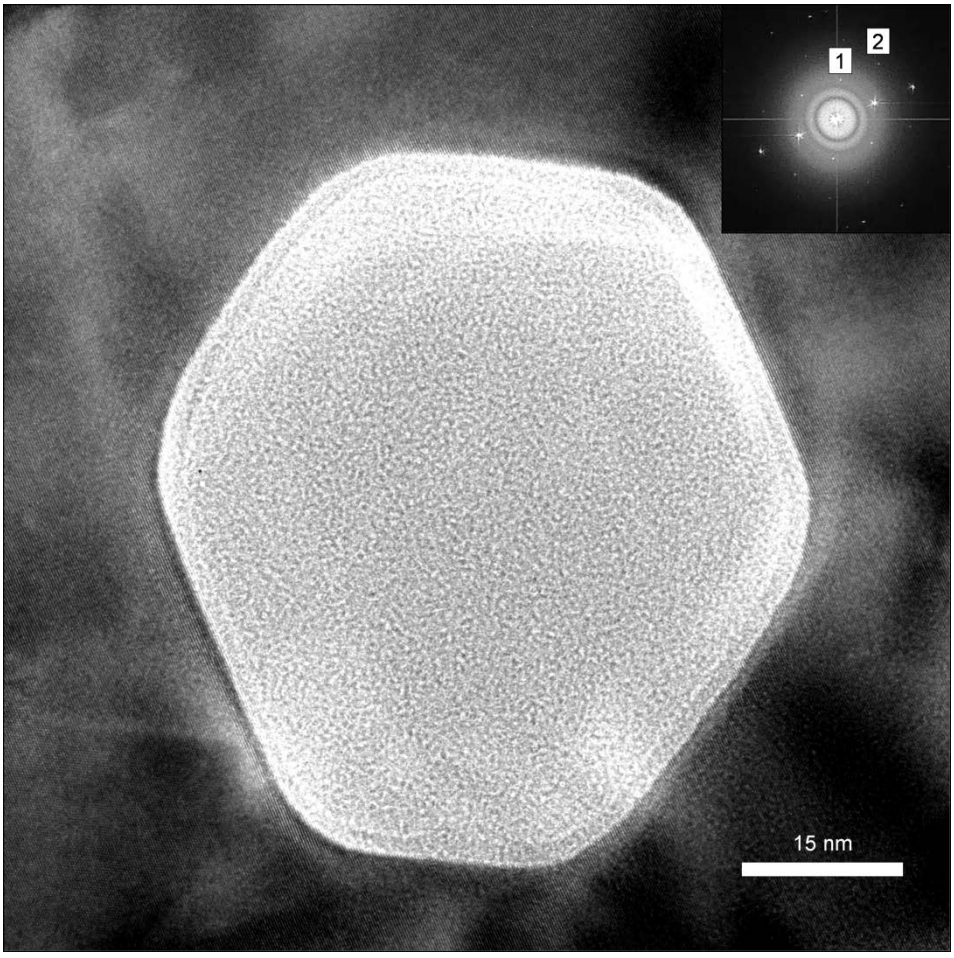

Figure 49. HR-TEM and corresponding FFT (inset) of gold nanoring from GOsGS-1 showing a well-ordered, seemingly single-crystal gold structure.

In some cases, nuclei (and subsequently sheets) may form on both sides of the GO resulting in stacked rings, Figure 48A, -B, -G, and –K and App. fig. 12A, -C and -L. The perfect facets of the holes may arise by rearrangement of edge atoms to reduce surface energy.It is difficult to see the very low-contrast GO in the presence of high-contrast gold nanorings. In some case GO was observed together with the discs made clear by increasing the contrast of the image, Figure 48J. In other cases no GO was found in association with the nanorings. The SAED of a section of one nanoring shown in Figure 48L confirms that the large surface area is a (111) facet. The lattice spacings of the innermost and second innermost spots were 2.37 and 1.37 Å corresponding to (11-1) and (02-2), respectively, with [111] as zone axis. High resolution (HR) TEM revealed lattice fringes continuing across the entire ring in several instances one of which is shown in Figure 49. This means that the entire ring was made up of one crystal or several identically oriented crystals supporting a highly controlled growth process. The observed fringes agreed with (11-1) and (02-2) and a [111] zone axis, Figure 49, App. fig. 13 and App. fig. 14.

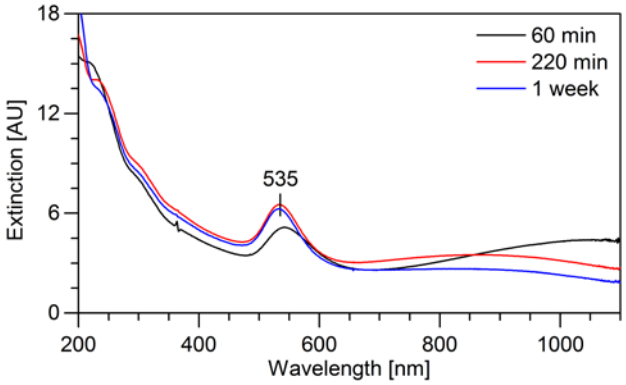

Figure 50. UV-vis spectra of GOsGS-2 at 60 min (black), 220 min (red) and 1 week (blue) after precursor addition (dil: 10).

The experiment was repeated, GOsGS-2, to reproduce the nanorings but with reduced cooling time, 60 min. The optical behaviour, Figure 50, was similar to that of GOsGS-1. The LSPR was shifted from 543 nm at 60 min to 535 nm after 220 min and weak peaks from GO were present around 230 and 300 nm. Low concentration of large particles was detected with NTA resulting in an increased measured size of 200 ± 100 nm but the majority of particles were around 50-60 nm, App. fig. 11B. Again the sample had completely aggregated after one month leaving a colourless solution with black, “fluffy” sediment. A TEM sample was prepared shortly after cooling was terminated. The amount of synthesis mixture on the TEM grid was too high making imaging difficult. However, a few nanoring, many small sheets and spherical particles were observed, Figure 51.

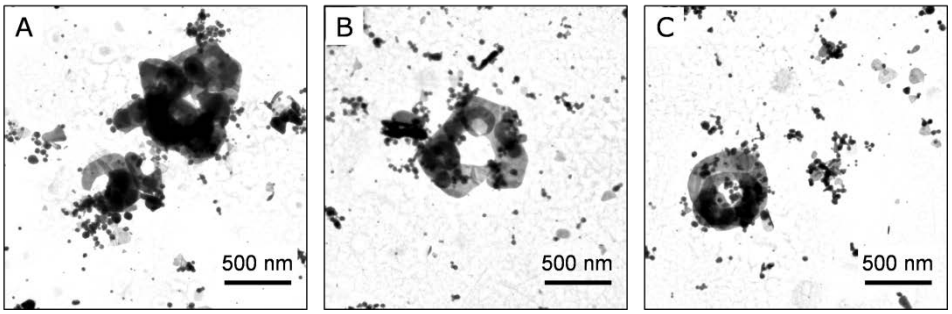

Figure 51. TEM images of GOsGS-2. The TEM sample was prepared a few hours after precursor addition and contained several nanorings.

The reaction conditions were modified in order to optimize the yield of nanosheets and nanorings. Two new samples were prepared. One sample was prepared with half concentrations of $HAuCl_4$ and buffer (GOsGS-3) and the other half concentrations of $HAuCl_4$, buffer and GO (GOsGS-4). The $LSPR_{trans}$ and $LSPR_{long}$ were not separated in the UV-vis spectra, Figure 52, but rather the spectra showed peaks at 560 nm with a long tail towards the infrared suggesting that less anisotropic nanostructures had formed. Both samples contained a large number of small sheets as well as spherical nanoparticles and -rods, Figure 53.

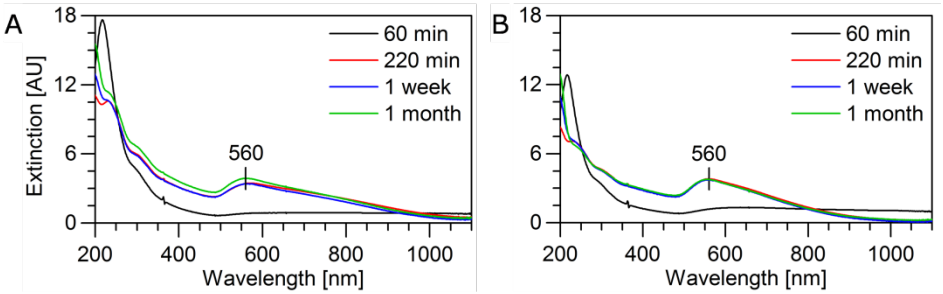

Figure 52. UV-vis spectra of (A) GOsGS-3 and (B) GOsGS-4 (dil: 10).

TEM studies of GOsGS-3 revealed one large sheet similar to the nanoring structures shown in Figure 53A. However, the sheet was less well defined and had several faceted holes, in contrast to the previously synthesized nanorings. Within a month the GO of these samples had also aggregated but the solution was not colourless. Instead, the solution was slightly opaque with a purple colour. Even after 20 months the UV-vis spectra still displayed LSPR with peak maxima at 555 and 570 nm for GOsGS-3 and -4, respectively, App. fig. 15. The coloured solutions suggest that the gold nanostructures were not completely associated with the aggregated GO but also stable in solution. This was not the case for GOsGS-1 and -2.

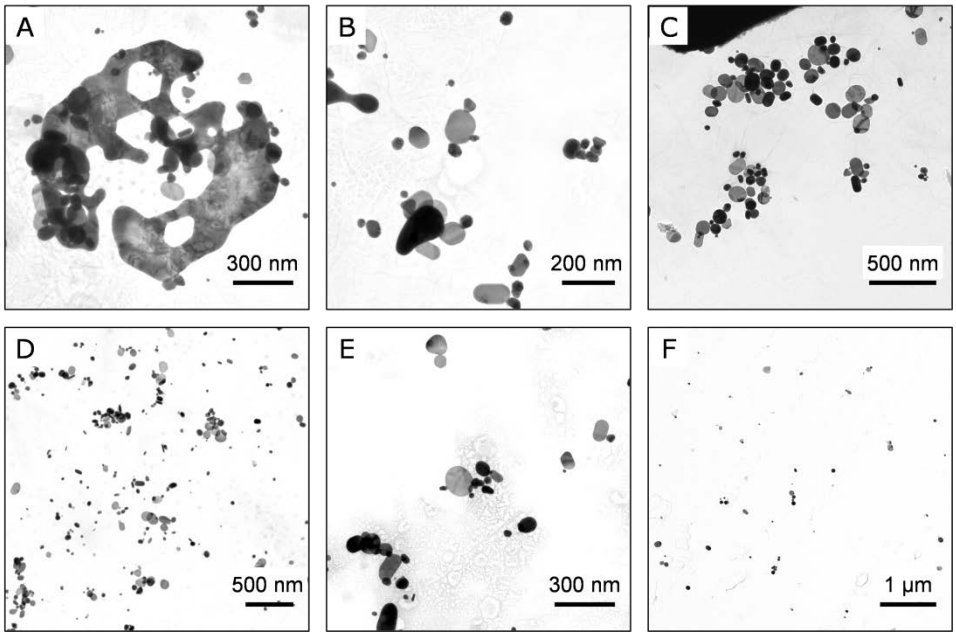

Figure 53. TEM images of (A-C) GOsGS-3 and (D-F) GOsGS-4. Two TEM samples were prepared for each sample; (A-B, D-E) one after terminated cooling and (C, F) one 19 days later.

The utilization of GO for flat gold nanostructures clearly had a large effect. GO templated synthesis produced the largest content of nanosheets of all the experiments associated with flat nanostructure synthesis and an interesting new nanoring structure. An intimate interaction between gold precursor and GO is evident and the results show great promise for future composite nanomaterials.

2.4.3 Concluding remarks on flat gold nanostructure synthesis

The synthesis of flat Au nanostructures was difficult to obtain at r.t even with slow addition of Au precursor of slow reduction by glucose. Decreasing the reduction rate under standard MOS conditions by running the synthesis in an ice bath did provide a significant formation of sheets. The positive influence of lowered reaction temperature was further combined with the addition of a 2-dimensional template, GO. No stabilizing agent was used to further facilitate interaction between Au and GO. The presence of the flat GO sheets enabled gold to crystallize and grow along their surfaces. Peculiar ring-shaped, flat Au nanostructures with well-defined, faceted holes in the middle were formed. The growth mechanisms responsible for the generation of holes rather than filled sheets are not yet disclosed. The best conditions for nanoring formation were the standard MOS synthesis, ≈ 100 µg/L GO and <3 °C. In particular, the GO templated sheets show promise for further utilization for

Pt-based catalyst preparation. The Au nanorings may serve as cores for the growth of flat Pt shells and GO as a highly conductive support material.

2.5 Unidentified UV peaks

An unidentified UV peak at 366 nm (referenced henceforth as "A366") was discovered during work with AuNP-copper wire interactions prior to the PhD studies. A peak appeared when AuNPs were synthesized at r.t. without glucose and starch, i.e. the OBS procedure. The absorbance was very strong (stronger than that of the LSPR) when it was at maximum intensity. The source of A366 was not determined at that time but systematic investigations were carried out in the current project to elucidate this phenomenon.

The peak was monitored by UV-vis spectroscopy to determine the stability of the UV active compound, Figure 54. The peak decayed slowly over time and was still very intense after several days in the native AuNP solution at r.t. It took more than 6 days for the peak to disappear so the compound is not a short-lived intermediate, providing hope for its identification.

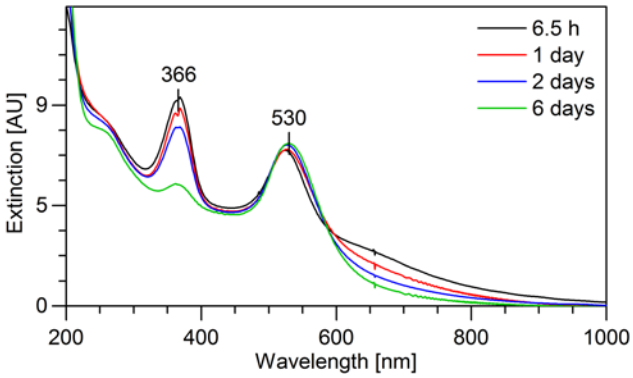

Figure 54. Long-term development of A366. UV-vis spectra were recorded over a period of 6 days (dil: 20).

2.5.1 Formation kinetics and UV sensitivity of A366

A366 grew in intensity within the first few hours of precursor addition. Spectra recorded at various times are shown in black in Figure 55 and the absorbance is plotted as function of time in Figure 56. The LSPR peak remained stable while the UV peak grew exponentially with time. It was discovered that repeat UV-vis measurements caused an increase in A366 intensity and within less than a minute of "pumping" the intensity had reached the maximum that would otherwise require hours.

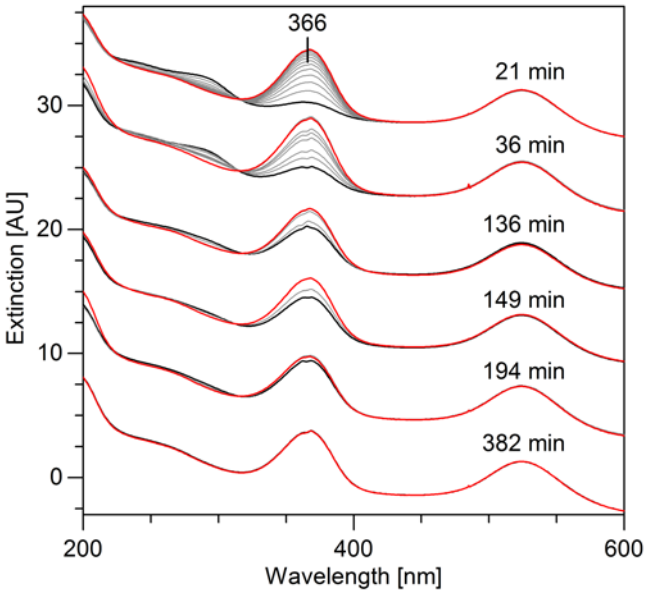

Figure 55. Peak growth with time and "pumping" (from black to red) by repeat UV-vis measurements (dil:20). The spectra are grouped in sets by reaction time. Each set consists of first (black), intermediate (grey) and final (red) measurements.

It could be UV light that is responsible for the "pumping" since the native solution is always exposed to visible light. A very weak peak around 290 nm was present in the early stages of synthesis and decayed during repeat measurements suggesting a link between this peak and A366.The maximum absorbance reached by "pumping" decayed slightly with time and at roughly 6 h no effect of "pumping" was observed, red diamonds in Figure 56.

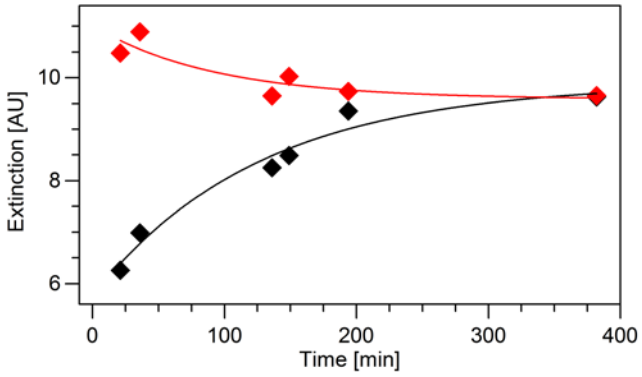

Figure 56. Absorbance as a function of time of first (black) and final (red) spectra during "pumping" of the UV peak shown in Figure 55.

2.5.2 Isolation of UV active compound

Without starch present the AuNPs are no longer sterically stabilized. Instead, adsorbed MES molecules provide charges on the surface and electrostatic stabilization. The electrostatic effects can be screened by increasing the ionic strength of the medium leading to aggregation. Forced aggregation by addition of a few mL of 20 mM $CuCl_2$[vii] was used to remove the AuNPs from solution. This procedure very effectively eliminated the AuNPs from solution leaving black sediment and a colourless supernatant as shown in Figure 57. Further centrifugation treatment did not change the UV response. The difference spectrum (dotted line) clarifies that the $CuCl_2$ treatment effectively removed all traces of OBS AuNPs. This clearly showed that A366 was not associated with the AuNPs and were stable at high ionic strength. It is not optimal for the identification of A366 to add additional species to the supernatant, i.e. treatment with $CuCl_2$.

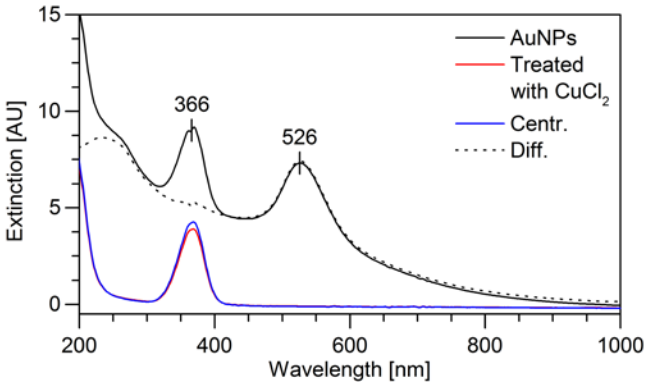

Figure 57. Isolation of UV active compound by disruption of electrostatic stabilization and centrifugation. UV-vis spectra of fresh OBS AuNPs (solid black), supernatant after treatment with $CuCl_2$ (red), supernatant from centrifugation (blue) and the difference between fresh and agglomerated sample (dotted black) (dil: 20). 100 µL 20 mM $CuCl_2$ was added to the UV-vis sample corresponding to a Cu-to-Au molar ratio of 40. UV-vis spectra of pure $CuCl_2$ are shown in App. fig. 16 and show no significant absorbance above 250 nm.

As an alternative, forced aggregation and precipitation of the AuNPs was achieved by filtering through a standard 0.2 µm syringe filter. Occasionally, one filter did not suffice so two filters were used in tandem. Filtrates were prepared at 45 min intervals starting 45 min into the synthesis, F1-F4, Figure 58. The peak at 293 nm (referenced as “A293”) was very intense after removal of the AuNPs.

[vii] $CuCl_2$ was used for other studies not included here in attempts to synthesize CuO shells on AuNPs leading to the observation of induced aggregation.

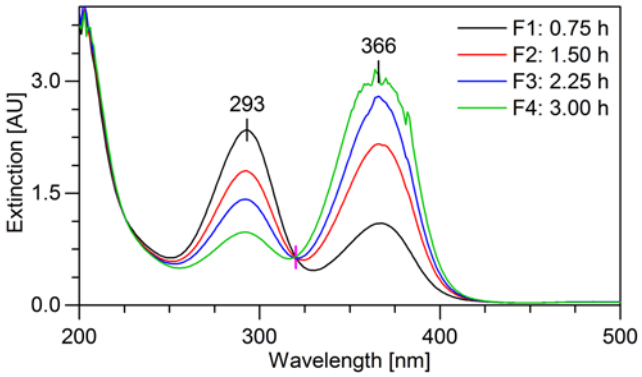

Figure 58. UV-vis spectra of samples taken from the OBS AuNPs and filtered in 45 min intervals showing two correlated UV-peaks at 293 and 366 nm (dil: 1). The isosbestic point at 320 nm is indicated by the magenta bar.

It was surprising to see such strong absorbance of the A293 since it is barely visible in the presence of AuNPs. It is possible that the cause of A293 is associated with surface of AuNPs and released to the solution upon aggregation of the AuNPs. An isosbestic point at 320 nm showed that the two peaks were correlated, suggesting that A293 was converted to A366. The ratio between the two peaks in the filtrates was very stable. The peaks did not change noticeable in the timescale for A366 growth in the native AuNP solution. The "pumping" behaviour observed in the AuNP solution, Figure 55, was not found for the filtrates where the peaks were unaffected by repeat measurements. These two points further indicate a close interaction between at least A293 and the AuNPs.

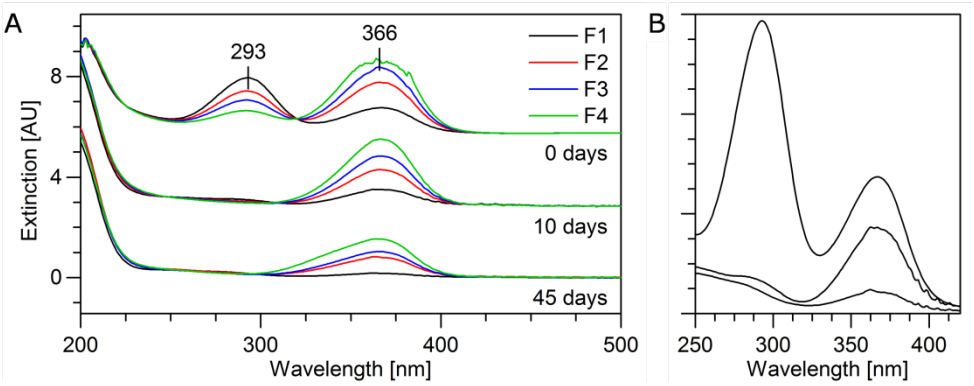

Figure 59. Long-term stability of the isolated UV active compounds (dil: 1). (A) UV-vis spectra of filtrates 1-4 are recorded on the day of filtration (top), after 10 days (middle) and after 45 days (bottom). (B) Overlay of the spectra of F1 at 0, 10 and 45 days.

These observations also yield another possible explanation for the mechanism of "pumping". It might be excitation of the LSPR that is the driving force for the conversion

of A293 to A366 and that the different behaviour in native solution and during UV-vis measurement is a matter of light intensity and, since the UV-vis measurements are done in diluted samples, dosage (photons per AuNP). The stability of the filtrates was followed over 45 days again showing a much higher stability in the absence of AuNPs. Even after 45 days, Figure 59, absorbance around 50 % was retained compared to a decay of more than 80 % in the AuNP solution in just 6 days. This further supports the explanation of plasmon resonance induced conversion.

The A293 and A366 appear in the OBS synthesis so the filtrates were spiked with additional MOS synthesis components to check what their influence is on the origin of these UV peaks. Neither starch nor glucose had any effect on the UV peaks. This rules out that the origin is a synthesis by-product that reacts further with starch/glucose in the MOS procedure making them only transient under these conditions. Major changes were found upon addition of MES stock solution (pH 7), Figure 57.

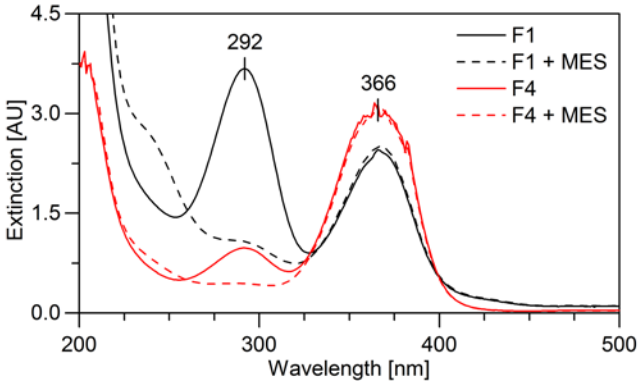

Figure 60. Sensitivity to MES. UV-vis spectra are recorded of F1 (black, dil: 10) and -4 (red, dil: 1) before (solid) and after (dashed) addition of MES stock solution. 40 µL of 0.1 M MES (pH 7) is added to 1 mL filtrate (10 times diluted for F1 and undiluted for F4) corresponding to a 4 mM increase from 1 and 10 mM for F1 and -4, respectively.

A293 was almost quenched entirely while no change to A366 occurred. This mechanism must be different than the previously encountered conversion from A293 to A366. The decay of A293 was accompanied by increased absorbance around 240 nm. These observations can be explained by either chemical reactions with MES buffer, change in pH or change in ionic strength. pH of the filtrate from OBS synthesis is around 3 so addition of buffer at pH 7 entails an increase in pH. MES is already in excess relative to the gold precursor so it seems unlikely that the change to A293 is a result of chemical reaction with MES. Addition of MES buffer does bring an increase in ionic strength through the content of KOH but it was previously shown that the UV peaks were robust towards addition of $CuCl_2$ so ionic strength effects must be negligible. Sensitivity of A293 to increasing pH

implies that deprotonation is involved. If the origin is related to metallic clusters, deprotonation may lead to a loss in electrostatic stabilization and aggregation. On the other hand, if the origin of the UV peaks is molecular, deprotonation may change the electronic structure so the observed transition no longer exists. Only few deprotonizable functional groups are present in the OBS synthesis; tertiary amine, sulfonic acid and amine oxide. The sulfonic acid is a strong acid with a pKa below 0. The amine and amine oxide are potentially deprotonated in the given pH range with pKa values of 6.15 and around 4.5, respectively.

2.5.3 Fluorescence of the UV active compound

The optical properties of the filtrates were examined further with fluorescence spectrometry. The first studies were done by scanning the emission spectrum for a series of fixed excitations. The emission scans were recorded for excitations at 220, 230, 240, 250, 260, 270, 280 and 290 nm corresponding to a-h in Figure 61.

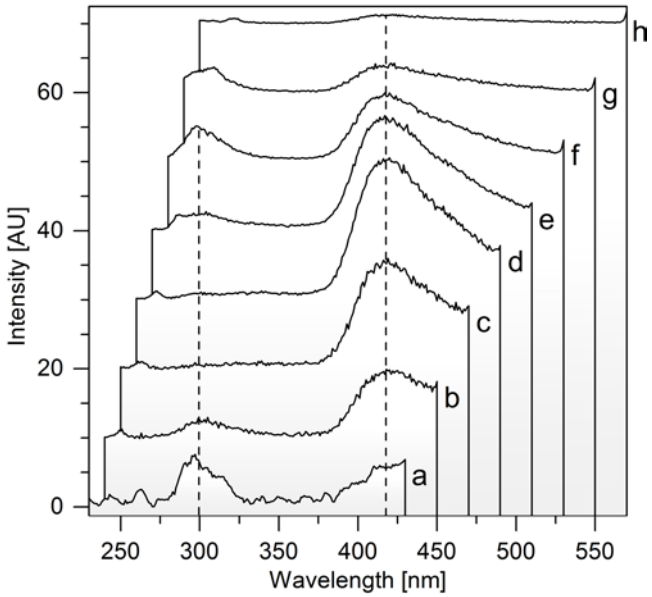

Figure 61. (a-h) Emission scans for excitations from 220 to 290 nm in increments of 10 nm. Dashed lines indicate the position of the emission peaks at 300 and 420 nm.

Two emission peaks were found around 300 and 420 nm, respectively (dashed lines in Figure 61). The excitation wavelength was subsequently scanned for fixed emission at 300 and 420 nm to determine precisely the maximum excitation. The maxima were located at 273 nm for emission at 300 nm and 250 nm for emission at 420, shown in Figure 62 in red and black, respectively.

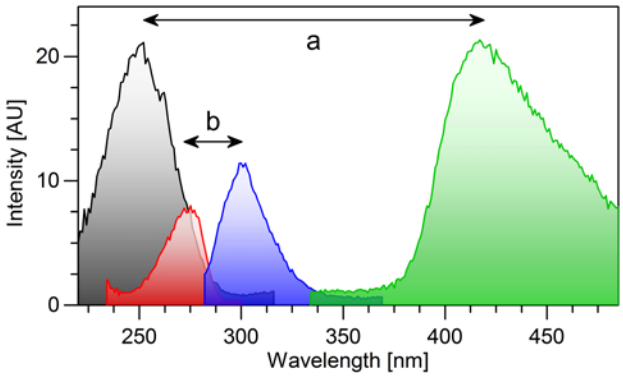

Figure 62. Two fluorescence pairs observed for the filtrate. Pair "a" is shown with an excitation scan for emission at 420 nm (black) and an emission scan for excitation at 250 nm (green). Pair "b" is shown with an excitation scan for emission at 300 nm (red) and an emission scan for excitation at 273 nm (blue).

The corresponding emission scans at these fixed excitations are shown in blue and green. The two fluorescence signals correspond to shifts in energy from excitation to emission of 1.99 and 0.40 eV for "a" and "b" in Figure 62, respectively. Plots of the UV-vis spectrum of F2 (App. fig. 17) and the fluorescence signals (App. fig. 18) versus photon energy are shown in appendix. A 3D scan of pair "a" was obtained by scanning the emission spectrum from 365 to 450 nm for excitations between 235 and 265 nm with 1 nm increments, App. fig. 19. The higher resolution of the excitation range only confirmed that maximum emission was obtained with excitation/emission at 250/420 nm.

2.5.4 Mass spectrometry and electron microscopy

A possible molecular origin of the UV peaks was investigated further. Chromatography was used to separate and purify the unknown species and MS for characterization. Two setups were employed; (1) UPLC coupled with both a UV detector and MS and (2) GC coupled with MS. UPLC separates species in solution based on their affinity to the column material and MS uses an alternating electric field to separate charged species by their mass-to-charge ratio. Samples from early $CuCl_2$ treatment experiments were extracted with ammonium acetate, NH_4Ac and run in a reverse phase setup. This entails that the polar mobile phase (the solvent) is pushed through an apolar stationary phase (the UPLC column) and the compounds are retained according to their hydrophobicity. The compounds of the sample were ionized by electrospray ionisation (ESI), both positive (ESI^+) and negative (ESI^-). Three distinct peaks were seen in the UV trace, Figure 63, which means that at least three UV active species are contained in the sample.

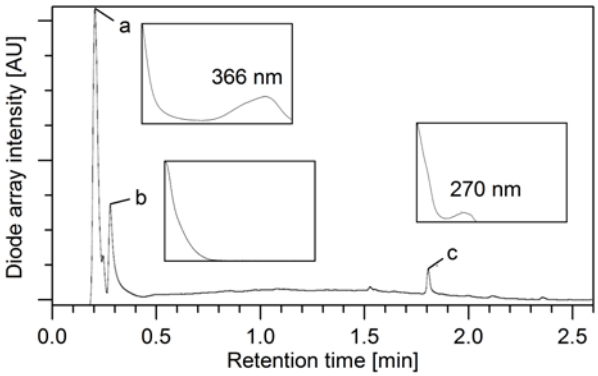

Figure 63. UV signal over retention time during UPLC. Insets show UV spectra of the three fractions from 210 to 400 nm.

The corresponding UV spectra are shown in the insets and it is clear that the A366 is eluted together with the buffer, peak "a", and is not retained at all by the hydrophobic column. Peak "c" may correspond to A293 but the shift in peak maximum is significant. The ESI^- trace showed one peak around the retention of "a" and "b" with one main m/z intensity in the MS at 194. This fits very well with MES buffer with deprotonated sulfonate and amine providing a negative ion with the mass of 194. The ESI^+ trace shows a range of m/z intensities at the same retention time. The majority of the peaks fit with monomers, dimers, trimers and tetramers of MES with protonated amine and sulfonate and possible cation exhange on both positions, App. fig. 20. No significant contributions apart from MES appeared in the MS at the retention time of A366. Either MES had somehow changed its UV response or the origin of A366 is not visible in the MS. That might be because it is not easily ionized or that it is outside the m/z range of the MS. Clean mass spectra were obtained for retention "c" (Figure 63) for both positive and negative ionisation showing a m/z of 342, App. fig. 21. This compound was retained well and must be quite apolar.

In GC a liquid sample is injected in to a flow of carrier gas, the mobile phase, which is led through a long column, stationary phase, at elevated temperatures. Only compounds that enter the gas phase and "fly" with the carrier gas are analysed and separated based on their affinity to the column. The outgoing stream is analysed by MS. The instrument applied here was fitted with tandem MS, (MSMS). This allows for individual compounds to be broken into fragments that provide information on the parent species. The filtrate containing the A366 was analysed with the GC-MSMS providing only two signals, "a" and "b" in Figure 64. The fragment spectra of the two compounds were matched to morpholine ("a") and 1,4-butane sultone ("b"), App. fig. 22.

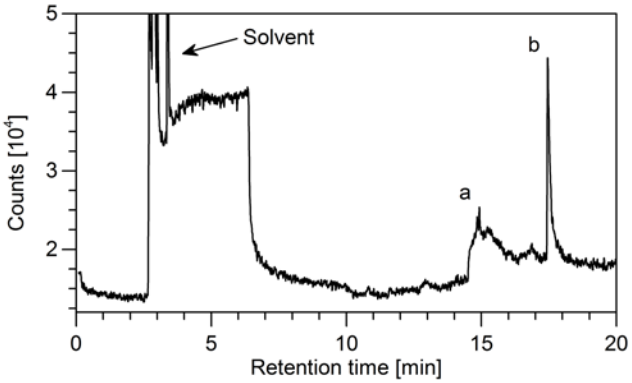

Figure 64. GC-MS of the isolated UV active compound. Apart from solvent signals, two peaks appeared at 15 (“a”) and 17.5 min (“b”).

Morpholine could be formed by decomposition of MES or MES_{OX} but the sultone contains a butane section which requires the formation of a C-C bond since MES only contains 2C fragments. This seems unlikely, but it may be an erroneous match for another compound containing a sulfonate. No new compounds that could be the source of A293 and A366 were identified with the HPLC and GC-MS.

The filtrate was studied with TEM to search for small metallic nanoclusters. STEM was chosen to enhance the contrast between the carbon support and gold as the limited amount of material in the small nanoclusters make imaging challenging. It was difficult to find any particles on the TEM grid, but certain areas contained small individual particles. The STEM image in Figure 65A shows a number of 2-4 nm spherical particles.

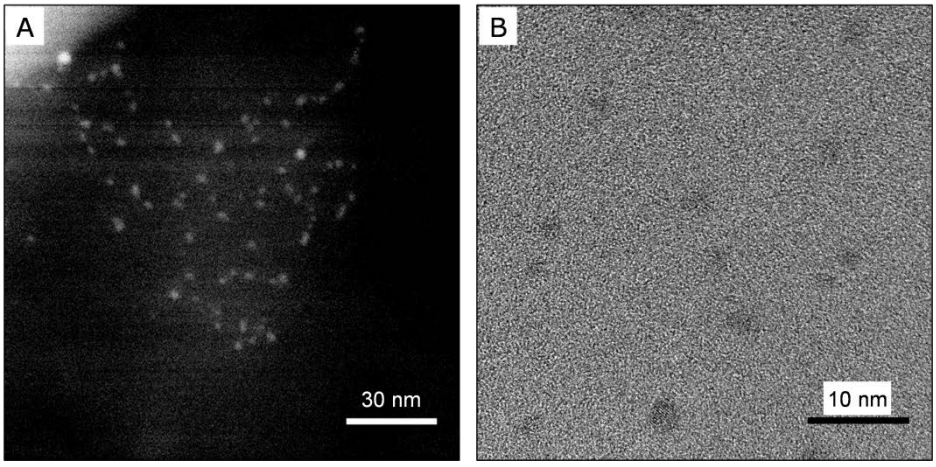

Figure 65. (A) STEM and (B) HR-TEM image of filtrate containing the UV active compound.

Unfortunately, good STEM resolution was not obtained. HR-TEM also revealed nanoparticles down to 1.5 nm, Figure 65B and App. fig. 23. It is clear, that particles of this size are on the limit of what can be detected in normal TEM mode. The smallest of the particles are barely visible on the background of the carbon film. TEM confirmed that nanoparticles were still present in the filtrate. This is not surprising with the simple separation procedure of syringe filtration. AuNPs of 2-4 nm should exhibit LSPR and are unlikely to be causing the A293 and A366. However, the particles observed with TEM could have formed by aggregation of smaller clusters during drying and/or imaging in the vacuum of the TEM. Smaller clusters could still be present in the sample but "invisible" on the thick carbon film.

2.5.5 A general phenomenon?

In unrelated experiments phenomena similar to those described in the previous sections was observed, Figure 66. During the work with photoelectrocatalysis by AuNP/TiO_2 composites (section 4.4) water-free AuNPs was prepared. The standard MOS AuNPs were forced to aggregate by dilution in ethanol to remove the aqueous phase by centrifugation. The supernatant was clearly yellow in colour but the UV-vis characterization showed no indication of remaining precursor. Instead, 3 peaks were found at 285, 340 and 440 nm, the first two of which are at similar positions as A293 and A366. Similar observations were made during the work with AuPt core-shell NPs catalyst (section 3.2.3). Amicon filtrate from purification of standard MOS AuNP solution showed a peak at 285 nm with a shoulder at 340 nm, while the filtrate from purification of AuPt core-shell catalyst sharp peaks at 285 and 347 nm.

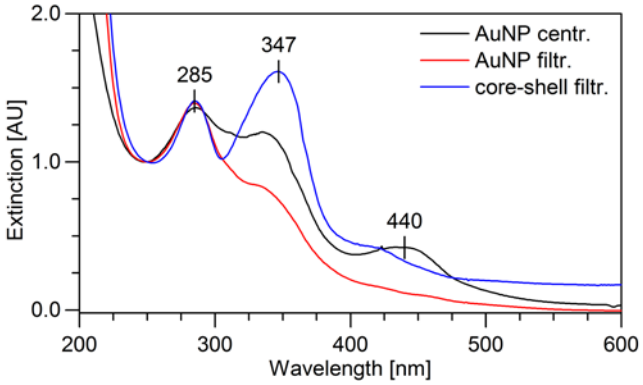

Figure 66. UV-vis spectra of three other cases of unidentified peaks appearing during NP synthesis after removal of main NP product. (A) Supernatant obtained after forced precipitation of MOS AuNPs by ethanol. (B) Amicon filtrate from MOS AuNPs using 100 kDa membrane. (C) Filtrate obtained after immobilization of core-shell NPs on G-CB. Spectra are normalized at the minimum around 250 nm.

The core-shell filtrate also exhibited fluorescence, Figure 67 and App. fig. 24. Excitation with blue laser (405 nm) resulted in emission of red-shifted light while no interaction with green (532 nm) and red (650 nm) lasers was seen.

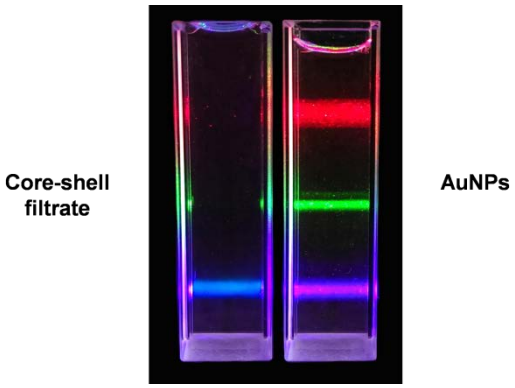

Figure 67. Photographs illustrating the fluorescence of the filtrate from the core-shell NP catalyst preparation. The core-shell filtrate (left) and a solution of large AuNPs (right) were irradiated with red (650 nm), green (532 nm) and blue (405 nm) lasers. The filtrate did not scatter any of the lasers but emission of red-shifted light was found for the blue laser. The AuNPs scattered light of all three colours with no change in colour.

In conclusion, despite the many efforts towards characterizing the origin of the A293 and A366, no conclusive evidence was found. Two competing hypotheses are currently considered; (1) an intermediate molecule and or metal complex generated as a side-product of the AuNP synthesis and (2) the formation of semi-stable metal nanoclusters (presumably < 1-2 nm). The behaviour of the unidentified peaks in terms of conversion from A293 to A366 and the flat baseline of the isolated compounds suggest a molecular origin. If indeed the peaks in Figure 66 have the same origin as A293 and A366 they must arise from MES as this is the only common compound. The reaction of $[AuCl_4]^-$ and MES discussed in section 2.1 does not provide any obvious candidates for fluorescent side-product originating from MES.

Support for the second hypothesis, a metal cluster origin, is found in TEM showing the presence of very small AuNPs and the fact that nanoclusters of Au are known to be fluorescent.[113-115] The emission/excitation depends on the cluster size[114] and adsorbate[115]. Fluorescent Au nanoclusters have even been synthesized in MES solution resembling the conditions of the OBS synthesis.[116] The reports on such clusters show no peaks in UV-vis spectra but a continuum.[113,117] If the presently observed fluorescence arises from Au nanoclusters the UV peaks must have a different origin and the clusters exist in low concentration because no continuum is visible in the UV-vis spectra. However, the reported

excitation/emission pairs of fluorescent Au nanoclusters do not correlate with those found in the present work.

Separation of the unidentified compound(s) by chromatography and additional MS are central for further work towards identification. Deeper characterization of the fluorescence observed in cases such as those in Figure 66 may also provide information that can point towards either of the two hypotheses.

Chapter 3

Better utilization of platinum in catalysis

3.1 The scarcity of platinum

Pt is a widely used metal for heterogeneous catalysis. It shows many desirable properties in terms of catalytic activity, versatility, stability etc.[105,118] However, major drawbacks limiting the feasibility of using Pt in a large scale to solve energy-related challenges are availability and cost. The concentration of Pt in the earth's crust is only 5 µg/kg.[36] Additionally, it is mined in low concentration ores (in the order of grams per ton) containing a mixture of Pt-group metals that need to be separated in complicated processes that can take many months.[119,120] The global supply and demand of Pt increased exponentially till late 1990s but have started to plateau in recent years. The demand has exceeded the supply since around 2000 enabled by an increase in reuse particularly of autocatalysts. The added demand of reusability puts further restraints on Pt usage.

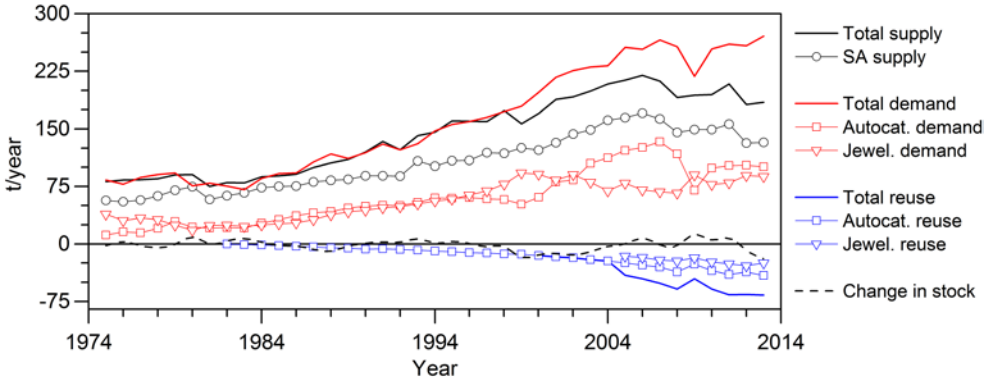

Figure 68. Supply and demand of Pt over the past 40 years. The graph shows data for supply (black), demand (red) and reuse (blue). Totals are in thick solid lines while partial contributions are marked with symbols; supply from South Africa, SA (circles), autocatalysts (squares) and jewellery (triangles). The change in stock per year is indicated with the dashed line. The data are compiled from tables from Johnson Matthey.[37]

Due to the limited supply, high demand and expensive production cost, the price of Pt is very high at around 50 $/g (average in 2013 was 48 $/g).[121] Consequently, despite the excellent performance of Pt in many energy-related technologies, Pt consumption for catalysts needs to be drastically reduced or substituted.

The initial efforts in limiting Pt consumption in catalysts focused on switching from bulk high-surface-area Pt to Pt NPs dispersed on support material. Later, the size of the NPs was reduced to increase the specific surface area. This approach has been very successful but has drawbacks. Some reactions are catalysed by facet atoms (as described in section 2.3) the concentration of which decreases with decreasing size. Activity then depends on size by two opposing effects. Smaller sizes entail less inactive bulk atoms but at the same time less active facet atoms as the relative concentration of corner and edge atoms increases. Very small NPs tend to be less stable on a support and agglomerate and sinter easily resulting in loss of activity.

Two alternative strategies are explored in this chapter; (1) Pt shells in core-shell NPs, section 3.2, and (2) Diluting Pt with alloying metals, section 3.4.

3.2 Au-Pt core-shell nanoparticles

Exchanging bulk Pt with another metal reduces the Pt consumption without affecting the Pt surface area. Here, gold was chosen as the model for the core element in the Pt shell approach. The synthesis of Au-Pt core-shell NPs following the SAMENS method was investigated and their electrochemical properties studied. Finally, the synthesis was scaled up and the NPs loaded on support for future application in catalysis.

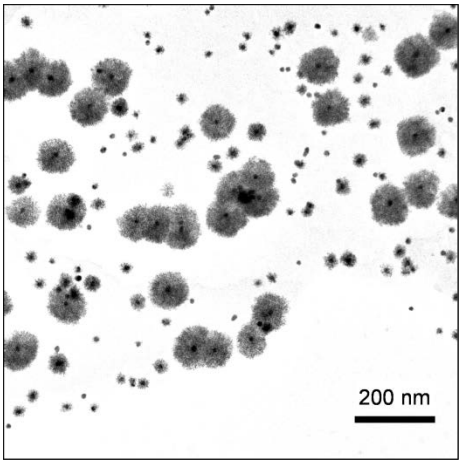

Figure 69. Representative TEM image of the previously studied AuPt NFs. **[Prior data]**

This work builds on a previously developed synthesis procedure for so-called AuPt nanoflowers (NFs). These structures consist of a single AuNP core coated by a thick network of 2-3 nm platinum nanoparticles (PtNPs), Figure 69. The NF synthesis entailed sequential reduction of Au and Pt precursors separated by a variable duration of "resting" that governed the thickness of the resulting PtNP coating.

3.2.1 Synthesis of Pt monolayer shells on AuNPs

The Pt precursor reduces very slowly at r.t. resulting in weeks-long syntheses for NFs. NF synthesis was therefore attempted at elevated temperatures to increase the rate of Pt reduction. A set of samples were prepared with a 1-day resting period. Pt precursor reduction was done at r.t. in MES buffer and PB and the samples denoted NF-RT1 and -RT2, respectively. Reduction was carried out at 90-95 °C for sample NF-HT.

Table 7. Experimental conditions for core-shell AuPt synthesis. The number in parentheses refers to pH of the buffer stock solution. The temperature[a] was 90-95 °C for all samples. Heating was maintained for 2 h during AuNP formation for NF samples, 2 h after Pt precursor addition for NF-HT and 1 h 40 min[b] for csAuPt samples. NF-RT1 and -2 were not heated during Pt reduction.

Sample ID	A	B	C	D	E
NF-RT1 [c]	$HAuCl_4$ 0.5 mM	MES (7) 2.5 mM	Starch 1.5 wt‰	Glucose 2.5 mM	H_2PtCl_6 0.2 mM
NF-RT2 [c]	$HAuCl_4$ 0.5 mM	PB (7) 2.5 mM	Starch 1.5 wt‰	Glucose 2.5 mM	H_2PtCl_6 0.2 mM
NF-HT [c]	$HAuCl_4$ 0.5 mM	MES (7) 2.5 mM	Starch 1.5 wt‰	Glucose 2.5 mM	H_2PtCl_6 0.2 mM
csAuPt-1	$HAuCl_4$ 0.5 mM	MES (7) 2.5 mM	Starch 1.5 wt‰	Glucose 2.5 mM	H_2PtCl_6 0.2 mM
csAuPt-2	$HAuCl_4$ 0.5 mM	MES (7) 2.5 mM	Starch 1.5 wt‰	Glucose 2.5 mM	H_2PtCl_6 0.5 mM
csAuPt-3	$HAuCl_4$ 0.5 mM	MES (7) 2.5 mM	Starch 1.5 wt‰	Glucose 2.5 mM	H_2PtCl_6 1.0 mM

[a] The sample was heated in a water bath on a hotplate with feedback via a thermometer. [b] MES, starch and glucose were pre-heated for 5 min before Au precursor addition. After another 30 min, the mixture was diluted 4 times with ultrapure water and heated for 5 min. Then, Pt precursor was added and heating maintained for 1 h. [c] The AuNP solution "rested" (no heating, no stirring) for 22 h before 4-fold dilution and Pt precursor addition.

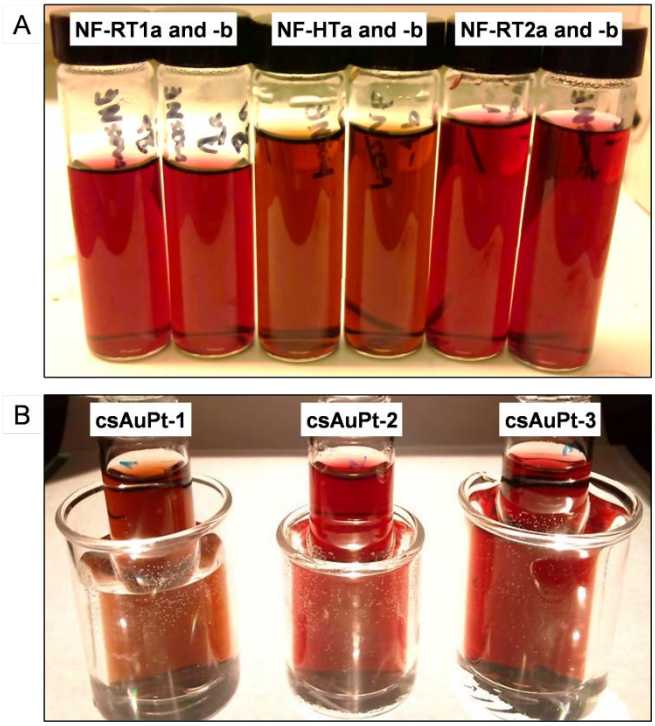

Figure 70. Photograph of (A) NF and (B) csAuPt samples immediately after synthesis. The samples containing core-shell NPs were clearly identifiable.

These conditions did not provide NFs but an interesting colour change was observed for NF-HT, Figure 70. It was hypothesized that Pt had formed a shell in close contact with the AuNP core affecting the LSPR rather than the expected PtNP coating.

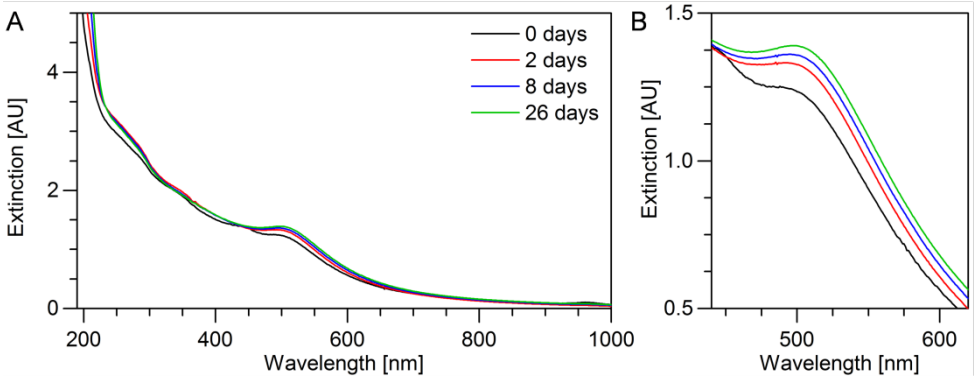

Figure 71. UV-vis spectra of NF-HT at different times showing a slow change around the LSPR (dil: 2).

UV-vis characterization of NF-HT revealed that the LSPR had almost disappeared. The peak maximum was below 500 nm which is unusual for Au and the peak got slightly narrower and better defined after several weeks.

EDX showed that Pt was present in all areas of the sample. Distinctly different NP populations were not observed. The Au and Pt distribution was uniform on the TEM sample and their ratio 3.2 ± 0.2 (12 EDX measurements). Either, NPs of similar shape/size of pure Au and pure Pt had formed or both elements were present in the same NPs. The AuNP core NPs and the NF-HT NPs were studied with TEM to look for evidence of a Pt shell, Figure 72 and App. fig. 25. No signs of core-shell structures were found with imaging. There was also no discernible difference in size of the core AuNPs and NF-HT NPs, both of which were 8 ± 2 nm in diameter, App. fig. 26. If a Pt shell had grown on the NPs, the resulting change in size must be significantly smaller than the inherent variation of size within the NP distributions. The core AuNPs considered above had not been subjected to the dilution and reheating that the NF-HT NPs had. The effects of this treatment on size were studied with a reference AuNP sample.

TEM samples were prepared immediately after synthesis and after the procedure of 1-day resting, 4-fold dilution and heating for 2 h. The size of the freshly formed AuNPs was again 8 ± 2 nm and the AuNPs that have been exposed to the conditions of NF synthesis were 7 ± 2 nm, App. fig. 27. This difference was not significant and sizing did not provide evidence of a Pt shell.

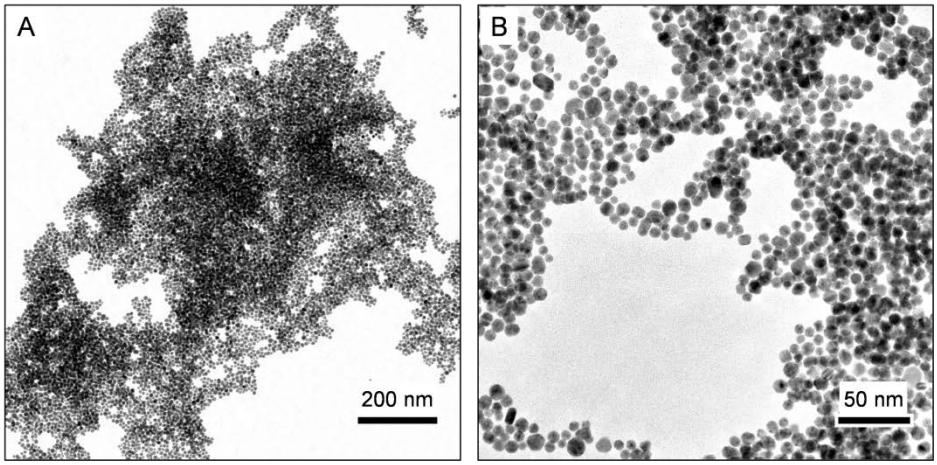

Figure 72. TEM images of NF-HT where Pt was reduced at 90-95 °C. The uniform NPs did not suggest the presence of two different types of NPs but rather a single structure containing both Au and Pt.

Knowing the outer diameter of the presumed core-shell NPs along with the relative molar concentrations of Au and Pt, it is possible to estimate the shell thickness assuming a perfect

spherical core and shell. Converting mol% of Au to vol% and multiplying with the total volume of a sphere (Ø = 8 nm) gives the volume of the core. The core diameter and shell thickness can then be estimated. The relative molar volumes are calculated from the unit cell volumes of Au and Pt with lattice parameters of 408 [122] and 392 pm[123], respectively. This estimation provides a core diameter of 7.4 nm and a shell thickness of 3.1 Å. This is in the order of a single Pt atom (2.77 Å) which correlates well with the difficulty in finding evidence for a shell with TEM imaging and sizing.

The intriguing core-shell NP synthesis was studied further. The resting period was eliminated and the Pt precursor added immediately after AuNP formation, Scheme 6. Three different molar ratios of Au-to-Pt were tested, namely 2.5, 1 and 0.5.

Scheme 6. Synthesis of Au-core Pt-shell NPs.

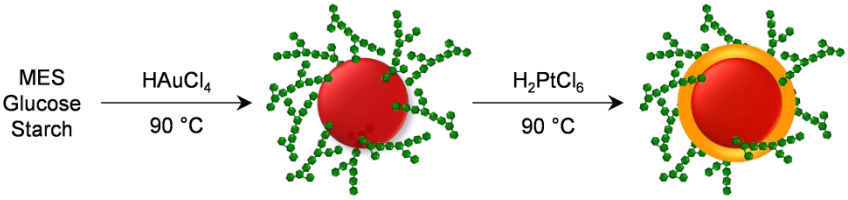

The colour of the csAuPt-1 solution changed to orange/brown about 30 min after Pt precursor addition. In contrast, csAuPt-2 and -3 did not change visibly from the characteristic red colour of the AuNPs, Figure 70. Such a drastic colour change as observed for csAuPt-1 indicates that the surfaces of the AuNPs have been disrupted. The extinction again showed almost complete quenching of the LSPR leaving only a shoulder around 495 nm (solid black, Figure 73). On the other hand, the spectra of csAuPt-2 and -3 displayed the expected LSPR of the AuNPs at 527 nm. Strong absorbance from the Pt precursor was still present in those two samples. The intensities of the precursor peaks relative to the precursor concentrations suggested that insignificant amounts of Pt precursor had been reduced.

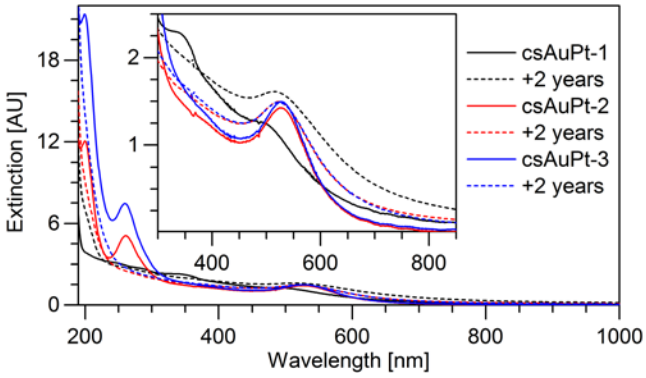

Figure 73. UV-vis spectra of csAuPt-1 (black), -2 (red) and -3 (blue) shortly after preparation (solid) and after storage at r.t. for 2 years (dashed) (dil: 10).

It seems counterintuitive that less Pt had been reduced in the samples with higher concentration. Spectra were recorded again after 2 years at which point all Pt had been reduced in all samples. The shoulder observed for csAuPt-1 had red-shifted to 513 nm and grown in intensity similar to the observations for NF-HT. The LSPR of csAuPt-2 and -3 had not changed notably despite the complete reduction of Pt but a 4 nm blue-shift had occurred.

It is worth noting, that all csAuPt samples exhibited very high stability. No agglomeration or precipitation appeared even after 2 years and with no post synthesis treatment and no special storage conditions.

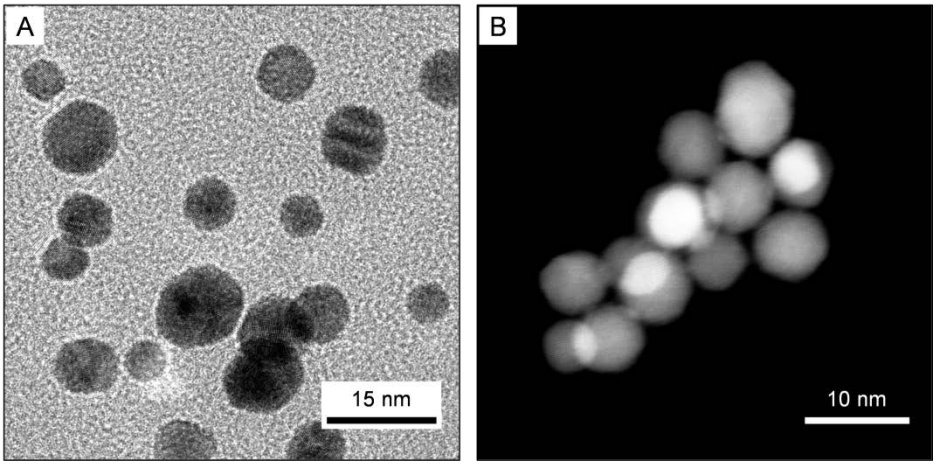

Figure 74. TEM studies using the ATEM facilities at DTU CEN. (A) HR-TEM image of AuPt core-shell NPs prepared by Nedjelko Šešelj following the procedure of csAuPt-1. (B) STEM image of Amicon filtered (see section 3.2.2) csAuPt-1.

HR-TEM, Figure 74A and App. fig. 28, and STEM, Figure 74B, did not provide any further insight into the composite structure but confirmed the presence of both single-crystals and polycrystalline NPs agreeing with the conclusions from the size-control studies regarding the nature of the AuNPs. EDX measurements on 16 individual NPs were carried out and the shell thickness calculated for each following the same procedure as described above. It was found that the smaller the NP the larger the relative Pt content, Figure 75A. There was no correlation between size and shell thickness which was 2.9 ± 0.7 Å, Figure 75B. It should be noted that the assumptions made for the estimation of the shell thickness are crude when applied to individual particles as their shapes often deviate from spherical.

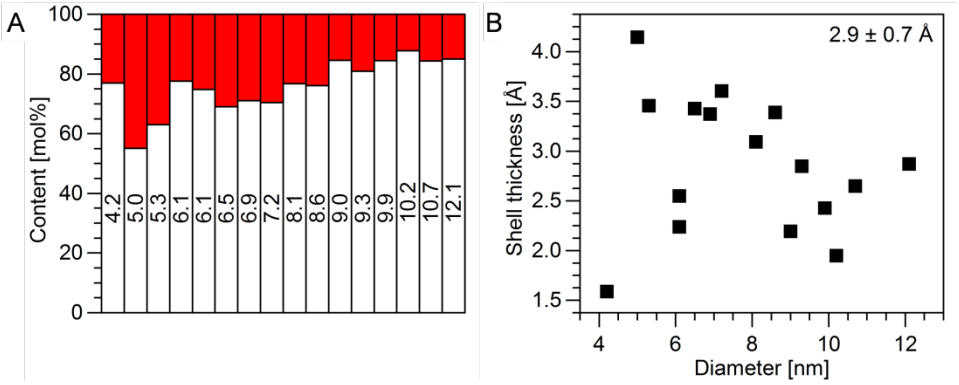

Figure 75. (A) Au (white) and Pt (red) mol-based content of individual NPs arranged by size. The diameters in nm are indicated on the columns. (B) Calculated shell thickness versus diameter based on the metal contents in (A) and their size assuming perfect spherical core-shell geometry. The average shell thickness is given in the plot.

No measurement directly showed a Pt shell. In fact, the reduction of Pt in NF-HT and csAuPt-1 did not entail any changes to the particles that were detectable with TEM. Yet, the optical properties changed dramatically. The LSPR of the AuNPs was quenched almost completely. This must arise from a pronounced and intimate structural change on the surface of the AuNPs. Similar behaviour has been reported for AuPt core-shell NP systems.[124,125] Alternatively, the reduced Pt could have dissolved in the Au lattice creating an alloy which might impose similar disruption of the electronic structure of the AuNPs. However, Au and Pt are not miscible and the heat of formation of an alloy is positive relative to their pure bulk state. This is not absolutely true for nanoscale systems. Theoretical evaluation of NP alloys of Au and Pt has demonstrated that reducing the size of the NPs led to a decrease in the heat of formation which ultimately turned negative.[126] However, experimental studies of AuPt alloys showed that the two elements phase segregated upon heating.[127] Au-Pt core-shell NPs even mixed initially before segregating into two joined phases of Au and Pt.[128] That being said, many studies report stable core-shell structures.[124,125,129,130] Alloying at r.t. of our structures seems unlikely but the separation of an Au and Pt phase might not be absolute.

3.2.2 Electrochemical characterization

The AuPt NPs were studied by CV to characterize the chemical nature of the NP surface. EC measurements are very sensitive to the presence of contaminants so it is important to have a purified system. The csAuPt-1 sample was purified by Amicon filtration to remove excess reactants and synthesis by-products, i.e. Cl^-, glucose/gluconic acid and MES_{ox}. The Amicon filtration system uses a backpressure of gas (Ar) on top of the solution which is forced through a membrane with nanoscale pores under mechanical stirring. These

membranes are conventionally used for protein purification and the pore classification is based on molecular mass of the proteins they retain. It is therefore not straight-forward to evaluate whether or not a given much heavier NP will be retained.

It was important that the core-shell NPs (≈ 8 nm) would be retained. However, it was equally important that "free" Pt in the form of PtNPs would pass through in order not to interfere with the EC signal of Pt from the core-shell NPs. A 100 kDa membrane from Millipore was tested[viii] to see if standard MOS AuNPs (8 nm) and MOS PtNPs (2 nm) would be retained or pass through. This process was following by UV-vis spectroscopy of the retentates and filtrates, Figure 76.

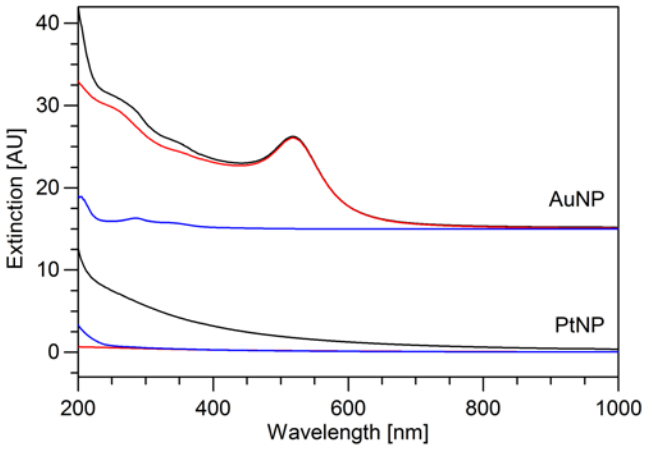

Figure 76. UV-vis spectra of unfiltered NP solution (black) with retentate (red) and filtrate (blue) from Amicon filtration of AuNP (dil: 10 for black and red and 1 for blue) and PtNP (dil: 5 for black and 1 for red and blue) solutions using a 100 kDa membrane.

The AuNPs were efficiently retained by the membrane resulting in close to identical spectra of unfiltered and retentate solutions. Interestingly, a peak at 285 nm and a shoulder at 340 nm were found in the spectrum of the filtrate. This relates to the unidentified peaks described previously and is discussed in section 2.5.5. The spectra of the filtrate and retentate of the PtNP solution provided no evidence of PtNPs. It is believed that the particles were stuck in the membrane, possible due to agglomeration triggered by the filtration process. Most importantly, the PtNPs could not be recovered in the filtrate.

[viii] The membranes are cleaned before use to remove excess chemicals from their manufacture. This is done by soaking in ultrapure water for at least 1 h, exchanging the water every 15 min.

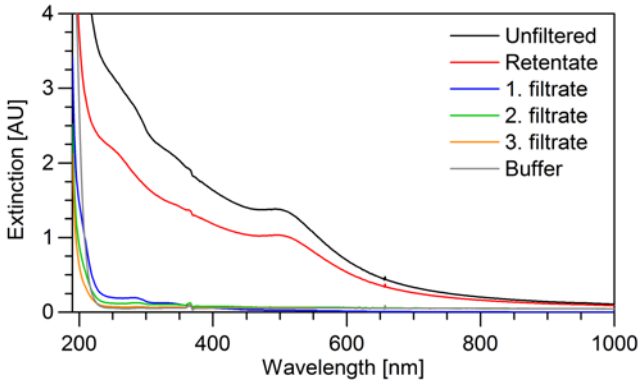

Figure 77. UV-vis spectra of unfiltered sample (black), retentate (red), filtrates (blue, green, orange) and cleaning buffer (grey) from Amicon filtration of csAuPt-1 (dil: 2).

A fresh 100 kDa membrane was cleaned and used for purification of csAuPt-1. The NPs were cleaned using a MES buffered starch solution with identical concentrations as for csAuPt-1 sample to avoid agglomeration resulting from pH change and loss of capping agent. 5 mL sample was diluted with buffer to 10 mL and filtered to about 2 mL removing 80 % of the unwanted components. This was repeated twice to obtain a > 99 % pure sample. The NPs were redispersed in 5 mL buffer ready for EC characterization. UV-vis spectroscopy confirmed that the core-shell NPs were completely retained, Figure 77. The concentration was a bit lower in the retentate. The final redispersion of NPs following Amicon filtration was done by eye so the final volume was not precise which may have led to slight dilution. It is also possible that some particles were deposited in the filter.

A BPG electrode (Ø = 0.5 cm) was polished by increasingly fine-grained silicon carbide papers (1200, 2400 and 4000 grit) and alumina slurries (1, 0.3 and 0.05 µm) before ultrasonication in ultrapure water. 10 µL of the purified core-shell NP solution was drop-cast on the cleaned BPG surface and the electrode dried at 60 °C for 2.5 h. Meanwhile, an electrochemical cell had been boiled in 15 vol% HNO_3, rinsed and ultrasonicated twice in ultrapure water. A supporting electrolyte solution of 0.1 M H_2SO_4 was prepared from > 95 % H_2SO_4 stock solution by weight-based dilution. The cell was filled with the supporting electrolyte solution and degassed with Ar for > 30 min.

The lower vertex potential was fixed at -0.25 V vs. SCE to include the region of hydrogen adsorption and desorption on Pt. The upper vertex potential was increased from 0.4 to 1.4 V vs. SCE revealing the potentials at which oxidation of the metals occur. At small potential ranges, no significant oxidation of Pt and Au was observed, Figure 78A. Pt started to oxidize above 0.7 V resulting in the appearance of a cathodic peak around 0.4 V, characteristic of reduction of oxidized Pt, Figure 78B.

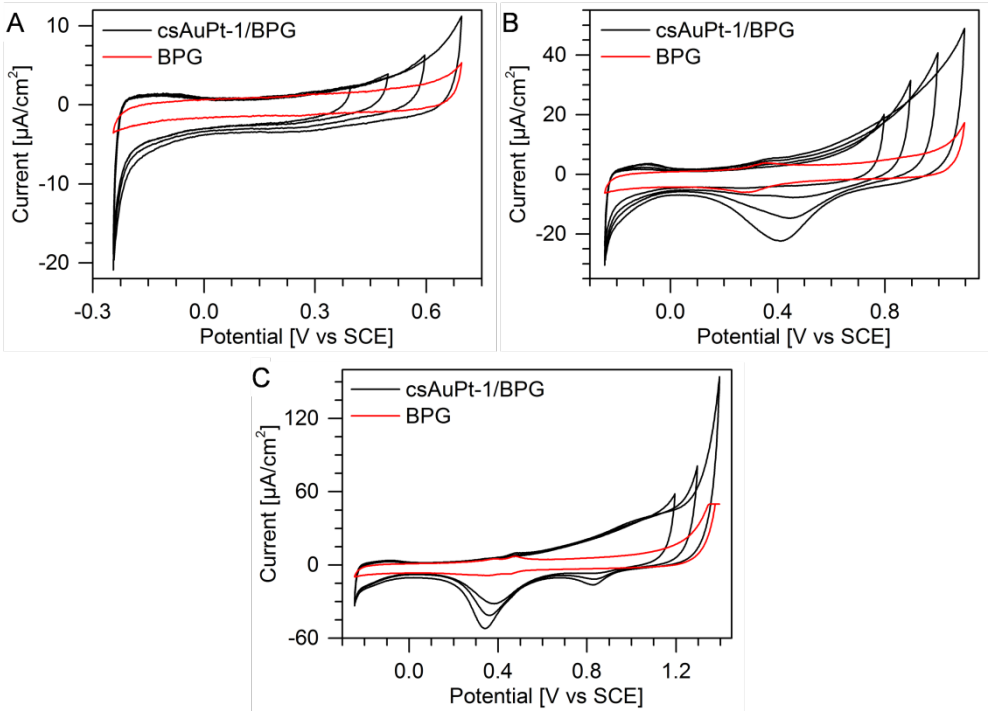

Figure 78. CVs of csAuPt-1 at increasing potential ranges divided in three sections; (A) No oxidation from metals, (B) Pt oxidation and (C) Pt and Au oxidation. The lower vertex point was fixed at -0.25 V and the higher vertex point increased from 0.4 V to 1.4 V in 0.1 V increments. Conditions: 0.1 M H_2SO_4, oxygen-free, 50 mV/s, RE = RHE, CE = Bright Pt wire.

Above 1.1 V, Au was oxidized and a cathodic peak at 0.83 V emerged, Figure 78C. CVs of bare BPG in the same potential ranges are included in each panel of Figure 78. Almost no EC activity was found for BPG under these conditions. A pair of weak peaks developed at the widest potential ranges. They are also present in the CVs of the core-shell NPs and relate to functional groups on the graphite surface generated after oxidation above ca. 1.3 V vs. SCE.

CVs of flame annealed single-crystal electrodes of Pt(111) and Au(111) were recorded for reference in addition to freshly cleaned BPG. The EC response of the pure metals correlated well with the composite CVs of the core-shell NPs. The cathodic peaks at 0.4 and 0.83 V vs. SCE were identified as reduction of Pt and Au oxide monolayers, respectively.

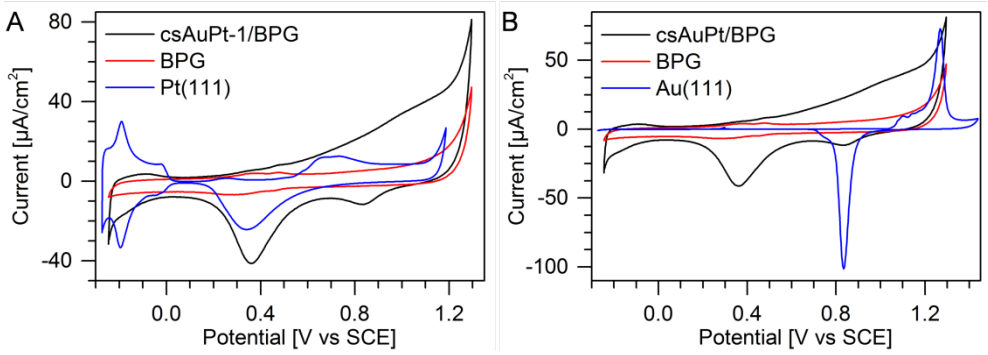

Figure 79. CVs of purified csAuPt-1 on BPG (black) and reference systems in 0.1 M H_2SO_4 and oxygen free condition. Core-shell NPs were compared to bare BPG (red) and single-crystal electrodes (blue) of (A) Pt(111) and (B) Au(111). All CVs were recorded at 50 mV/s. RE = RHE, CE = Bright Pt wire.

The presence of an EC signal from Au is small but visible. This suggests that Au surface was exposed to the electrolyte and the Pt shell did not cover the AuNP cores entirely. The far majority of the total NP surface was Pt according to the relative areas under the peaks of Pt and Au.

The EC study of the core-shell NPs confirmed that their surface was rich in Pt and that parts of the AuNP core was exposed. The core-shell structure with a very thin Pt layer entails that the bulk Pt atoms are practically non-existent leading to a potentially very high specific activity of Pt. Application in heterogeneous catalysis is therefore obvious.

3.2.3 Towards catalytic application of AuPt core-shell NPs

Work towards applying the core-shell NPs as catalysts in fuel cell systems and catalysts for chemical syntheses were initiated towards the end of the PhD project. The first steps when going from dedicated synthetic work and structure characterization toward application of NPs is to scale up the production, purify the system and find a way to easily handle the NPs in a test setup. The last two points are often achieved by immobilizing the active nanomaterials on a micro- or macroscale support material which allows for easy washing by filtration and handling of the dried catalyst powder.

A low Pt loading procedure was setup to fit a specific test system at CSC at DTU Chemistry and to conserve Pt consumption for the initial tests. A carbonaceous support supplied by associate professor Li Qingfeng from DTU Energy Conversion was chosen. Commercial carbon black (CB), Vulcan XC-72R, had been treated (“graphitized”) in inert atmosphere at 2800 °C (denoted G-CB).[131] The treatment made the amorphous CB collapse creating a crystalline ribbon structure similar to glassy carbon. The surface area was

reduced by almost 70 % but the resulting material was very stable and more robust towards corrosion than untreated CB.

Table 8. Experimental conditions for 120 mL core-shell AuPt catalyst synthesis. The number in parentheses refers to pH of the buffer stock solution. The temperature[a] was kept at 90-95 °C for the whole procedure. Heating was maintained for 2h 10 min including 10 min pre-heating before addition of Au precursor, 30 min during AuNP formation, 1 h after dilution and Pt precursor addition and 30 min after adding G-CB.

Sample ID	A	B	C	D	E	F
csAuPt-cat	$HAuCl_4$ 0.5 mM (11.8 mg)	MES (7) 2.5 mM	Starch 1.5 wt‰	Glucose 2.5 mM	H_2PtCl_6 0.2 mM (4.68 mg)	G-CB powder (967 mg)

[a] The synthesis was carried out with stirring in a round-bottomed flask fitted with a condenser and heated in an oil bath with temperature feedback to the hotplate.

A total of ≈ 1 g of core-shell catalyst was prepared containing roughly 5 mg Pt (0.5 wt%), 12 mg Au (1.2 wt%) and 965 mg G-CB, Table 8. 30 mL of standard MOS AuNP solution was first prepared followed by 4 times dilution and Pt precursor addition. After Pt reduction a core-shell NP formation, G-CB was added to the 120 mL mixture and adsorption of NPs on the G-CB surface was allowed for 30 min at maintained heating.

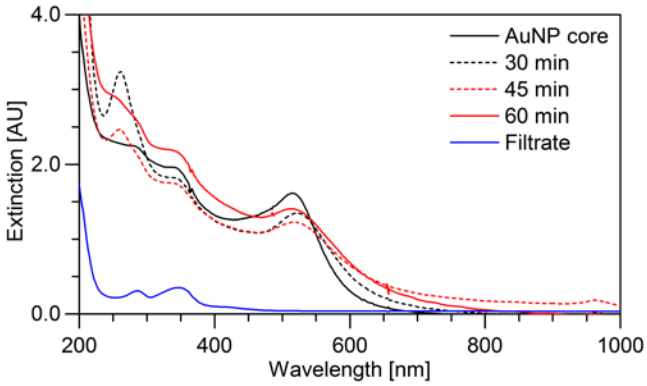

Figure 80. UV-vis characterization of the synthesis of csAuPt-cat. Spectra were recorded just before Pt precursor addition (black), after 30, 45 (dashed) and 60 min (red) of Pt reduction and of the filtrate obtained during isolation of the catalyst powder (blue) (dil: 10).

A UV-vis spectrum was recorded just before addition of Pt precursor showing the spectrum of freshly formed AuNPs and a LSPR max at 516 nm, Figure 80 (solid black). Characteristic peaks from the Pt precursor were found at 200 and 260 nm after 30 and 45 min of Pt precursor reduction, (dashed). The LSPR of the AuNPs decreased in intensity,

broadened and blue-shifted with time and after 60 min complete reduction was obtained (solid red). The support was added and the core-shell NPs adsorbed before recovering the catalyst powder by vacuum filtration. No indication of core-shell NPs were found in the filtrate spectrum indicating a practically quantitative immobilization process.[ix] Again, peaks relating to the unidentified peaks of section 2.5 were present (see section 2.5.5 for discussion hereof).

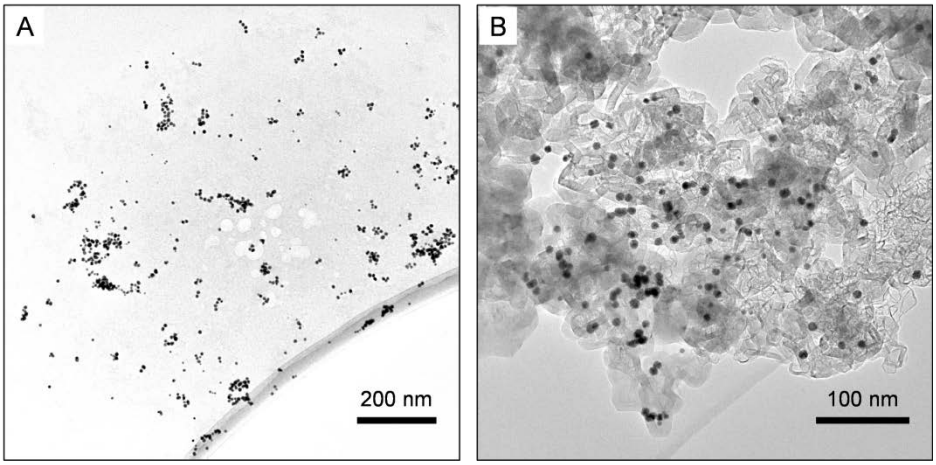

Figure 81. TEM images of the core-shell NPs prepared for catalysis (A) before and (B) after loading on G-CB.

The slightly increased synthesis volume did not change the size and shape of the resulting NPs. TEM showed monodisperse NPs around 8 nm both in the synthesis solution before immobilization on the support and on the G-CB after washing and drying of the catalyst powder Figure 81. EDX suggested that some Pt was washed away during filtration and not associated with the NPs with Au-Pt ratios of 2.2 ± 0.3 (4 measurements) before immobilization and 3.1 ± 0.3 (3 measurements) for the purified catalyst powder. However, the statistical basis is not sufficient and the results from the catalyst powder EDX are not very precise due to the low metal concentration relative to the support. The NPs were poorly dispersed on the G-CB support with some areas having no NPs and others having a high density of NPs, App. fig. 30.

Due to time limitations, work on using the core-shell NPs in catalytic systems will be undertaken after the completion of the PhD. This area is promising but improvements are needed to exploit the full potential of this material. These mainly relate to the

[ix] During related work on immobilization of the same core-shell NPs on a porous carbon structure specially made by a collaborator (not included here) partial adsorption of NPs on the support was obtained and the filtrate UV-vis spectrum showed a high concentration of NPs.

immobilization procedure (i.e. particle dispersion on support and metal loading) and removal of the starch capping to expose and utilize efficiently the NP surface. Focus will be directed to these topics in future work.

3.3 Using palladium with platinum

Palladium (Pd) is a noble, platinum-group metal and neighbour to ruthenium and silver. It has about half the atomic mass of Pt (106.42 vs. 195.08 g/mol)[132] but almost identical crystal structure with lattice parameters of 389.07 and 392.42 pm for Pd and Pt, respectively.[133] The similar crystal packing makes the elements miscible and the growth of alloy crystal possible. Thus, Pd is a good candidate for an element with which to dilute Pt and form stable nanostructures. Pd is three times as abundant in the earth's crust[36] as Pt and is sold at almost half the price, Figure 82. It is also important to note the large fluctuations in Pt price which is very sensitive to the financial situation. As an example, the Pt price dropped 60 % within a few months at the start of the financial crisis in 2008.

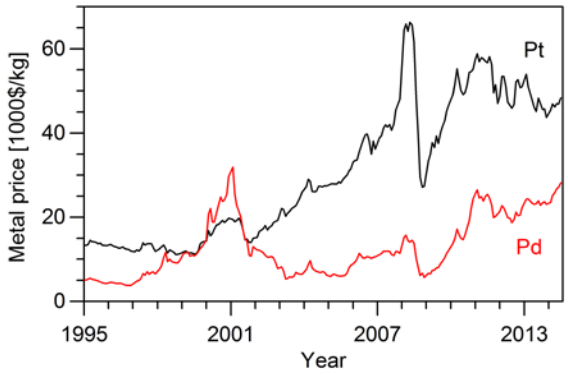

Figure 82. Price development for platinum (black) and palladium (red) over the last 20 years. Prices are reported by Johnson Matthey.[121] The large drop (60 %) in platinum price in 2008 was a result of the financial crisis starting around the crash of the Lehman Brothers (American bank) in late 2008.

Pd has been widely used as a homogenous catalyst in organic synthesis, e.g. in C-C bond formation.[134,135] Since the 1950s, Pd catalysis has grown immensely and in 2010 the Nobel Prize was awarded to Heck, Negishi and Suzuki acknowledging their contributions to this field.[136] More recently, Pd NPs were also employed for the catalysis of organic synthesis and other heterogeneous catalytic systems.[137] A well-known example is PdPt catalytic converters for CO oxidation in cars.

However, for the present project it is the application in energy technology that is of interest. Nørskov et al. used density functional theory (DFT) to evaluate reaction intermediates of the oxygen reduction reaction (ORR) to explain the overpotential of oxygen reduction on

Pt.[138] They also provided the famous volcano plot of ORR activity vs. oxygen binding energy. Pt is on the top of the volcano and very close to optimal activity. Just beneath Pt, Pd can be found. Pd has been used for fuel cell applications as a single metal catalyst and as alloys or core-shell NPs with other metals, especially Pt.[139,140] Pd has shown superior activity for certain fuel cell reactions but the real potential lies in bimetallic NPs. Recent examples of interesting structures include Pd-Pt core-shell nanowires[141] and hollow PdPt nanospheres on graphene[142]. In the present work, extension of the SAMENS method to produce bimetallic nanostructures of Pd and Pt in a facile and simple way for fuel cell application was explored.

3.4 Palladium-platinum nanostructures

The behaviour of Pd and $PdCl_2$ in relation to the SAMENS synthesis was studied first to evaluate the reducibility by glucose or MES, the timing of this process and the stability of the possible NP product. A bimetallic NP synthesis was developed and the resulting material applied in fuel cell technology.

3.4.1 Palladium nanoparticles

The first step towards utilization of Pd was to study how this metal behaved in the SAMENS synthesis setup. $PdCl_2$ was used as precursor but has poor solubility in ultrapure water. Hydrochloric acid was added in excess to facilitate formation of $PdCl_4^{2-}$ and complete dissolution of the precursor. Palladium nanoparticles (PdNPs) were synthesized following the MOS and OBS procedures.

Table 9. Experimental conditions for PdNP synthesis. The number in parentheses refers to pH of the buffer stock solution.

Sample ID	A	B	C	D	Temp.	Time	Stir.
Pd-MOS	$PdCl_2$ 2 mM	MES (7) 10 mM	Starch 0.6 wt%	Glucose 10 mM	90-95 °C [a]	1 h	Yes
Pd-OBS	$PdCl_2$ 2 mM	MES (7) 10 mM			85-90 °C [b]	6.5 h	Yes

[a] The sample was heated in a water bath on a hotplate with feedback via a thermometer. [b] The sample was heated directly on the hotplate with feedback through a thermometer placed in an adjacent vial with water.

The colour changed from light yellow to brown 30 min after precursor addition indicating formation of NPs, although, after 1 h of heating the Pd precursor was still only partially reduced. The two characteristic peaks of the precursor at 207 and 236 nm were still clearly

observed but a steady decay from 200 to 600 nm indicated formation of nanoparticles, Figure 83. Even after 1 month at r.t. no significant further reduction was observed suggesting that heating is required for the reaction. The NPs aggregated and precipitated with time.

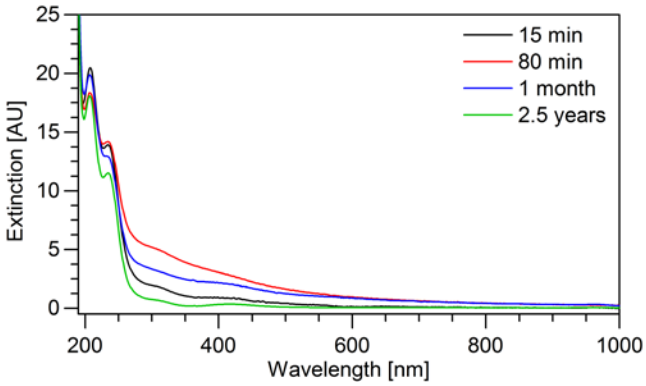

Figure 83. UV-vis spectra of Pd-MOS at different times (dil: 10).

TEM showed a mixture of 20-40 nm NPs and large spherical structures both containing Pd (from EDX), Figure 84 and App. fig. 32.

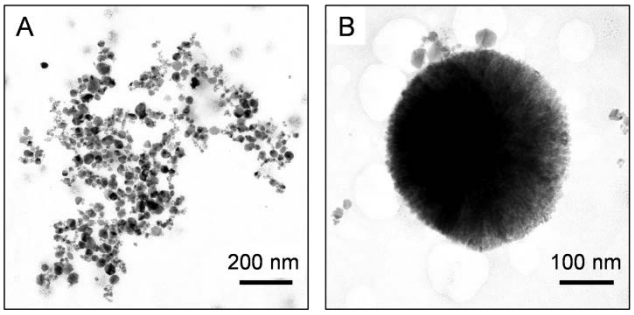

Figure 84. TEM images of Pd-MOS showing (A) aggregates of small individual NPs and (B) large spherical structures.

The remaining precursor could have reacted with the copper grid making it difficult to evaluate which of the nanostructures were present in solution. A new TEM sample was prepared and measured after 1 year providing the same results. Some of the large aggregates then showed signs of dendritic growth indicating growth on the TEM substrate rather than in solution, App. fig. 33. Such dendritic metal nanostructures often form when the growth is surface confined. It is likely that the large spherical aggregates formed by remaining precursor reacting with the copper grid and the individual PdNPs formed in solution. This is supported by NTA results where the main population of particles were just under 40 nm in diameter, Figure 85.

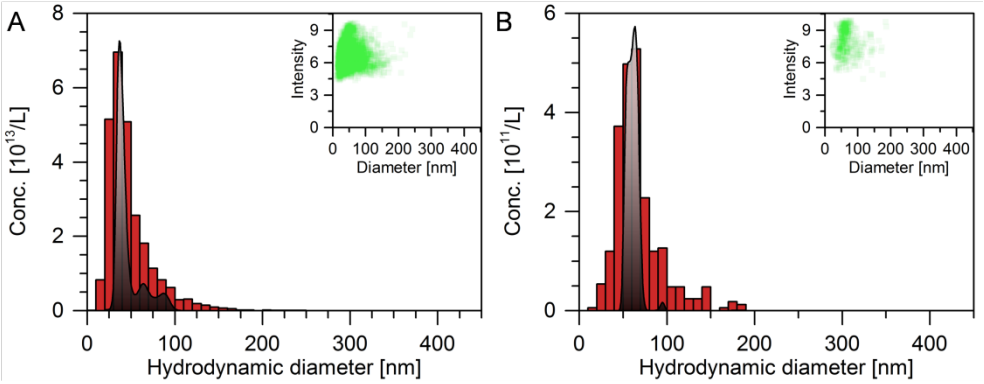

Figure 85. NTA measurements of (A) Pd-MOS after termination of heating and (B) Pd-OBS the day after initiating the synthesis by precursor addition. Size and concentration was (A) 50 ± 20 nm and $1.0 \cdot 10^{15}$/L and (B) 60 ± 8 nm and $9.7 \cdot 10^{12}$/L.

Reduction of the precursor was not detected in the synthesis following the OBS procedure, Pd-OBS, even with the extended heating of the sample, Figure 86. It is clear that MES cannot reduce Pd and glucose was responsible for the reduction in Pd-MOS. TEM images of Pd-OBS showed the same result as for Pd-MOS, App. fig. 34. NTA underlined the unsuccessful reduction in Pd-OBS with a particle concentration from NTA 2 orders of magnitude below Pd-MOS. Assuming spherical particles, size and concentration as measured by NTA results in a total measured particle volume ratio between Pd-OBS and Pd-MOS of 1:50.

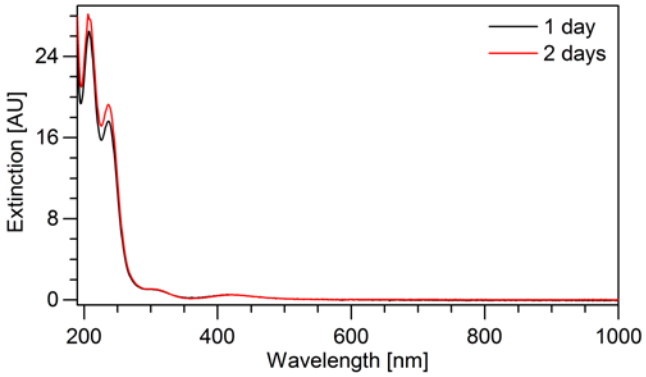

Figure 86. UV-vis spectra of Pd-OBS 1 and 2 days after precursor addition (dil: 10).

The slow reduction by glucose and the optical behaviour of the formed NPs are very similar to the behaviour of H_2PtCl_6 in the MOS procedure. These observations suggest that preparation of bimetallic nanostructures of Pd and Pt should be possible with the MOS procedure.

3.4.2 Synthesis of Pd/Pt nanostructures

The rate of reduction of Pd and Pt precursors with glucose is comparable. The synthesis of bimetallic nanostructures was therefore attempted by a co-reduction approach where both precursors were added simultaneously each at 1 mM final concentration.

Table 10. Experimental conditions for PdPt nanostructure synthesis. The number in parentheses refers to pH of the buffer stock solution.

Sample ID	A	B	C	D	E	Temp.	Time	Stir.
PdPt-1	H_2PtCl_6 1 mM	$PdCl_2$ 1 mM	MES (7) 10 mM	Starch 0.6 wt%	Glucose 10 mM	60-70 °C [a]	2 h	Yes

[a] The sample was heated in a water bath on a hotplate with feedback via a thermometer. The measured temperature was 60-70 °C.

The thermostat on the hotplate or the feedback through the connected thermometer had problems during synthesis of the PdPt nanostructures resulting in the temperature only reaching 60-70 °C. Despite problems with heating, no indication of remaining precursor was found in the UV-vis spectrum, Figure 87. The extended heating, 2 h, improved reduction of the Pd precursor. It was also noted that the stability of the colloid was greatly increased for the bimetallic NPs compared with the PdNPs. No significant changes to the extinction occurred.

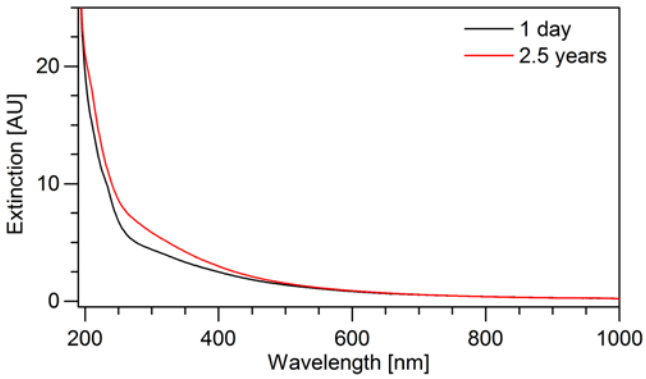

Figure 87. UV-vis spectra of PdPt NPs prepared by co-reduction. The colloid is stable even after 2.5 years (dil: 10).

A very low NP concentration was detected with NTA and the particles were large, 120 ± 60 nm, and poorly defined, App. fig. 35. TEM confirmed that the sample contained mainly spherical agglomerates of small NPs around 2-4 nm, Figure 88 and App. fig. 36. 56 ± 3 mol% of the total Pd-Pt content was Pd based on three EDX measurements on individual

agglomerates indicating that the structures contain approximately equal amounts of Pd and Pt and the two metals do not separate during synthesis.

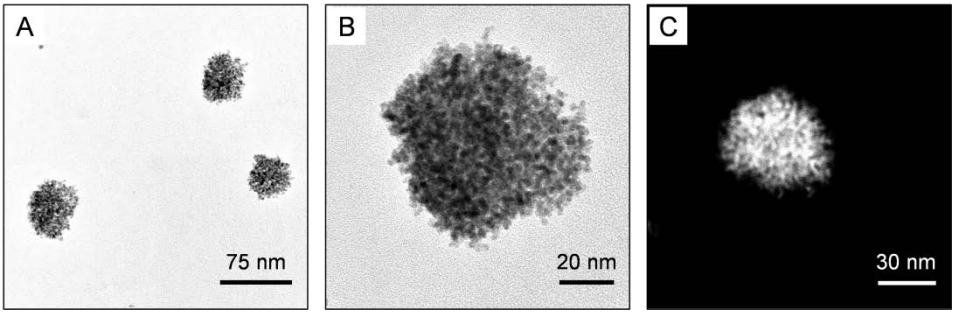

Figure 88. TEM images of PdPt nanostructures synthesized by co-reduction. Most particles were arranged in spherical aggregates of NPs.

This dense structure is not appropriate for use in catalysis as the specific surface area is relatively small. Avoiding agglomeration and obtaining stable well-dispersed NPs are crucial for application in catalysis. Improving the heating to reduce the metals faster will facilitate the formation of smaller NPs and subsequent loading of the NPs on a support material will stabilize them to prevent agglomeration. A synthesis with these modifications was carried out with associate professor Pengchao Si (Shandong University) at DTU. Synthesis of 500 mg catalyst with 30 wt% metal loading was planned corresponding to 150 mg metal and 350 mg support. A 600 mL batch of PdPt NPs was prepared following the same procedure as the previous sample. G-CB was again chosen as support material.

MES, starch and glucose was heated to > 90 °C before addition of the Pd and Pt precursors to ensure fast reduction. After 30 min of reaction, 350 mg of G-CB was added to the mixture. Heating was terminated after another hour and adsorption of PdPt NPs on the support overnight with stirring allowed. The following day, the catalyst was filtered out and washed with water and ethanol and dried at 100 °C in the oven for a few hours. Both catalyst and filtrate was studied with TEM. A small amount of the dried flaky powder was transferred to ethanol for redispersion leading to an interesting observation. A drop of ethanol at the tip of a disposable pipette was used to “pick up” a fragment of the catalyst. When the ethanol soaked a small area of the still hot powder an exothermic reaction proceeded and the carbon support started to ember. This hinted towards good catalytic activity for ethanol oxidation. The catalyst had a high loading of NPs that were evenly dispersed on the support as seen in Figure 89 and App. fig. 37.

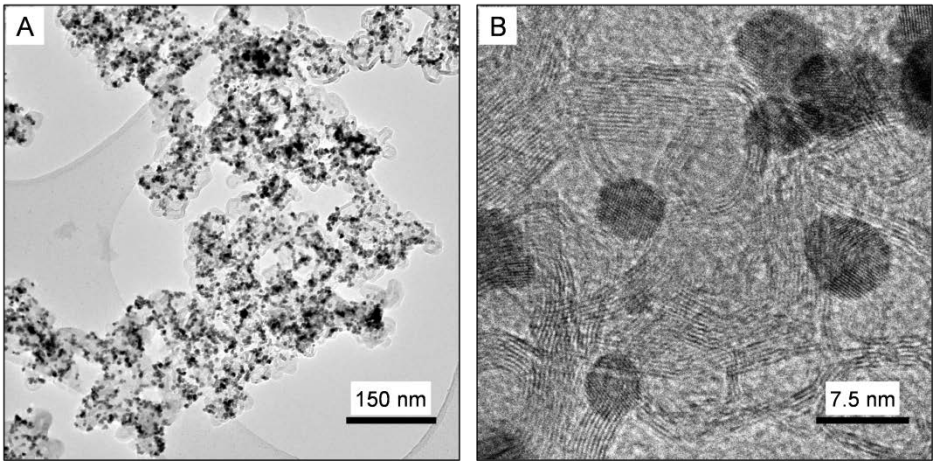

Figure 89. TEM images of PdPt NPs loaded on G-CB. (A) Overall catalyst structure. (B) High resolution image of PdPt NPs and G-CB.

Good interaction between NPs and support was obtained leading to high loading and dispersed individual NPs without agglomeration. The PdPt NPs were 6 ± 1 nm in size and the Pd-to-Pt mol-ratio 3 based on 17 different EDX measurements, App. fig. 38. This is drastically different from the expected 1:1 ratio. PdPt NPs were also found in the filtrate, App. fig. 39, with a similar molar ratio, App. fig. 38B. The unexpected metal ratio may relate to issues with the precursor stock solution. The very hygroscopic powder from which the stock solution was prepared might have been exposed to moisture resulting in overestimation of the concentration. It is also possible that unreduced Pt was lost in the filtrate even though no indication of precursor was found in the UV-vis measurement of the PdPt NP solution.

The catalyst was brought to SDU for further functional testing (section 3.5.1).

3.5 Application of PdPt nanostructures in fuel cells

A number of fuel cell systems operate by splitting electrons and protons from a fuel followed by separation with electrons travelling through the circuit and protons through a proton conducting membrane, Figure 90. They subsequently recombine with dioxygen to form water. The splitting of the fuel and the ORR both require catalysts, the “golden standard” being PtNPs.

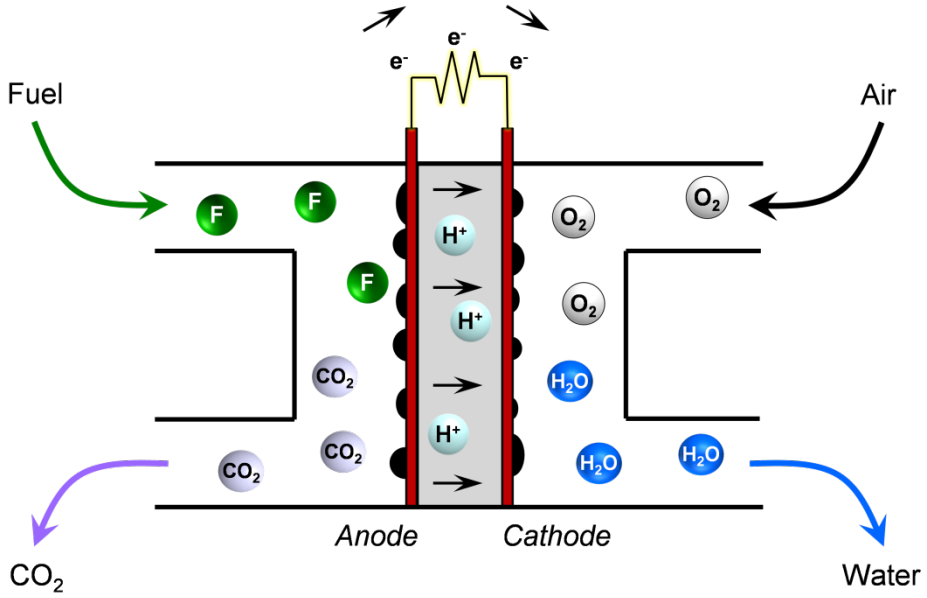

Figure 90. Scheme of a fuel cell operating with organic acids or alcohol as a fuel. The fuel molecule (green) decomposes on the anode catalyst to CO_2 (purple), H^+ (light blue) and e^-. CO_2 leaves with the exhaust. The protons travel through the membrane (grey) and the electrons through the circuit to recombine with ambient oxygen (white) at the cathode forming water (blue).

The simplest fuel is dihydrogen giving only water as a product. However, the production (electrolysis) and handling/storage of dihydrogen is challenging. Alternatives have been found in fuels that can be obtained from biomass such as organic acids and alcohols. The hydrogen density in such fuels is obviously lower than in dihydrogen and the oxidation generates CO_2. On the other hand, the potential of fuel production from biomass as well as major advantages in terms of handling and storing fuels that are liquid at ambient conditions make these technologies realistic for future application.

3.5.1 Initial fuel cell tests

The PdPt catalyst prepared at DTU was brought to SDU in Jinan, China and characterized for fuel cell application in the lab of associate professor Pengchao Si. The catalyst was tested as anode in a direct formic acid fuel cell (DFAFC) setup and as cathode in a direct methanol fuel cell (DMFC) setup. “Direct” is used to emphasize that the fuels are fed directly to the fuel cells and do not require reforming to dihydrogen.

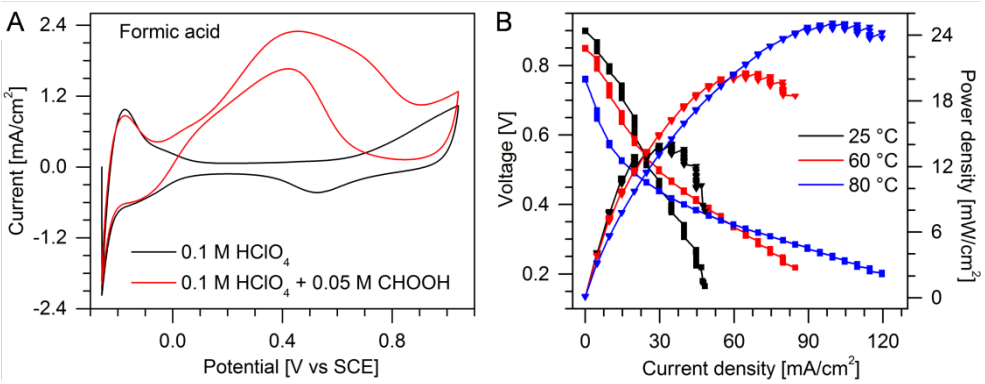

Figure 91. (A) CV of PdPt NPs on G-CB in 0.1 M $HClO_4$ with (black) and without (red) 0.05 M formic acid. Scan rate was 50 mV/s. (B) Characterization of PdPt NPs on G-CB as anode in a formic acid fuel cell setup with voltage (squares) and power density (triangles) as function of current density at three different temperatures. Cathode: Commercial Pt on CB. Data is obtained with the help of associate professor Pengchao Si at SDU.

Formic acid oxidation on Pt is not straight-forward. First, formic acid adsorbs on Pt through the protonated oxygen. Subsequently, the reaction can occur through three different pathways; the direct, the formate and the indirect pathway.[143] In the direct pathway, formic acid is directly oxidized by adsorbing through C and rapidly decomposing to water and desorbed CO_2. The formate pathway entails partial oxidation generating a surface bound formate group followed by another one-electron oxidation step to obtain CO_2.

Scheme 7. Formic acid oxidation pathways.[143,144]

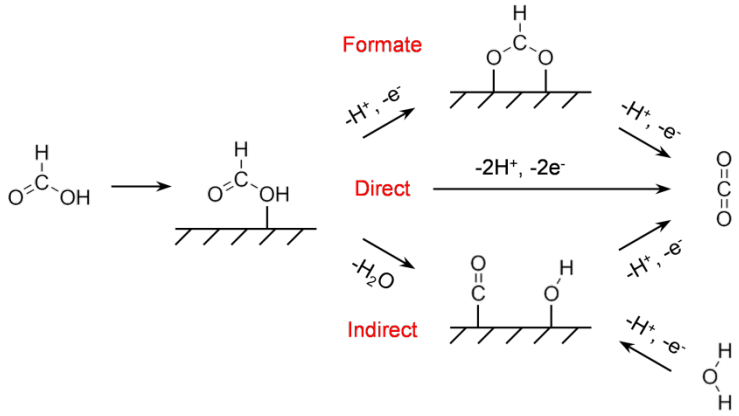

The indirect pathway is critical as adsorbed formic acid undergoes dehydration to form adsorbed CO. CO acts as a poison on Pt surfaces because the strong adsorption inactivates

the surface. The intermediate of the indirect pathway is the most stable in the potential range of 0-1 V vs. NHE and only around 1 V is CO oxidation downhill.[143] This has been observed during formic acid oxidation with pure Pt catalysts. Very small currents are seen in the positive scan direction of CV of Pt catalyst in formic acid containing electrolyte.[145] A very small anodic peak is found close to 1 V vs. NHE corresponding to the removal of CO. The formation of CO in the indirect pathway requires 3 adjacent triangularly arranged Pt atoms while the two other pathways only require 1-2 atoms.[143] The indirect pathway is thus much more sensitive to surface structure. Apart from being active for formic acid oxidation itself, the incorporated Pd in the PdPt NPs had the advantage of diluting surface Pt and limiting the number of 3-atom sites vulnerable to CO poisoning.

CV showed catalytic activity of the PdPt NPs towards formic acid oxidation, Figure 91A, evident from the greatly increased currents in the presence of fuel. The large positive currents in both positive and negative scan directions indicate that the catalyst was not poisoned significantly by CO. Open circuit voltage was 0.9 V at r.t. which is on the same level as recent reports on Pd-Ni type catalysts[146] and Pt atoms dispersed on NPG[145].

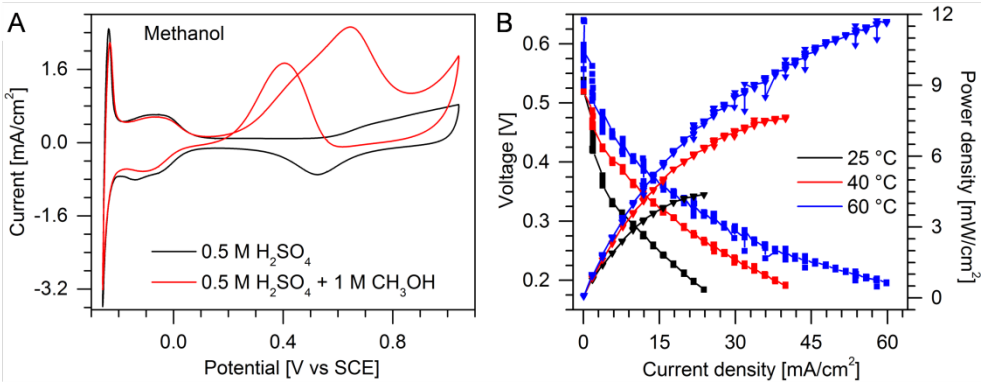

Figure 92. (A) CV of PdPt NPs on G-CB in 0.5 M H_2SO_4 with (black) and without (red) 1 M methanol. Scan rate was 50 mV/s. (B) Characterization of PdPt NPs on G-CB as cathode for ORR in a direct methanol fuel cell setup with voltage (squares) and power density (triangles) as function of current density at three different temperatures. Anode: Commercial PtRu. Data obtained with the help of associate professor Pengchao Si at SDU.

Similar studies were conducted with methanol. Electrooxidation of methanol on the PdPt NPs by CV resembled results reported for Pt and Pt-containing multi-component catalysts.[147] The PdPt NPs were used as catalysts on the cathode of the DMFC to reduce oxygen rather than oxidize methanol. The obtained open circuit voltages of around 600 mV were comparable with Pt catalysts[148] and recent multi-component catalysts of Pt-Fe and Pt-TiO_2.[149]

3.5.2 Synthesis of PdPt NP catalyst at Shandong University

The work described in this section was carried out in the lab of associate professor Pengchao Si at SDU in Jinan during a 10-day intensive visit to work on the full process from NP synthesis to fuel cells assembly and test.

The procedure developed at the NanoChemistry group of DTU Chemistry had been modified in Jinan to facilitate use of "soluble starch" (CAS 9005-84-9) rather than the "Zulkowsky starch" (CAS 9005-25-8) employed in the SAMENS method at DTU. For reasons unknown, the latter is expensive and difficult to acquire in China. "Soluble starch" (CAS 9005-84-9) was therefore used. Soluble starch consists of longer polymer chains and is less soluble than Zulkowsky starch. Specific conditions are necessary to dissolve the soluble starch, i.e. lower starch concentrations and extended heating. PdPt NP synthesis was first run at SAMENS conditions resulting in incomplete dissolution of the starch and blocking of the filter during catalyst retrieval. The starch concentration was lowered drastically from 0.6 wt% to 0.03 wt% for the next synthesis, Table 11.

Table 11. Experimental conditions for PdPt NP synthesis at SDU. The sample was heated at 90 °C for 30 min after precursor addition. The number in parentheses refers to pH of the buffer stock solution.

Sample ID	A	B	C	D	E	F
PdPt-SDU	H_2PtCl_6 1 mM	$PdCl_2$ 1 mM [a]	MES (7) 10 mM	Starch [b] 0.03 wt%	Glucose 10 mM	G-CB 99 mg [c]

[a] $PdCl_2$ was dissolved in 2 equivalents of HCl. 88 mg $PdCl_2$ and 170 µL of conc. HCl was mixed in 50 mL ultrapure water. [b] Soluble starch, CAS 9005-84-9. [c] The total metal content was 150 mg.

Soluble starch was first dissolved in 400 mL ultrapure water and heated to 90 °C for 1-2 h until the solution turned transparent. MES, glucose and KOH was added and pH adjusted to 7.3. Each metal precursor was dissolved in 50 mL ultrapure water. $PtCl_2$ was dissolved in 2 equivalents of HCl and ultrasonicated to assist dissolution. The two precursors were added simultaneously to the hot synthesis mixture and heating was maintained for another 30 min. 99 mg of G-CB was added under vigorous stirring and heating turned off. 99 mg support and a metal content of 150 mg corresponds to a maximum loading of 60 wt%. The mixture was allowed to cool to r.t. naturally for 1 h while the PdPt NPs adsorbed on the G-CB. Ultimately, the mixture was ultrasonicated to further enhance adsorption.

The catalyst was retrieved by vacuum filtration with a vacuum pump through a 0.25 µm filter. The G-CB was efficiently recovered in the filter but the filtrate still strongly coloured indicating the presence of significant amounts of NPs. The adsorption process had not thus been 100 % efficient. Prolonged heating after G-CB addition might have improved

adsorption. The structure of the support is also crucial. The surface area of G-CB relative to conventional CB is only 25 %. Loadings of 60 wt%, as is common for Pt on CB, were therefore unlikely to be achieved here. After filtration and thorough rinsing of the catalyst with ultrapure water the powder was dried in an oven at 100 °C for 1 h. The powder was transferred to a vacuum oven and the remaining organic compounds removed by oxidation at 200 °C for 1 h to provide the final catalyst product. The final yield was ≈ 130 mg implying an actual metal loading of 25-30 wt%.

3.5.3 Electrochemical characterization of PdPt catalyst

Electrochemical characterization of the PdPt NP catalyst was done by immobilization on glassy carbon electrode (GCE) in a Nafion® polymer matrix. Nafion is a DuPont trademark name for a sulfonated polytetrafluoroethylene (PTFE) polymer which is commonly used for immobilization on electrodes and as proton conducting membranes in fuel cell systems. 7.6 mg catalyst was redispersed in 5 mL 0.05 vol% Nafion in ethanol by ultrasonication and 10 µL of the homogenized suspension was drop-cast on a freshly cleaned GCE. The catalyst was first activated by potential cycling. CVs of 20 potential cycles between 1.2 and -0.25 V vs. SCE in 0.1 M $HClO_4$ at 50 mV/s were recorded, Figure 93.

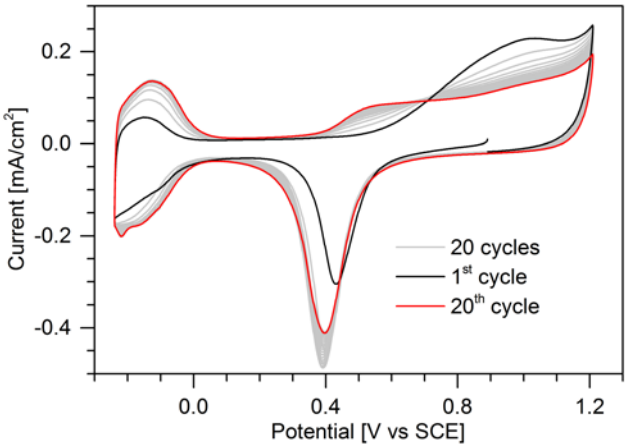

Figure 93. Activation of PdPt-SDU/G-CB by continuous potential cycling. 20 cycles were recorded in 0.1 M $HClO_4$ at 50 mV/s with a mercury/mercury sulfate electrode (MSE) as reference and a 1 cm^2 Pt sheet as counter electrode. The first (black) and last (red) cycles are highlighted. Data obtained with the help of Wenxin Wang at SDU.

A drastic change in EC behaviour was observed during cycling. On the one hand, this process served to clean the surface of any contaminant remaining from the synthesis. On the other hand, Pd dissolved from the surface resulting in a switch from alloy type behaviour to pure Pt behaviour.[150] This is supported by the increased currents between -0.25

and 0.00 V vs. SCE. This is the hydrogen adsorption/desorption region which directly relates to the available metal surface area.

The activated electrode was then transferred to another setup with a rotating disc electrode (RDE) to measure the activity towards ORR. The rotation of the electrode forces the solution away from the electrode at its periphery giving rise to a flow towards the electrode surface in the direction of the rotation axis. This ensures a fast supply of analyte from the bulk to the surface plus transport of product away from the electrode effectively removing diffusion as a parameter for the observed current. The signal is instead limited by mass transport which is governed by the rotation speed.[151] CVs were recorded in a potential range covering the ORR while the electrode was rotated at 1600 revolutions per minute (rpm). Three features of the ORR test are important; the onset potential (the potential at which current starts to flow when scanning negatively), the half-wave potential (HWP) (the potential at half the limiting current) and the limiting current (current of the plateau at low potential). The onset potential and HWP both describe the catalytic efficiency of the material towards ORR while the limiting current relates to the number of active sites on the electrode. The latter is effected by the shape/size/composition of the catalytic NPs, the loading of these on the support, and the amount of catalyst deposited on the electrode.

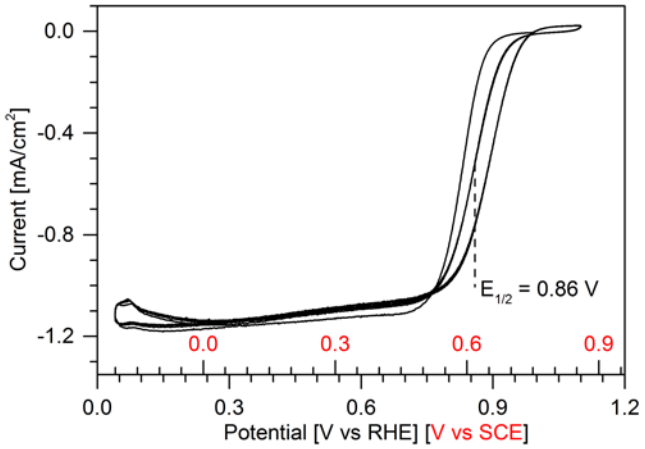

Figure 94. Oxygen reduction reaction by PdPt-SDU/G-CB using RDE in 0.1 M $HClO_4$ oxygen saturated solution at 10 mV/s with an RHE as reference and a 1 cm^2 Pt sheet as counter electrode. The electrode is rotated at 1600 rpm and potential given vs. RHE (black) for comparing with literature and SCE (red) . Data obtained with the help of Wenxin Wang at SDU.

The HWP was 0.86 V vs. RHE which is higher than reported values for similar systems.[152-155] Recent reports on PdPt bimetallic NPs show a comparable HWP for NPs with low surface concentration of Pt which approached 0.9 V vs. RHE as the surface concentration of Pt was increased.[156,157] Precise engineering of pure Pt systems have pushed the HWP as

high as 0.95 V vs. RHE for nanorod arrays[158] and 0.97 V vs. RHE for highly concave cubic nanocrystals on reduced graphene oxide[159] highlighting the superiority of Pt and that design of new materials is a trade-off between activity and Pt consumption.

3.5.4 Cathode preparation, DMFC assembly and fuel cell test

The PdPt-SDU/G-CB catalyst material was tested in a single-cell DMFC setup as cathode catalysing the ORR. 98 mg of catalyst powder was dispersed in 20 mL ethanol containing 22 mg Nafion and a drop of water to avoid oxidation of the ethanol by the catalyst. The 30 mL glass vial was ultrasonicated for 1-2 h. Ice was added to the ultrasonic bath to avoid overheating. The catalyst/Nafion solution was painted onto a 4 x 4 cm^2 piece of carbon paper fixed between 4 glass slides, Figure 95A, and placed on a heater at 60 °C to facilitate drying. The solution was applied one layer at a time by painting it on with a brush. The paper was allowed to dry after each applied layer. The glass slide was rotated 90 ° for each repetition to ensure homogeneous application. It was estimated that the application process involved a 15 % loss of material in the brush, glass vial etc. 83 mg catalyst had thus been applied. After complete application and drying, the carbon paper was cut into 1 x 1 cm^2 pieces to be used as cathode material, Figure 95B. Each piece contained one 16^{th} of the applied catalyst, or 5.21 mg. Consequently, each piece carried 3.12 mg metal considering the maximum possible loading of 60 wt% or 1.56 mg if the more likely loading of 30 wt% is chosen.

A 5 x 5 cm^2 piece of Nafion-115 (DuPont) was activated by a sequential process including treatment with H_2O_2, ultrapure water, H_2SO_4 and ultrapure water. The Nafion-115 was placed onto one of the prepared 1 cm^2 catalyst paper pieces and a corresponding 1 cm^2 commercial anode paper (Pt/Ru) placed on top. This sandwich structure is known as the membrane electrode assembly (MEA) and efficient contact between the layers was achieved by compression at high pressure and temperature. The final MEA is shown in Figure Figure 95C.

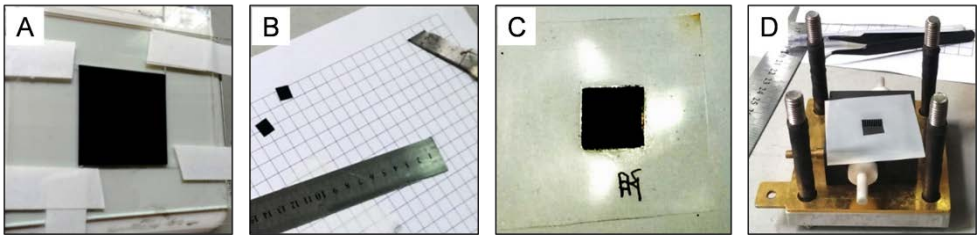

Figure 95. The DMFC cathode preparation and cell assembly. (A) Application of catalyst dispersion on carbon paper. (B) Cutting of dried catalyst paper into 1 cm^2 pieces. (C) The MEA consisting of anode and cathode paper pieces separated by a Nafion membrane. (D) Assembly of single-cell DMFC.

The cell was assembled in a symmetric, layered structure, Figure 95D. Outermost were the collection plates responsible for collecting the generated current and next the bipolar plates. These contained small channels for guiding the reactant gas/liquid onto the electrodes. The setup used here employed a linear cross-flow design. The reactants enter the bipolar plates on one side and exit on the other while the flow directions over the two electrodes anti-parallel. A PTFE sheet with a whole matching the catalyst papers separated the bipolar plates and the MEA on both sides ensuring that short-circuiting of the bipolar plates did not occur. The voltage between the bipolar plates was measured during operation. The half-assembled cell is shown in Figure 95D. The fuel cell must be tightly assembled so the cell was pressed together by a machine and the bolts tightened. The complete cell was then connected to the test facility. The electrodes were activated by running 80 °C ultrapure water over both anode and cathode. This improved the wetting of the catalyst material. The half-cell reactions taking place in the DMFC are given in Eq. (3.1).

$$\begin{aligned} &\text{Anode:} && CH_3OH + H_2O \rightarrow CO_2 + 6H^+ + 6e^- \\ &\text{Cathode:} && \tfrac{3}{2}O_2 + 6H^+ + 6e^- \rightarrow 3H_2O \end{aligned} \tag{3.1}$$

Each methanol molecule is considered to be fully oxidized on the catalyst material of the anode and delivers 6 protons and 6 electrons. The protons diffuse through the MEA and while electrons travel through the circuit including bipolar plates and collection plates. Protons, electrons and dioxygen react on the catalyst material of the cathode to produce water.

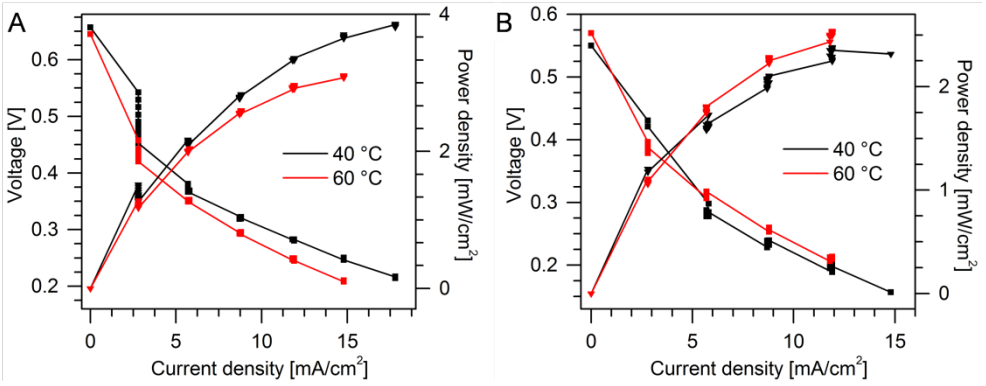

Figure 96. DMFC test with PdPt-SDU/G-CB on the cathode. (A) and (B) represents two different samples prepared by the same procedure with a total metal content of 1.84 mg. Voltage (squares) and power density (triangles) is given as function of current density at 40 (black) and 60 °C (red) different temperatures. Anode: 3.74 mg commercial PtRu/C.

Two MEAs of the same PdPt-SDU/G-CB catalyst were prepared and tested under real DMFC operating conditions. First, a significantly different behaviour of the two MEAs was

observed. This underlines the challenges in testing catalysts in real FC setups. The process includes many steps and has to be tweaked for each new material. The open circuit voltage was similar to what was initially observed for the PdPt/G-CB prepared at DTU (0.66 and 0.57 compared to 0.64 V). This suggests that the catalytic performances of the prepared NPs were comparable and not affected by the synthesis challenges involving soluble starch.

The maximum observed power density was 3.86 mW/cm^2. Normalizing this to the metal content this gives 1.24 mW/mg_{metal} if the maximum possible metal loading is considered (60 wt%). The synthesis showed that the actual loading was more likely 30 wt% resulting in a specific power density of 2.47 mW/mg_{metal}. Further normalization of the performance to the Pt content can be done to evaluate how efficiently Pt is utilized. Assuming equimolar contents of Pd and Pt (≈ 65 wt% Pt) the specific power density becomes 3.82 mW/mg_{Pt}. This is just over 20 % compared to a commercial 20 wt% Pt/C catalyst from Johnson Matthey tested on the same setup.[145] A similar rough estimation can be done for the initial tests of the PdPt/G-CB prepared at DTU assuming a 100 % efficient loading procedure (which is conservative as non-adsorbed NPs were found in the filtrate) and 1:3 molar ratio between Pt and Pd. These assumptions lead to a total Pt loading on the cathode in the fuel cell of about 1 mg and a specific power density up to 12 mW/mg_{Pt}.

In conclusion, the facile synthesis of bimetallic NPs of Pd and Pd was successful and decent loadings on the G-CB support were obtained with good dispersion. The catalyst was active for several important reactions in fuel cell technology, i.e. formic acid oxidation, methanol oxidation and oxygen reduction. Within the very condensed frame of a 10-day program, the catalyst was synthesized and tested in functional fuel cells. This is not a trivial feat and a testimony to the efficient organization at SDU. Despite, technical challenges relating to the synthesis, good performance was achieved. The NPs synthesized at DTU and SDU did not show significantly different catalytic properties, but higher specific power densities were obtained for DTU synthesized particles resulting from better dispersion and metal loading on the G-CB.

The application of SAMENS PdPt NPs in fuel cells proved fruitful and future work on system optimization (such as alloy vs. core-shell, alloy composition and incorporation of a third component) is expected to improve the performance significantly.

Chapter 4

Minerals and hybrids with metal NPs

4.1 Earth-abundant solutions

Many technologies involved in the transition from a petroleum-based society to a sustainable one not only require very efficient catalysts but also implementation on a large scale. Abundance is thus an equally important component for the success of new technology in this field. Search for catalytically active materials comprised of earth-abundant metals is essential. Vesborg et al. identified 25 top elements of which the supply is sufficient for meaningful application, including Fe, Al, Mg, Cr, Cu, Mn, Zn, Mg, Si and Ti.[160]

Efforts towards extending the SAMENS method to the synthesis of less noble metal compounds has focused on Cu. Cu is most stable under ambient conditions as Cu(II). Materials with Cu in this oxidation state were chosen as targets in order to keep the synthesis and handling easy and cheap. The behaviour of Cu in relation to the SAMENS method was investigated and one product, copper(II) oxide, was used as catalyst for alcohol oxidation reactions.

4.2 Selective synthesis of $Cu_2(OH)_3Cl$ and CuO

Different from the noble metals previously dealt with, the chemistry of copper is very rich. It forms many stable minerals with a range of organic and inorganic anions. It is not easy to predict what minerals will form as it depends on specific conditions, such as pH, temperature and anion composition.

The synthesis of Cu compounds by modifications to the SAMENS method was investigated with a view to preparing well-defined and phase-pure nanomaterials. Prior to the PhD project it was found that using $CuCl_2$ as precursor instead of $HAuCl_4$ resulted in the precipitation of brown particles that re-dissolved at r.t. This corresponds to the reactions happening in the Benedict's test for reducing sugars where Cu^{2+} is reduced forming Cu_2O.

The OBS synthesis in which starch and glucose is omitted was tested to avoid redissolution of the product. A stable colloid was formed but no further characterization was done at the time. The investigations were continued during the PhD programme.

4.2.1 pH effect on product phase

Cu forms many different stable hydroxides, oxides and chlorides so pH must influence the synthesis. A series of samples was prepared following the OBS method with varying starting pH, Table 12.

Table 12. Experimental conditions for pH study of copper mineral synthesis. All samples were heated at 90-95 °C for 10 min in a water bath with stirring.

Sample ID	A	B	$pH_{initial}$	pH_{final}	pH adjustment
Cu-pH-1	2 mM $CuCl_2$	10 mM MES	4.0	4.1	[a]
Cu-pH-2	2 mM $CuCl_2$	10 mM MES	4.3	4.4	[b]
Cu-pH-3	2 mM $CuCl_2$	10 mM MES	5.6	5.7	[a]
Cu-pH-4	2 mM $CuCl_2$	10 mM MES	6.0	5.8	[b]
Cu-pH-5	2 mM $CuCl_2$	10 mM MES	6.4	6.0	[a]
Cu-pH-6	2 mM $CuCl_2$	10 mM MES	6.6	6.2	[b]
Cu-pH-7	2 mM $CuCl_2$	10 mM MES	7.0	6.2	[a]
Cu-pH-8	2 mM $CuCl_2$	10 mM MES	8.5	6.3	[a]
Cu-pH-9	2 mM $CuCl_2$	10 mM MES	10.3	6.4	[a]
Cu-pH-10	2 mM $CuCl_2$	10 mM MES	10.5	6.4	[a]
Cu-pH-11	2 mM $CuCl_2$	10 mM MES	10.6	6.6	[b]
Cu-pH-12	2 mM $CuCl_2$	10 mM MES	11.5	7.0	[a]
Cu-pH-13	2 mM $CuCl_2$	10 mM MES	12.7	12.6	[a]

[a] pH of the samples was adjusted by adding small amounts of 4 M KOH to 18 mL of 11 mM MES solution. [b] The 0.1 M MES stock solution was adjusted to the given pH values before addition to the sample.

The pH was adjusted either by addition of 4 M KOH to the dilute buffer solution before precursor addition (9 samples) or by adjusting the pH of the 0.1 M MES stock solution (4 samples). The samples were denoted Cu-pH-1 to -13 according to pH (low to high). Only brief heating (10 min) was necessary for a stable coloured solution to form.

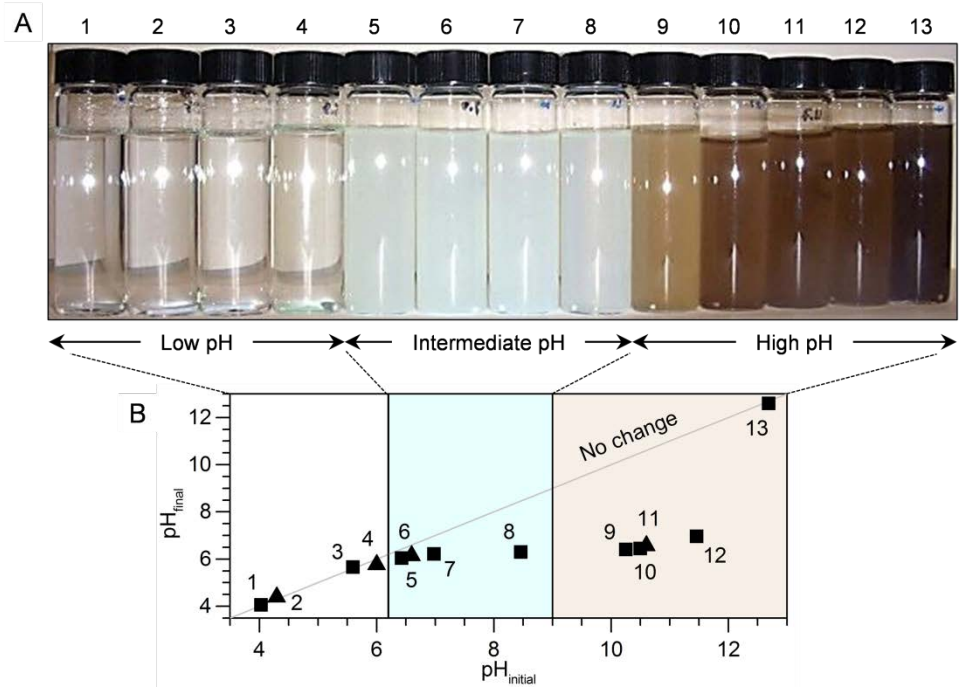

Figure 97. (A) Photograph of Cu-pH-1 to -3 arranged by increasing initial pH from left to right. Three pH regions are clearly visible. (B) Plot of final pH vs. initial pH. Indexes of Cu-pH samples are indicated on the graph and the three pH regions highlighted with the background colour. The grey line corresponds to identical initial and final pH.

Figure 97 shows all samples. Three distinct pH regions were clearly observed; (1) low pH were no particles had formed, (2) intermediate pH providing white opaque solutions with a bluish tone and (3) high pH resulting in a dark brown precipitate.

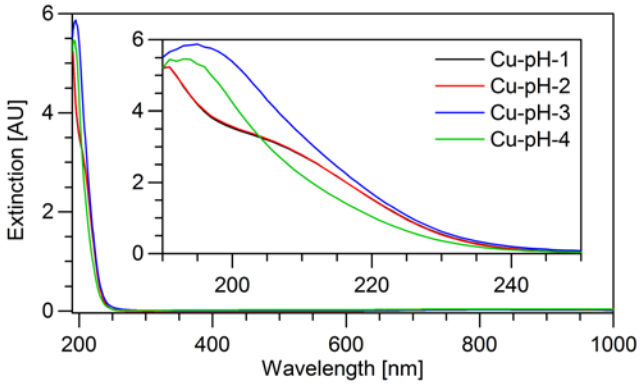

Figure 98. UV-vis spectra of samples Cu-pH-1 to -4 comprising the low pH region (dil: 2). Inset shows a magnified view of the changes in the UV absorbance.

UV-vis spectra of the samples from the low-pH region showed only minor changes to the absorbance of the Cu(II) species in solution, Figure 98. Initial pH above 6 resulted in formation of particles. The white/blue particles formed in the intermediate pH region showed a double-peak in their extinction spectrum at the low end of the pH region. One part decreased with increasing pH while the other one increased to form a well-defined peak at 255 nm at initial pH of 8.5 (Cu-pH-8), Figure 99.

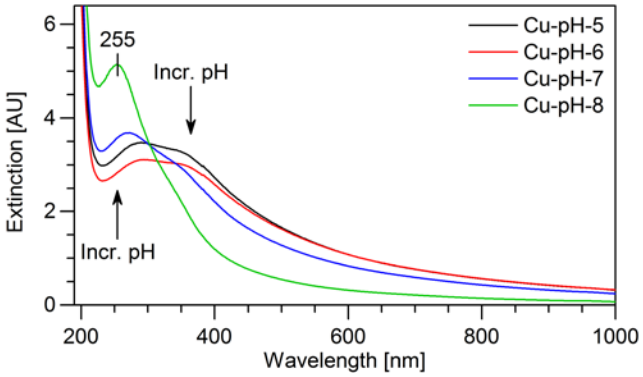

Figure 99. UV-vis spectra of samples Cu-pH-5 to -8 comprising the intermediate pH region providing a white/blue product (dil: 2).

Initial pH of 10.3 (Cu-pH-9) marks the onset of formation of a brown product, Figure 100. At this pH a mixture of the white/blue and brown product was observed and the extinction a mixture of the spectra of Cu-pH-8 and -13. No contribution from the white/blue product was found above initial pH 10.5. The brown product of the high pH region exhibited a broad extinction between 250 and 900 nm. Increasing pH led to a decrease in extinction at the NIR region and the emergence of a peak at 368 nm.

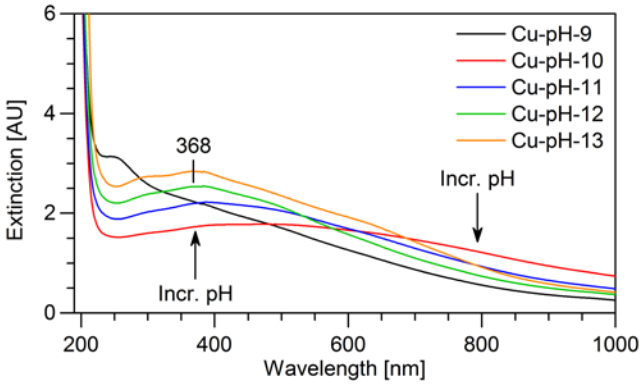

Figure 100. UV-vis spectra of samples Cu-pH-9 to -13 comprising the intermediate pH region providing a white/blue product (dil: 2).

The pH dropped significantly in all samples with particle formation which is expected from mineral formation with O^{2-} and OH^- while no pH change was found below initial pH of 6. The pKa of utilized MES buffer was very suitable for maintaining particle forming conditions keeping pH above 6.

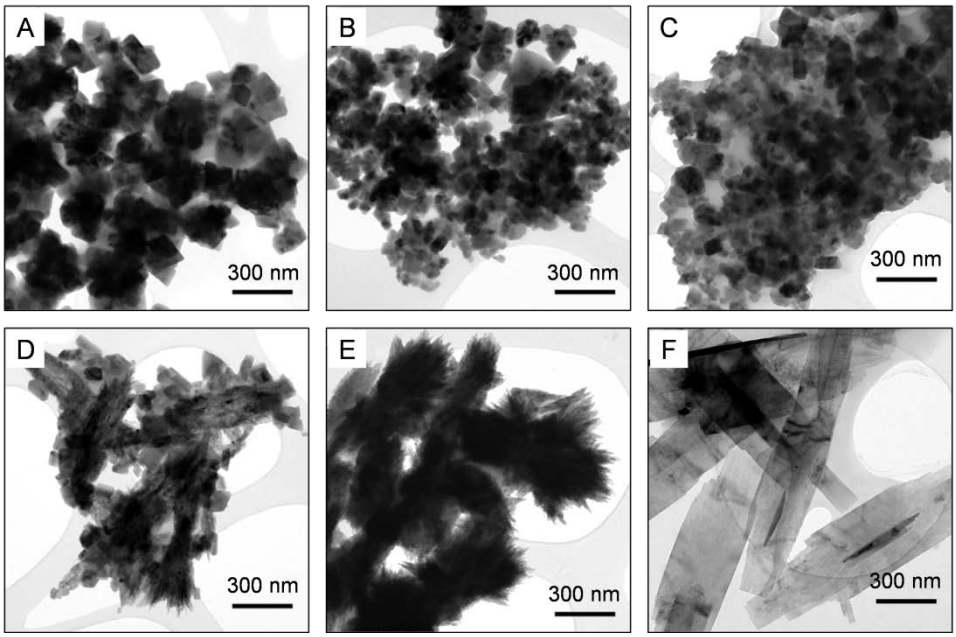

Figure 101. (A) to (B) TEM images of as-synthesized NPs found in Cu-pH-6 to -10 and -13, respectively.

The synthesized particles of selected samples were studied by TEM. The white/blue product was cubic to rhomboidal in shape and seemingly single-crystal. Their size decreased with increasing initial pH from hundreds of nm to tens of nm as seen in Figure 101A to -C corresponding to Cu-pH-6 to -8. The brown product formed at high pH consisted of much larger particles of more than a micron and their morphology was highly pH dependent going from aggregates of needle-like structures to thin ribbons, Figure 101E and -F. As expected, a mixture of the two types of nanostructures was found in Cu-pH-9, Figure 101D. The ribbons in Cu-pH-13 had a more well-defined faceted structure. This suggested a highly ordered crystalline character which was further evidenced by ordered pattern of lattice fringes in the HR-TEM images, App. fig. 40. They were widest at the middle and narrowed towards the ends in right-angled steps. Their width and length were 370 ± 40 and 1400 ± 100 nm, respectively, and their thickness 30-65 nm at the center and 10-20 nm at the tips, App. fig. 41 and App. fig. 42.

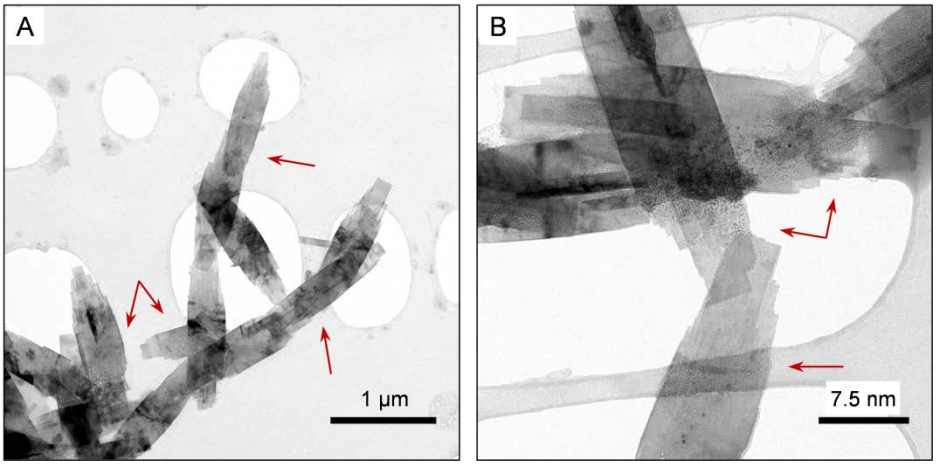

Figure 102. TEM images of beam damage to the ribbons in Cu-pH-13. The arrows indicate areas with clear structural changes.

Beam damage was observed during TEM measurements. The smooth intensity of the ribbons changed to a disordered pattern and particles seemed to form, Figure 102. The beam damage was especially severe where ribbons were in contact with other ribbons or the carbon film. The process was observed at high magnification, App. fig. 43. High resolution showed only one set of lattice fringes covering the entire image. After prolonged beam exposure, this lattice was disrupted and many small crystals appeared.

Several repeats of 20 mL samples at Cu-pH-7 and -12 conditions representing the two different overall products were carried out and the initially obtained results were reproducible, attesting to a robust procedure. pH 11 consistently produced the spiky bundles, or nanowhiskers, App. fig. 44. SAED of the two products supported single-crystallinity in the white/blue product and that particles found in the brown product was polycrystalline, App. fig. 45. MES has previously been shown to reduce Au^{3+} in $[AuCl_4]^-$ so Cu^{2+} reduction was investigated with STXM. The synthesized particles sedimented over time and sediments of the white/blue and brown products were collected for characterization. These experiments were carried out at the Soft X-ray Spectromicroscopy beamline, BL08U1A, at SSRF part of SINAP in Shanghai. The products were characterized with dual contrast and stack imaging techniques. These techniques basically provide the same information for the two samples, i.e. the oxidation state of Cu. The $L_{2,3}$ absorption edge of Cu lies in the soft X-ray range around 930-940 eV. These transitions depend on oxidation state making it possible to distinguish these based on the position of the edge.[161-163] A series of STXM images were recorded in an energy range covering the Cu(I) and Cu(II) peaks at 937 and 940 eV, respectively. This process is equivalent to recording an absorption spectrum in each point of the image and the employed software identified regions of the image with specific absorption profiles.

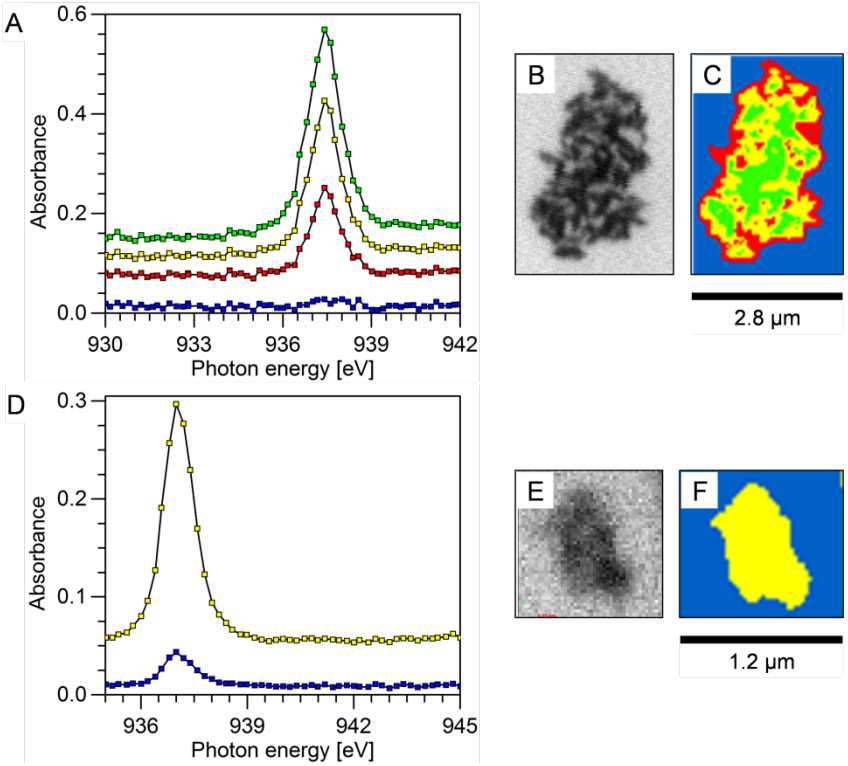

Figure 103. STXM stack imaging of brown product (top) and white/blue product (bottom). The fill colours of the spectra in (A) and (D) correspond to the coloured regions in the stack images (C) and (F), respectively. (B) and (F) show fixed energy STXM image of the stack imaged areas in (C) and (E), respectively.

Figure 103 shows stack imaging data for brown, (A) to (C), and the white/blue product, (D) to (F). The spectra are coloured according to their corresponding areas of the stack image and only Cu(II) was detected for both products. The edge shifts to 940 eV for Cu(I) as seen for a reference sample containing Cu_2O, App. fig. 46. Stack imaging is time-demanding as a large number of images has to be recorded to cover the desired energy range with sufficient resolution. Knowing where to expect the peaks enables dual-energy imaging for which only two images are recorded for each edge of interest (one before and one on top of the edge). Such measurements were done for the product formed at intermediate pH as the stack imaging was not satisfactory, Figure 104.

The STXM studies provided no evidence of Cu(I) so redox chemistry is unlikely to be involved in either of the reactions to form the two different products. Copper was thus present only as Cu(II) and the nucleation of nanostructures arose from insolubility of the compounds under the applied conditions.

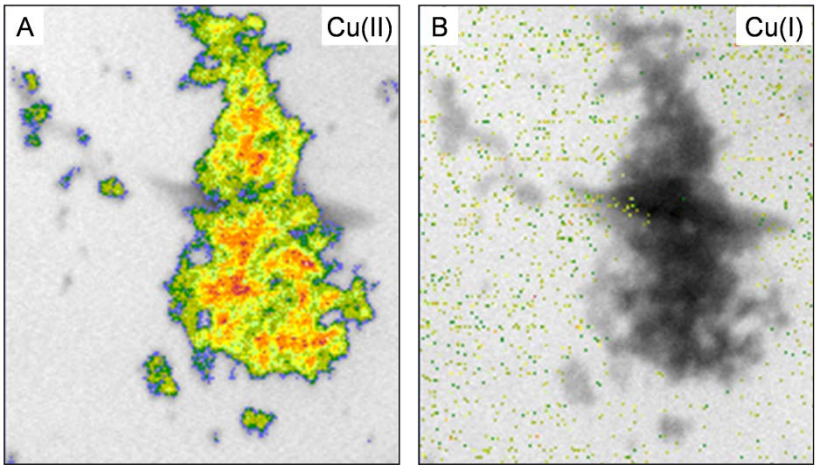

Figure 104. Dual-energy STXM images of the white/blue product showing the absorption difference between (A) 935.0 and 937.6 eV and (B) 938.5 and 939.8 eV corresponding to mapping of Cu(II) and Cu(I), respectively. The magnitude of the difference is shown with blue, green, yellow and red going from low to high local concentration. The colour map is superimposed on a fixed energy STXM image (greyscale). The four fixed energy images used for the dual-energy images are shown in App. fig. 47. The images are 8 by 10 µm.

4.2.2 Scale-up and product identification

Because Cu forms many closely related minerals, a purified product is needed for detailed characterization. Techniques such as XRPD and ATR-FTIR require powdered samples in the order of tens of mg per measurement so the syntheses had to be scaled up. An additional benefit of an increased synthesis output was the option of purification by vacuum filtration which is not feasible for 20 mL samples.

Table 13. Experimental conditions for scaling up the copper mineral syntheses.

Sample ID	A	B	$pH_{initial}$ [a]	Temp.	Time	Pre-heat.
LS-Cu-A1	$CuCl_2$ 2 mM	MES 10 mM	7	90-95 °C	15 min	No
LS-Cu-B1	$CuCl_2$ 2 mM	MES 10 mM	11	90-95 °C	60 min	No
LS-Cu-B2	$CuCl_2$ 2 mM	MES 10 mM	11	90-95 °C	10 min	20 min

[a] The dry powder of MES was dissolved in 750 mL ultrapure water. pH of this solution was adjusted to the desired value with KOH.

One pH value was chosen for each of the intermediate and high pH regions, i.e. 7 and 11, for the scale-up experiments with batch sizes of 1 L. The 1 L volume allows for weighing off the pure chemicals instead of using stock solutions. MES was dissolved in 750 mL ultrapure water and adjusted by KOH to the desired pH while Cu precursor was dissolved in 250 mL ultrapure water. The precursor was either added to the buffer at r.t. (LS-Cu-A1 and -B1) or after pre-heating (LS-Cu-B2), Table 13.

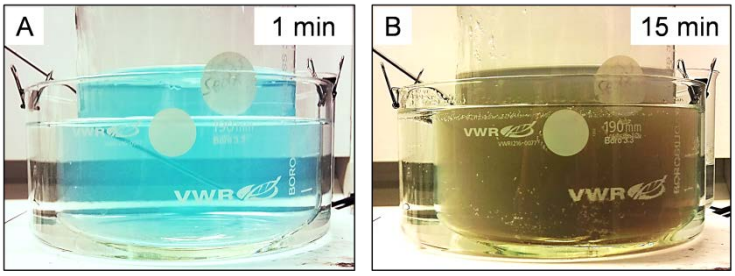

Figure 105. Photographs of LS-Cu-B1 (A) 1 min and (B) 15 min after precursor addition. Colour representation is only indicative.

The scaling up had no visible effect on the synthesis of the white/blue product but affected the brown product synthesis, LS-Cu-B1. The mixture turned bright blue in the first min after precursor addition and a brown colour only appeared after 15 min, Figure 105. TEM confirmed that a mixture of nanostructures had formed in LS-Cu-B1, Figure 106. Two well-defined populations of NPs similar to those of the white/blue product and large leaf-shaped sheets were observed. The nanoleaves were 1300 ± 100 nm long, 350 ± 50 nm wide and 60-100 nm thick which is identical to the overall dimensions of the ribbons in Cu-pH-13.

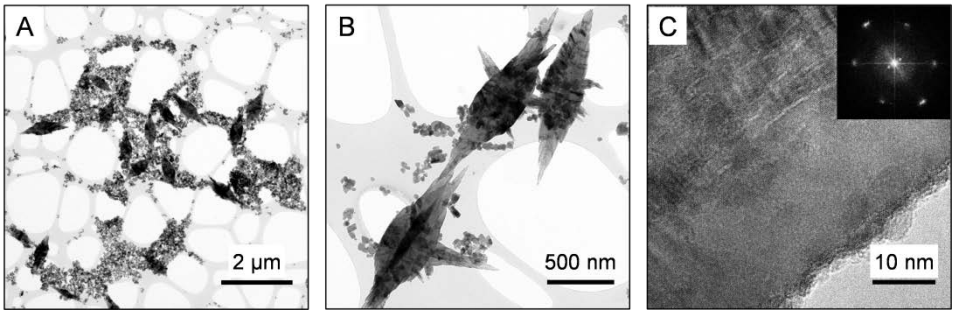

Figure 106. (A-B) TEM images of LS-Cu-B1 containing a mixture of large leaf-shaped sheets and small NPs. (C) High-resolution image with corresponding FFT (inset).

Occasionally, leaves were standing on their edge allowing for the thickness to be measured. The flat structure was further evidenced by images taken at increasing sample tilt. This series of images in App. fig. 48 clearly shows the flat nature of the nanoleaves. The nanoleaves appeared to be polycrystalline due to the very rough surface and edges but high-

resolution showed lattice fringes continuing over large areas of the sheets, Figure 106C, suggesting single-crystal nature. The FFT in Figure 106C supports a highly ordered structure and resembles a single-crystal diffraction pattern. If the structure is polycrystalline, the crystallite orientation must be ordered and uniform.

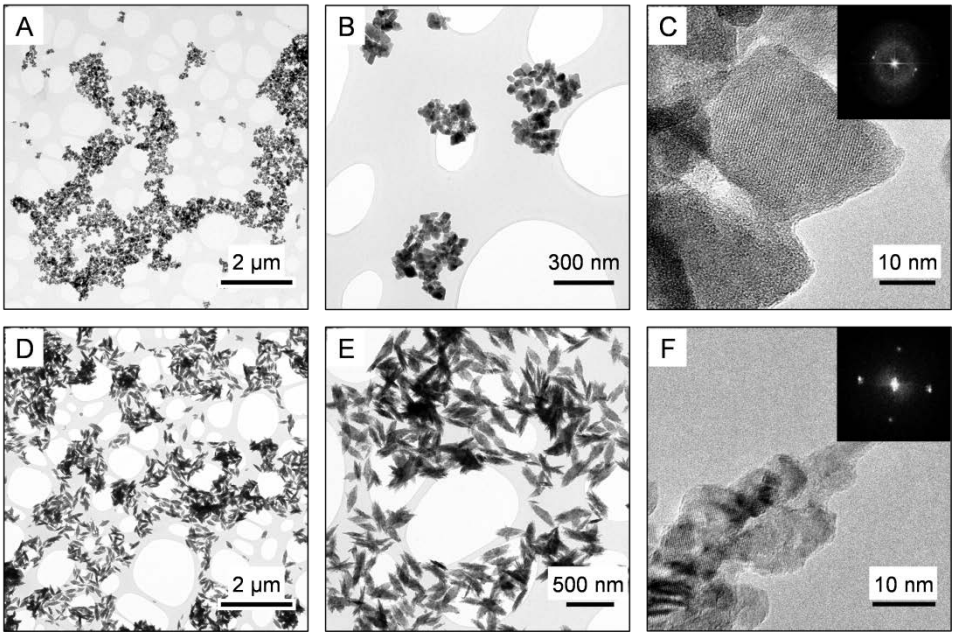

Figure 107. TEM images of (A-C) LS-Cu-A1 and (D-F) LS-Cu-B2. (C, F) HR images indicated single-crystalline character for both samples. Insets show corresponding FFTs.

The addition of precursor at r.t. was not suitable for the 1 L batch as the temperature increased very slowly compared to the experiments with the 20 mL vials. A new synthesis was carried out for which the buffer was pre-heated 20 min until its temperature surpassed 90 °C, LS-Cu-B2. This improved the synthesis significantly. The solution turned green for a few seconds before turning brown after precursor addition. All three 1 L synthesis mixtures were purified by filtration with in-house vacuum using a nylon membrane with 0.2 µm pores providing a colourless and clear filtrate suggesting good retention of the product. The retentates were washed at least 3 times with about 200 mL ultrapure water and once with ethanol. Finally, the filtration flask was emptied and vacuum applied for a few hours to remove remaining ethanol. The white/blue product from the 1 L synthesis was very similar to that formed at small volumes containing rhomboidal single-crystals in the tens of nm range, Figure 107A to -C. The UV peak was red-shifted slightly compared to the small volume synthesis due to the removal of MES which absorbs strongly below 240 nm. The NPs of the brown product had a similar shape as those in the 1 L batch heated from r.t.,

Figure 107D to -F, but the particles were much smaller; 300 ± 70 nm long and 100 ± 20 nm wide, App. fig. 50. The edges of the particles were rough and the structure referred to as jagged nanoleaf. They were flat but their shape was not as regular as the ribbons or previous leaves so the thickness could not be determined. An SAED of an area similar to Figure 107E was recorded supporting the polycrystallinity of the particles, App. fig. 51. The extinction spectrum agreed with Cu-pH-11 and -12 synthesized at similar pH.

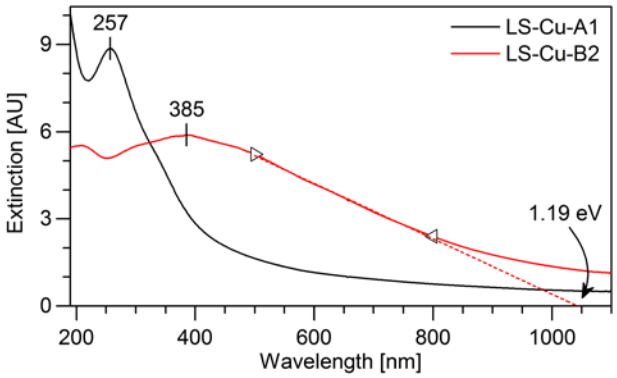

Figure 108. UV-vis spectra of purified product of LS-Cu-A1 (black) and -B2 (red) redispersed in ultrapure water at 585 and 570 mg/L, respectively (dil: 5). Dotted line represents a linear fit of LS-Cu-B2 between 500 and 800 nm (marks) extrapolated to zero extinction to get a rough estimate of the band gap.

XRPD was measured for the purified powders to match the patterns against a database of known structures to identify the compounds formed at intermediate and high pH. The XRPD pattern of the brown product matched CuO as the monoclinic mineral tenorite while that of the white/blue product matched several polymorphs[x] with the composition $Cu_2(OH)_3Cl$. The UV-vis spectra[164-166] of the synthesized CuO nanostructures and a rough estimation of the CuO band gap (≈ 1.2 eV)[167] agreed with previous reports on CuO nanomaterials. The band gap was estimated from the wavelength where absorbance increases. The linear part of the spectrum is extrapolated to zero absorbance due to the lack of a clear onset, Figure 108. $Cu_2(OH)_3Cl$ exists as the naturally occurring minerals atacamite (orthorhombic[168]), paratacamite (trigonal[169]), clinoatacamite (monoclinic[170]), botallackite (monoclinic[171]) and anatacamite (triclinic[172]). Rietveld refinement was applied to determine the precise polymorph of the synthesized material, Figure 109. This narrowed it down to clinoatacamite and anatacamite which are so closely related that their structures are indistinguishable by XRPD.[172] The refinements shown in Figure 109 provided crystallite sizes of 26.8 and 11.6 nm for the $Cu_2(OH)_3Cl$ and CuO NPs, respectively,

[x] Polymorphs describe crystalline materials with the same chemical formula but different crystal packing.

agreeing with the observations from TEM. LS-Cu-B1 contained 69 wt% 25.1 nm $Cu_2(OH)_3Cl$ and 31 wt% 19.5 nm CuO, App. fig. 53.

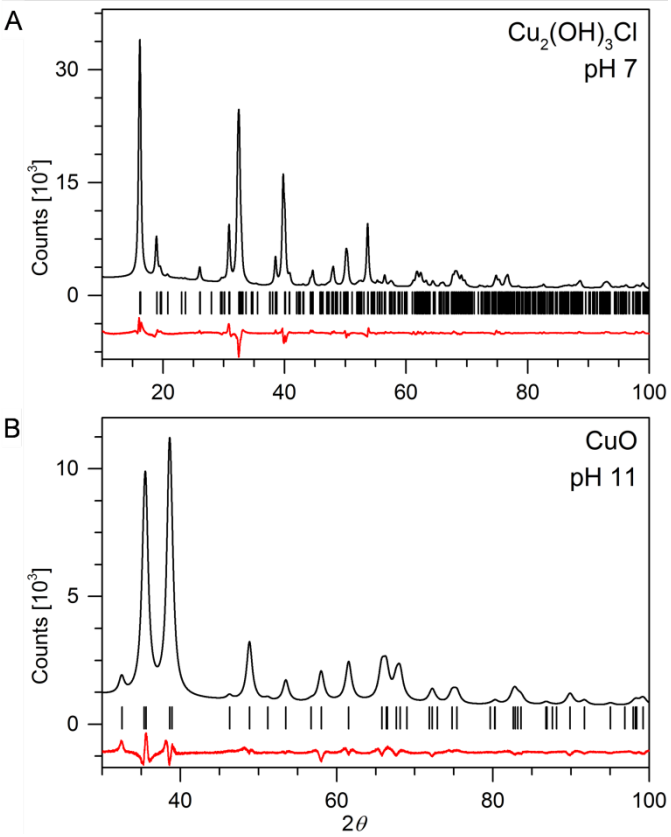

Figure 109. Rietveld refined XRPD patterns of (A) the blue/white product and (B) the brown product. The black bars represent Bragg positions for (A) clinoatacamite and (B) tenorite and the red curves are the differences between raw data and fitted patterns. Refinements were carried out by PhD student Jonas Andersen at DTU Chemistry.

Anatacamite was discovered 2009[172] and recently, a Raman spectroscopy method to distinguish this polymorph from clinoatacamite was presented.[173] Vibrational spectroscopy was employed to characterize the synthesized $Cu_2(OH)_3Cl$. The data collection and analysis was carried out with PhD student Phillip Malcho at DTU Chemistry. Raman spectroscopy was attempted but no convincing spectrum obtained. It was believed that the nanocrystals were not stable during measurement. Instead, focus was placed on less energy-intense infrared spectroscopy. In order to identify the polymorph, reference materials of the different polymorphs were needed. Natural atacamite crystals were obtained from the Natural History Museum of Denmark (Copenhagen, Denmark, sample ID “Gl. Nr. 29”).

The sample originated from the Atacama Desert in Chile. Apart from blue atacamite crystals, the sample contained natural impurities of other minerals arising from sample acquisition. Two anatacamite crystals were provided by Mineralogical Museum, University of Hamburg in Germany. They were acquired from the La Vendida mine, Sierra Gorda, Chile. Apart from natural reference materials, a synthetic mixture of clinoatacamite and atacamite was prepared by a modification of a previously reported procedure.[174] 1.32 g $Cu_2(OH)_2CO_3 \cdot H_2O$ and 0.86 g $CuCl_2 \cdot H_2O$ was mixed in 20 mL ultrapure water and heated in a water bath at 95 °C for 1 h. Rapid CO_2 evolution caused immense bubbling during synthesis. The product was filtered through a glass membrane filter, washed with pure water and ethanol. XRPD data for the mixed reference materials was acquired and Rietveld refinement carried out, App. fig. 54. The atacamite sample contained quartz impurity of 7.6 wt% and the synthesized mixture 68.4 and 31.6 wt% of clino- or anatacamite and atacamite, respectively. The refinements are summarized in App. table 2. Atacamite was sorted from quartz crystals and the macro-crystalline natural minerals, atacamite and anatacamite, were ground in a mortar to produce a fine powder. Photographs of the prepared powders and visible-light micrographs of the natural crystals of atacamite and anatacamite are shown in App. fig. 55 and App. fig. 56.

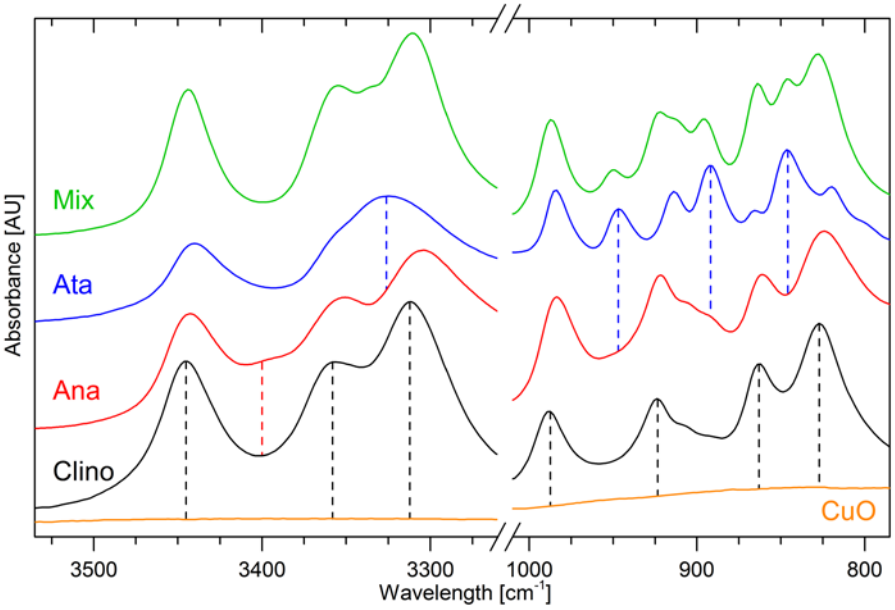

Figure 110. ATR-FTIR spectra of LS-Cu-A1 (black), natural anatacamite (red), natural atacamite (blue), synthesized mixture of clino- and atacamite (green) and LS-Cu-B2 (orange). Data obtained by PhD Phillip Malcho at DTU Chemistry.

The IR features of the $Cu_2(OH)_3Cl$ minerals are divided into a hydroxyl stretching region (3500-3200 cm^{-1}), hydroxyl deformation region (1000-800 cm^{-1}) and O-Cu-O/Cl-Cu-Cl

modes found below 600 cm^{-1}.[173,175] Focus was put on the first two regions due to the limitations of the ATR-FTIR instrument. IR spectra in the range 4000-600 cm^{-1} were recorded for LS-Cu-A1, the two natural pure minerals and the synthesized mixture, Figure 110. The spectra of LS-Cu-A1 and anatacamite were very similar. The peak positions of LS-Cu-A1 are indicated with black, dashed lines. Apart from slight changes to peak positions (5 cm^{-1} or less), the only difference between LS-Cu-A1 and anatacamite was the presence of a small buried peak in the anatacamite spectrum at 3401 cm^{-1} indicated with a dashed, red line. This agreed with the observations with Raman spectroscopy by Malcherek et al.[173] but had not previously been reported for IR. Only three articles have been published on anatacamite at the time of this writing and none include IR characterization. The possibility of using ATR-FTIR to distinguish clino- and anatacamite is crucial for mineral identification of synthetic nanomaterials for which single-crystal X-ray diffraction and Raman spectroscopy are not possible. Peaks that are characteristic for atacamite are indicated with dashed, blue lines in Figure 110. These are found at 3330, 946 and 845 cm^{-1}.

Table 14. Summary of IR band positions from the present work and reported values.

1 Clino.[a]	2 Ata.[b]	3 Ana.[c]	4 Ata.[176]	5 Ata.[177]	6 Ata.[178]	7 Clino.[175]	8 Para.[179]	9 Para.[180]	10 Para.[178]
				3692					
			3458	3590	3457				
3444	3438	3443		3443	3433	3447	3445	3450	
		(3401)							3420
3359	(3357)	3355	3355	3358	3364	3360	3355		
					3349				
	3330			3335	3328			3336	3330
3310		3305	3314			3314	3315		
									3280
					3208				
987	983	984	995	986	987	988	988	988	987
					974				
	946	(951)		949	957		949		
923		922	931			920	925	920	926
(906)	914	(905)		914	912				915
(892)	891	(895)		893			896		900
863	(867)	862			864	864	865		865
	845		855	849	845		848	845	
827		825			827	828	831		
	819		819	820	819				

[a] Purified nanopowder of LS-Cu-A1. [b] Natural atacamite from the National History Museum of Denmark. [c] Natural anatacamite from the Geological Museum, University of Hamburg.

The exact peak positions in all spectra were determined by fitting the spectral sections with Gaussian functions, App. fig. 57, and summarized in Table 14. The obtained spectra of LS-Cu-A1 and natural atacamite correlates well with the reported values for clino- and

atacamite given in entry 7 and 5 of Table 14, respectively. Major discrepancies are however found in the literature. This has previously been noted[173,178] and may be explained by false identification, impure samples and inconsistent use of the mineral names. All peaks from the pure phases of clinoatacamite (LS-Cu-A1) and atacamite could be identified in the 1:2 synthesis mixture, App. fig. 57E-F.

4.2.3 Formation mechanisms

A mechanism of Cu mineral formation is discussed to explain the pH and temperature dependent behaviour. Clinoatacamite forms by $CuCl_2$ reacting with water:

$$2CuCl_2 + 3H_2O \rightleftharpoons Cu_2(OH)_3Cl + 3H^+ + 3Cl^- \quad (4.1)$$

1.5 mol H^+ is released for 1 mol Cu and the reaction occurs around neutral pH. Lowering the pH pushes the equilibrium to left and clinoatacamite dissolves in acidic media. This explains why no particles were synthesized in Cu-pH-1 to -4. Basic conditions lead to the immediate formation of copper hydroxide which consumes 2 mol OH^- per mol Cu:

$$CuCl_2 + 2OH^- \rightleftharpoons Cu(OH)_2 + 2Cl^- \quad (4.2)$$

In the hot reaction medium, copper hydroxide decomposes to CuO:

$$Cu(OH)_2 \rightleftharpoons CuO + H_2O \quad (4.3)$$

The decomposition is rapid in efficiently heated systems providing rough particles with a random crystallite assembly as was seen for the nanowhiskers formed in 20 mL samples heated from r.t. and the jagged nanoleaves prepared by the 1 L, pH 11, pre-heated synthesis. Heating the reaction mixture slowly from r.t. results in slow growth by diffusion and formation of large crystals, as seen for LS-Cu-B1. The initial formation of $Cu_2(OH)_3Cl$ lowers pH making the condition unfavourable for CuO synthesis and only about 30 wt% is formed. CuO and $Cu(OH)_2$ are in equilibrium with dissolved hydroxo species[181-183]:

$$CuO + H_2O + 2OH^- \rightleftharpoons Cu(OH)_4^{2-} \quad (4.4)$$

$$Cu(OH)_2 + 2OH^- \rightleftharpoons Cu(OH)_4^{2-} \quad (4.5)$$

These equilibria are shifted to the left under high pH conditions (≈ 11) and do not influence the product.

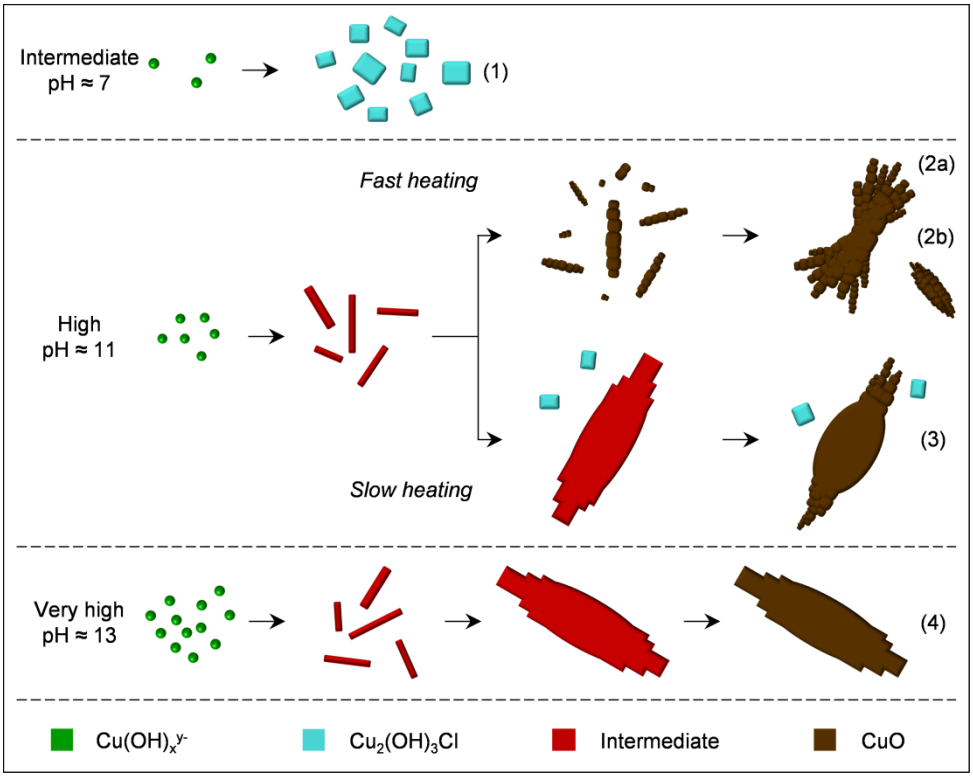

Figure 111. Schematic representation of the formation of copper minerals at different pH and temperature. (1) $Cu_2(OH)_3Cl$ (clinoatacamite), (2a) CuO from 20 mL synthesis, (2b) CuO from 1 L synthesis, (3) mixture of $Cu_2(OH)_3Cl$ and CuO from 1 L synthesis starting at r.t. and (4) CuO ribbons formed at high pH.

At very high pH (≈ 13) the equilibria shifts further to the right and play a crucial role for the morphology of the product (e.g. Cu-pH-13). The ability of high-surface area and high-energy structures to dissolve and redeposit in a more stable structure guides the morphology towards well-defined, smooth ribbons. The formation of anisotropic polycrystalline mesostructures, such as spikes (1-dimensional) and leaves (2-dimensional), relates to the process of crystallite (or nuclei) aggregation. This process is not random and often referred to as oriented attachment.[164,182-185] The assembly into mesostructures occur through attachment of two small nucleated CuO NPs via equivalent facets; (001) attach to (001), (100) to (100) and (010) to (010).[185] The relative interfacial energies of these facets control the rate at which they assemble. The most stable facet (001) grows very slowly resulting in the flat CuO mesostructures that have been observed consistently. The assembly occurs preferentially through the less stable facets (100) and (010) and is affected by temperature. The observations of the influence of pH and temperature on mineral type and morphology are summarized in Figure 111.

In conclusion, systematic investigation of the influence of initial pH was used to develop a new synthesis platform for producing phase-pure clinoatacamite ($Cu_2(OH)_3Cl$) or tenorite (CuO) simply by changing pH by. Several procedures for the synthesis of these minerals have been reported but they are time and energy consuming compared to the present work. Examples of conditions employed in clinoatacamite synthesis are autoclave or hydrothermal treatment at 200 °C[186], 180 °C for 48 h[187] and 210 °C for 2 days[174]. Similar requirements are reported for CuO synthesis where high base-to-copper ratios are used, e.g. 100 °C for 24 h with a ratio of 200 (NaOH)[181], 130 °C for 5 h[185], 200 °C for 24 h with a ratio of 100 (NaOH/KOH)[188] and 180 °C for 24 h[189]. The synthesis presented here is complete in less than 15 min at 90-95 °C. It is believed that the buffered media, which have not been used previously, maintain favourable conditions for mineral formation and lower the requirement for external energy.

Detailed characterization was needed to identify the exact polymorph of the synthesized $Cu_2(OH)_3Cl$. The combination of XRPD and ATR-FTIR was proven to be able to distinguish the closely related polymorphs anatacamite and clinoatacamite and the synthesized product was identified as the latter.

4.3 Benzyl alcohol oxidation by CuO

The presence of two relatively stable oxidation states (Cu(I) and (Cu(II)) has made Cu a element for electron transfer in nature where many redox enzymes utilize the copper chemistry, e.g. blue copper proteins and copper enzymes.[190] CuO has been recently been reported as an effective support material for noble metal catalysts in oxidation/dehydrogenation reactions but the CuO support itself was inactive.[191] Further investigations of the ability of CuO to catalyse these reactions were however suggested by PhD student Raju Poreddy from DTU Chemistry due to the advantages of non-noble metal catalysts in terms of availability and cost. As described already, specific surface structure is crucial for the activity of catalysts. The well-defined nanostructured surfaces of the CuO described in section 4.2 could potentially improve the catalytic activity relative to bulk CuO support materials and prompted these studies. The project was undertaken with Raju Poreddy with optimization of the catalyst synthesis and TEM characterization of materials carried out by me. An overview of results of this project will be presented here with focus on the catalyst synthesis and characterization.

pH 11 had been established as optimal conditions for CuO synthesis for which the MES buffer (pKa ≈ 6.15) was not the best choice. The MES buffer was therefore exchanged with *N*-cyclohexyl-3-aminopropanesulfonic acid (CAPS). The conc. of 2 mM CuO produced in the original synthesis was too low with regards to the amounts necessary for the

experimental evaluation of the catalytic properties. All conc. were therefore doubled[xi] to obtain a fabrication of 320 mg/L CuO (assuming 100 % yield). MES buffered CuO was also prepared for reference under similar conditions but at initial pH of 12 to account for the increased conc. CAPS and MES buffered CuO NP samples are referred to as A-CuO and B-CuO, respectively.

Table 15. Experimental conditions for scaling up the fabrication of CuO catalyst. Stirring was maintained in all syntheses.

Sample ID	A	B	Volume	$pH_{initial}$ [a]	Temp.	Time	Pre-heat.
A-CuO	$CuCl_2$ 4 mM	CAPS 20 mM	1 L	11	> 95 °C	30 min	≈ 50 min [b]
B-CuO	$CuCl_2$ 4 mM	MES 20 mM	1 L	12	> 95 °C	30 min	≈ 50 min [b]

[a] Buffer was dissolved in 950 mL ultrapure water and pH adjusted to ≈ 11 with KOH. [b] Pre-heating was maintained until the reaction mixture reached ≈ 95 °C, generally around 50 min.

The buffer was dissolved in 950 mL ultrapure water and adjusted to 11 (CAPS) or 12 (MES) with KOH. The buffer was pre-heated to about 95 °C before instantaneous addition of 50 mL 0.8 M $CuCl_2$. For both buffers, the solution turned dark brown within 1 second indicating rapid CuO formation. Heating was maintained for 30 min and the suspension taken off the hotplate/stirrer and allowed to cool to r.t. for several hours or overnight. After cooling, CuO had settled at the bottom. Vacuum filtration through a 0.2 µm Nylon membrane was used to isolate and wash the CuO. The supernatant above the sedimented CuO was decanted for filtration first followed by the sediment. The CuO product was washed several times with ultrapure water. Water was removed by washing with ethanol, emptying the vacuum flask and reapplying vacuum to facilitate ethanol evaporation. Finally, a brittle film of CuO NPs was easily recovered from the membrane. The powder was lightly crushed and left under vacuum overnight.

CAPS buffered medium provided flat CuO nanostructures with lengths ranging from 30 to 150 nm, Figure 112A. The structures were made up of 5-8 nm wide rods assembled side-by-side. Similar but slightly larger structures were formed in MES buffer, Figure 112B. Rietveld refined XRPD patterns afforded crystallite sizes around 18 nm for samples indicating that the crystallites are similar in CAPS and MES buffer and differences in NP size and shape relate to assembly processes during synthesis, App. fig. 58 and App. table 3.

[xi] Syntheses with 5 times the conc. used in section 4.2 and MES buffer was also carried out but led to formation of $Cu_2(OH)_3Cl$ with no detectable CuO.

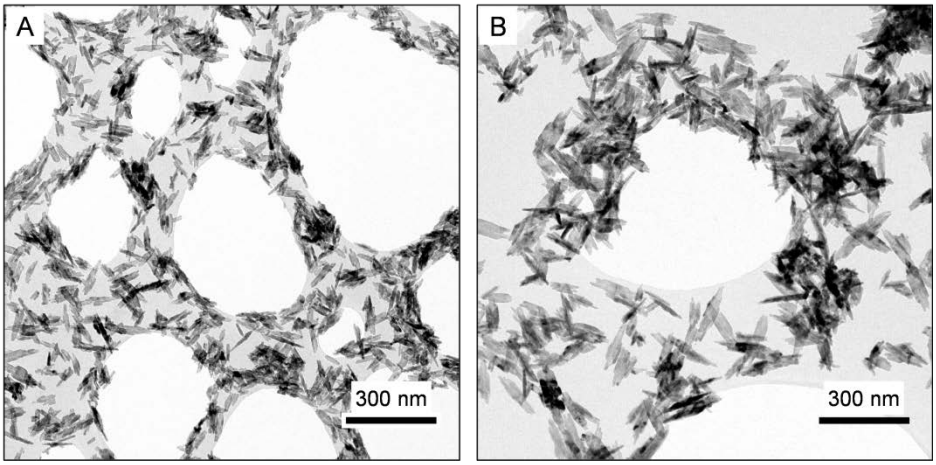

Figure 112. TEM images of as-synthesized (A) A-CuO and (B) B-CuO showing the uniform flat CuO nanostructures.

The NPs are much larger than the crystallite sizes determined by Rietveld refinement and must be poly-crystalline. HR-TEM however showed that crystal lattices seemed to extend over entire particles providing a single-crystal appearance, Figure 113 and App. fig. 59. These observations support the mechanism of growth by oriented attachment in which single crystals assemble in a controlled process and crystal facets are aligned in resulting nanostructure.

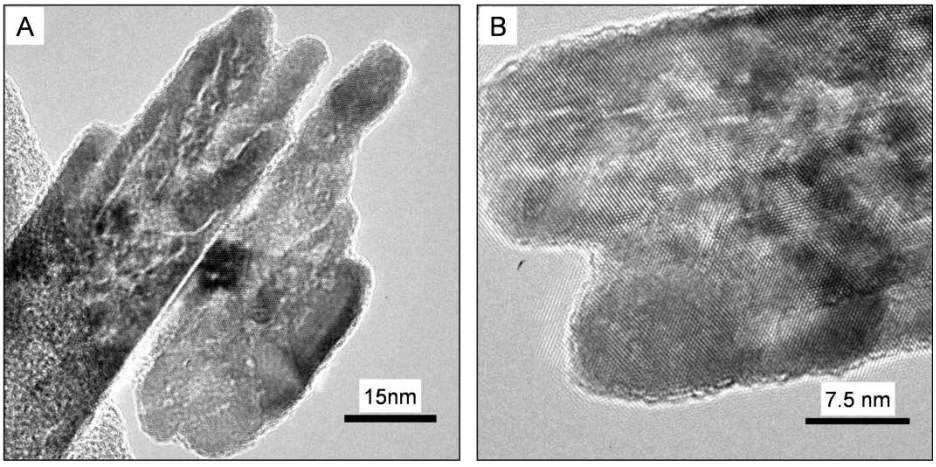

Figure 113. HR-TEM images of as-synthesized (A) A-CuO and (B) B-CuO showing continuous lattices spanning entire particles. Indexed FFTs are shown in App. fig. 59.

A- and B-CuO was tested for the catalytic conversion of benzyl alcohol to benzaldehyde, Scheme 8. In a typical experiment, 60 mg (0.75 mmol) CuO was dispersed in 3 mL toluene

by ultrasonication. 1 mmol benzyl alcohol was added and reaction carried out at 100 °C in air for 24 h.

Scheme 8. Oxidative dehydrogenation of benzyl alcohol with dioxygen.

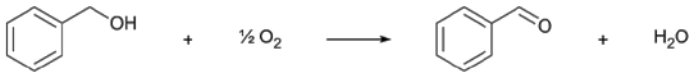

Anisole was added as internal standard for GC data evaluation. The reaction station provided heating, stirring and reflux. The conditions were optimized in terms of catalyst loading, temperature and atmosphere and the best performance was found for the conditions described above.

Table 16. Surface area and activity of nanostructured CuO catalysts.

Sample ID	S_{BET} [m^2/g]	Conversion [%] [a]	Selectivity [%]
A-CuO	46.2	> 99	> 99
B-CuO	37.4	71	> 99
C-CuO	13.1	69	91

[a] Conditions: 2 mmol benzyl alcohol, 0.2 mmol anisole, 6 mL toluene, 120 mg catalyst, 100 °C, 24 h in air.

9 different commercial and prepared copper oxides, chlorides and hydroxychlorides (CuO, Cu_2O, $Cu_2(OH)_3Cl$, $CuCl_2$ and CuCl) were tested. Most showed no to low activity but all nanostructured CuO provided high conversion in 24 h, Table 16. The conversion with these catalysts, A- and B-CuO as well as commercial CuO NPs (C-CuO), was followed by extracting samples during reaction, Figure 114.

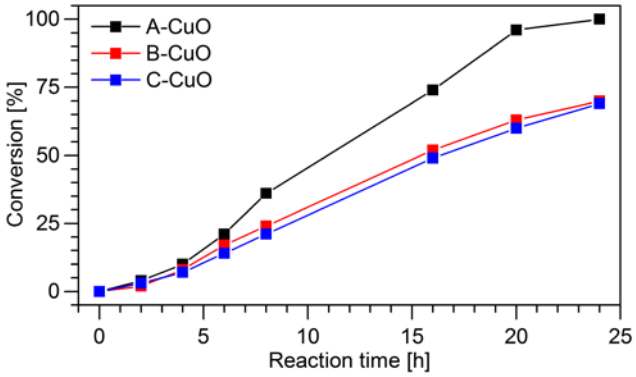

Figure 114. The time-course of benzyl alcohol conversion catalyzed by A- (black), B- (red) and C-CuO (blue). Conditions: 1 mmol benzyl alcohol, 0.1 mmol anisole, 3 mL toluene, 60 mg catalyst, 100 °C in air. Data obtained with PhD student Raju Poreddy at DTU Chemistry.

An induction period of about 4 h followed by steady conversion was observed for all catalyst. The rate of conversion was however significantly higher for A-CuO than B- and C-CuO exhibiting similar behaviour. The surface area of A-CuO is larger than that of B-CuO but even after normalizing to the surface area, conversion is about 20 % higher for A-CuO from 8 h. The structure of the catalysts after 24 h reaction was studied to clarify the differences in activity. Rietveld refined XRPD revealed that the CuO was partially reduced during reaction. 22.9 wt% Cu_2O and 1.57 wt% Cu^0 was found in spent A-CuO while B-CuO contained 77.9 wt% Cu_2O and 17.0 wt% Cu^0, App. fig. 60 and App. table 4. The reduction of the catalyst was considered in relation to the oxidation of the substrate to see if the observed conversion was a simple matter of CuO acting as a oxidizing agent. Assuming that (1) 1 electron per Cu atom is obtained to form Cu_2O and 2 for Cu^0, (2) each molecule of benzyl alcohol loses 2 electrons to form benzaldehyde and (3) molar amount of Cu is constant (0.75 mmol for 1 mmol benzaldehyde), shows that the reduced forms of copper correspond to about 11 and 43 % of the observed conversion for A- and B-CuO, respectively. Dioxygen and not CuO is therefore the reducing agent. The structures of the spent catalysts were studied with TEM.

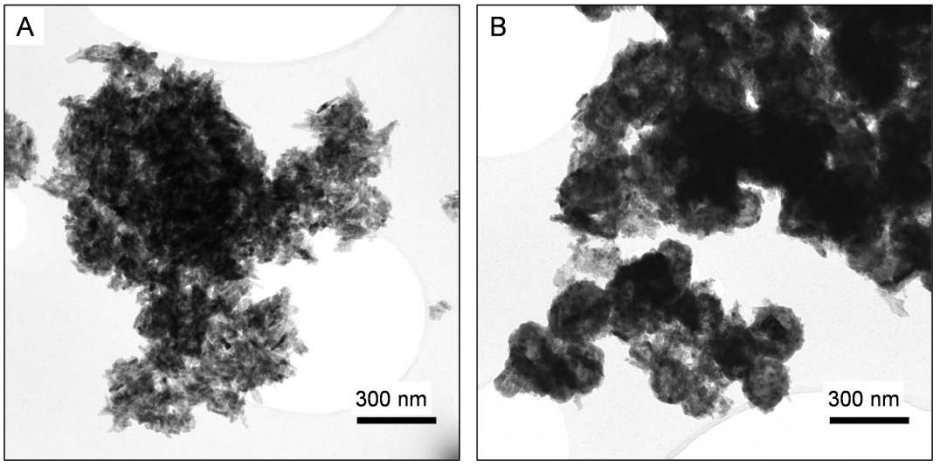

Figure 115. TEM images of spent (A) A-CuO and (B) B-CuO catalysts after 24 h reaction. Conditions: 1 mmol benzyl alcohol, 0.1 mmol anisole, 3 mL toluene, 60 mg catalyst, 100 °C in air.

The shape of the A-CuO NPs did not change significantly after 24 h reaction. The sample had aggregated and very few individual NPs were found on the TEM grid but the flat, rod-shaped structure seemed intact, Figure 115. This was not the case for B-CuO. The significant reduction of the CuO had led to a severe change in NP morphology. The sample contained mainly spherical structures with dense edges. The lower conversion relative to A-CuO may relate to instability of B-CuO as it deactivating during reaction. B-CuO was not stable under the reactions conditions and is this not a good candidate for application in this

type of system. A-CuO on the other hand showed good conversion and stability. Reusability of A-CuO was investigated by scaling up 5 times, retrieving and washing the catalyst by filtration (similar to that described in the CuO synthesis section), drying it at 120 °C, weighing it and starting a new reaction. After the second run, the conversion in 24 h started to decline and less than 10 % was found for the fourth run, Figure 116.

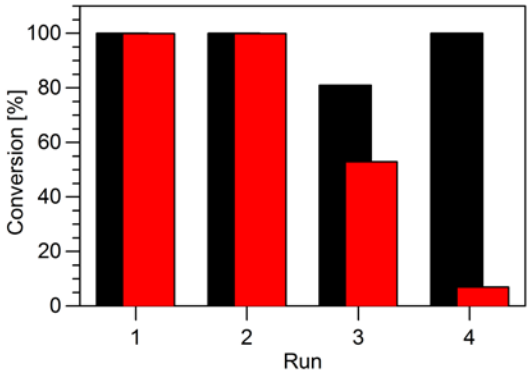

Figure 116. Reusability test of A-CuO with (black) and without (red) regeneration between runs. Concentrations of catalyst, benzyl alcohol and anisole were identical for each run and those described in Figure 114. Conditions: 24 h, 100 °C.

The catalyst after the first and fourth run was studied with TEM to find the reason for the declining activity. Unexpectedly, no apparent change to the NPs had occurred at either point in the reusability study. Well dispersed, flat, rod-like CuO NPs were observed with some aggregates, Figure 117. Under high magnification, it was very difficult to obtain atomic resolution and indications of an amorphous layer on the NPs were present.

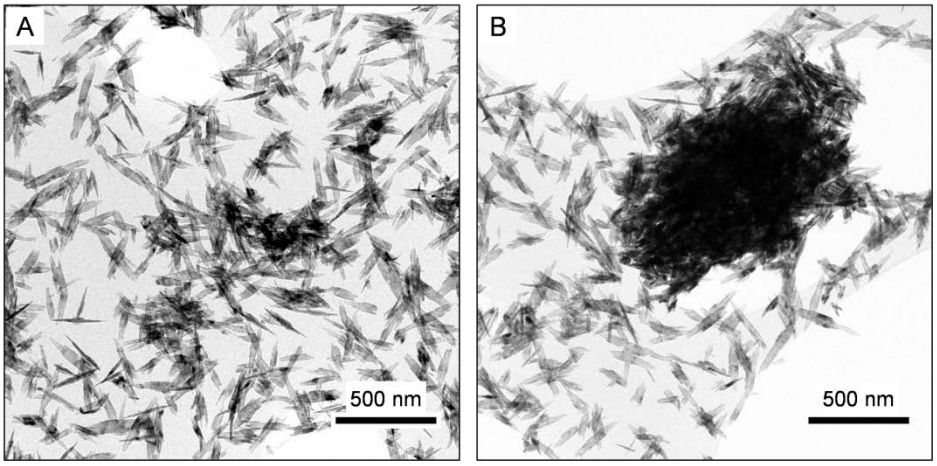

Figure 117. TEM images of catalyst after (A) first and (B) fourth run of the reusability test without regeneration.

Spent A-CuO was studied with thermogravimetric analysis and ATR-FTIR and both confirmed the presence of an organic deposited layer that could be removed at about 300 °C. A regeneration procedure was setup and a new reusability experiment carried out. Between each catalytic run, the catalyst was heated at 300 °C for 45 min in air. On the one hand, this treatment served to remove any deposited organic compounds and on the other hand, to fully re-oxidize the catalyst to CuO. The regeneration treatment significantly improved the reusability and > 99 % conversion was obtained even at the fourth recycling of the catalyst. A slightly reduced conversion was found for the third run which is believed to relate to instrumental issues.

In summary, a synthesis protocol for preparing surfactant-free, high-surface-area, uniform CuO nanostructures for application in heterogeneous catalytic oxidative dehydrogenation was developed. A range of copper-based minerals were tested and good performance was obtained with nanostructured CuO. The catalyst could be recycled and retain high activity at least 4 times by including a regeneration step between cycles. The findings hold great potential for several reasons; (1a) the use of an earth-abundant metal, (1b) noble metals are not required, (2) the synthesis method is mild, rapid and reproducible, (3) the catalyst can be reused without losing activity. One apparent drawback of this system is the large concentration of catalyst employed, i.e. 75 mol% relative to the substrate. Considering the CuO as a catalyst on the same premise as fx supported Au leads to a relatively poor specific activity of the CuO. However, if the total catalyst, support + noble metal, is considered, the CuO system can be regarded as achieving comparable performance with the support itself. In any case, catalytic oxidative dehydrogenation with the pure CuO catalyst can be expected to be significantly cheaper than with the noble metal catalyst. Further efforts to increase specific activity of the nanostructured CuO include dispersion on a cheap support.

4.4 Plasmonic photocatalysis

Energy technologies that can harvest energy directly from the sun are very appealing as solar energy is plentiful and free. Photovoltaic devices that convert sunlight to electricity have been a hot research topic for more than 30 years.[192] With major leaps in efficiency and reduction of cost, solar cells have been commercialized and are applied in widely different areas such as mobile charging devices, residential power generations and industrial power stations.

When semiconductor materials with suitable band gaps are exposed to sunlight, an electron can be excited from the valence band to the conduction band. The excited electron and the positively charges hole it left in the valence band represent charge carriers that can be utilized to do work. In solar cells, the charges are separated and passed through an external circuit to recombine generating electricity. Charge carriers can also be used to drive

chemical reactions and thus convert solar energy to chemical energy; photocatalysis. Work on improving the efficiency of photocatalytic systems is focused on many different areas, one of which is the exploitation of the entire solar spectrum. Cheap semiconductor materials like TiO_2 already harvest light in the UV range (< 400 nm) but not visible light.

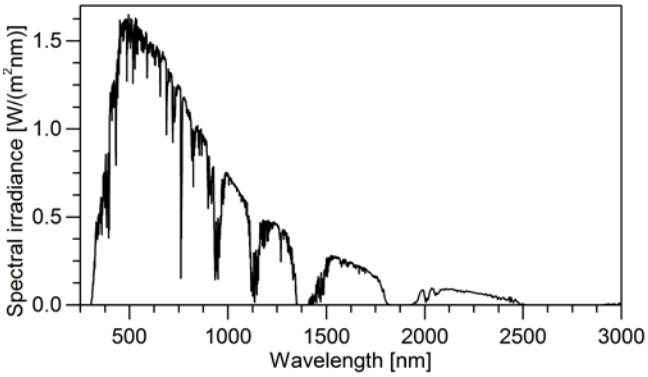

Figure 118. The solar spectral irradiance as it reaches the Earth's surface (see reference for exact conditions).[193]

It is clear from Figure 118 that the visible range, 400-800 nm, encompasses a large part of the solar energy. AuNPs interact strongly with light at these wavelengths making them a potential candidate for extending the working energy range of photocatalytic systems. The use of plasmonic materials to enhance photocatalysis started in the early 2000s, while the term *plasmonic photocatalysis* is only 6 years old.[194]

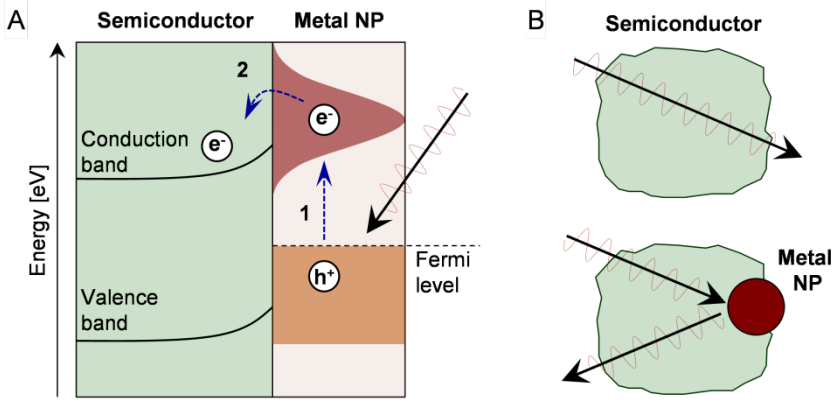

Figure 119. Mechanisms of plasmonic enhancement of photocatalysis. (A) Charge transfer from LSPR excited electrons. Electrons are first excited from the Fermi level to the LSPR state (1) followed by injection into the conduction band of the semiconductor (2). (B) Increasing the photon path through the semiconductor by scattering.[194-196]

The mechanism of catalytic enhancement of semiconductors by metal NPs is complex. The effects of the plasmonic materials relates to charge-transfer (Figure 119A), electromagnetic field enhancement and scattering (Figure 119B).[194-196] (1) The absorbance of light at the LSPR of the metal NP brings electrons to an excited state above the energy level of the conduction band of the semiconductor. The excited electrons are then injected into the conduction band leaving an electron hole in the metal. This can be filled by accepting an electron from a donor molecule in solution, or in specific cases (≈ 2 nm AuNPs) directly from water to form O_2. (2) The LSPR excited NPs generate very localized and inhomogeneous electric fields at their surface and so-called hot spots with extremely high electric field enhancements. The electron-hole generation rate in the semiconductor is proportional to the local electric field and the enhancement from the NPs increases the rate up to several orders of magnitude. The very local nature of the enhancement from the NPs has further advantages as it increases the rate of electron-hole generation mainly at the semiconductor surface where they are useful limiting the diffusion length and probability of recombination[xii]. (3) The rate of electron-hole pair generation depends on how long the path of the photon through the semiconductor is. Scattering of photons exerted by the metal NPs effectively increases the photon path length as illustrated in Figure 119B which increases efficiency. The scattering cross-section[xiii] of the metal NPs depends on size and only relatively large NPs have significant scattering cross-sections (> 20 nm for AuNPs) leading to increased performance from this effect.

The potential of the SAMENS AuNPs for plasmonic photocatalysis was investigated during a research stay at Shanghai University. A composite paste of AuNPs and TiO_2 was applied in a thin layer to titanium (Ti) sheet electrodes followed by calcination. The photocatalyst electrodes were tested for degradation of model organic compounds under different light conditions.

4.4.1 Materials preparation

The testing of the prepared AuNP/TiO_2 composite material was done under in an EC setup by application of the composite to a Ti sheet support which also functioned as an electronic contact, the photoanode. A “bare” Ti sheet was used as CE, the cathode, and a bias applied between them to drive the degradation reaction. Focus was on the utilization of visible light

[xii] Electrons and holes have a certain probability to recombe after their generation. This can be either radiatively, by light emission, or non-radiatively, by heat generation. In photovoltaics and photocatalysis, recombination is unwanted giving rise to a lowered efficiency.

[xiii] Scattering and absorption cross-sections describe the probability of a scattering or absorption event in terms of a hypothetical area. The larger the cross-sectional area, the larger the probability.

which was used exclusively for catalytic tests. The preparation of the photoelectrocatalyst required the optimization of both composite paste Ti support.

Several steps were needed to obtain the desired composite paste materials for application to the metal electrodes, Scheme 9. AuNPs were synthesized according to the standard MOS synthesis in 100 mL batches at > 85 °C in an oil bath. The next step was to remove water as the presence of water causes cracking of the catalyst layer during calcination. Initially, ethanol was used as a redispersion agent that could be easily removed again.

Scheme 9. Preparation of AuNP/TiO_2 composite by AuNP synthesis, AuNP separation and paste grinding.

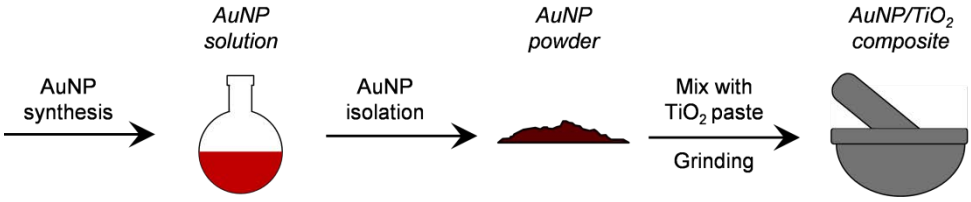

The AuNP solution was centrifuged at 15 k rpm for 20 min resulting in partial sedimentation of the particles. The supernatant still retained a strong red colour, red curve Figure 120. The sediment was efficiently redispersed in water without aggregation and with no change to the LSPR, blue curve Figure 120. This signifies that the aggregation was not irreversible and the integrity of the AuNPs was retained. However, when redispersed in ethanol, the AuNPs aggregated. Part of the sedimented macroparticles could not be redispersed.

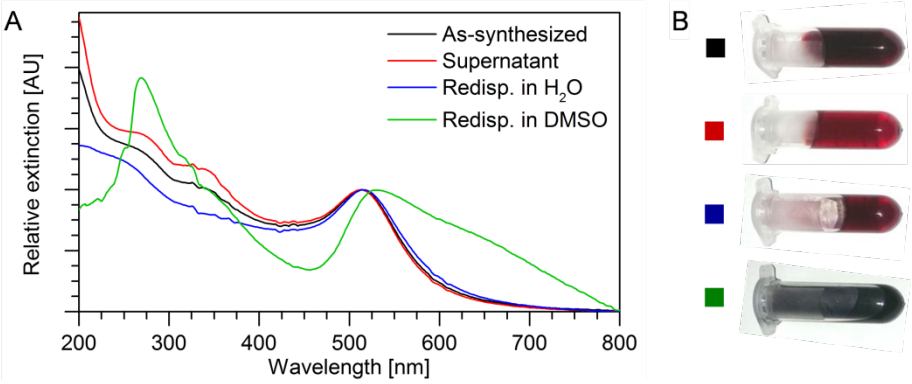

Figure 120. (A) UV-vis spectra of first test of separation by centrifugation. The LSPR of as-synthesized AuNPs (black), supernatant AuNPs (red) and AuNPs redispersed in water were almost identical. Severe aggregation was found when redispersed in DMSO (green). The spectra are normalized at the $LSPR_{max}$. (B) Photographs of the solutions used for UV-vis measurements. The colour of the square indicates the colour of the corresponding spectrum.

The key to this behaviour was identified to be the solubility of starch. The starch molecules are sufficiently solvated by water causing swelling of the coating layer around the particles by extension of the polymer chains. This is not the case for ethanol. The exchange from water to ethanol causes dehydration of the coating layer and the polymer collapses. This effectively reduces the coating layer thickness drastically and compromises the steric stabilization of the particles. The effect can be partly reversed by addition of water to again extend the polymer chains but an irreversible growth of the particles and shift of the LSPR was observed. Figure 121 shows starch dissolved at 2 wt% in ethanol and water. A milky, opaque solution was obtained with ethanol due to the high concentration of undissolved starch particles. Starch completely dissolves in water leaving a transparent solution.

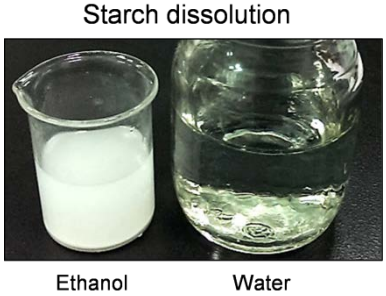

Figure 121. Photographs of starch powder dispersed in 2 wt% ethanol (left) and water (right) at r.t.

Dimethyl sulfoxide (DMSO) is known to dissolve starch completely[197] but redispersion of the centrifugate in DMSO resulted in highly aggregated AuNPs evidenced by the red-shift of the LSPR and strong extinction above 600 nm, green curve in Figure 120. Two obstacles had to be overcome to proceed further; redispersion issues and poor separation by centrifugation. The partial sedimentation of the AuNPs by centrifugation in water made it difficult to evaluate the Au amount in the sediment. UV-vis spectroscopy might be applied by comparing the extinction of the as-synthesized AuNPs and the supernatant to estimate the amount of AuNP in supernatant and sediment. However, the LSPR strongly depends on environment around the AuNPs and might change itself in the process of purification. A different approach was therefore taken. Ethanol was chosen as solvent due to the advantages of ethanol for further processing deliberately compromising the stability of the AuNPs. By forcing the AuNPs to aggregate it was possible to get much better isolation of the particles in the sediment during centrifugation. In fact, partial aggregation of particles may be helpful by extending the extinction towards the NIR and generating more hotspots for high electric field enhancements. The as-synthesized AuNP solution was mixed with ethanol in a 2:3 ratio and the AuNPs were quantitatively isolated in the sediment leaving a clear solution, App. fig. 61. The following steps only required mild centrifugation due to

the aggregated state of the AuNPs. Precise parameters are given in App. table 5. This procedure provided an efficient way to remove water and synthesis components from the AuNPs.

Next step was to set up a procedure for electrode fabrication. Ti sheet metal of different thickness was obtained to assess the optimal thickness for electrode preparation. The sheets were first cut into relevant shapes. Next, a strip of tape was placed along each long side of the Ti sheet so that the tape covered a few mm on each side. The remainder of the tape strip was used to fix the sheet to the cover underneath. The complete adherence of the tape was ensured by pressing it down with a glass rod. The glass rod was then used to apply a thin layer of TiO_2 paste to the bare area of the Ti sheet. Small amounts of TiO_2 paste was dragged carefully over the sheet by pressing the glass rod down on the tape on both sides. This ensures an even, homogenous, thin layer to be applied and the thickness is controlled by the thickness of the tape. A 0.5 mm thick Ti sheet was tested but too rigid. Bending of the sheet arose during cutting and was not possible to straighten again leading to an uneven paste layer, App. fig. 62. Instead, two thin sheets were tried; 0.1 and 0.05 mm.

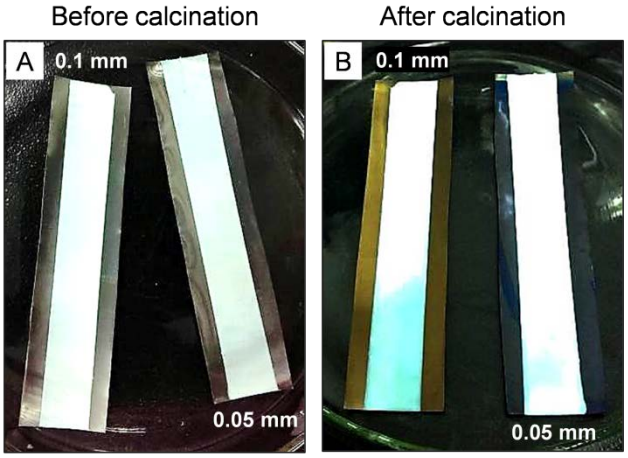

Figure 122. Photographs of 0.1 and 0.05 mm thick Ti sheets coated with TiO_2 paste (A) before and (B) after calcination at 500 °C for 30 min in air (blue colour of the paste was an artefact of the camera).

Cutting of the sheets and application of paste worked well and both Ti sheet types with paste were calcinated at 500 °C for 30 in air. This is done to remove solvent and oxidize organic constituents from the paste to gaseous components leaving a porous TiO_2 film. In both cases, a uniform film was formed. The 0.1 mm Ti had changed to a golden colour while the 0.05 had taken a slightly blue appearance arising from oxidation of the Ti surface during calcination. Submicron layers of oxidized Ti are coloured (golden to blue) and their optical properties depend on thickness and impurities.[198] The slightly more rigid 0.1 mm

sheet was easier to cut and handle than the 0.05 mm and was chosen for the preparation of composite catalysts.

4.4.2 Photoelectrode fabrication

30 electrode supports were cut from the 0.1 mm Ti sheet according to the dimensions given in Figure 123. The cut-outs were treated in a sequence of steps to clean and activate the Ti surface before paste application.

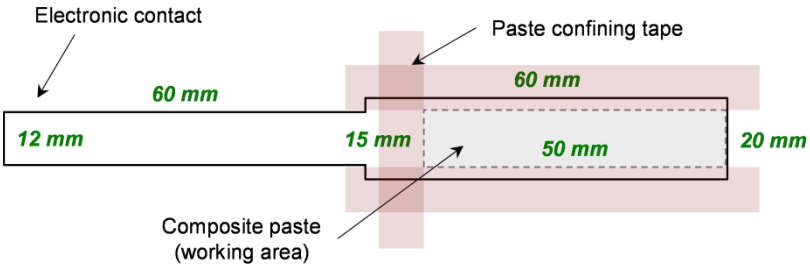

Figure 123. Sketch and dimensions of photoanode cut from 0.1 mm Ti sheet. Solid line marks the outline of the Ti strip cut-out, grey area represents the working area containing the composite catalyst and the red area indicates the placement of tape outlining the working area.

The outer layers of the Ti cut-outs were dissolved by etching in a very corrosive mixture of concentrated HF, concentrated HNO_3 and water in a ratio of 1:4:10. The metal surface reacted strongly with the mixture and rapid gas evolution was observed, Figure 124B. The acid remaining on the surface was rinsed off by dipping successively in two cups of deionized water, Figure 124C. The acid solution changed from colourless to yellow presumably caused by formation of fluorinated complexes of Ti^{4+}, Figure 124D. Simultaneously, the second deionized water washing solution became opaque and white in colour. The opacity must arise from suspended particles, most likely being TiO_2. The cleaned Ti cut-outs were dried in an oven at 500 °C for 30 min in air with a rate of 5 °C/min. The sheets became coloured ranging from purple to golden due to formation of oxide layers, Figure 124E. The cut-outs were finally treated in a boiling mixture of 1 part H_2O_2, 2 parts concentrated $NH_3 \cdot H_2O$ and 5 parts water (by volume) for >20 min, Figure 124F. This was done to increase the concentration of hydroxyl groups on the sheet surface increasing its hydrophilicity and allowing for a more intimate contact between support and catalyst layer.

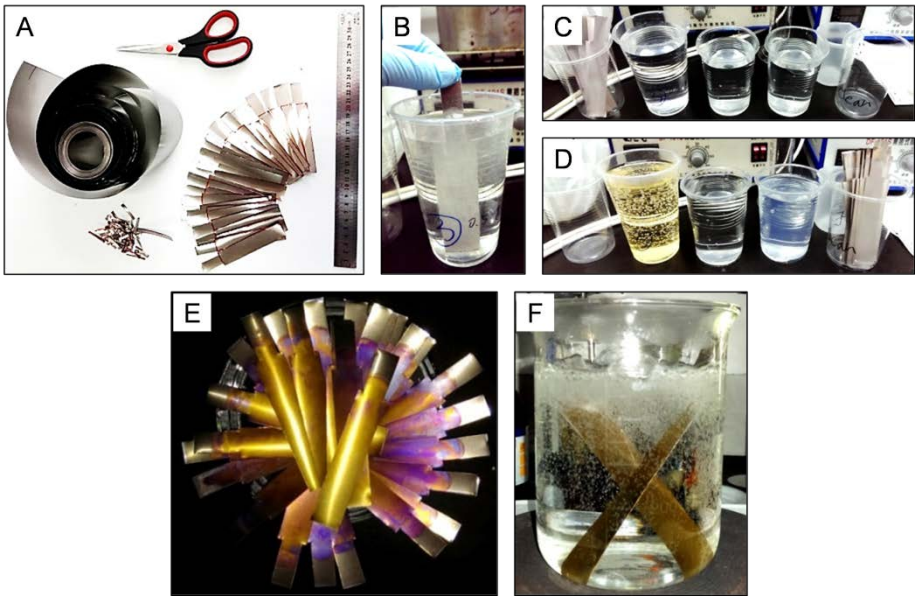

Figure 124. Fabrication and pre-treatment of Ti cut-outs for photoanodes. (A) The Ti sheet metal and cut-outs. (B) Etching of the Ti cut-outs in a 1:4:10 volume ratio mixture of conc. HF, conc. HNO_3 and water. Solutions used for etching and rinsing (C) before and (D) after treatments of 30 cut-outs showing plastic cups with untreated cut-outs, etching medium, water, water and treated cut-outs from left to right. (E) Ti cut-outs after etching and drying at 500 °C for 30 min with a heating ramp of 5 °C/min. (F) Surface activation in a 1:2:5 volume ratio H_2O_2, conc. $NH_3 \cdot H_2O$ and deionized water for > 20 min.

The commercial TiO_2 paste was purchased in 10 g bottles and a full bottle used for each batch of composite paste. A 2 wt% loading of AuNPs (relative to TiO_2) was chosen and the paste itself contained 15.5 wt% TiO_2. A total of 31.0 mg Au was required for 10 g of composite paste containing 1.55 g TiO_2. This entailed the need for 79 mL as-synthesized MOS AuNP solution.

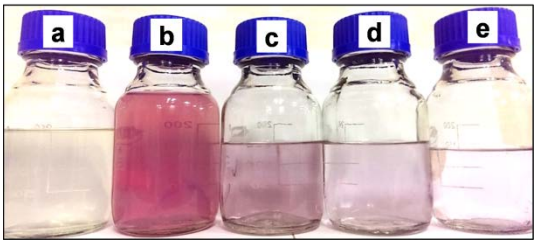

Figure 125. Photograph of supernatants obtained after step 1 to 5 of the centrifugation procedure (a-e).

A fresh batch of AuNPs was synthesized for the preparation of composite paste. According to the centrifugation procedure determined previously, 80 mL AuNP solution was mixed with 120 mL ethanol to destabilize the AuNPs. This mixture was divided into 6 plastic centrifugation tubes and centrifuged for 30 min at 12 k rpm. The supernatant could be decanted efficiently and showed no colour from AuNPs, Figure 125a. The sediments were easily redispersed and released from the tube walls in a 1:1 mixture of deionized water and ethanol. After centrifugation for 5 min at 12 k rpm, complete sedimentation was not achieved. More ethanol was added to obtain the previously used volume ratio of 2:3 (water to ethanol). Still complete sedimentation was not achieved after centrifugation for 5 min at 12 k rpm, Figure 125b. The sediments were washed totally 4 times with 2:3 (volume based) mixtures of water and ethanol to remove the inorganic components in the AuNP mixture, Figure 125c-e. Subsequently, the sediments in the 6 tubes were redispersed in small amounts of pure ethanol and collected in a single tube. The remaining 5 tubes were rinsed several times with small amounts of ethanol to efficiently transfer all the AuNPs to a single tube. The high-concentration AuNP dispersion was centrifuged for 5 min at 12k rpm. The AuNPs were washed twice with pure ethanol to remove water. Finally, the clean sediment of AuNPs was redispersed in a small volume of pure ethanol for mixing with the TiO_2 paste, Figure 126A.

Figure 126. (A) Final high concentration of AuNPs in ethanol purified by centrifugation. (B) The mixing of AuNPs and commercial TiO_2 paste by grinding. (C) The final composite paste product.

One bottle of commercial TiO_2 paste (10 g) was transferred to a mortar and the bottle rinsed with small amounts of pure ethanol to retrieve as much paste as possible. The AuNP slurry was added to the mortar and the two nanoparticle dispersions ground thoroughly for 40 min, Figure 126B. The composite paste was transferred to a glass vial, Figure 126C, and mildly dried in the oven at 50 °C for a few hours. Only minor losses were associated with the grinding process as residues on the used equipment. The first batch of composite paste is referred to as CP1. A second batch of composite paste, CP2, was prepared following the same procedure as described above but using a 2:3 volume ratio mixture of water and ethanol for the first 5 centrifugation steps (centrifugation treatment is summarized in App.

table 6). This enabled complete sedimentation and the efficient separation of the AuNP-free supernatant. This time the supernatant from the first centrifugation was strongly yellow in colour. The UV-vis spectrum is shown in Figure 127 with the spectra of the as-synthesized AuNPs and the precursor solution of $HAuCl_4$. It is clear, that the peaks do not arise from $AuCl_4^-$ remaining in solution due to incomplete reduction. Also, the peaks can be found in the as-synthesized mixture and therefore are not a product of the ethanol treatment or centrifugation. The peaks in the supernatant might relate to the unidentified UV peaks A293 and A366 described previously and are discussed in this context in section 2.5.5.

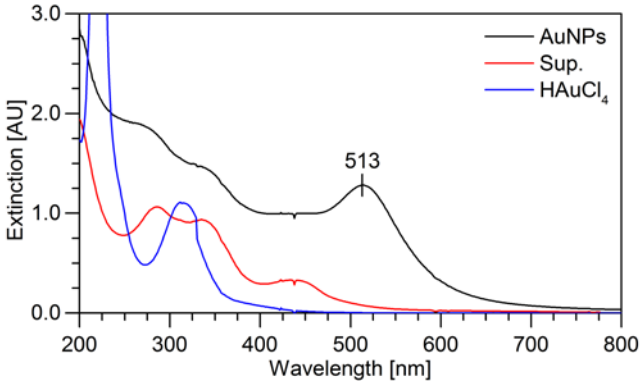

Figure 127. UV-vis spectra of as-synthesized AuNPs for CP2 (black), supernatant obtained after sedimentation with ethanol (red) and $HAuCl_4$ solution (blue).

The composite paste was applied to the cleaned and pre-treated Ti cut-outs. The table was cleaned and dried. A piece of broad transparent tape was taped on the table to provide a clean surface that the Scotch tape used to confine the working are could adhere to. Because the Ti supports were cut out of a roll of sheet metal there was a slight curvature of the width of the cut-out. The Ti support was placed with the concave side facing up. First, a piece of tape was put along one side covering a few mm of the Ti sheet and fixing it to the table. Then 1.5 cm was measured from the edge of the tape in both ends of the sheet and marked on the transparent tape. A clean glass rod was used to force down the sheet making it lie flat while a piece of tape was used to fix the other side to the table following the marks to provide a 1.5 cm gap between the tape pieces. 5 cm was measured from the broad end and marked on either side of the Ti sheet. A third piece of tape was placed across the sheet along the 5 cm markings effectively enclosing a 1.5 x 5 cm^2 working area. It was important to make sure that the tape adhered properly to the Ti cut-out all the way along the edge to avoid the paste leaking outside the enclosed area. A clean glass spatula was used to apply a small amount of composite paste to the working area and spread it to roughly cover the entire area uniformly. The paste layer was made uniform by slowly dragging a glass rod over the sheet lightly resting on the tape pieces on either side. This was repeated until a smooth uniform layer was obtained, Figure 128A.

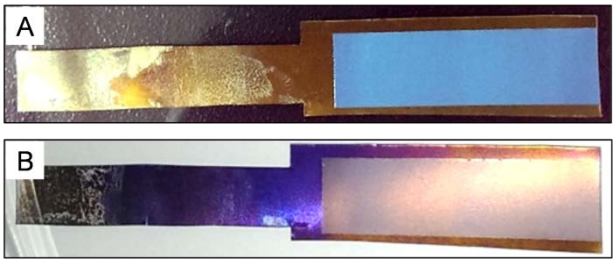

Figure 128. Photographs of composite paste (CP2) coated electrodes (A) before and (B) after calcination at 500 °C for 30 min in air with a heating ramp of 5 °C/min.

The tape was carefully removed and the electrodes calcinated at 500 °C for 30 min in air to remove all organic constituents and leave a porous layer of TiO_2 nanoparticles decorated with AuNPs. The Ti sheets changed colour from golden to purple/blue as the calcination process induced thickening of the oxide layer, Figure 128B. The first electrode (denoted CP1-1) was prepared with CP1, had a working area of 5.4 x 1.5 cm^2 and a mass increase from bare Ti sheet to finished electrode of 22.5 mg. This corresponded to a composite loading of 2.78 mg/cm^2 and a maximum Au content of 450 µg at 56 µg/cm^2 if 100 % transfer of AuNPs to the sediment during centrifugation was considered. Later, 3 electrodes were prepared with CP2. These together with 2 "bare" electrodes (no paste) were weighed before paste application and after calcination.

Table 17. Mass of applied composite paste. The mass of three electrodes with CP2 and two electrodes without paste was determined before paste application and after calcination.

Electrode ID	$m_{initial}$ [mg]	m_{final} [mg]	Δm [mg]	m_{Au} [µg]	Catalyst loading [mg/cm^2]
1-CP2	746.4	755.2	8.8	180	1.2
2-CP2	747.9	758.3	10	200	1.3
3-CP2	712.4	719.7	7.3	150	0.97
Ref1	730.3	730.9	0.6	-	-
Ref2	668.5	669.0	0.5	-	-
Average ± SD			9 ± 1	180 ± 30	1.2 ± 0.2

The bare electrodes showed an increase in mass of about 0.5 mg during calcination. Formation of oxide on the Ti sheets may account for 5-7 % of the mass increase observed for the paste electrodes. The preparation procedure provides a catalyst and Au loading of 9 ± 1 mg and 180 ± 30 µg, respectively corresponding to a catalyst loading of 1.2 ± 0.2 mg/cm^2 and a thickness variation of ± 17 % assuming constant density of the produced

catalyst layer. The preparation led to reproducible catalyst layers as seen from the mass evaluations of electrodes CP2-1 to -3. The large difference between the mass increase of CP1-1 and CP2-x however indicates that great care must be taken during paste application to ensure homogenous loadings from electrode to electrode requiring practice.

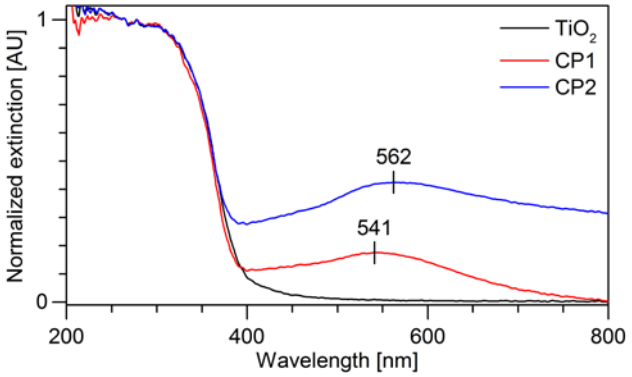

Figure 129. Solid UV-vis spectra of TiO_2 (black) and composite catalysts made from CP1 (red) and CP2 (blue) normalized around 280 nm.

The optical properties of the final catalyst were evaluated by UV-vis spectroscopy of powder made from the paste. The powder was prepared by spreading a thin layer of paste on a freshly cleaned 5 x 5 cm^2 piece of Ti sheet, running the calcination process as described above and gently scraping the dry catalyst off of the Ti sheet. The measurement had to be carried out on a densely compressed disc of powder. The volume of the holder was too large compared to the sample volumes we had available so a base of reference material ($BaSO_4$) was made and the sample compressed on top of this. The measurements were done on powder from pure TiO_2 paste, CP1 and CP2, Figure 129. As expected, the pure TiO_2 showed no interaction with visible light. This was greatly changed by the incorporation of AuNPs. Broad absorption was observed in the entire visible light spectrum with peaks at 541 and 562 nm for CP1 and CP2, respectively, corresponding to the LSPR peak of the AuNPs. The LSPR had red-shifted relative to the as-synthesized AuNPs due to aggregation which also gave rise to broad absorption of the low-energy end of the visible spectrum. This could allow for utilization of a broader spectral range and increased efficiency.

4.4.3 Photoelectrocatalytic activity tests

The performance of the composite nanostructured films was evaluated by investigating the photoelectrocatalytic degredation of two compounds commonly used in this research area, namely methylene blue (MB) and phenol shown in Scheme 10.

Scheme 10. Molecular structures of organic molecules used for degradation tests.

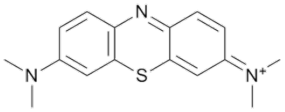

Methylene blue

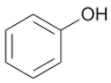

Phenol

The photoelectrodes were tested by immersion in 40 mL 6 mg/L aqueous solution of the target molecule in a quarts tube. The WE (the anode containing the composite catalyst layer) and the CE (the cathode made from a clean Ti sheet) were mounted in a rubber stopper. Two parallel slits were cut in the stopper to fix the electrodes on either side of the tube. A hole was made in the centre of the stopper to allow for sampling during the experiments and facilitate oxygen diffusion. Prior to the initiation of the degradation the electrodes are immersed in the target molecule solution, the tube fixed on top of a stirrer and the setup left for 1 h (or overnight) in the dark to allow for establishment of the adsorption/desorption equilibrium of molecules on the electrode surfaces. The light source was turned on 1 h before initiation of degradation to warm up the lamps and be at maximum intensity when the experiments were initiated. After adsorption but before starting the degradation the first sample was acquired to obtain the starting concentration of the target, defined as 0 h. The tube was then fixed inside a light-isolated box with a distance of 3 cm from the light source and the composite film facing the light. The photoelectrocatalytic test setup is shown in Figure 130.

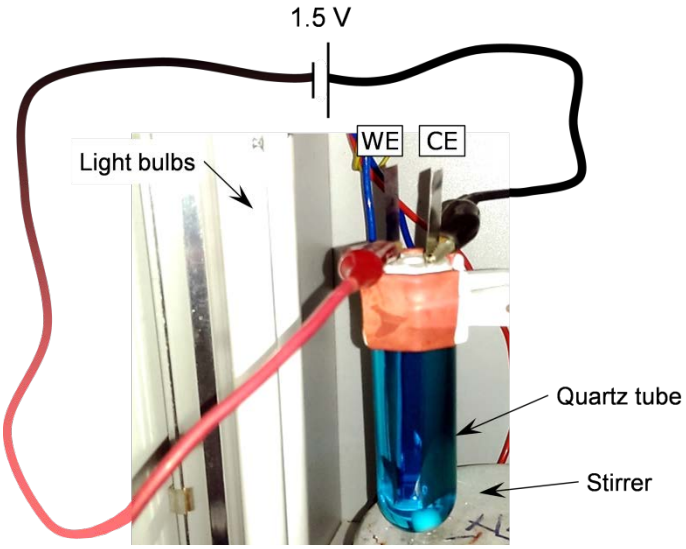

Figure 130. Photograph of the setup used to test photoelectrocatalytic activity, here for the degradation of MB. 1.5 V bias was applied between WE and CE.

During the degradation test 1.5 V bias between the electrodes was applied and the solution stirred. Every 30 min or 2 h (depending on the experiment) a small volume of sample was extracted (200 - 400 µL) and a UV-vis spectrum recorded directly. Samples taken during MB degradation however was stored in Eppendorfer tubes and kept in complete darkness for later UV-vis measurements due to technical issues with the in-house spectrometer. The apparent degradation rate constant, k_{app}, is determined from the following relation[199]:

$$\ln\left(\frac{c_0}{c_i}\right) = k_{app}\, t_i \tag{4.6}$$

where c_0 is the starting concentration, c_i the concentration at time t_i. Since absorbance is directly proportional to concentration, it can be used in the place of concentration in Eq. (4.6). Plotting $\ln(c_0/c_t)$ vs t allows for extraction of k_{app} by linear fitting. The half-time of the reaction, the time it takes obtain half the concentration, can then be calculated from[199]:

$$t_{½} = \frac{\ln(2)}{k_{app}} \tag{4.7}$$

First test of activity was done with MB and samples taken every 30 min during the degradation test. Unfortunately, no sample was acquired after equilibration of adsorption/desorption, so the starting concentration was unknown. The stock solution was used as t = 0 in Figure 131 resulting in a large initial drop comprising both the pre-adsorption and the first 30 min of degradation. MB was found to adsorb strongly on the glassware and the quartz cuvettes making it challenging to avoid carry-over during UV-vis measurements and get precise concentrations. Between 600 and 800 µL was extracted from the reaction tube for each sample to fill the UV-vis cuvette. Consequently, a significant amount of the total volume was removed during the experiment providing further issues for data analysis. Figure 131 shows the UV-vis spectra of the samples taken out during the degradation experiment. MB has several peaks both in the UV and visible region. The strongest absorbance is at 664 nm which is used for concentration evaluation. The measurement did not show a consistent decrease which suggests that the accuracy of measurement is not sufficient for this sampling rate. However, the data were treated to obtain an approximate rate constant of 0.087 h^{-1} and a half-time of roughly 8 h. The test protocol was optimized in terms of longer experiment duration, lower sampling frequency and smaller UV-vis cuvettes needing smaller volumes per measurement. Further experiments were done with phenol as the substrate to avoid problems with adsorption to the cuvette and visible light absorption by the substrate.

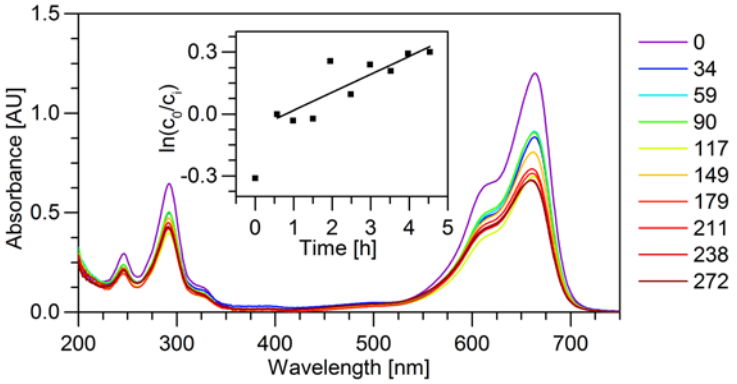

Figure 131. UV-vis spectra at different stages of MB degradation with visible light (dil: 1). Numbers in the legend refers to min after "light on". The inset shows $\ln(c_0/c_i)$ vs t. The slope of the linear fit is 0.087.

The degradation of phenol was carried out according to the previous description. Newly acquired low-volume cuvettes were used for UV-vis measurements decreasing the needed volume for each measurement to 200 µL. The sampling rate was lowered to 1 sample every 2 h and the experiment run for 10 h, App. fig. 63A. Reports in literature provided different spectra than those we could observe. It turned out that the phenol solution was able to dissolve some component used for the assembly of the cuvettes. This resulted in serious contamination of the samples with a compound that absorbs strongly at 207 and 245 nm, B, completely obscuring the signal from phenol. Another type of quartz cuvette was acquired with a less complex design but a narrow (1 mm) sample width. The thick quartz walls were transparent which allowed for a significant amount of light within the spectrometer to always be transmitted through the wall outside the narrow sample compartment. This resulted in a high baseline signal and low sensitivity. Finally, a similar design was purchased where the walls had been "blanked" by incorporation of fibers blocking light outside the sample compartment. Two new degradation experiments were carried out with 6 mg/L, one with composite paste and one with pure TiO_2. Two UV-vis spectra were recorded for each sample during the CP1 test. During the experiment it was discovered that some of the fibers of the cuvette protruded into the sample volume possibly obstructing some of the light during measurement. This was discovered after 4 h at which point the protrusions were removed and the previous samples re-measured. All individual measurements (4 for samples before 4 h and two after) are represented as circles in Figure 132A and -B. Several issues were apparent after data analysis. Firstly, the absorbance increased after the adsorption step (0 h) relative to the stock solution implying an increase in concentration. This is of course not sensible. Secondly, the re-measurements provided substantially different data than the original measurements questioning the sampling or stability during storage in the Eppendorfer tubes.

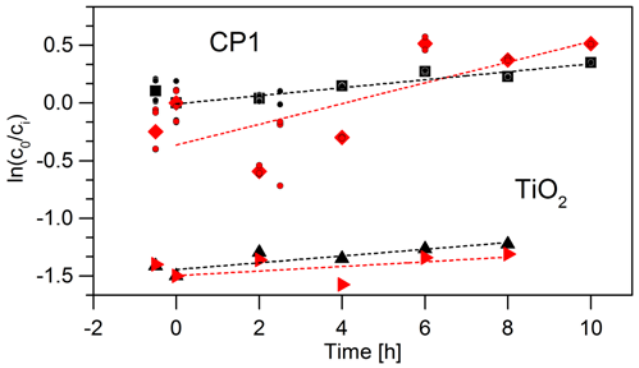

Figure 132. Evaluation of degradation kinetics of 2. phenol degradation experiment and phenol degradation by pure TiO_2 both with visible light. Data from the peaks at 210 nm (black) and 270 nm (red) were evaluated.

Lastly, there was not a very good correlation between evaluation of the absorbance at 210 and 270 nm. This is believed to result from interference by UV absorption of oxidation products of phenol. Especially, the peak at 270 nm suffers from increasing absorbance close to the peak around 240 nm. The low concentration (and thus small UV-vis signal) makes the experiment very sensitive to sampling issues and unwanted adsorption. However, a tendency seems to be present when evaluating the 210 nm data resulting in a degradation of ≈ 30 % and a rate constant, k, of 0.035. It is also observed that the concentration decreases without the presence of AuNPs but at a slightly lower rate, k = 0.029.

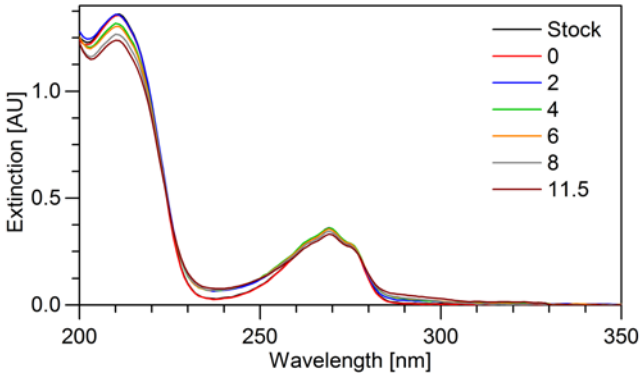

Figure 133. UV-vis spectra recorded during the 3. phenol degradation experiment with CP2, visible light and 25 mg/L phenol starting concentration (dil: 1). Numbers refer to h after “light on”.

Due to the weak UV signal for the 6 mg/L phenol concentration, 25 mg/L was used for the following tests. All spectra recorded during degradation using CP2 are shown in Figure 133. The greatly increased concentration of phenol resulted in only 9 % or 7 % degradation after 11.5 h based on absorbance at 210 and 269 nm, respectively. This low degree of

degradation was expected due to the approximately 4-fold increase in phenol concentration. However, the data seemed to be more stable due to the increased UV-vis signal. The absorbance at both 210 and 269 nm seem to show a biphasic evolution, Figure 134A. The rate constant evaluation also showed better agreement between 210 and 269 nm and a rate constant around k = 0.008, Figure 134B. However, the logarithmic plots are not linear during degradation which means that the mechanisms involved are more complex than what this method of evaluation can be used for. Fitting from 2 h gives slightly better agreement with apparent rate constants of 0.0097 and 0.0089 h^{-1} for 210 and 269 nm, respectively.

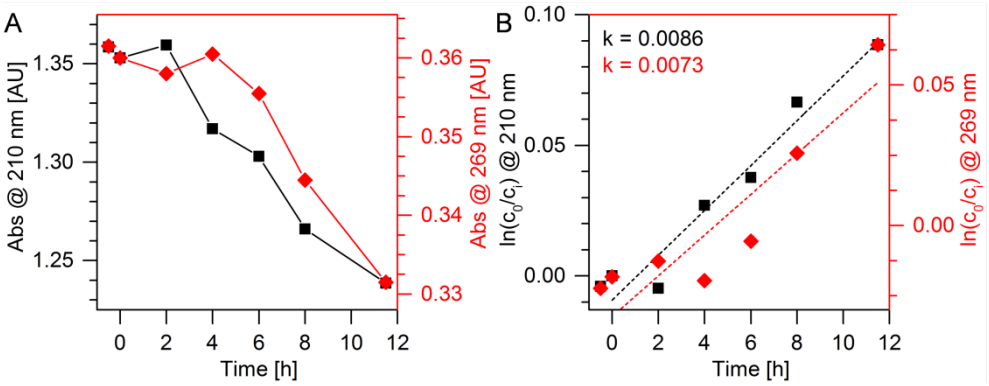

Figure 134. Kinetics information obtained from UV-vis data from the 3. phenol degradation (25 mg/L) experiment with CP2 and visible light. (A) Absorbance over time at 210 nm (black) and 269 nm (red). (B) $\ln(c_0/c_i)$ vs t at 210 nm (black) and 269 nm (red). The slopes of the linear are indicated in the figure.

Preliminary experiments for degradation of phenol (6 mg/L) were carried out in the dark giving rise to some degradation but at a much slower rate, Figure 135. However, the adsorption/desorption step was continued for about 40 h due to unforeseen circumstances, so the results can only be considered as indicative. A similar degradation rate was observed during 0.5-2 h with and without light. This was the fastest period of degradation without light but the slowest with light. The application of bias might induce additional adsorption in the beginning of the experiment. The visible light induced degradation might require an induction period explaining the observed trends. More experiments are however needed to clarify these points.

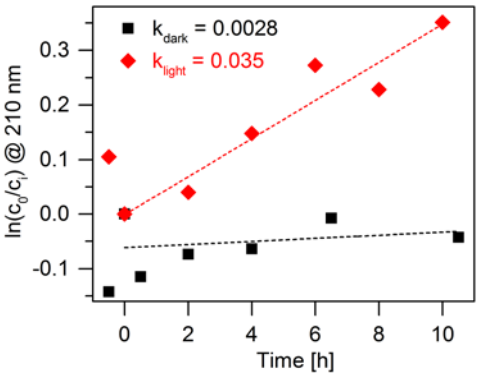

Figure 135. Comparison of phenol (6 mg/L) degradation kinetics under dark (black) and light (red) conditions.

In summary, a procedure for preparing a mixed photocatalyst paste of SAMENS AuNPs and TiO_2 and the fabrication of Ti sheet-based electrode support was attempted. The composite photocatalyst showed activity towards degradation of MB and phenol under visible light irradiation. The system was tested at both 6 and 25 mg/L phenol leading to about 30 and 9 % degradation, respectively, both corresponding to about 2 mg/L. These results indicate a better utilization of the solar spectrum relative to pure TiO_2 and are promising for enhancing the activity of TiO_2-based photoelectrocatalysts. The fabricated composite catalyst films were very stable during the experiment and no indication of detachment of catalyst or cracking of the film was observed in any experiment.

At the current stage, the system is promising but the full picture of its performance is not yet known. The results presented here are at an early stage and a number of additional experiments are required for bringing this system further, Table 18. The presence of any background degradation occurring on the calcinated oxide-containing surfaces of the must be examined.

Table 18. Future experiments for characterizing the system and evaluating performance.

Cat.	UV, Vis., Bias	To study
Calcinated support	1. **On**, **Off**, **On** 2. **Off**, **On**, **On**	Degradation by the electrode support
AuNPs	3. **Off**, **On**, **Off** 4. **Off**, **Off**, **Off**	Heterogeneous cat. by the AuNPs
TiO_2	5. **On**, **Off**, **On** 6. **On**, **On**, **On**	Baseline degradation by TiO_2
AuNPs/TiO_2	7. **On**, **Off**, **On** 8. **On**, **On**, **On**	Additional test of composite catalyst performance

The performance of the AuNPs themselves under visible light conditions and the performance of TiO_2 under UV light and UV/visible light in this system must also be evaluated to verify the individual contributions and disclose any synergetic behaviour. Finally, additional evaluation of the composite photocatalyst under UV and UV/visible light conditions is needed. The experimental procedure can be optimized by quantifying the degradation with chromatography (GC or HPLC) coupled with either an MS or UV detector. This would improve quantification of the phenol concentration limiting the interference from degradation products. It would be interesting to look closer at what happens around the beginning of the experiment, i.e. adsorption/desorption before initiation and the first 1-2 h after initiation. Especially, studying the effect on the solution concentration of applying the bias on a short time-scale may provide an understanding of the occasional and counterintuitive initial increase of the concentration.

Chapter 5

Conclusions

Many aspects of modern technology rely on precise engineering of nanomaterials. Energy technology in particular demands highly efficient catalysts for their successful implementation as viable alternatives to the fossil fuel based society. Precise structural control of nanomaterials is here crucial for catalytic efficiency. Solution synthesis of metal and mineral nanostructures was studied in detail for the control of size, shape and composition and the green synthesis of active nanomaterials for applications in catalysis. These efforts were concentrated on two main topics:

1. The study of the NP formation processes to control size and shape with gold as model system.
2. The controlled synthesis of composite nanomaterials of metals and minerals.

Many promising nanomaterials have been prepared and several tested as catalysts in relevant technology exhibiting good performance.

Control of gold nanostructure synthesis

The study of synthesis control was focused on (1) monitoring the processes involved in AuNP formation, (2) the control of AuNP size and (3) the synthesis of flat nanostructures.

The imminent need to control the structure of nanomaterials prompts the need to understand the processes of NP formation and for methods to study these. A platform for the study of SAMENS AuNP formation was developed. Widely available electrochemical and optical techniques were utilized including chronopotentiometry, time-resolved pH, conductivity and turbidity, and UV-vis spectroscopy. These sensitive methods disclosed the presence of two redox chemical phases and several distinct phases related to nucleation and growth of the AuNPs. The platform developed represents an important alternative to the typically used synchrotron spectroscopy and scattering experiments. Apart from the limited availability of synchrotrons, these techniques focus mainly on the changes to the metal. The

platform presented here provides information about redox species in solution, changes to the chemical environment in terms of pH and conductivity and the formation of NIR-active species, i.e. nuclei/NPs. Two distinct redox phases were observed strongly supporting the sequential reduction of $[AuCl_4]^-$ via intermediate $[AuCl_2]^-$. The delay of increased conductivity during the second phase indicates that chloride ions are associated with the monomers of Au^0 and released upon nucleation. Evidence for the immediate immobilization of MES and starch of the freshly formed nuclei was found in pH measurements. Capping by starch was preferred over MES leading to different pH developments after nucleation and the rapid exchange of MES by starch on the AuNP surface (≈ 10 s). Turbidity was sensitive to the formation of solid particles and the rapid response of the optical system enabled the accurate detection of nucleation. The chronopotentiometric studies were very sensitive and rich in information about the complex interplay between different redox couples and dramatic concentration variations. Strong support from theoretical descriptions of such systems is however needed to fully exploit these data.

Controlling the size of AuNPs is a powerful tool to tune their optical properties which are important in sensing and photocatalytic applications. The size of SAMENS AuNPs could be controlled in the range of 8-80 nm with a seeded growth approach. The starch capping layer allowed for diffusion of precursor/monomer and the unhindered growth of the NPs. Highly faceted decahedra and hexagons were found for size distributions above 40 nm resulting from the partial polycrystalline nature of the seed AuNPs.

Synthesizing nanostructures with particular shape can increase the concentration of active sites and enhance their specific catalytic activity. The synthesis of flat gold nanostructures was attempted for the subsequent deposition of a thin platinum layer. Two strategies for anisotropic growth were tested; controlling the rate of precursor reduction and templated growth. The best results for allowing specific adsorption of coating agents and two-dimensional growth by reducing the rate of reduction were obtained by lowering the temperature of the standard MOS to < 3 °C. High concentration of flat, rounded NPs of up to 100 nm was observed with (111) as the main facet. The main product was, however, still spherical AuNPs. The graphene oxide templated synthesis provided some exciting nanostructures. $[AuCl_4]^-$ was reduced by MES in the presence of GO at < 3 °C without using starch as stabilizer. The main product was ring-shaped, flat gold nanostructures up to 1 µm in diameter and the large sheets consistently had a hole in the middle. HR-TEM and SAED suggested that the rings were single crystalline and with (111) as main exposed facets. These structures are very promising as supports for the growth of platinum layers to produce mainly Pt(111). The GO already present in the sample can serve as a highly-conductive support, removing the need for additional steps of immobilization on a support material.

Better utilization of platinum

The very high catalytic activity of platinum makes this metal attractive in energy technology, e.g. fuel cells, but the scarcity and high cost limits the feasibility of traditional platinum-based catalysts. Efforts in the current project worked toward more efficient use of platinum by lowering the amount of inactive atoms, and thus increasing the specific catalytic activity. Two types of materials were synthesized; (1) AuPt core-shell NPs and (2) PdPt alloy NPs.

A synthesis protocol to produce 8 nm NPs with a gold core and a monolayer platinum shell in one pot was developed and the structures carefully characterized. The atomically thin shell was not detectable by microscopy but induced major changes to the electronic surface structure of the NPs. The LSPR of the AuNPs was almost completely quenched as the gold surface was disrupted by the platinum shell. EC studies proved that the surface consisted mainly of platinum but that areas of gold were still exposed. The synthesis was scaled up and the core-shell NPs loaded on graphitized carbon black support for future application as catalysts in chemical synthesis and fuel cells. Bulk platinum has effectively been avoided by the atomically thin platinum layer and high specific catalytic activity is expected.

A co-reduction synthesis based on the standard MOS conditions was set up for the preparation of alloy NPs of platinum and palladium. The 6 ± 1 nm NPs were efficiently loaded and dispersed on graphitized carbon black. The catalyst was active for formic acid and methanol oxidation, and oxygen reduction and showed good performance in real direct formic acid and methanol fuel cell systems. The fuel cell results are promising and improved specific activity is expected through optimization of the procedure of NP loading on the support, the platinum content and the elemental distribution within the NPs, e.g. and platinum shells on palladium and alloy cores.

Minerals and hybrids with metal NPs

A parallel approach to reduce the dependence on rare metals was taken by focusing on minerals of earth-abundant transition metals. The controlled synthesis of copper minerals was studied, CuO nanostructures synthesized and applied for chemical synthesis, and composite photocatalysts of gold and TiO_2 prepared and applied for catalytic degradations.

Controlled synthesis of copper minerals by precipitation in basic buffered media was developed. Phase-pure 20-50 nm single-crystal NPs of clinoatacamite $Cu_2(OH)_3Cl$ and 300 ± 70 nm long, 100 ± 20 nm wide, flat, jagged-leaf tenorite CuO were synthesized. Systematic studies of pH effects identified that $Cu_2(OH)_3Cl$ was synthesized at neutral pH

(pH > 6) while CuO was favoured in basic conditions (pH > 10). $Cu_2(OH)_3Cl$ exists in a series of closely related polymorphs. The only viable technique for complete distinction described in the literature was Raman spectroscopy, but the synthesized NPs were not stable during Raman measurements. Instead, the polymorph was successful identified using ATR-FTIR. The morphology of the synthesized CuO nanostructures changed drastically with temperature and pH due to an oriented attachment growth mechanism. The buffered reaction media improved conditions for copper mineral nanostructure formation thus lowering the requirements for reaction time, temperature and pressure. It is believed that similar approaches can be used for the synthesis of other minerals by tuning the buffer pKa to match the optimal conditions of the given system.

The synthesis of CuO nanostructures was optimized in terms of buffer pKa and reactant concentration to provide uniform flat, rod-shaped nanostructures. These were employed as heterogeneous catalysts for the oxidative dehydrogenation of alcohols to selectively obtain the corresponding aldehydes. The activity was comparable to reports on AuNPs on CuO and good recyclability observed. This system will be developed further in the future by loading on supports and a deeper investigation of the mechanisms involved in the catalyzed reaction will be undertaken.

Finally, plasmonic photocatalysis was studied during an external stay at Shanghai University. The spectral range utilized by traditional photocatalysts (TiO_2) was extended by incorporating AuNPs. Concentrated AuNP slurry was obtained through destabilization by lowering the solubility of the starch capping. The AuNP slurry was mixed with commercial TiO_2 paste by grinding and the blue/purple composite nanomaterial exhibited interaction with both UV and visible light. Preliminary photoelectrocatalytic results indicated that the composite photocatalyst was able to utilize light in the visible range to drive electrochemical degradation of the chosen model compounds. This project is at an early stage but shows already promise towards improved utilization of the solar spectrum.

Bibliography

1 M. S. Dresselhaus and I. L. Thomas, "Alternative energy technologies", *Nature*, 2001, **414,** 332-337

2 F. Raimondi, G. Scherer, R. Kotz and A. Wokaun, "Nanoparticles in energy technology: Examples from electrochemistry and catalysis", *Angewandte Chemie-International Edition*, 2005, **44,** 2190-2209

3 E. Serrano, G. Rus and J. Garcia-Martinez, "Nanotechnology for sustainable energy", *Renewable & Sustainable Energy Reviews*, 2009, **13,** 2373-2384

4 "Climate Change: Evidence & Causes" (report), *The Royal Society and National Academy of Sciences*, 2014

5 Editorial, "The science of climate change", *Science*, 2001, **292,** 1261-1261

6 P. M. Jackson and L. K. Smith, "Exploring the undulating plateau: the future of global oil supply", *Philos. Trans. R. Soc. A*, 2014, **372,** 20120491

7 I. Chapman, "The end of Peak Oil? Why this topic is still relevant despite recent denials", *Energ. Policy*, 2014, **64,** 93-101

8 D. J. Murphy, "The implications of the declining energy return on investment of oil production", *Philos. Trans. R. Soc. A*, 2014, **372,** 20130126

9 K. J. Chew, "The future of oil: unconventional fossil fuels", *Philos. Trans. R. Soc. A*, 2014, **372,** 20120324

10 I. Kubiszewski, C. J. Cleveland and P. K. Endres, "Meta-analysis of net energy return for wind power systems", *Renew. Energ.*, 2010, **35,** 218-225

11 L. Gagnon, C. Belanger and Y. Uchiyama, "Life-cycle assessment of electricity generation options: The status of research in year 2001", *Energ. Policy*, 2002, **30,** 1267-1278

12 "Data", http://data.worldbank.org/, *The World Bank*, 2014.08.04

13 J. E. Jamal, "Fire from urine: Henning Brand's search for the Philosopher's Stone", *J. Urol.*, 2008, **179,** 309-309

14 "Joseph Wright gallery | Derby Museum", http://www.derbymuseums.org/joseph-wright-gallery/, *derbymuseums.org*, 2014.07.10

15 "Tutankhamen (king of Egypt)", http://global.britannica.com/EBchecked/topic/610635/Tutankhamen, *Encyclopedia Britannica*, 2014.07.10

16 "British Museum - The Lycurgus Cup", http://www.britishmuseum.org/explore/online_tours/museum_and_exhibition/the_art_of_glass/the_lycurgus_cup.aspx, *British Museum*, 2014.07.10

17 C. Louis and O. Pluchery, *"Gold Nanoparticles in the Past: Before the Nanotechnology Era"* in Gold Nanoparticles in Physics, Chemistry and Biology, *Imperial College Press*, 2012, p. 1

18 G. Hornyak, C. Patrissi, E. Oberhauser, C. Martin, J. Valmalette, L. Lemaire, J. Dutta and H. Hofmann, "Effective medium theory characterization of Au/Ag nanoalloy porous alumina composites", *Nanostruct. Mater.*, 1997, **9,** 571-574

19 "Stherb Nano Gold Breast Series", http://www.puerariamirifica.com/pueraria-mirifica-products/nano-gold-breast-series.htm, *St.herb Cosmetics International Co., Ltd*, 2014.07.28

20 "Colloidal Gold", https://www.harmonicinnerprizes.com/products/colloidal-technology/colloidal-gold/, *Harmonic Innerprizes*, 2014.07.28

21 "Colloidal Gold", http://www.thecolloidalcompany.com/colloidalgold, *The Colloidal Company*, 2014.07.28

22 R. C. Blodgett, M. A. Heuer and R. G. Pietrusko, "Auranofin - a Unique Oral Chrysotherapeutic Agent", *Semin. Arthritis Rheum.*, 1984, **13,** 255-273

23 D. H. Brown and W. E. Smith, "The Chemistry of the Gold Drugs used in the Treatment of Rheumatoid-Arthritis", *Chem. Soc. Rev.*, 1980, **9,** 217-240

24 D. A. Giljohann, D. S. Seferos, W. L. Daniel, M. D. Massich, P. C. Patel and C. A. Mirkin, "Gold Nanoparticles for Biology and Medicine", *Angew. Chem. Int. Edit.*, 2010, **49,** 3280-3294

25 L. C. Kennedy, L. R. Bickford, N. A. Lewinski, A. J. Coughlin, Y. Hu, E. S. Day, J. L. West and R. A. Drezek, "A New Era for Cancer Treatment: Gold-Nanoparticle-Mediated Thermal Therapies", *Small*, 2011, **7,** 169-183

26 X. Li, L. Jiang, Q. Zhan, J. Qian and S. He, "Localized surface plasmon resonance (LSPR) of polyelectrolyte-functionalized gold-nanoparticles for bio-sensing", *Colloid Surf. A-Physicochem. Eng. Asp.*, 2009, **332,** 172-179

27 Y. Cheng, M. Wang, G. Borghs and H. Chen, "Gold Nanoparticle Dimers for Plasmon Sensing", *Langmuir*, 2011, **27,** 7884-7891

28 J. Ye, K. Bonroy, D. Nelis, F. Frederix, J. D'Haen, G. Maes and G. Borghs, "Enhanced localized surface plasmon resonance sensing on three-dimensional gold nanoparticles assemblies", *Colloid Surf. A-Physicochem. Eng. Asp.*, 2008, **321,** 313-317

29 M. Stratakis and H. Garcia, "Catalysis by Supported Gold Nanoparticles: Beyond Aerobic Oxidative Processes", *Chem. Rev.*, 2012, **112,** 4469-4506

30 M. S. Ide and R. J. Davis, "The Important Role of Hydroxyl on Oxidation Catalysis by Gold Nanoparticles", *Acc. Chem. Res.*, 2014, **47,** 825-833

31 M. Haruta, "Catalysis of gold nanoparticles deposited on metal oxides", *Cattech*, 2002, **6,** 102-115

32 M. Shekhar, J. Wang, W. Lee, W. D. Williams, S. M. Kim, E. A. Stach, J. T. Miller, W. N. Delgass and F. H. Ribeiro, "Size and Support Effects for the Water-Gas Shift Catalysis over Gold Nanoparticles Supported on Model Al2O3 and TiO2", *J. Am. Chem. Soc.*, 2012, **134,** 4700-4708

33 I. Laoufi, M. -. Saint-Lager, R. Lazzari, J. Jupille, O. Robach, S. Garaudee, G. Cabailh, P. Dolle, H. Cruguel and A. Bailly, "Size and Catalytic Activity of Supported Gold Nanoparticles: An in Operando Study during CO Oxidation", *J. Phys. Chem. C*, 2011, **115,** 4673-4679

34 M. Haruta, "Size- and support-dependency in the catalysis of gold", *Catal. Today*, 1997, **36,** 153-166

35 S. Panigrahi, S. Basu, S. Praharaj, S. Pande, S. Jana, A. Pal, S. K. Ghosh and T. Pal, "Synthesis and size-selective catalysis by supported gold nanoparticles: Study on heterogeneous and homogeneous catalytic process", *J. Phys. Chem. C*, 2007, **111,** 4596-4605

36 *"Abundance of Elements in the Earth's Crust and in the Sea"* in CRC Handbook of Chemistry and Physics, *Taylor and Francis*, 2014-2015, 95th Ed.p. 14-18

37 "Platinum Today: Market Data Tables", http://www.platinum.matthey.com/publications/market-data-tables, *Johnson Matthey*, 2014.07.27

38 "Gold supply and demand trends", http://goldresearcher.com/gold-supply-demand-trends/, *The Gold Researcher*, 2014.07.27

39 "China Gold Production Rises", http://www.forbes.com/sites/kenrapoza/2013/02/25/china-gold-production-rises/, *Forbes*, 2014.07.27

40 H. Renner, G. Schlamp, D. Hollmann, H. M. Lüschow, P. Tews, J. Rothaut, K. Dermann, A. Knödler, C. Hecht, M. Schlott, R. Drieselmann, C. Peter and R. Schiele, *"Gold, Gold Alloys, and Gold Compounds"* in Ullmann's Encyclopedia of Industrial Chemistry, *Wiley-VCH Verlag GmbH & Co. KGaA*, 2000,

41 W. Stange, "The process design of gold leaching and carbon-in-pulp circuits", *J. S. Afr. Inst. Min. Metall.*, 1999, **99,** 13-25

42 Editorial, "'Plenty of room' revisited", *Nat. Nanotechnol.*, 2009, **4,** 781-781

43 G. Binning, H. Rohrer, C. Gerber and E. Weibel, "Surface Studies by Scanning Tunneling Microscopy", *Phys. Rev. Lett.*, 1982, **49,** 57-61

44 "The Nobel Prize in Physics 1986", http://www.nobelprize.org/nobel_prizes/physics/laureates/1986/, *Nobel Media AB*, 2014.07.11

45 European Commission, "Commission Recommendation of 18 October 2011 on the definition of nanomaterial Text with EEA relevance", *Official Journal of the European Union*, 2011, **L 275/38,** 1-3

46 Y. Sun, "Controlled synthesis of colloidal silver nanoparticles in organic solutions: empirical rules for nucleation engineering", *Chem. Soc. Rev.*, 2013, **42,** 2497-2511

47 D. Erdemir, A. Y. Lee and A. S. Myerson, "Nucleation of Crystals from Solution: Classical and Two-Step Models", *Acc. Chem. Res.*, 2009, **42,** 621-629

48 V. K. LaMer and R. H. Dinegar, "Theory, Production and Mechanism of Formation of Monodispersed Hydrosols", *J. Am. Chem. Soc.*, 1950, **72,** 4847-4854

49 A. Weddemann, I. Ennen, A. Regtmeier, C. Albon, A. Wolff, K. Eckstaedt, N. Mill, M. K. -. Peter, J. Mattay, C. Plattner, N. Sewald and A. Huetten, "Review and outlook: from single nanoparticles to self-assembled monolayers and granular GMR sensors", *Beilstein J. Nanotechnol.*, 2010, **1,** 75-93

50 C. Destree and J. B. Nagy, "Mechanism of formation of inorganic and organic nanoparticles from microemulsions", *Adv. Colloid Interface Sci.*, 2006, **123,** 353-367

51 C. Murray, C. Kagan and M. Bawendi, "Synthesis and characterization of monodisperse nanocrystals and close-packed nanocrystal assemblies", *Annu. Rev. Mater. Sci.*, 2000, **30,** 545-610

52 B. Derjaguin and L. Landau, "Theory of the stability of strongly charged lyophobic sols and of the adhesion of strongly charged particles in solutions of electrolytes", *Prog Surf Sci*, 1993, **43,** 30-59

53 E. J. W. Verwey, "Theory of the Stability of Lyophobic Colloids.", *J. Phys. Colloid Chem.*, 1947, **51,** 631-636

54 G. Malescio, "Intermolecular potentials - past, present, future", *Nat. Mater.*, 2003, **2,** 501-503

55 S. E. Lohse and C. J. Murphy, "The Quest for Shape Control: A History of Gold Nanorod Synthesis", *Chem. Mat.*, 2013, **25,** 1250-1261

56 K. A. Willets and R. P. Van Duyne, "Localized surface plasmon resonance spectroscopy and sensing", *Annu. Rev. Phys. Chem.*, 2007, **58,** 267-297

57 "Technology: Nanosight", http://www.nanosight.com/technology, *Nanosight*, 2014.06.20

58 V. Filipe, A. Hawe and W. Jiskoot, "Critical Evaluation of Nanoparticle Tracking Analysis (NTA) by NanoSight for the Measurement of Nanoparticles and Protein Aggregates", *Pharm. Res.*, 2010, **27,** 796-810

59 "Introduction to electron microscopy", http://advanced-microscopy.utah.edu/education/electron-micro/, *The University of Utah*, 2014.09.04

60 C. A. Schneider, W. S. Rasband and K. W. Eliceiri, "NIH Image to ImageJ: 25 years of image analysis", *Nat. Methods*, 2012, **9,** 671-675

61 "XAFS Data Library", http://cars.uchicago.edu/~newville/ModelLib/search.html, *Center for Advanced Radiation Sources*, 2014.09/09

62 J. Turkevich, P. C. Stevenson and J. Hillier, "A study of the nucleation and growth processes in the synthesis of colloidal gold", *Discuss. Faraday Soc.*, 1951, **11,** 55

63 M. Watzky and R. Finke, "Transition metal nanocluster formation kinetic and mechanistic studies. A new mechanism when hydrogen is the reductant: Slow, continuous nucleation and fast autocatalytic surface growth", *J. Am. Chem. Soc.*, 1997, **119,** 10382-10400

64 E. E. Finney and R. G. Finke, "Nanocluster nucleation and growth kinetic and mechanistic studies: A review emphasizing transition-metal nanoclusters", *J. Colloid Interface Sci.*, 2008, **317,** 351-374

65 B. Pong, H. I. Elim, J. Chong, W. Ji, B. L. Trout and J. Lee, "New insights on the nanoparticle growth mechanism in the citrate reduction of Gold(III) salt: Formation of the au nanowire intermediate and its nonlinear optical properties", *J. Phys. Chem. C*, 2007, **111,** 6281-6287

66 X. Ji, X. Song, J. Li, Y. Bai, W. Yang and X. Peng, "Size control of gold nanocrystals in citrate reduction: The third role of citrate", *J. Am. Chem. Soc.*, 2007, **129,** 13939-13948

67 B. Abecassis, F. Testard, O. Spalla and P. Barboux, "Probing in situ the nucleation and growth of gold nanoparticles by small-angle x-ray scattering", *Nano Lett.*, 2007, **7,** 1723-1727

68 B. Abecassis, F. Testard, Q. Kong, B. Francois and O. Spalla, "Influence of Monomer Feeding on a Fast Cold Nanoparticles Synthesis: Time-Resolved XANES and SAXS Experiments", *Langmuir*, 2010, **26,** 13847-13854

69 J. Polte, T. T. Ahner, F. Delissen, S. Sokolov, F. Emmerling, A. F. Thuenemann and R. Kraehnert, "Mechanism of Gold Nanoparticle Formation in the Classical Citrate Synthesis Method Derived from Coupled In Situ XANES and SAXS Evaluation", *J. Am. Chem. Soc.*, 2010, **132,** 1296-1301

70 J. G. Parsons, V. Armendariz, M. L. Lopez, M. Jose-Yacaman and J. L. Gardea-Torresdey, "Kinetics and thermodynamics of the bioreduction of potassium tetrachloroaurate using inactivated oat and wheat tissues", *J. Nanopart. Res.*, 2010, **12,** 1579-1588

71 J. Polte, R. Erler, A. F. Thuenemann, S. Sokolov, T. T. Ahner, K. Rademann, F. Emmerling and R. Kraehnert, "Nucleation and Growth of Gold Nanoparticles Studied via in situ Small Angle X-ray Scattering at Millisecond Time Resolution", *ACS Nano*, 2010, **4,** 1076-1082

72 Y. Fong, B. R. Visser, J. R. Gascooke, B. C. C. Cowie, L. Thomsen, G. F. Metha, M. A. Buntine and H. H. Harris, "Photoreduction Kinetics of Sodium Tetrachloroaurate under Synchrotron Soft X-ray Exposure", *Langmuir,* 2011, **27,** 8099-8104

73 T. Tanaka, J. Ohyama, K. Teramura and Y. Hitomi, "Formation mechanism of metal nanoparticles studied by XAFS spectroscopy and effective synthesis of small metal nanoparticles", *Catal. Today,* 2012, **183,** 108-118

74 J. Ma, Y. Zou, Z. Jiang, W. Huang, J. Li, G. Wu, Y. Huang and H. Xu, "An in situ XAFS study-the formation mechanism of gold nanoparticles from X-ray-irradiated ionic liquid", *Phys. Chem. Chem. Phys.,* 2013, **15,** 11904-11908

75 M. A. Uppal, A. Kafizas, M. B. Ewing and I. P. Parkin, "The room temperature formation of gold nanoparticles from the reaction of cyclohexanone and auric acid; a transition from dendritic particles to compact shapes and nanoplates", *J. Mater. Chem. A,* 2013, **1,** 7351-7359

76 C. Engelbrekt, P. S. Jensen, K. H. Sorensen, J. Ulstrup and J. Zhang, "Complexity of gold nanoparticle formation disclosed by dynamics study", *J. Phys. Chem. C,* 2013, **117,** 11818-11828

77 "Lightsources of the world", http://www.lightsources.org/regions, *Lightsources.org,* 2014.08/24

78 Y. Xia, Y. Xiong, B. Lim and S. E. Skrabalak, "Shape-Controlled Synthesis of Metal Nanocrystals: Simple Chemistry Meets Complex Physics?", *Angew. Chem. Int. Edit.,* 2009, **48,** 60-103

79 C. Engelbrekt, K. H. Sorensen, J. Zhang, A. C. Welinder, P. S. Jensen and J. Ulstrup, "Green synthesis of gold nanoparticles with starch-glucose and application in bioelectrochemistry", *J. Mater. Chem.,* 2009, **19,** 7839-7847

80 B. Liu, J. Xie, J. Y. Lee, Y. P. Ting and J. P. Chen, "Optimization of High-Yield Biological Synthesis of Single-Crystalline Gold Nanoplates", *J. Phys. Chem. B,* 2005, **109,** 15256-15263

81 P. Sen, A. Bilkis and K. Sen Gupta, "Kinetics and mechanism of the oxidation of glycolaldehyde by tetrachloroaurate(III)", *Int. J. Chem. Kinet.,* 1998, **30,** 613-619

82 V. Soni and R. N. Mehrotra, "Mechanism of the oxidation of hydrazoic acid by tetrachloroaurate(III) ion", *Transition Met. Chem.,* 2008, **33,** 367-376

83 F. H. Fry, G. A. Hamilton and J. Turkevich, "The Kinetics and Mechanism of Hydrolysis of Tetrachloroaurate(III)", *Inorg. Chem.,* 1966, **5,** 1943-1946

84 V. Soni, R. S. Sindal and R. N. Mehrotra, "Kinetics and mechanism of the oxidation of oxalic acid by tetrachloroaurate(III) ion", *Inorg. Chim. Acta,* 2007, **360,** 3141-3148

85 J. J. Lingane, "Standard potentials of half-reactions involving + 1 and + 3 gold in chloride medium", *J. Electroanal. Chem. (1959),* 1962, **4,** 332-342

86 J. J. Lingane, "Coulometric titration of gold with electrogenerated chloro-cuprous ion", *Anal. Chim. Acta,* 1958, **19,** 394-401

87 C. H. Gammons, Y. Yu and A. E. Williams-Jones, "The disproportionation of gold(I) chloride complexes at 25 to 200°C", *Geochim. Cosmochim. Acta,* 1997, **61,** 1971-1983

88 X. Zhou, W. Xu, G. Liu, D. Panda and P. Chen, "Size-Dependent Catalytic Activity and Dynamics of Gold Nanoparticles at the Single-Molecule Level", *J. Am. Chem. Soc.,* 2010, **132,** 138-146

89 T. V. W. Janssens, B. S. Clausen, B. Hvolbaek, H. Falsig, C. H. Christensen, T. Bligaard and J. K. Norskov, "Insights into the reactivity of supported Au nanoparticles: combining theory and experiments", *Top. Catal.,* 2007, **44,** 15-26

90 R. Fenger, E. Fertitta, H. Kirmse, A. F. Thuenemann and K. Rademann, "Size dependent catalysis with CTAB-stabilized gold nanoparticles", *Phys. Chem. Chem. Phys.,* 2012, **14,** 9343-9349

91 Kate Y. J. Lee. , "Colloidal gold nanoparticles for cancer therapy: Effects of particle size on treatment efficacy, toxicology, and biodistribution" (Ph.D. thesis), *Georgia Institute of Technology,* 2011

92 S. Hirn, M. Semmler-Behnke, C. Schleh, A. Wenk, J. Lipka, M. Schäffler, S. Takenaka, W. Möller, G. Schmid, U. Simon and W. G. Kreyling, "Particle size-dependent and surface charge-dependent biodistribution of gold nanoparticles after intravenous administration", *Eur. J. Pharm. Biopharm.,* 2011, **77,** 407-416

93 N. G. Bastus, J. Comenge and V. Puntes, "Kinetically Controlled Seeded Growth Synthesis of Citrate-Stabilized Gold Nanoparticles of up to 200 nm: Size Focusing versus Ostwald Ripening", *Langmuir,* 2011, **27,** 11098-11105

94 "Gaussian Function", http://mathworld.wolfram.com/GaussianFunction.html, *Wolfram MathWorld,* 2014.06.20

95 I. Pastoriza-Santos and L. M. Liz-Marzan, "Synthesis of silver nanoprisms in DMF", *Nano Lett.,* 2002, **2,** 903-905

96 J. Lee, K. Kamada, N. Enomoto and J. Hojo, "Polyhedral gold nanoplate: High fraction synthesis of two-dimensional nanoparticles through rapid heating process", *Cryst. Growth Des.,* 2008, **8,** 2638-2645

97 C. Lofton and W. Sigmund, "Mechanisms controlling crystal habits of gold and silver colloids", *Adv. Funct. Mater.,* 2005, **15,** 1197-1208

98 A. Sanchez-Iglesias, I. Pastoriza-Santos, J. Perez-Juste, B. Rodriguez-Gonzalez, F. J. Garcia de Abajo and L. M. Liz-Marzan, "Synthesis and optical properties of gold nanodecahedra with size control", *Adv. Mater.,* 2006, **18,** 2529-+

99 M. Shekhar, J. Wang, W. Lee, W. D. Williams, S. M. Kim, E. A. Stach, J. T. Miller, W. N. Delgass and F. H. Ribeiro, "Size and Support Effects for the Water-Gas Shift

Catalysis over Gold Nanoparticles Supported on Model Al2O3 and TiO2", *J. Am. Chem. Soc.*, 2012, **134,** 4700-4708

100 S. H. Brodersen, U. Gronbjerg, B. Hvolbaek and J. Schiotz, "Understanding the catalytic activity of gold nanoparticles through multi-scale simulations", *J. Catal.*, 2011, **284,** 34-41

101 Y. Ding, Y. J. Kim and J. Erlebacher, "Nanoporous gold leaf: "Ancient technology"/advanced material", *Adv. Mater.*, 2004, **16,** 1897-1900

102 T. Fujita, P. Guan, K. McKenna, X. Lang, A. Hirata, L. Zhang, T. Tokunaga, S. Arai, Y. Yamamoto, N. Tanaka, Y. Ishikawa, N. Asao, Y. Yamamoto, J. Erlebacher and M. Chen, "Atomic origins of the high catalytic activity of nanoporous gold", *Nat. Mater.*, 2012, **11,** 775-780

103 Y. Ishikawa, Y. Yamamoto and N. Asao, "Selective hydrosilylation of alkynes with a nanoporous gold catalyst", *Catal. Sci. Technol.*, 2013, **3,** 2902-2905

104 I. E. L. Stephens, A. S. Bondarenko, U. Gronbjerg, J. Rossmeisl and I. Chorkendorff, "Understanding the electrocatalysis of oxygen reduction on platinum and its alloys", *Energ. Environ. Sci.*, 2012, **5,** 6744-6762

105 I. E. L. Stephens, A. S. Bondarenko, F. J. Perez-Alonso, F. Calle-Vallejo, L. Bech, T. P. Johansson, A. K. Jepsen, R. Frydendal, B. P. Knudsen, J. Rossmeisl and I. Chorkendorff, "Tuning the Activity of Pt(111) for Oxygen Electroreduction by Subsurface Alloying", *J. Am. Chem. Soc.*, 2011, **133,** 5485-5491

106 R. Sitko, E. Turek, B. Zawisza, E. Malicka, E. Talik, J. Heimann, A. Gagor, B. Feist and R. Wrzalik, "Adsorption of divalent metal ions from aqueous solutions using graphene oxide", *Dalton Trans.*, 2013, **42,** 5682-5689

107 B. Yu, J. Xu, J. Liu, S. Yang, J. Luo, Q. Zhou, J. Wan, R. Liao, H. Wang and Y. Liu, "Adsorption behavior of copper ions on graphene oxide–chitosan aerogel", *J. Environ. Chem. Eng.*, 2013, **1,** 1044-1050

108 S. Gan, L. Zhong, T. Wu, D. Han, J. Zhang, J. Ulstrup, Q. Chi and L. Niu, "Spontaneous and Fast Growth of Large-Area Graphene Nanofilms Facilitated by Oil/Water Interfaces", *Adv Mater*, 2012, **24,** 3958-3964

109 M. Hu, J. Chen, Z. Li, L. Au, G. V. Hartland, X. Li, M. Marquez and Y. Xia, "Gold nanostructures: engineering their plasmonic properties for biomedical applications", *Chem. Soc. Rev.*, 2006, **35,** 1084-1094

110 Y. Zhang, H. Ma, Q. Zhang, J. Peng, J. Li, M. Zhai and Z. Yu, "Facile synthesis of well-dispersed graphene by gamma-ray induced reduction of graphene oxide", *J. Mater. Chem.*, 2012, **22,** 13064-13069

111 H. Zhou, X. Wang, P. Yu, X. Chen and L. Mao, "Sensitive and selective voltammetric measurement of Hg2+ by rational covalent functionalization of graphene oxide with cysteamine", *Analyst*, 2012, **137,** 305-308

112 B. Li, X. Zhang, P. Chen, X. Li, L. Wang, C. Zhang, W. Zheng and Y. Liu, "Waveband-dependent photochemical processing of graphene oxide in fabricating reduced graphene oxide film and graphene oxide-Ag nanoparticles film", *RSC Adv.*, 2014, **4,** 2404-2408

113 D. Lee, R. Donkers, G. Wang, A. Harper and R. Murray, "Electrochemistry and optical absorbance and luminescence of molecule-like Au-38 nanoparticles", *J. Am. Chem. Soc.*, 2004, **126,** 6193-6199

114 J. Zheng, P. R. Nicovich and R. M. Dickson, "Highly fluorescent noble-metal quantum dots", *Annu. Rev. Phys. Chem.*, 2007, **58,** 409-431

115 E. M. Goldys and M. A. Sobhan, "Fluorescence of Colloidal Gold Nanoparticles is Controlled by the Surface Adsorbate", *Adv. Funct. Mater.*, 2012, **22,** 1906-1913

116 Y. Bao, H. Yeh, C. Zhong, S. A. Ivanov, J. K. Sharma, M. L. Neidig, D. M. Vu, A. P. Shreve, R. B. Dyer, J. H. Werner and J. S. Martinez, "Formation and Stabilization of Fluorescent Gold Nanoclusters Using Small Molecules", *J. Phys. Chem. C*, 2010, **114,** 15879-15882

117 Z. Wang, Q. Zhang, D. Kuehner, A. Ivaska and L. Niu, "Green synthesis of 1-2 nm gold nanoparticles stabilized by amine-terminated ionic liquid and their electrocatalytic activity in oxygen reduction", *Green Chem.*, 2008, **10,** 907-909

118 P. Hernandez-Fernandez, F. Masini, D. N. McCarthy, C. E. Strebel, D. Friebel, D. Deiana, P. Malacrida, A. Nierhoff, A. Bodin, A. M. Wise, J. H. Nielsen, T. W. Hansen, A. Nilsson, I. E. Stephens and I. Chorkendorff, "Mass-selected nanoparticles of PtxY as model catalysts for oxygen electroreduction", *Nat. Chem.*, 2014, **6,** 732-738

119 P. Enghag, , *"Platinum Group Metals"* in Encyclopedia of the Elements, *Wiley-VCH Verlag GmbH & Co. KGaA*, 2007, p. 707

120 "Platinum mining in South Africa", http://www.projectsiq.co.za/platinum-mining-in-south-africa.htm, *Mining Intelligence Database*, 2014.08/01

121 "Platinum Today: Price charts", http://www.platinum.matthey.com/prices/price-charts, *Johnson Matthey*, 2014.06.20

122 M. E. Straumanis, "Neubestimmung der Gitterparameter, Dichten und thermischen Ausdehnungskoeffizienten von Silber und Gold, und Vollkommenheit der Struktur", *Monatshefte Für Chemie / Chemical Monthly*, 1971, **102,** 1377-1386

123 J. W. Edwards, R. Speiser and H. L. Johnston, "High Temperature Structure and Thermal Expansion of Some Metals as Determined by X-Ray Diffraction Data. I. Platinum, Tantalum, Niobium, and Molybdenum", *J. Appl. Phys.*, 1951, **22,** 424

124 Y. Xu, Y. Dong, J. Shi, M. Xu, Z. Zhang and X. Yang, "Au@Pt core-shell nanoparticles supported on multiwalled carbon nanotubes for methanol oxidation", *Catal. Commun.*, 2011, **13,** 54-58

125 L. Qian, Y. Sha and X. Yang, "Simple and convenient preparation of Au–Pt core-shell nanoparticles on surface via a seed growth method", *Thin Solid Films*, 2006, **515,** 1349-1353

126 S. Xiao, W. Hu, W. Luo, Y. Wu, X. Li and H. Deng, "Size effect on alloying ability and phase stability of immiscible bimetallic nanoparticles", *Eur. Phys. J. B*, 2006, **54,** 479-484

127 B. N. Wanjala, J. Luo, B. Fang, D. Mott and C. Zhong, "Gold-platinum nanoparticles: alloying and phase segregation", *J. Mater. Chem.*, 2011, **21,** 4012-4020

128 N. Braidy, G. R. Purdy and G. A. Botton, "Equilibrium and stability of phase-separating Au–Pt nanoparticles", *Acta Mater.*, 2008, **56,** 5972-5983

129 C. J. Serpell, J. Cookson, D. Ozkaya and P. D. Beer, "Core@shell bimetallic nanoparticle synthesis via anion coordination", *Nat. Chem.*, 2011, **3,** 478-483

130 J. Zhai, M. Huang and S. Dong, "Electrochemical Designing of Au/Pt Core Shell Nanoparticles as Nanostructured Catalyst with Tunable Activity for Oxygen Reduction", *Electroanal.*, 2007, **19,** 506-509

131 L. N. Cleemann, F. Buazar, Q. Li, J. O. Jensen, C. Pan, T. Steenberg, S. Dai and N. J. Bjerrum, "Catalyst Degradation in High Temperature Proton Exchange Membrane Fuel Cells Based on Acid Doped Polybenzimidazole Membranes", *Fuel Cells*, 2013, **13,** 822-831

132 P. Atkins and J. Paula, "Atkins' Physical Chemistry", *Oxford University Press*, Oxford, **7th Ed.,** 2002

133 "Lattice constants for all the elements in the periodic table", http://periodictable.com/ Properties/A/LatticeConstants.html, *Element Collection, Inc.*, 2014.06.22

134 V. Ritleng, C. Sirlin and M. Pfeffer, "Ru-, Rh-, and Pd-catalyzed C-C bond formation involving C-H activation and addition on unsaturated substrates: Reactions and mechanistic aspects", *Chem. Rev.*, 2002, **102,** 1731-1769

135 I. Beletskaya and A. Cheprakov, "The heck reaction as a sharpening stone of palladium catalysis", *Chem. Rev.*, 2000, **100,** 3009-3066

136 S. Johansson, C. C. Carin, M. O. Kitching, T. J. Colacot and V. Snieckus, "Palladium-Catalyzed Cross-Coupling: A Historical Contextual Perspective to the 2010 Nobel Prize", *Angew. Chem. Int. Edit.*, 2012, **51,** 5062-5085

137 D. Astruc, F. Lu and J. Aranzaes, "Nanoparticles as recyclable catalysts: The frontier between homogeneous and heterogeneous catalysis", *Angew. Chem. Int. Edit.*, 2005, **44,** 7852-7872

138 J. K. Nørskov, J. Rossmeisl, L. Lindqvist, J. R. Kitchin, T. Bligaard and H. Jónsson, "Origin of the overpotential for oxygen reduction at a fuel-cell cathode", *J. Phys. Chem. B*, 2004, **108,** 17886-17892

139 Nguyen Viet Long, Cao Minh Thi, Y. Yong, M. Nogami and M. Ohtaki, "Platinum and Palladium Nano-Structured Catalysts for Polymer Electrolyte Fuel Cells and Direct Methanol Fuel Cells", *J. Nanosci. Nanotechnol.*, 2013, **13,** 4799-4824

140 E. Antolini, "Palladium in fuel cell catalysis", *Energy Environ. Sci.*, 2009, **2,** 915-931

141 K. Gong, J. Park, D. Su and R. R. Adzic, "Metalizing carbon nanotubes with Pd-Pt core-shell nanowires enhances electrocatalytic activity and stability in the oxygen reduction reaction", *J. Solid State Electrochem.*, 2014, **18,** 1171-1179

142 S. Li, J. Zheng, X. Ma, Y. Hu, A. Wang, J. Chen and J. Feng, "Facile synthesis of hierarchical dendritic PtPd nanogarlands supported on reduced graphene oxide with enhanced electrocatalytic properties", *Nanoscale*, 2014, **6,** 5708-5713

143 M. Neurock, M. Janik and A. Wieckowski, "A first principles comparison of the mechanism and site requirements for the electrocatalytic oxidation of methanol and formic acid over Pt", *Faraday Discuss.*, 2008, **140,** 363-378

144 C. Rice, R. Ha, R. Masel, P. Waszczuk, A. Wieckowski and T. Barnard, "Direct formic acid fuel cells", *J. Power Sources*, 2002, **111,** 83-89

145 R. Wang, J. Liu, P. Liu, X. Bi, X. Yan, W. Wang, X. Ge, M. Chen and Y. Ding, "Dispersing Pt atoms onto nanoporous gold for high performance direct formic acid fuel cells", *Chem. Sci.*, 2014, **5,** 403-409

146 J. Chang, L. Feng, C. Liu, W. Xing and X. Hu, "An Effective Pd-Ni2P/C Anode Catalyst for Direct Formic Acid Fuel Cells", *Angew. Chem. Int. Edit.*, 2014, **53,** 122-126

147 J. N. Tiwari, R. N. Tiwari, G. Singh and K. S. Kim, "Recent progress in the development of anode and cathode catalysts for direct methanol fuel cells", *Nano Energy*, 2013, **2,** 553-578

148 H. Liu, C. Song, L. Zhang, J. Zhang, H. Wang and D. Wilkinson, "A review of anode catalysis in the direct methanol fuel cell", *J. Power Sources*, 2006, **155,** 95-110

149 E. Antolini, T. Lopes and E. R. Gonzalez, "An overview of platinum-based catalysts as methanol-resistant oxygen reduction materials for direct methanol fuel cells", *J. Alloys Compd.*, 2008, **461,** 253-262

150 K. Juodkazis, J. Juodkazyte, B. Sebeka, G. Stalnionis and A. Lukinskas, "Anodic dissolution of palladium in sulfuric acid: An electrochemical quartz crystal microbalance study", *Russian J. Electrochem.*, 2003, **39,** 954-959

151 "Hydrodynamic voltammetry", http://www.ceb.cam.ac.uk/research/groups/rg-eme/teaching-notes/hydrodynamic-voltammetry, *University of Cambridge*, 2014.08/14

152 J. Yang, J. Y. Lee, Q. Zhang, W. Zhou and Z. Liu, "Carbon-Supported Pseudo-Core–Shell Pd–Pt Nanoparticles for ORR with and Without Methanol", *J. Electrochem. Soc.*, 2008, **155,** B776-B781

153 Y. Tang, H. Zhang, H. Zhong, T. Xu and H. Jin, "Carbon-supported Pd-Pt cathode electrocatalysts for proton exchange membrane fuel cells", *J. Power Sources*, 2011, **196,** 3523-3529

154 D. A. Slanac, L. Li, A. Mayoral, M. J. Yacaman, A. Manthiram, K. J. Stevenson and K. P. Johnston, "Atomic resolution structural insights into PdPt nanoparticle-carbon interactions for the design of highly active and stable electrocatalysts", *Electrochim. Acta*, 2012, **64,** 35-45

155 S. Ghosh, R. K. Sahu and C. R. Raj, "Pt-Pd alloy nanoparticle-decorated carbon nanotubes: a durable and methanol tolerant oxygen reduction electrocatalyst", *Nanotechnology*, 2012, **23,** 385602

156 G. Zhang, Z. Shao, W. Lu, F. Xie, H. Xiao, X. Qin and B. Yi, "Core-shell Pt modified Pd/C as an active and durable electrocatalyst for the oxygen reduction reaction in PEMFCs", *Appl. Catal. B-Environ.*, 2013, **132,** 183-194

157 L. Liu, G. Samjeske, S. Nagamatsu, O. Sekizawa, K. Nagasawa, S. Takao, Y. Imaizumi, T. Yamamoto, T. Uruga and Y. Iwasawa, "Enhanced Oxygen Reduction Reaction Activity and Characterization of Pt-Pd/C Bimetallic Fuel Cell Catalysts with Pt-Enriched Surfaces in Acid Media", *J. Phys. Chem. C*, 2012, **116,** 23453-23464

158 W. J. Khudhayer, N. N. Kariuki, X. Wang, D. J. Myers, A. U. Shaikh and T. Karabacak, "Oxygen Reduction Reaction Electrocatalytic Activity of Glancing Angle Deposited Platinum Nanorod Arrays", *J. Electrochem. Soc.*, 2011, **158,** B1029-B1041

159 C. Wang, L. Ma, L. Liao, S. Bai, R. Long, M. Zuo and Y. Xiong, "A unique platinum-graphene hybrid structure for high activity and durability in oxygen reduction reaction", *Sci. Rep.*, 2013, **3,** 2580

160 P. C. K. Vesborg and T. F. Jaramillo, "Addressing the terawatt challenge: scalability in the supply of chemical elements for renewable energy", *RSC Advances*, 2012, **2,** 7933-7947

161 H. M. Hollmark, J. R. Vegelius, P. Kristiansen, L. Werme and L. Duda, "Exposure of Oxidized Copper Surfaces to Aqueous Na2S Solution Studied with Soft X-Ray Spectroscopy", *J. Electrochem. Soc.*, 2011, **158,** C1-C5

162 C. I. Pearce, R. A. D. Pattrick, D. J. Vaughan, C. M. B. Henderson and G. van der Laan, "Copper oxidation state in chalcopyrite: Mixed Cu d^9 and d^{10} characteristics", *Geochim. Cosmochim. Acta*, 2006, **70,** 4635-4642

163 C. Wang, Y. Wang, X. Liu, F. Diao, L. Yuan and G. Zhou, "Novel hybrid nanocomposites of polyhedral Cu2O nanoparticles-CuO nanowires with enhanced photoactivity", *Phys. Chem. Chem. Phys.*, 2014, **16,** 17487-17492

164 W. Jia, E. Reitz, H. Sun, B. Li, H. Zhang and Y. Lei, "From $Cu_2(OH)_3Cl$ to nanostructured sisal-like $Cu(OH)_2$ and CuO: Synthesis and characterization", *J. Appl. Phys.*, 2009, **105,** 064917

165 Y. Li, X. Yang, J. Rooke, G. van Tendeloo and B. Su, "Ultralong $Cu(OH)_2$ and CuO nanowire bundles: PEG200-directed crystal growth for enhanced photocatalytic performance", *J. Colloid Interface Sci.*, 2010, **348,** 303-312

166 A. Rahnama and M. Gharagozlou, "Preparation and properties of semiconductor CuO nanoparticles via a simple precipitation method at different reaction temperatures", *Opt. Quant. Electron.*, 2012, **44,** 313-322

167 J. Liu, J. Jin, Z. Deng, S. Huang, Z. Hu, L. Wang, C. Wang, L. Chen, Y. Li, G. Van Tendeloo and B. Su, "Tailoring CuO nanostructures for enhanced photocatalytic property", *J. Colloid Interface Sci.*, 2012, **384,** 1-9

168 J. B. Parise and B. G. Hyde, "The structure of atacamite and its relationship to spinel", *Acta Crystallogr. C*, 1986, **42,** 1277-1280

169 M. E. Fleet, "Crystal-structure of paratacamite, $Cu_2(OH)_3Cl$", *Acta Crystallogr. B*, 1975, **31,** 183-187

170 J. Grice, J. Szymanski and J. Jambor, "Crystal structure of clinoatacamite, a new polymorph of $Cu_2(OH)_3Cl$", *Can. Mineral.*, 1996, **34,** 73-78

171 X. G. Zheng, T. Mori, K. Nishiyama, W. Higemoto, H. Yamada, K. Nishikubo and C. N. Xu, "Antiferromagnetic transitions in polymorphous minerals of the natural cuprates atacamite and botallackite $Cu_2Cl(OH)_3$", *Phys. Rev. B*, 2005, **71,** 174404

172 T. Malcherek and J. Schlueter, "Structures of the pseudo-trigonal polymorphs of $Cu_2(OH)_3Cl$", *Acta Crystallogr. B*, 2009, **65,** 334-341

173 G. Bertolotti, D. Bersani, P. P. Lottici, M. Alesiani, T. Malcherek and J. Schlueter, "Micro-Raman study of copper hydroxychlorides and other corrosion products of bronze samples mimicking archaeological coins", *Anal. Bioanal. Chem*, 2012, **402,** 1451-1457

174 J. S. Park, A. N. Ponomaryov, K. Y. Choi, Z. Wang, J. van Tol, K. M. Ok, Z. H. Jang, S. W. Yoon and B. J. Suh, "Spin dynamics of the S=1/2 pyrochlore system $Cu_2(OH)_3Cl$ studied by using high-frequency ESR", *J. Korean Phys. Soc.*, 2011, **58,** 270-275

175 X. Liu, D. Meng, X. Zheng, M. Hagihala and Q. Guo, "Mid-IR and Raman spectral properties of clinoatacamite-structure basic copper chlorides", *Adv. Mater. Res.*, 2011, **146-147,** 1202-1205

176 J. Zhang, J. Xu, H. Zhang, X. Yin, J. Qian, L. Liu, D. Yang and X. Liu, "Fabrication of octahedral Atacamite microcrystals via a hydrothermal route", *Micro Nano Lett.*, 2011, **6,** 119-121

177 W. Tao, X. Liu, X. Zheng, D. Meng and Q. Guo, "Mid-IR and Raman spectral properties of geometrically frustrated atacamite hydroxyl copper chloride", *Adv. Mater. Res.*, 2011, **146-147,** 972-975

178 R. Frost, W. Martens, J. Kloprogge and P. Williams, "Raman spectroscopy of the basic copper chloride minerals atacamite and paratacamite: implications for the study of copper, brass and bronze objects of archaeological significance", *J. Raman Spectrosc.*, 2002, **33,** 801-806

179 D. Stoilova and V. Vassileva, "Infrared spectroscopic study of solids in the $Cu_2(OH)_3Cl$ (Paratacamite) - $Zn_5(OH)_8Cl_2.H_2O$ (Simonkolleite) series", *C. R. Acad. Bulg. Sci.*, 2002, **55,** 51-54

180 Y. Liu, W. Ren and H. Cui, "Large-scale synthesis of paratacamite nanoparticles with controlled size and morphology", *Micro & Nano Letters*, 2011, **6,** 823-826

181 Z. Yang, J. Xu, W. Zhang, A. Liu and S. Tang, "Controlled synthesis of CuO nanostructures by a simple solution route", *J. Solid State Chem.*, 2007, **180,** 1390-1396

182 Y. Zhao, J. Zhao, Y. Li, D. Ma, S. Hou, L. Li, X. Hao and Z. Wang, "Room temperature synthesis of 2D CuO nanoleaves in aqueous solution", *Nanotechnology*, 2011, **22,** 115604

183 S. Sun, X. Zhang, J. Zhang, L. Wang, X. Song and Z. Yang, "Surfactant-free CuO mesocrystals with controllable dimensions: green ordered-aggregation-driven synthesis, formation mechanism and their photochemical performances", *CrystEngComm*, 2013, **15,** 867-877

184 Y. K. Kim, D. H. Riu, S. R. Kim and B. I. Kim, "Preparation of shape-controlled copper oxide powders from copper-containing solution", *Mater Lett*, 2002, **54,** 229-237

185 L. Yang, Y. Zhu, H. Tong, L. Li and L. Zhang, "Multistep synthesis of CuO nanorod bundles and interconnected nanosheets using $Cu_2(OH)_3Cl$ plates as precursor", *Mater. Chem. Phys.*, 2008, **112,** 442-447

186 X. G. Zheng, T. Kawae, Y. Kashitani, C. S. Li, N. Tateiwa, K. Takeda, H. Yamada, C. N. Xu and Y. Ren, "Unconventional magnetic transitions in the mineral clinoatacamite $Cu_2Cl(OH)_3$", *Phys. Rev. B*, 2005, **71,** 052409

187 A. S. Wills and J. -. Henry, "On the crystal and magnetic ordering structures of clinoatacamite, gamma-$Cu_2(OD)_3Cl$, a proposed valence bond solid", *J. Phys. Condens. Mat.*, 2008, **20,** 472206

188 X. Wang, C. Hui, H. Liu, G. Du, X. He and Y. Xi, "Synthesis of CuO nanostructures and their application for nonenzymatic glucose sensing", *Sens. Actuators, B*, 2010, **144,** 220-225

189 N. Yusoff, N. M. Huang, M. R. Muhamad, S. V. Kumar, H. N. Lim and I. Harrison, "Hydrothermal synthesis of CuO/functionalized graphene nanocomposites for dye degradation", *Mater. Lett.*, 2013, **93,** 393-396

190 Q. Chi, J. Zhang, J. Nielsen, E. Friis, I. Chorkendorff, G. Canters, J. Andersen and J. Ulstrup, "Molecular monolayers and interfacial electron transfer of Pseudomonas aeruginosa azurin on Au(111)", *J. Am. Chem. Soc.*, 2000, **122,** 4047-4055

191 H. Wang, W. Fan, Y. He, J. Wang, J. N. Kondo and T. Tatsumi, "Selective oxidation of alcohols to aldehydes/ketones over copper oxide-supported gold catalysts", *J. Catal.*, 2013, **299,** 10-19

192 "Best research-cell efficiencies", http://www.nrel.gov/ncpv/images/efficiency_chart.jpg, *National Renewable Energy Laboratory*, 2014.08/29

193 "Solar spectral irradiance: Air mass 1.5", http://rredc.nrel.gov/solar/spectra/am1.5/, *National Renewable Energy Laboratory*, 2014.08/29

194 X. Zhang, Y. L. Chen, R. Liu and D. P. Tsai, "Plasmonic photocatalysis", *Rep. Prog. Phys.*, 2013, **76,** 046401

195 W. Hou and S. B. Cronin, "A Review of Surface Plasmon Resonance-Enhanced Photocatalysis", *Adv. Funct. Mater.*, 2013, **23,** 1612-1619

196 S. Linic, P. Christopher and D. B. Ingram, "Plasmonic-metal nanostructures for efficient conversion of solar to chemical energy", *Nat. Mater.*, 2011, **10,** 911-921

197 J. Han and S. Lim, "Structural changes of corn starches by heating and stirring in DMSO measured by SEC-MALLS-RI system", *Carbohydr. Polym.*, 2004, **55,** 265-272

198 M. V. Diamanti, B. Del Curto and M. Pedeferri, "Interference colors of thin oxide layers on titanium", *Color Res. Appl.*, 2008, **33,** 221-228

199 Y. Zhao, J. Liu, L. Shi, S. Yuan, J. Fang, Z. Wang and M. Zhang, "Surfactant-free synthesis uniform Ti1-xSnxO2 nanocrystal colloids and their photocatalytic performance", *Appl. Catal. B-Environ.*, 2010, **100,** 68-76

Appendix A Publications and dissemination

Only contributions made during the PhD are included. The total number of publications in international journals is 9 of which 2 were published before the PhD.

International Journals:

1. S. Gan, L. Zhong, C. Engelbrekt, J. Zhang, D. Han, J. Ulstrup, Q. Chi, L. Niu, "Graphene controlled H- and J-stacking of perylene dyes into highly stable supramolecular nanostructures for enhanced photocurrent generation", *Nanoscale*, 2014, **6**, 10516-10523
2. C. Engelbrekt, P. Malcho, J. Andersen, L. Zhang, K. Ståhl, B. Li, J. Hu, J. Zhang, "Selective synthesis of clinoatacamite $Cu_2(OH)_3Cl$ and tenorite CuO nanoparticles by pH control", *Journal of Nanoparticle Research*, 2014, **16:2562**, 1-12
3. J. Mielby, R. Poreddy, C. Engelbrekt, S. Kegnæs, "Highly selective formation of imines catalyzed by silver nanoparticles supported on alumina", *Chinese Journal of Catalysis*, 2014, **35,** 769-775
4. C. Engelbrekt, P. S. Jensen, K. H. Sørensen, J. Ulstrup, J. Zhang, "Complexity of gold nanoparticle formation disclosed by dynamics study", *Journal of Physical Chemistry C*, 2013, **117,** 11818-11828
5. N. B. Hartmann, C. Engelbrekt, J. Zhang, J. Ulstrup, K. O. Kusk, A. Baun, "The challenges of testing metal and metal oxide nanoparticles in algal bioassays: Titanium dioxide and gold nanoparticles as case studies", *Nanotoxicology*, 2013, **7,** 1082-1094
6. V. Joseph, C. Engelbrekt, J. Zhang, U. Gernert, J. Ulstrup, J. Kneipp, "Characterizing the kinetics of nanoparticle-catalyzed reactions by surface-enhanced Raman scattering", *Angewandte Chemie International Edition*, 2012, **51,** 7592-7596
7. P. S. Jensen, C. Engelbrekt, K. H. Sørensen, J. Zhang, Q. Chi, J. Ulstrup, "Au-biocompatible metallic nanostructures in metalloprotein electrochemistry and electrocatalysis", *Journal of Materials Chemistry*, 2012, **22,** 13877-13882

Oral presentations at international conferences:

8. "Dynamic approach to the study of gold nanoparticle formation", *14th International Symposium on Electroanalytical Chemistry*, **2013,** Changchun, China

Poster presentations at national/international conferences:

9. C. Engelbrekt, R. R. Nazmutdinov, J. Yan, T. T. Zinkicheva, B. Mao, J. Ulstrup, J. Zhang, "Adsorption dynamics and self-assembled L-cysteine on Au(100)", *65th Annual Meeting of the International Society of Electrochemistry*, **2014,** Lausanne, Switzerland
10. C. Engelbrekt, J. Ulstrup, J. Zhang, "Dynamics of green AuNP formation and their basis for Au-Pt core-shell nanostructure synthesis", *Nanocrystals*, **2014,** Punta Cana, Dominican Republic
11. C. Engelbrekt, P. S. Jensen, J. Ulstrup, J. Zhang, "Dynamic studies of green AuNP formation by electrochemical and optical techniques", *63rd Annual Meeting of the International Society of Electrochemistry*, **2012,** Prague, Czech Republic
12. C. Engelbrekt, K. H. Sørensen, P. S. Jensen, J. Ulstrup, J. Zhang, "Saccharide-based approach to green metallic nanostructure synthesis", *NanoDay*, **2011,** Lyngby, Denmark

Other conferences, workshops and seminars:

13. *Danscatt Annual Meeting*, conference, **2014,** Lyngby, Denmark
14. *Asia Energy Conference*, conference/workshop, **2014,** Copenhagen, Denmark
15. *Nanosight User Meeting*, seminar, **2014,** Greve, Denmark
16. Metrohm Autolab - Nova Software Seminar, seminar, **2014,** Glostrup, Denmark
17. C. Engelbrekt, "SAMENS: Introduction to our platform for metal-based nanostructure synthesis and dynamics of nanoparticle formation", seminar, *Shandong University*, **2013,** Jinan, China
18. C. Engelbrekt, "SAMENS: Introduction to our platform for metal-based nanostructure synthesis and dynamics of nanoparticle formation", seminar, *University of California Irvine*, **2013,** Los Angeles, USA
19. *Nanosight User's Meeting*, seminar, **2012,** Amsterdam, Netherlands
20. *NanoDay for EuroTech Alliance*, conference, **2012,** Lyngby, Denmark
21. Combined Technology Seminar at DTU by Malvern, seminar, **2012,** Lyngby, Denmark

22. C. Engelbrekt, “SAMENS: A green approach to the synthesis of classical and new metallic nanostructures”, seminar, *Shanghai University*, **2012,** Shanghai, China

23. C. Engelbrekt, “SAMENS: A green approach to the synthesis of classical and new metallic nanostructures”, seminar, *Shanghai Institute of Applied Physics*, **2012,** Shanghai, China

24. Workshop on DNA Nanotechnology: From Structure to Function, workshop, **2012,** Shanghai, China

25. C. Engelbrekt, “SAMENS: A green approach to the synthesis of classical and new metallic nanostructures*”, DTU Nanoparticle Network Workshop*, workshop, **2012,** Lyngby, Denmark

26. Vejen til en “sund” nanoteknologiudvikling, seminar, **2011,** Copenhagen, Denmark

Appendix B Supplementary data

Controlling the size of AuNPs in solution synthesis (2.2)

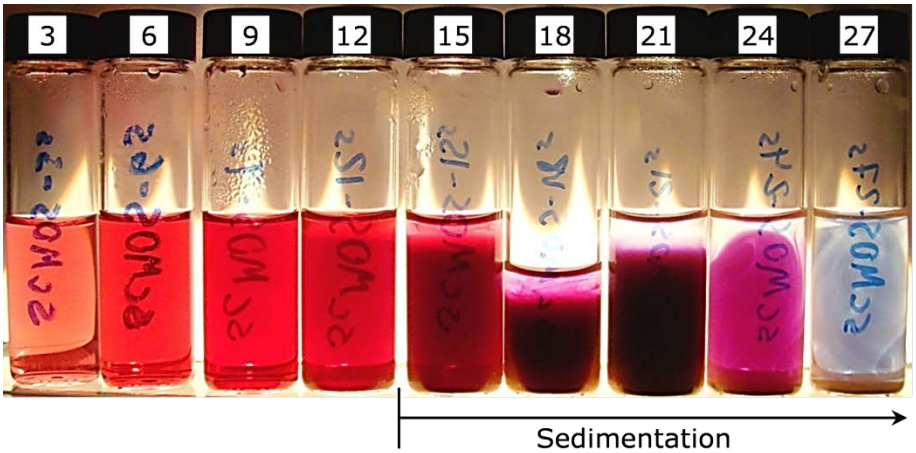

App. fig. 1. Photograph of fractions from the size control experiment that have been allowed to sediment. Corresponding step numbers are indicated on the figure. Sedimentation is only visible after 12-15 steps.

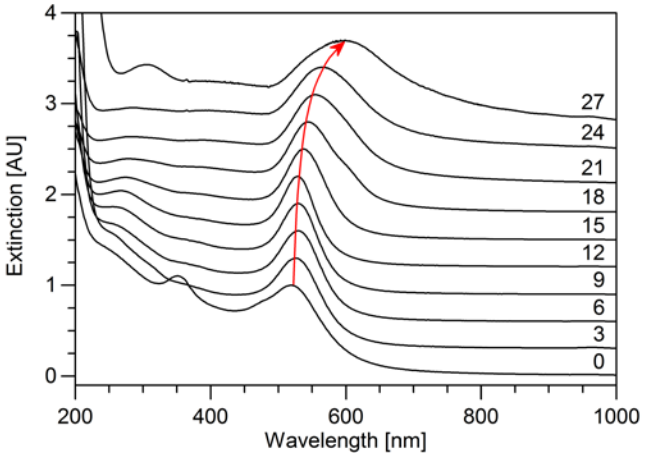

App. fig. 2. UV-vis spectral development during the size control experiment (steps are indicated on each curve) normalized at the LSPR. The trend in LSPR max is highlighted with the red arrow.

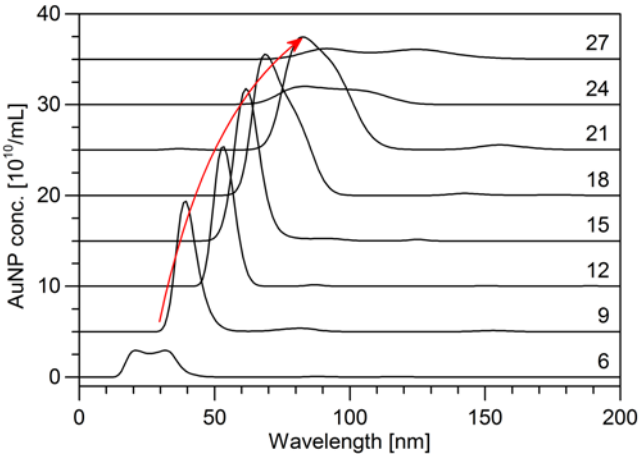

App. fig. 3. AuNP size distribution development from NTA measurements during the size control experiment (steps indicated on figure). The dilutions after every fraction are corrected for so that each curve ideally represents the same number of particles (step 6 is used as reference). The trend in size is highlighted with the red arrow.

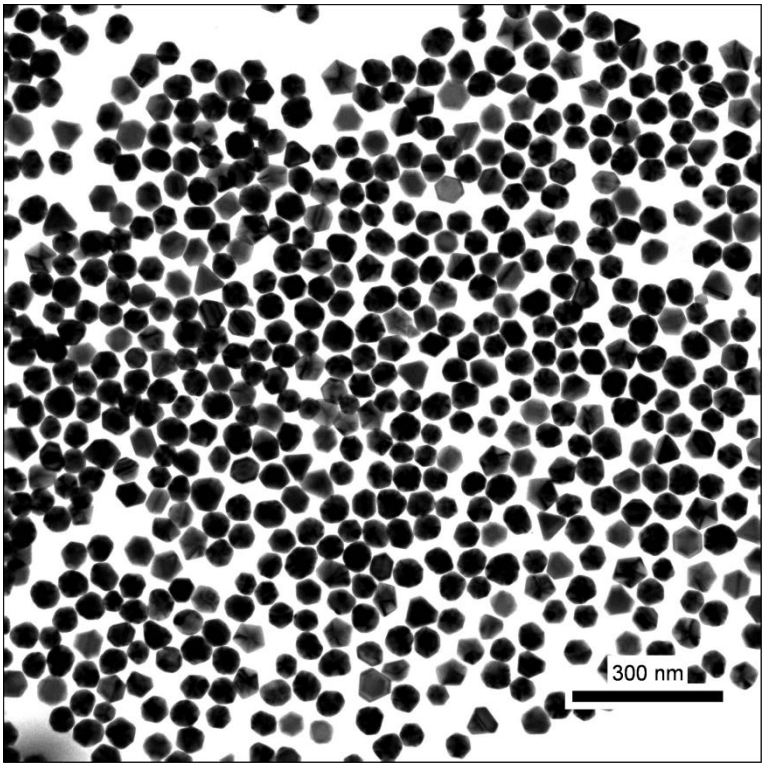

App. fig. 4. TEM of faceted nanoparticles in the fraction after 15 steps of the size control experiment. Decahedra consisting of 5 crystallites as well as single-crystal and twinned crystals (hexagons and triangles) are abundant.

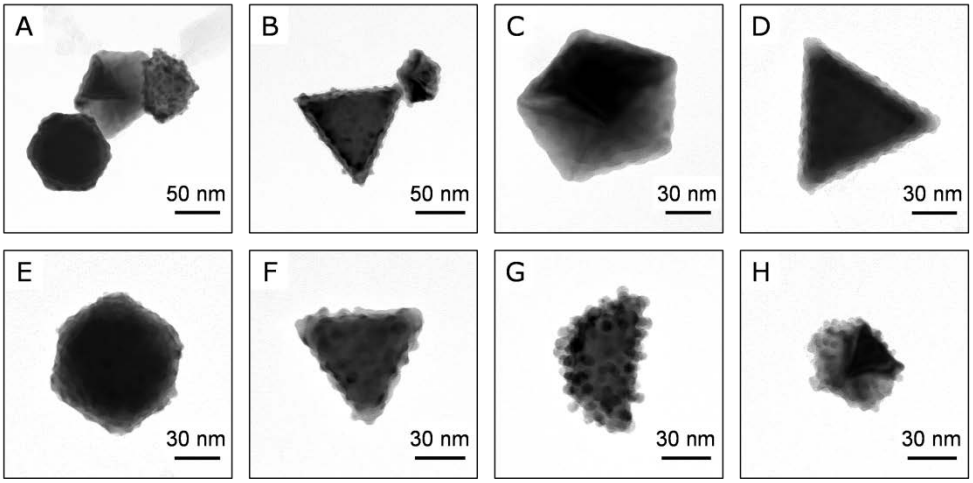

App. fig. 5. TEM images of decorated AuNPs found after step 27 in the size control experiment.

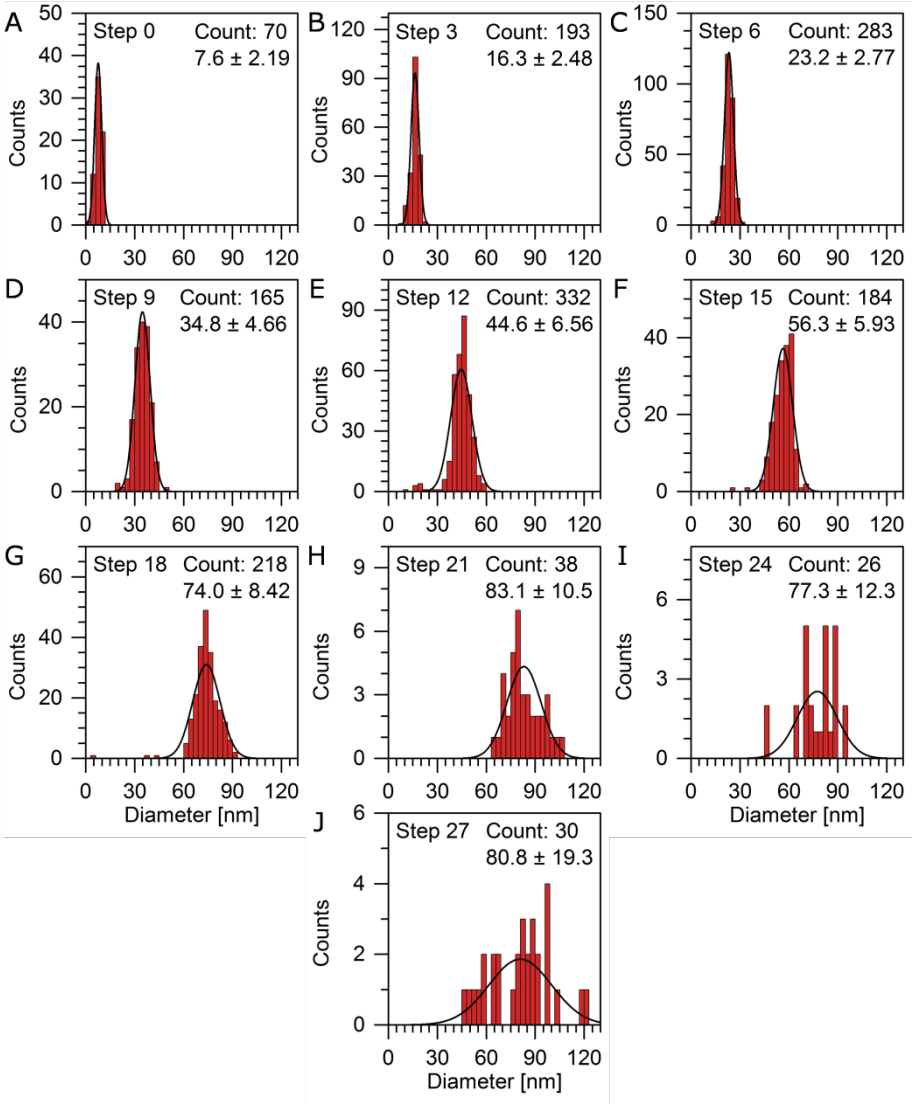

App. fig. 6. Size distributions and Gaussian fits of fractions from the size control experiment measured from TEM images. The numbers of measured particles and statistical sizes are noted on the graphs.

Flat gold nanostructure synthesis (2.4)

Two TEM images of GS-1 were analysed by the automated procedure in ImageJ. The area range was 3-infity nm^2 for both images and circularity 0.65-1 and 0.75-1.

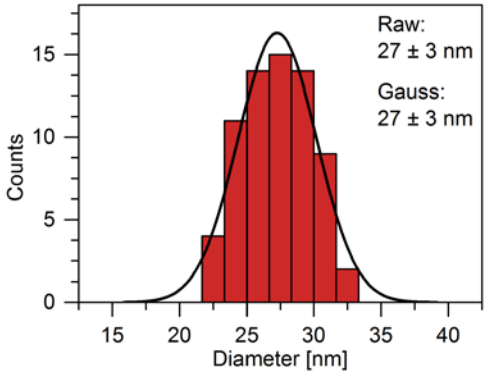

App. fig. 7. Size distribution and Gaussian fit of 69 measured particles from TEM images of sample "GS-1".

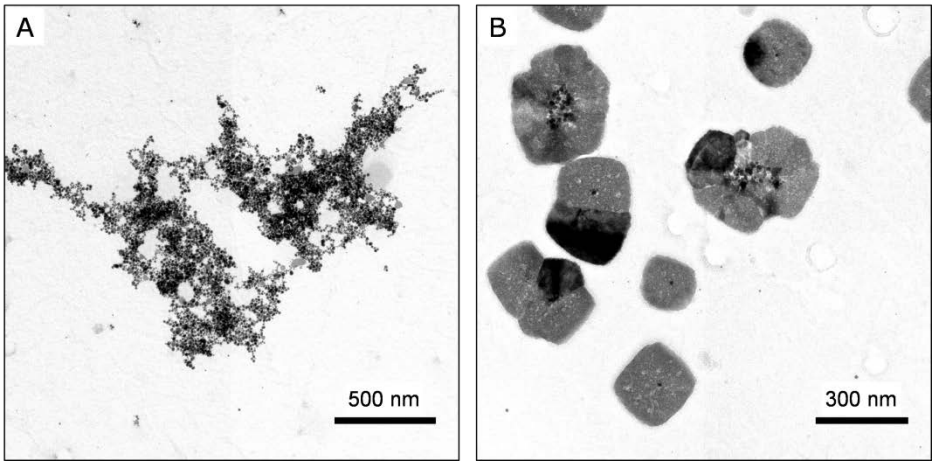

App. fig. 8. TEM images of GS-3. TEM sample prepared 1 day after synthesis showed the presence of cubic CuO structures indicating that unreduced gold was present in solution oxidizing the copper grid during drying.

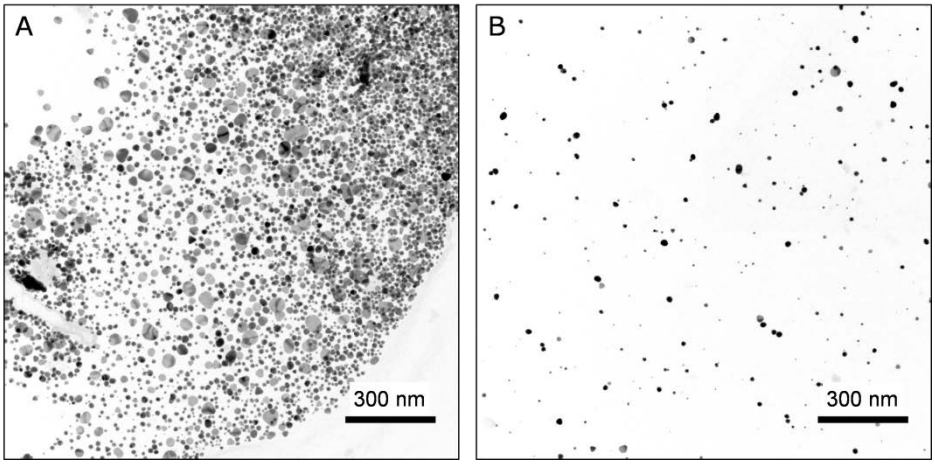

App. fig. 9. TEM images of GS-3. TEM sample prepared 57 days after synthesis. No oxidized copper was observed. Areas with many small sheets as well as areas with mainly spherical particles dominated the sample.

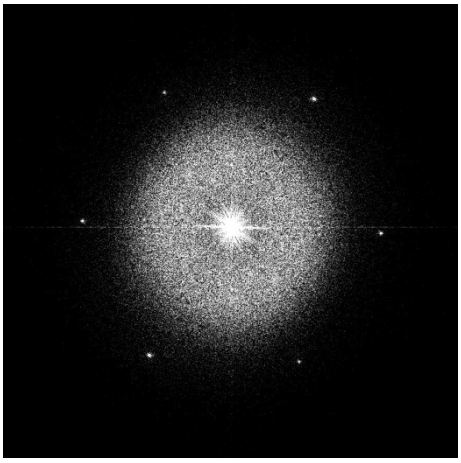

App. fig. 10. FFT of the HR-TEM image in Figure 46B spots from {111} crystal planes at 60 ° angles.

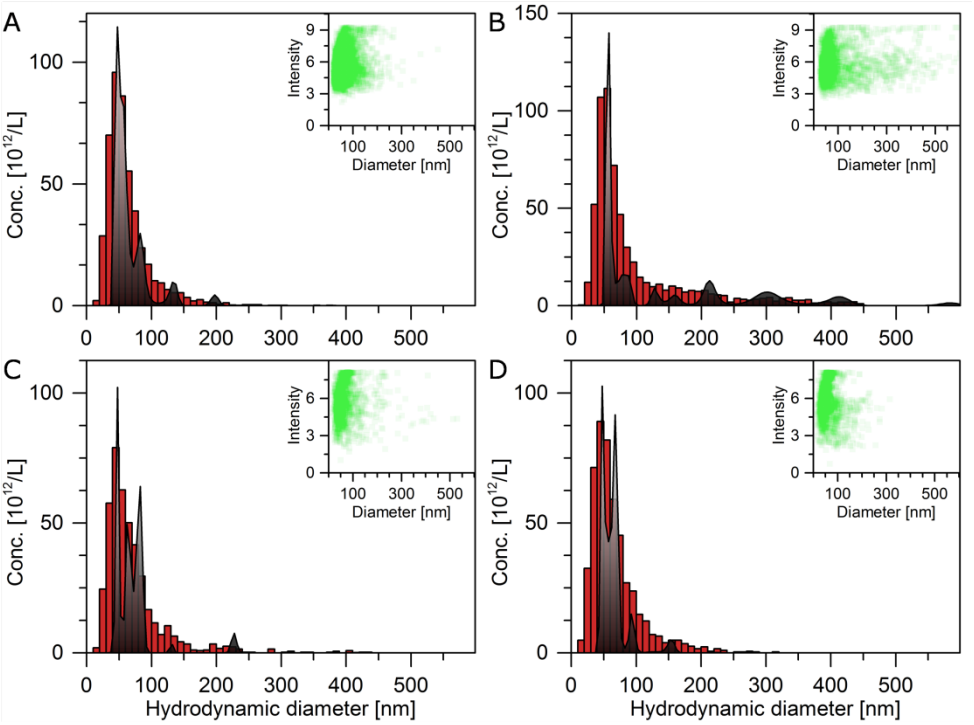

App. fig. 11. Particle size measurements by NTA of GOsGS-1 to -4. (A) GOsGS-1 a few hours after precursor addition. The size from NTA was 60 ± 30 nm with a mode at 48 nm and the concentration $5.6 \cdot 10^{14}$/L. (B) GOsGS-2 1 week after precursor addition. The size from NTA was 200 ± 100 nm with a mode at 57 nm and the concentration $5.8 \cdot 10^{14}$/L. (C) GOsGS-3 1 week after precursor addition. The size from NTA was 70 ± 40 nm with a mode at 48 nm and the concentration $4.1 \cdot 10^{14}$/L. (D) GOsGS-4 1 week after precursor addition. The size from NTA was 60 ± 20 nm with a mode at 48 nm and the concentration $4.5 \cdot 10^{14}$/L.

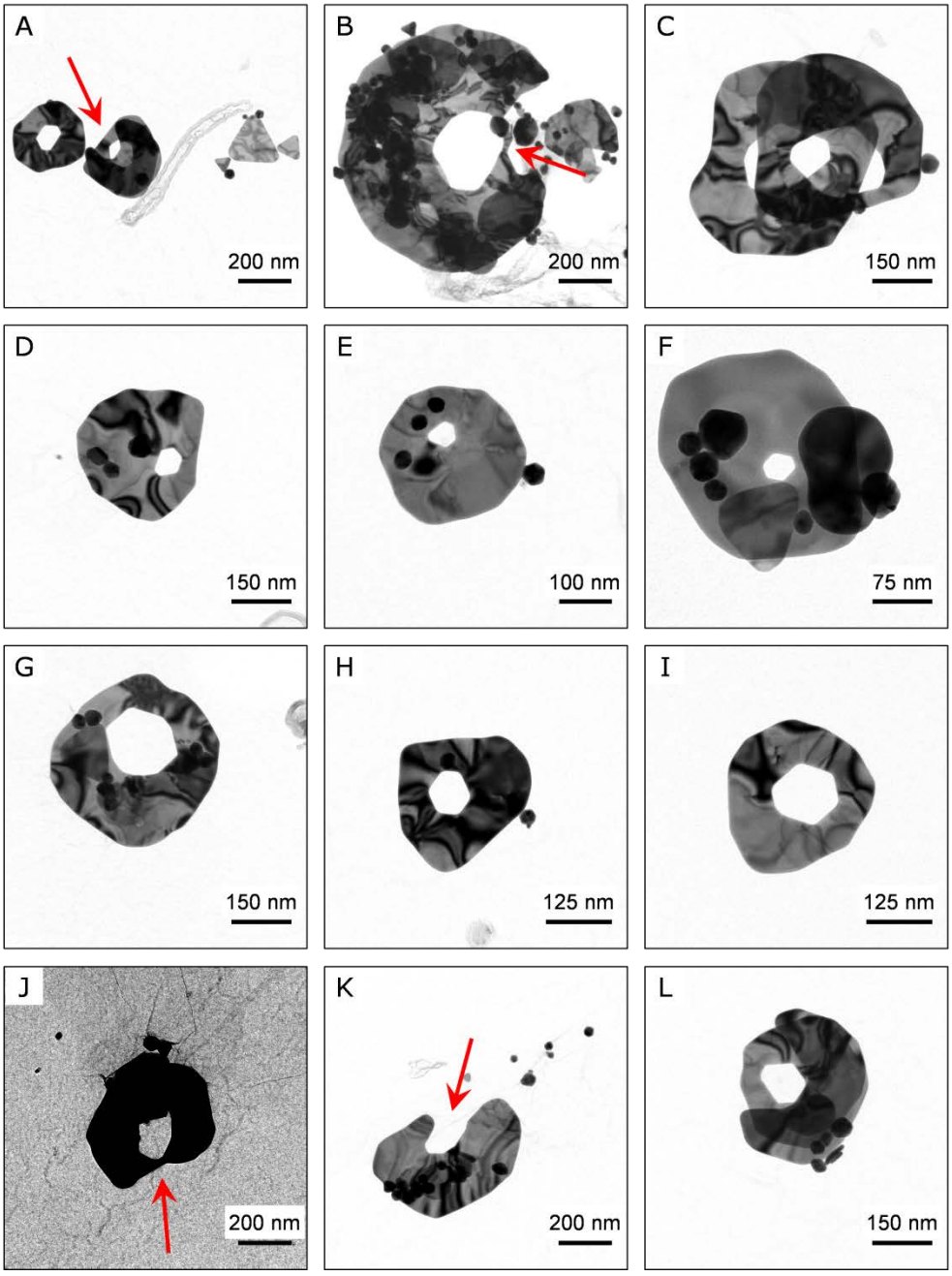

App. fig. 12. TEM images of gold nanorings GO templated synthesis. Red arrows indicate where rings are in the process of closing.

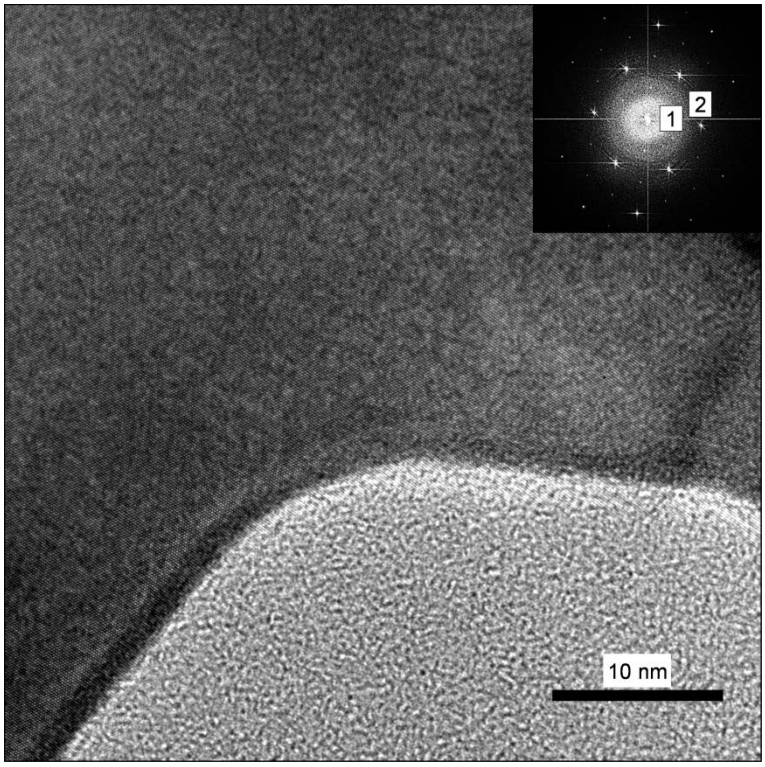

App. fig. 13. HR-TEM images and corresponding FFT (inset) of gold nanoring in GOsGS-1 showing consistent lattice fringes of {111} and {022} supporting a (111) surface facet.

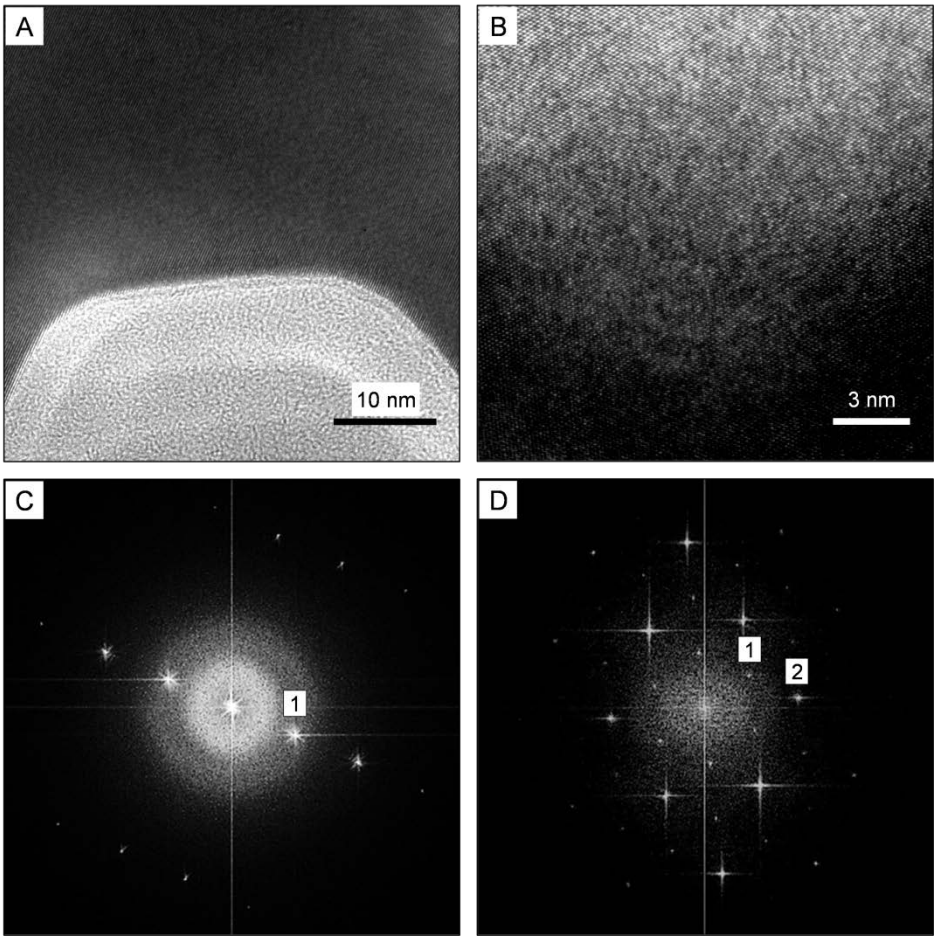

App. fig. 14. (A) and (B) HR-TEM images and (C) and (D) corresponding FFTs of gold rings in GOsGS-1 showing consistent lattice fringes of {111} and {022} supporting a (111) surface facet.

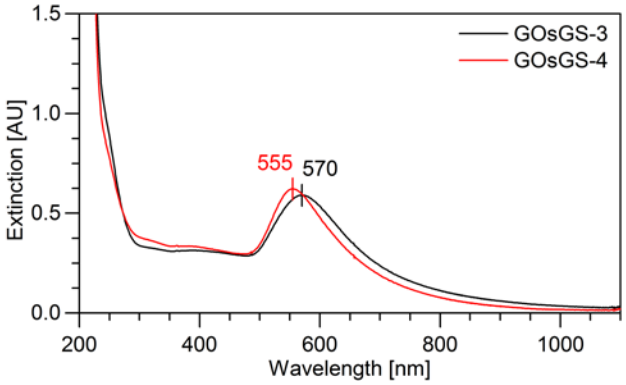

App. fig. 15. UV-vis spectra of the redispersed gold nanoparticles of GOsGS-3 (black) and -4 (red) recorded 20 months after precursor addition (dil: 1).

Unidentified UV peaks (2.5)

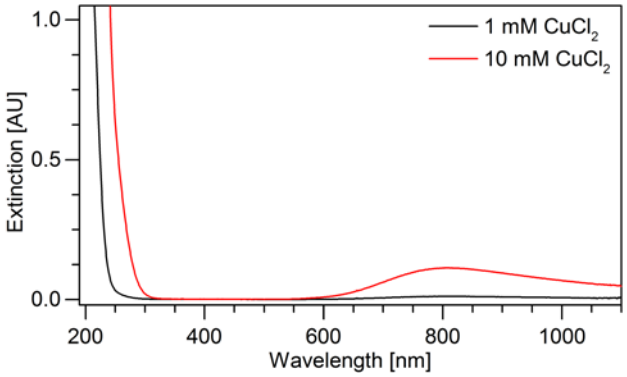

App. fig. 16. UV-vis spectra of 1 mM (black) and 10 mM (red) aqueous solution of $CuCl_2$. A very weak band around 800 nm gives rise to a slight blue colour of solutions above 20 mM.

UV-vis and fluorescence spectra are converted from wavelength to photon energy, E_p, by:

$$E_p = \frac{hc}{\lambda}$$

where h is Planck's constant, c the speed of light and λ the wavelength.

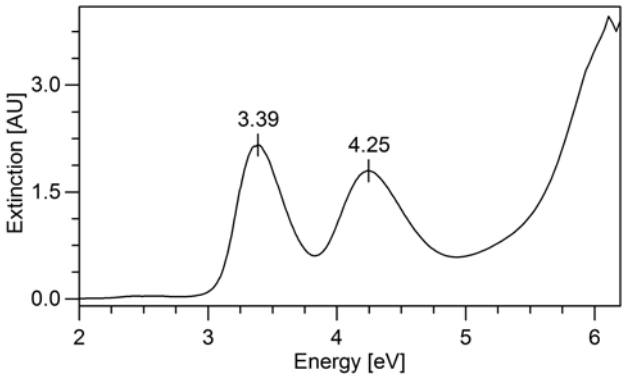

App. fig. 17. UV-vis spectrum of filtrate F2 shown in Figure 58 replotted against photon energy.

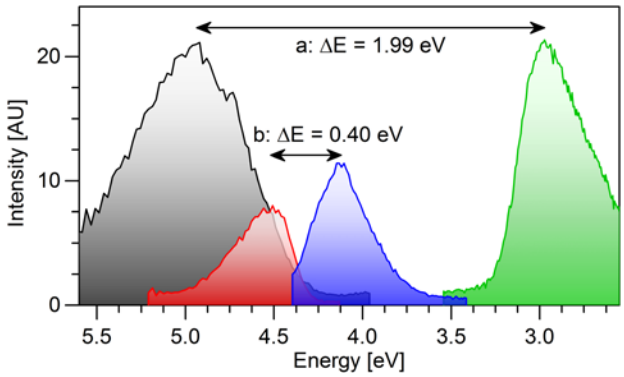

App. fig. 18. Fluorescence signals shown in Figure 62 replotted versus photon energy.

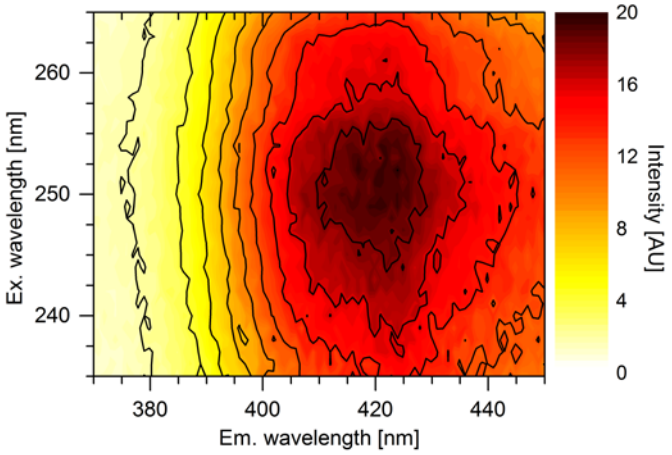

App. fig. 19. 3D fluorescence map produced by emission scanning from 365 to 450 nm at 1 nm increments in excitation from 235 to 265 nm.

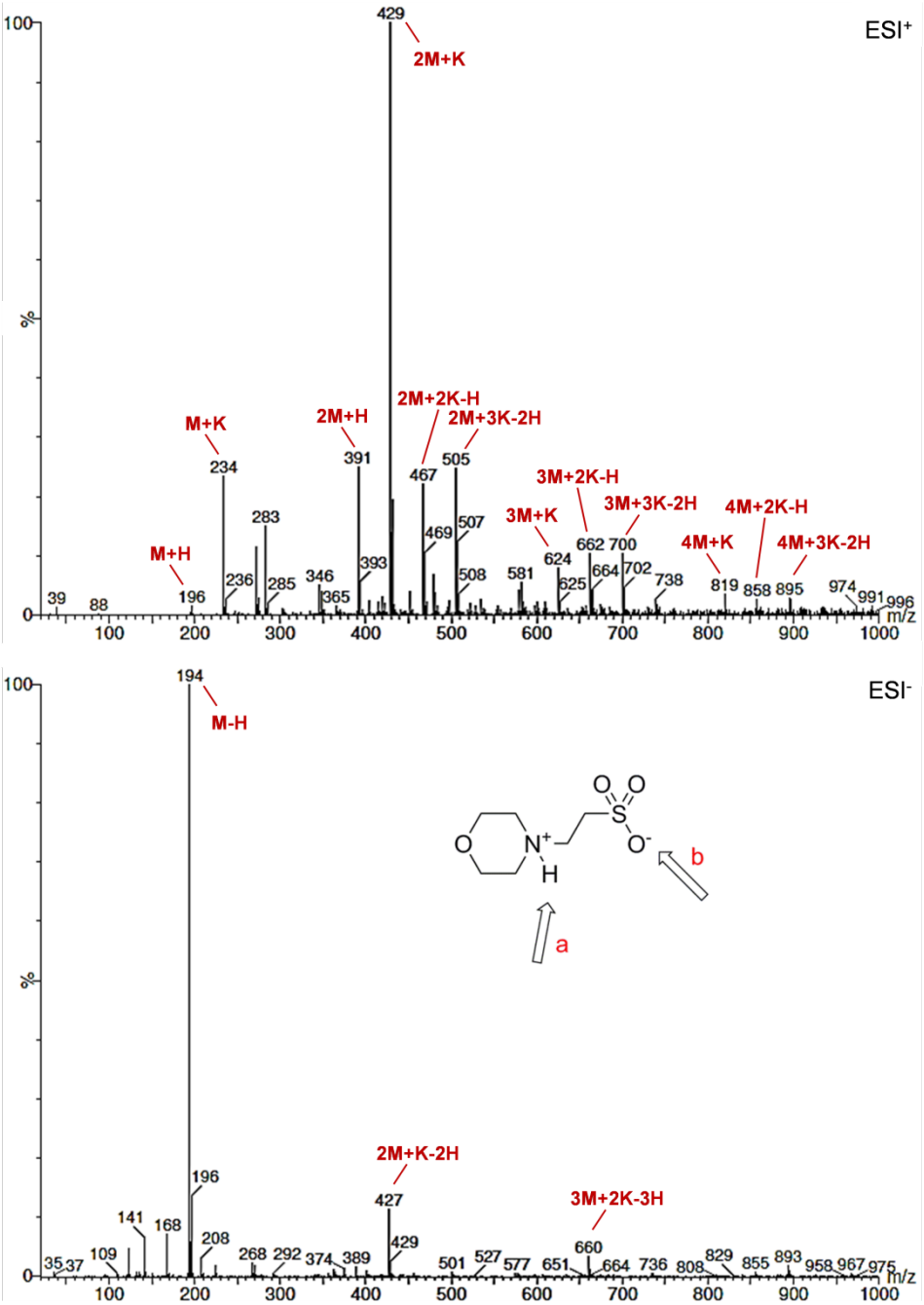

App. fig. 20. Mass spectra from positive (top) and negative (bottom) ionisation of the very first eluent. Negative charges from deprotonation of the amine (a) and positive from protonation of the sulfonate (b) (inset bottom). Subsequent ion exchange with K^+ can occur at both places.

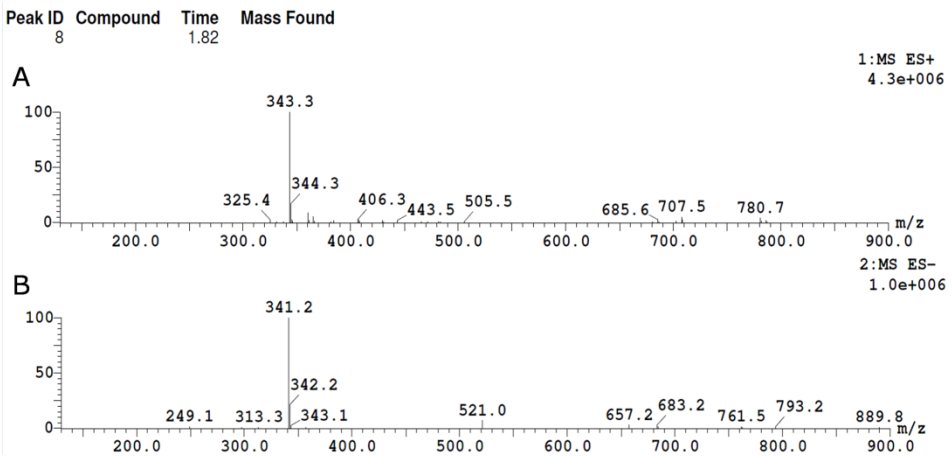

App. fig. 21. Mass spectra of the positive (top) and negative (bottom) ionisation of the UPLC peak “c” in Figure 63. The mass of the compound is likely 342 g/mol.

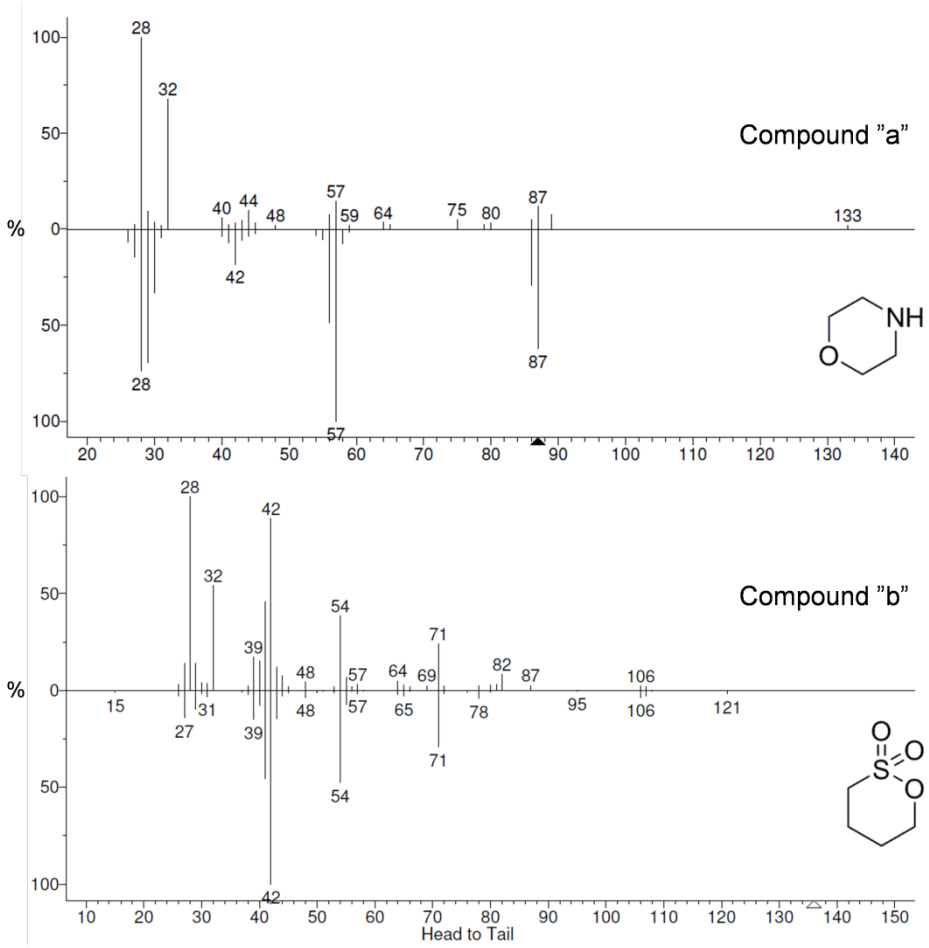

App. fig. 22. Fragment spectra of the compounds eluting around 15 (compound "a") and 17.5 min (compound "b"). The spectra are matched to a database and the best matches were morpholine for "a" and 1,5-butane sultone for "b".

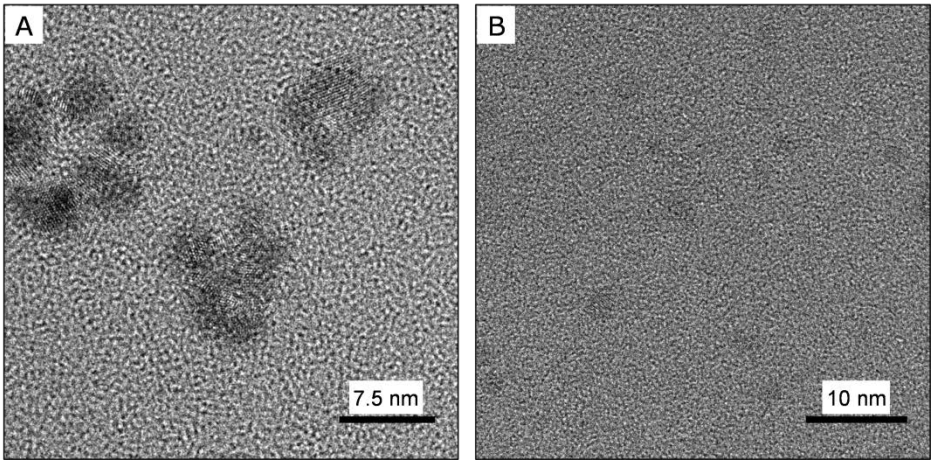

App. fig. 23. HR-TEM of filtrate containing the unidentified UV active compound.

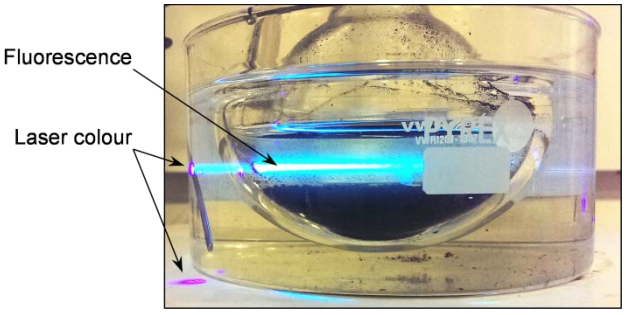

App. fig. 24. Photograph of fluorescence observed in the AuPt core-shell catalyst synthesis. The solution is excited by a purple laser (405 nm).

Au-Pt core-shell nanoparticles (3.2)

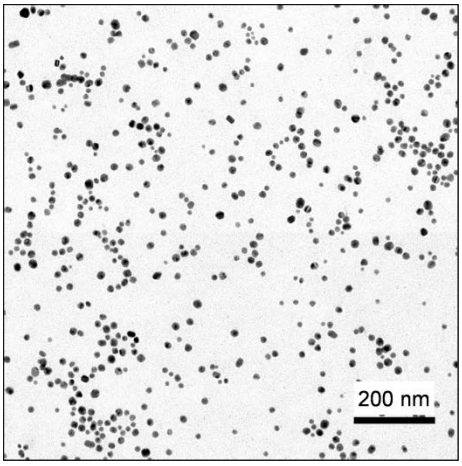

App. fig. 25. TEM image of the AuNPs used as core for the NF-HT and NF-RT1 samples.

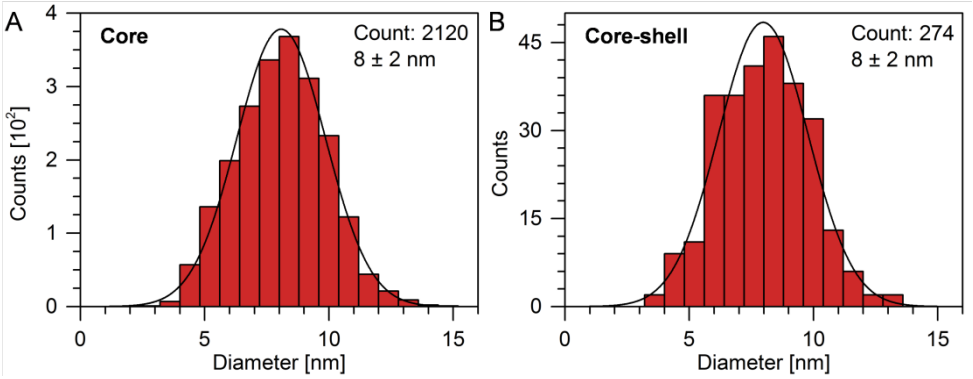

App. fig. 26. Size distributions and Gaussian fits of (A) 2120 and (B) 274 measured particles from TEM images of the AuNP core and core-shell NPs of NF-HT, respectively.

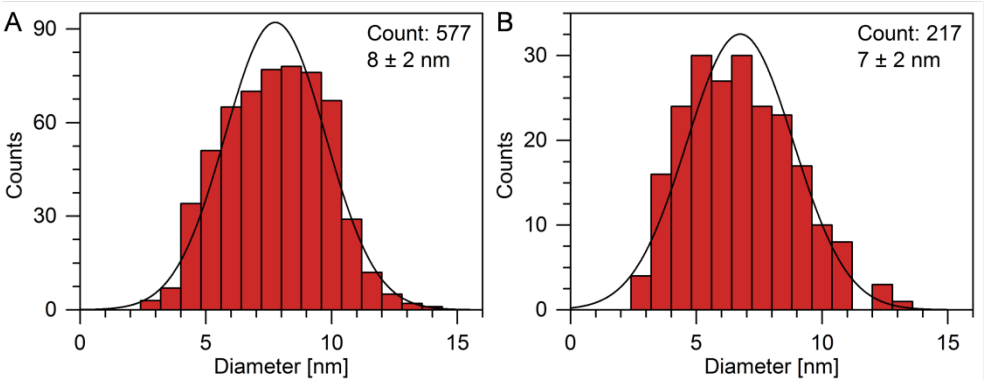

App. fig. 27. Size distributions and Gaussian fits of (A) 577 and (B) 217 measured particles from TEM images of freshly prepared AuNPs and AuNPs exposed to the NF synthesis conditions, respectively.

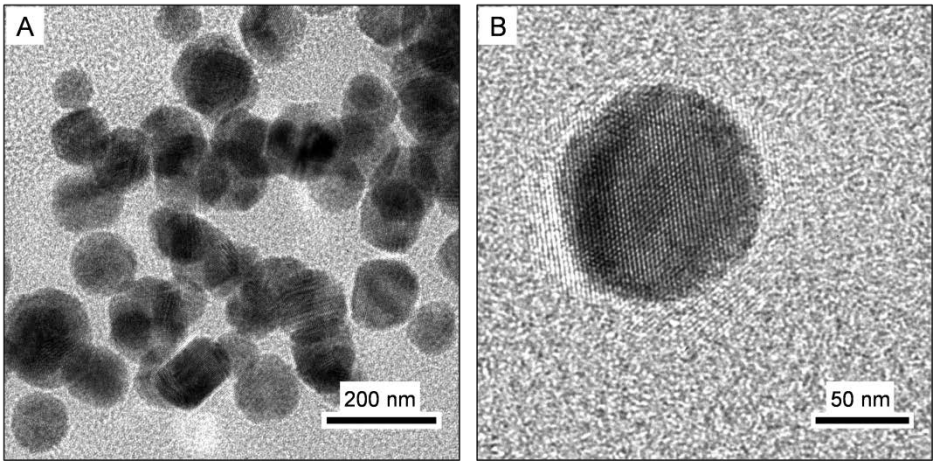

App. fig. 28. HR-TEM images of Au-Pt core-shell NPs prepared by the same procedure as csAuPt-1 by Nedjeljko Šešelj in the group.

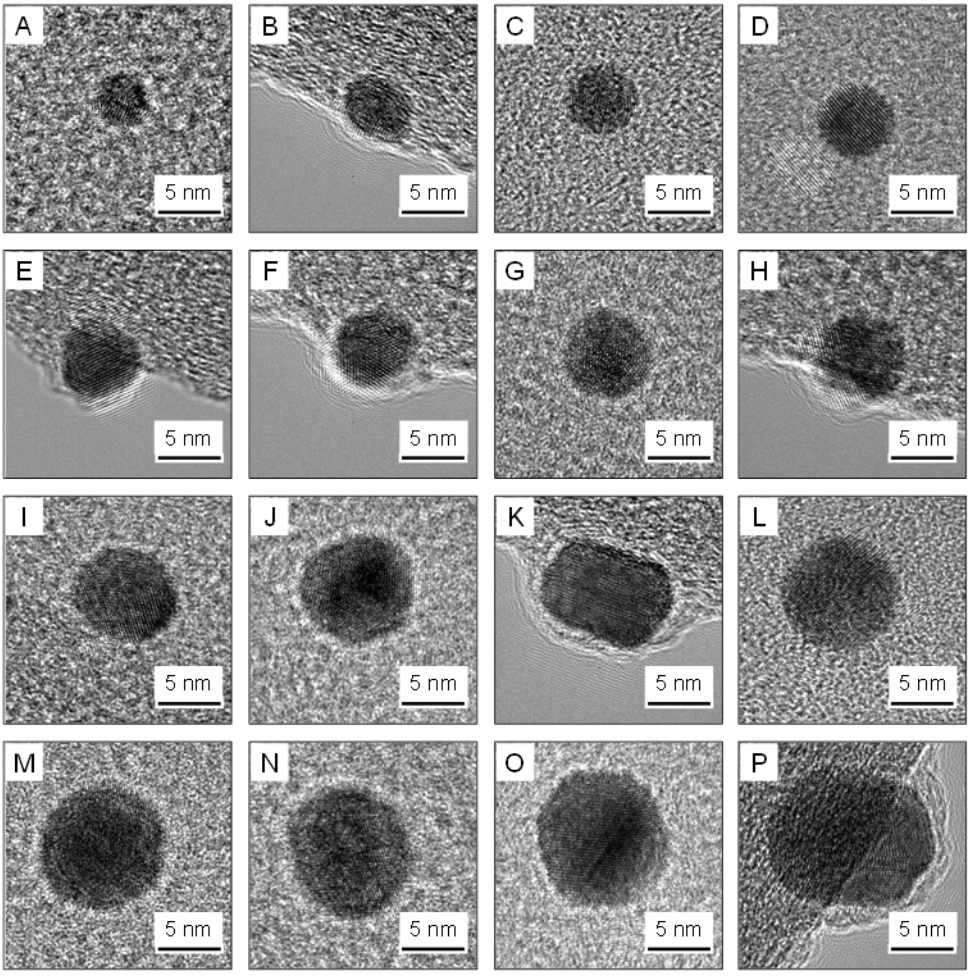

App. Fig. 29. HR-TEM images of individual core-shell NPs. The particles increase in size from (A) to (P) corresponding to measurement numbers from 1 to 16 in Figure 75A.

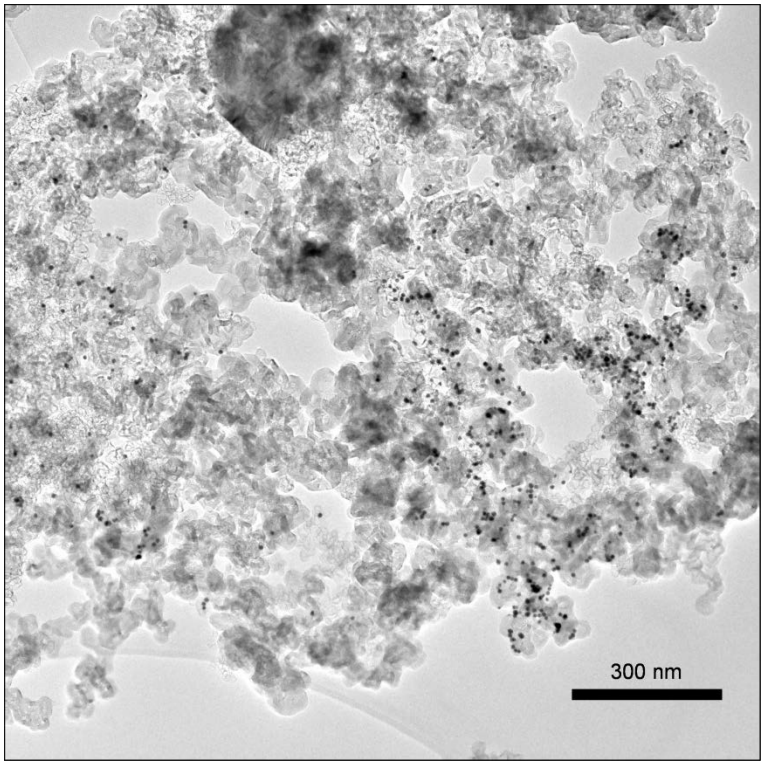

App. fig. 30. TEM image of the catalyst prepared by immobilization of core-shell NPs on G-CB showing the poor dispersion of NPs on the support.

Using palladium with platinum (3.3)

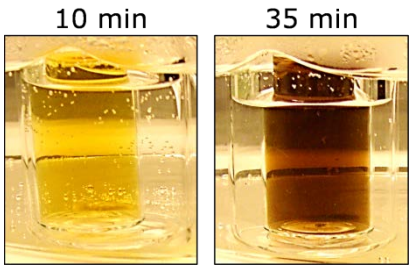

App. fig. 31. Synthesis of PdNPs following the MOS procedure. Photos show the synthesis mixture after 10 (left) and 35 (right) min of heating at 90-95 °C.

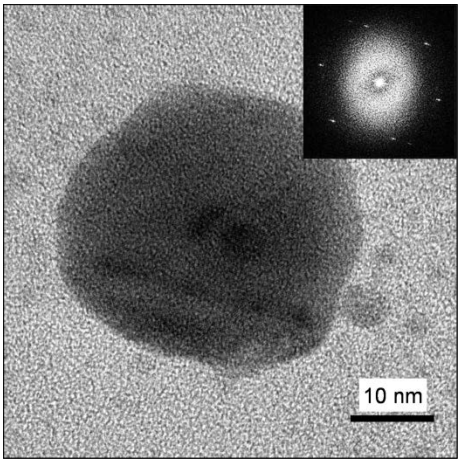

App. fig. 32. High-resolution TEM image of single PdNP in Pd-MOS. Inset shows the corresponding FFT with a hexagonal pattern of spots presumably corresponding to (111) lattices.

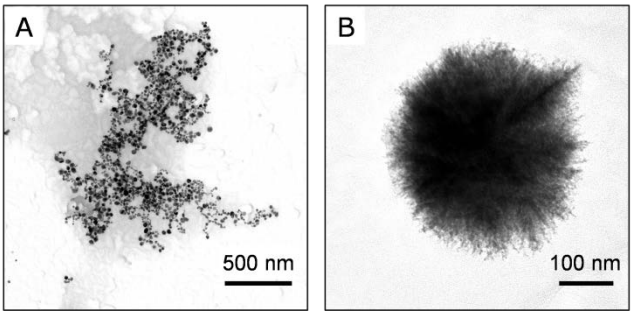

App. fig. 33. TEM images of Pd-MOS after 1 year. The sample again contained (A) 20-40 nm nanoparticles and (B) large spherical aggregates. (B) Dendritic structure is present.

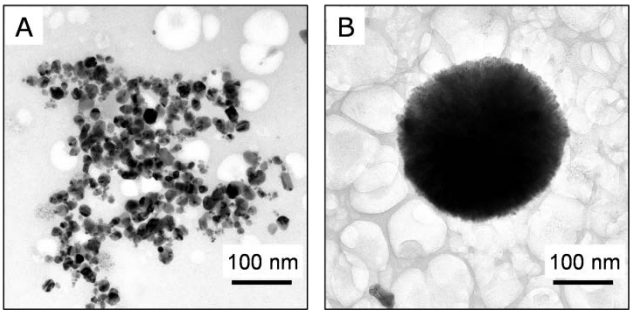

App. fig. 34. TEM images of Pd-OBS with (A) individual PdNPs and (B) large spherical aggregates.

Palladium-platinum nanostructures (3.4)

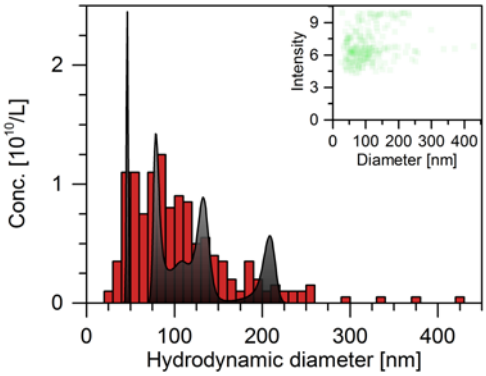

App. fig. 35. NTA measurement of the PdPt NPs synthesized by co-reduction. The size was 120 ± 60 nm and the concentration $5.6 \cdot 10^{11}$/L

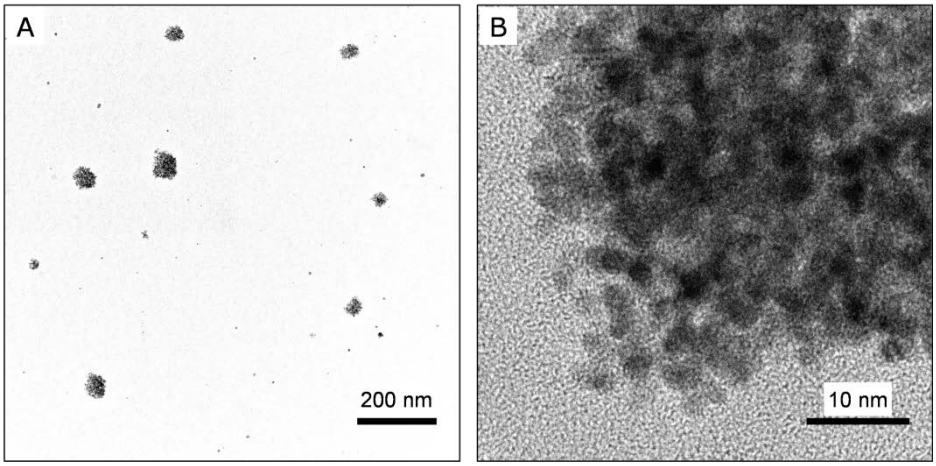

App. fig. 36. TEM images of PdPt NPs synthesized by co-reduction.

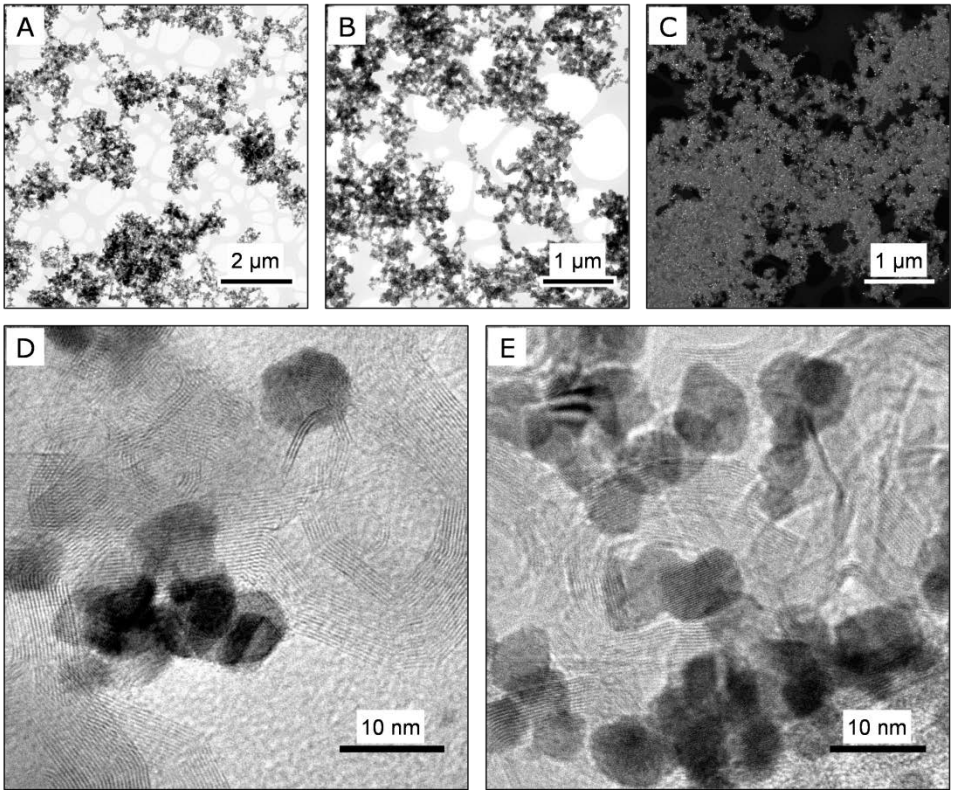

App. fig. 37. TEM images of the PdPt NPs loaded on G-CB. (C) Dark field (DF) image showing bright spots where the beam is diffracted by the metal particles. (D-E) High resolution images with lattice fringes from both the G-CB and PdPt NPs.

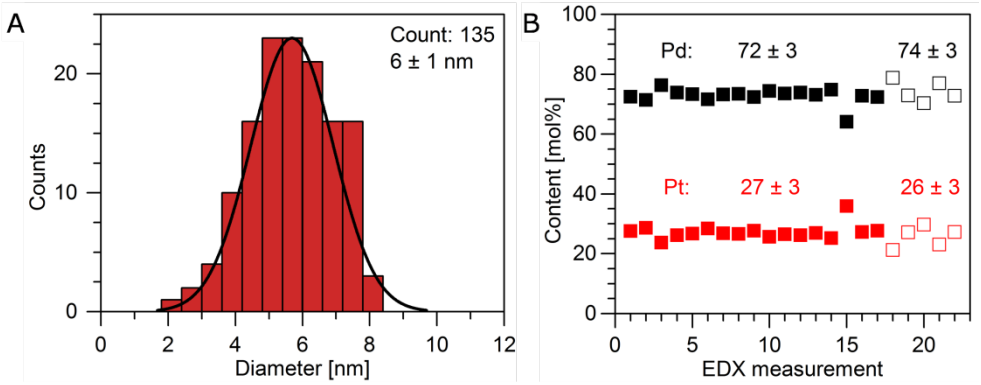

App. fig. 38. (A) Size distribution of 135 PdPt NPs on G-CB measured by hand on TEM images. (B) The Pd and Pt content (mol based) from EDX of the PdPt NPs on G-CB (filled, 17 measurements) and filtrate (empty, 5 measurements) from different areas of the grid and at different magnifications.

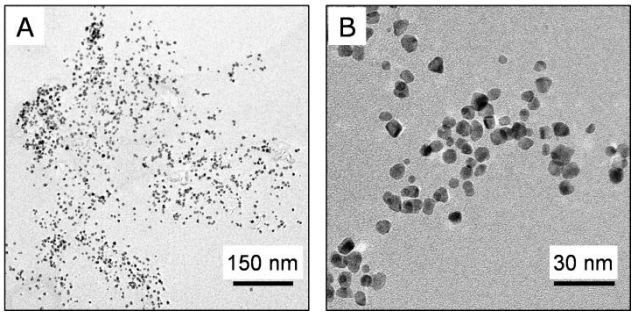

App. fig. 39. TEM images of PdPt NPs found in the filtrate of the G-CB loaded NPs.

Selective synthesis of $Cu_2(OH)_3Cl$ and CuO (4.2)

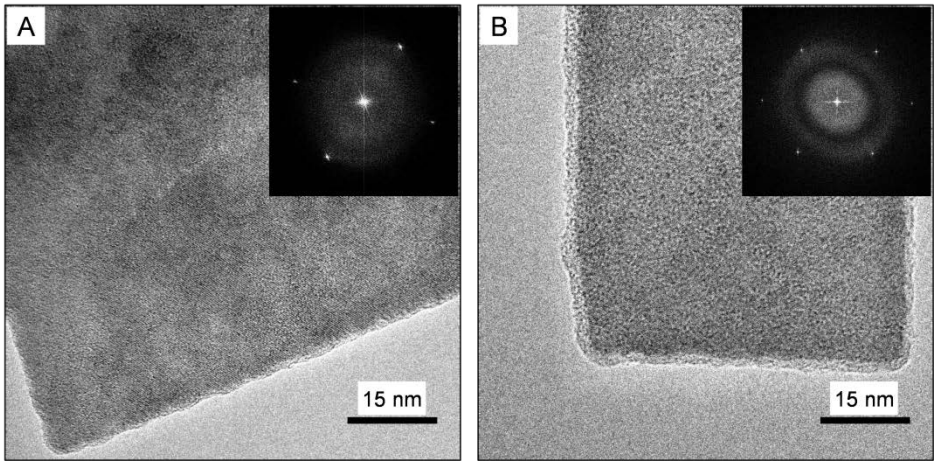

App. fig. 40. High-resolution TEM images of parts of single ribbons. The ordered crystal structure is evidenced by the FFTs (insets) showing an ordered pattern of spots.

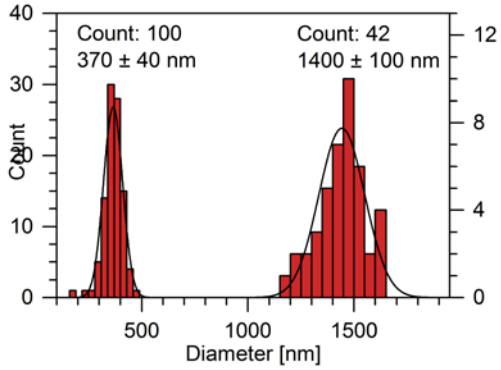

App. fig. 41. Width and length distribution of sheets in Cu-pH-13 measured by hand from TEM images.

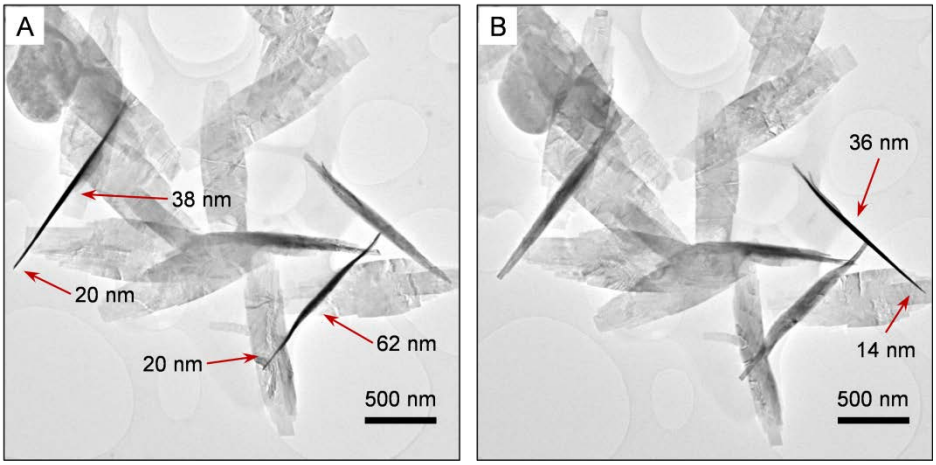

App. fig. 42. TEM images taken at slightly different tilt angles to align the ribbons along the beam direction. The sheet thickness at the center and tip are indicated on the figure.

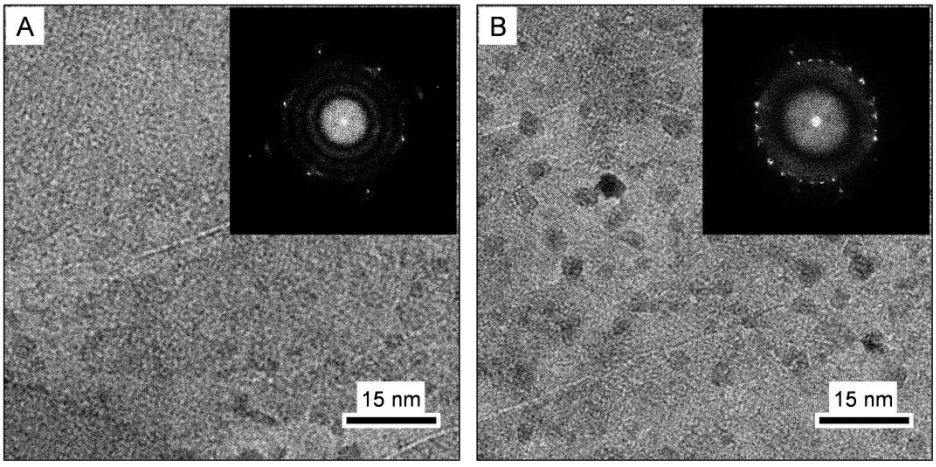

App. fig. 43. High-resolution TEM images (A) before and (B) after prolonged beam exposure. Insets show the corresponding FFTs and a clear transition from single- to poly-crystalline character.

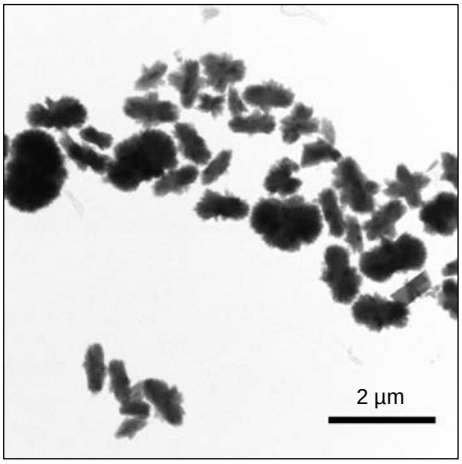

App. fig. 44. Representative TEM image of the nanowhiskers formed at initial pH 11 in 20 mL samples heated from r.t.

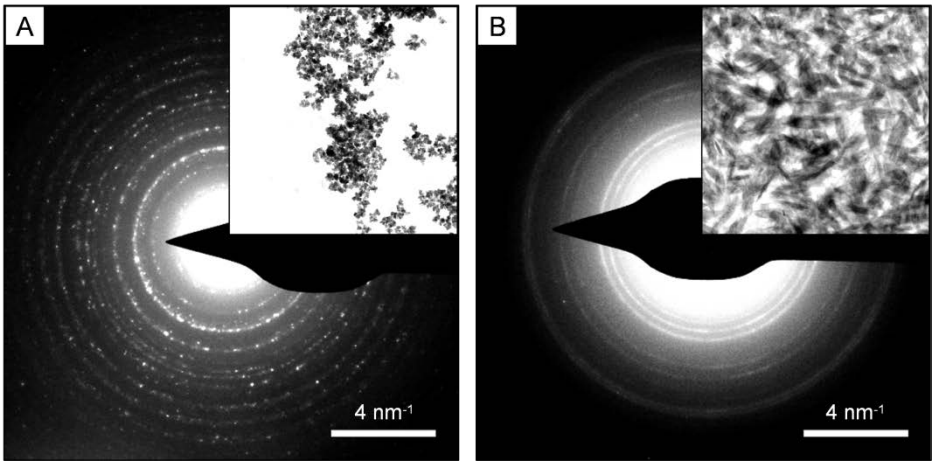

App. fig. 45. SAED of (A) the white/blue product (TEM image of the selected area shown in the inset, 4.3 by 4.3 µm) and (B) the brown product (TEM image of the selected area shown in the inset, 2.3 x 2.3 μm^2).

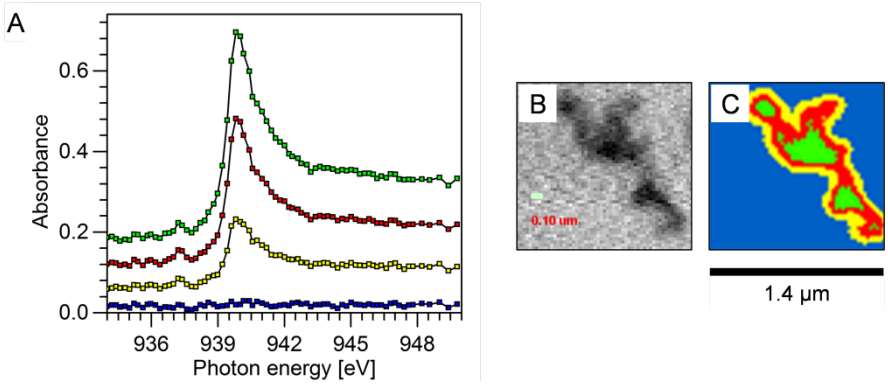

App. fig. 46. Stack imaging with STXM of 150 nm Cu_2O cubes containing 14 nm AuNP cores. The Cu(I) L-edge is found at 939.8 eV.

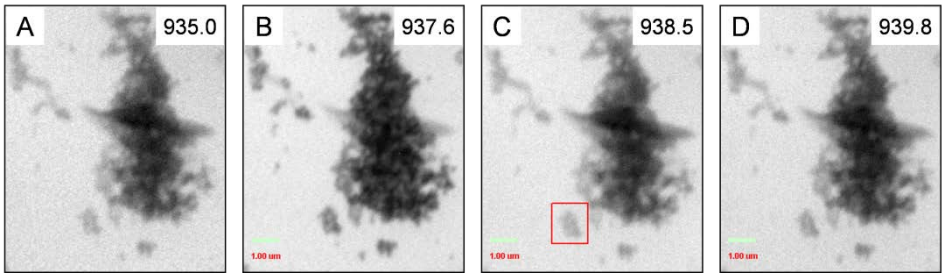

App. fig. 47. STXM images of the white/blue product. (A) and (B) were recorded at energies below and above the Cu(II) edge, respectively, and the absorption difference is shown in Figure 104A. (C) and (D) were recorded at energies below and above the Cu(I) edge, respectively, and the absorption difference is shown in Figure 104B. The images are 8 x 10 μm^2.

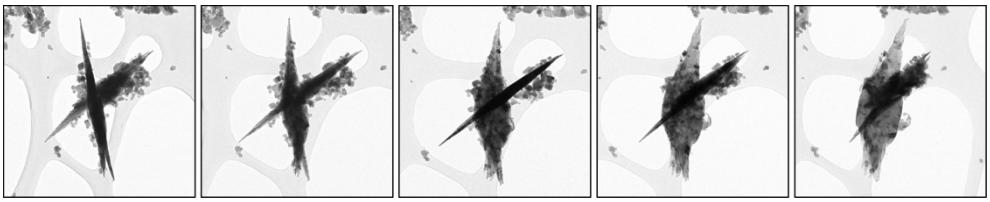

App. fig. 48. Series of TEM images of LS-Cu-B1 recorded at different tilt angles. All images are 1.5 x 1.5 μm^2.

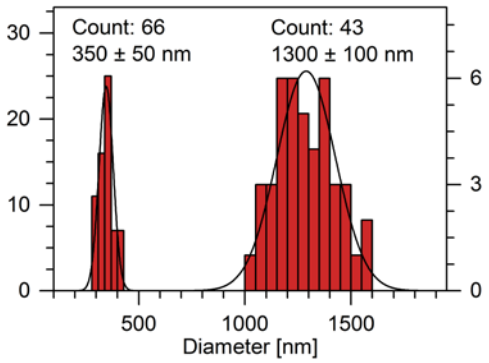

App. fig. 49. Width and length distribution of sheets in LS-Cu-B1 measured by hand from TEM images.

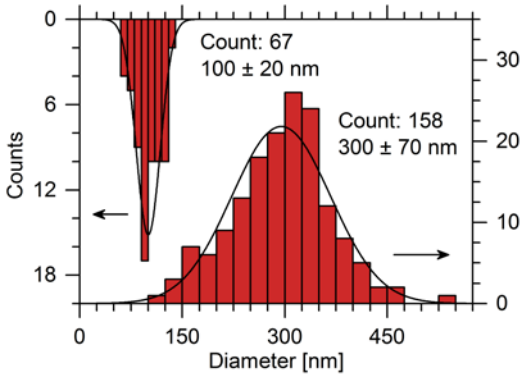

App. fig. 50. Width and length distribution of sheets in LS-Cu-B2 measured by hand from TEM images. The ordinate is reversed for the width distribution because of overlap.

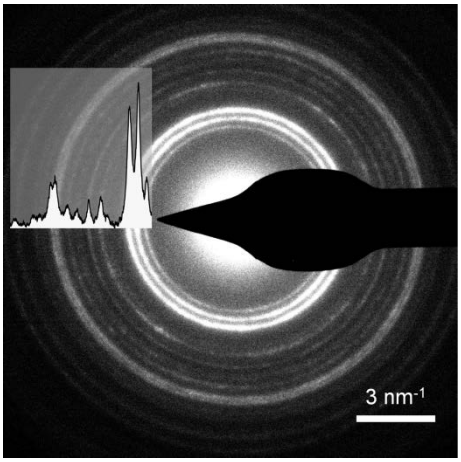

App. fig. 51. SAED of many particles in LS-Cu-B2 showing diffraction rings arising from a very large number of crystallites. The filled curve in the inset shows a line plot of the intensity in the SAED along the abscissa of the inset.

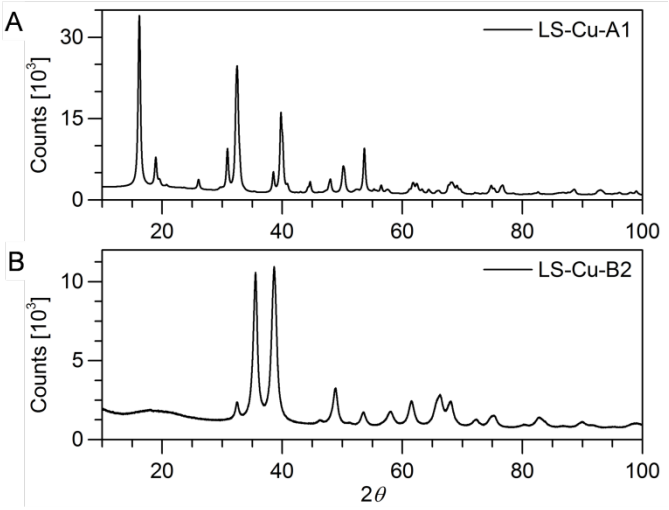

App. fig. 52. XRPD patterns of purified NPs from (A) LS-Cu-A1 and (B) LS-Cu-B2.

App. table 1. Crystallographic data and refinement summary for Rietveld refinement of XRPD patterns of synthesized copper mineral nanostructures. "Clino." = clinoatacamite.

Sample name	LS-Cu-A1	LS-Cu-B2	Cu-pH-13	LS-Cu-B1	
Mineral name	Clino. [a]	Tenorite	Tenorite	Clino. [a]	Tenorite
Formula	$Cu_2(OH)_3Cl$	CuO	CuO	$Cu_2(OH)_3Cl$	CuO
F_M (g/mol)	213.57	79.55	79.55	213.57	79.55
System	Monoclinic	Monoclinic	Monoclinic	Monoclinic	Monoclinic
Space group	P 1 21/n 1	C 1 2/c 1	C 1 2/c 1	P 1 21/n 1	C 1 2/c 1
***a* (Å)**	6.1396(2)	4.6829(2)	4.6794(2)	6.0768(3)	4.6798(3)
***b* (Å)**	6.8172(2)	3.4218(1)	3.4320(2)	6.8037(4)	3.4274(2)
***c* (Å)**	9.1180(2)	5.1382(2)	5.1232(3)	9.1835(4)	5.1301(3)
***α* (°)**	90	90	90	90	90
***β* (°)**	99.738(4)	99.125(2)	99.170(2)	99.515(4)	99.191(4)
***γ* (°)**	90	90	90	90	90
***V* (Å^3)**	376.14(3)	81.29(1)	81.22(1)	374.47(6)	81.23(2)
Z	4	4	4	4	4
***ρ* (g/cm^3)**	3.771	6.499	6.504	3.788	6.504
Size (Å)	268(1)	116(0)	245(1)	251(1)	195(1)
wt%				68.7(2)	31.3(1)
Parameters	33	24	24	26	
R_{wp} (%)	5.64	4.00	4.26	6.30	
χ^2	7.73	2.44	1.22	39.89	
R_p (%)	4.44	3.03	2.73	4.84	
Bragg refl.	426	46	46	426	46
R_B (%)	2.59	1.30	2.37	3.48	3.00

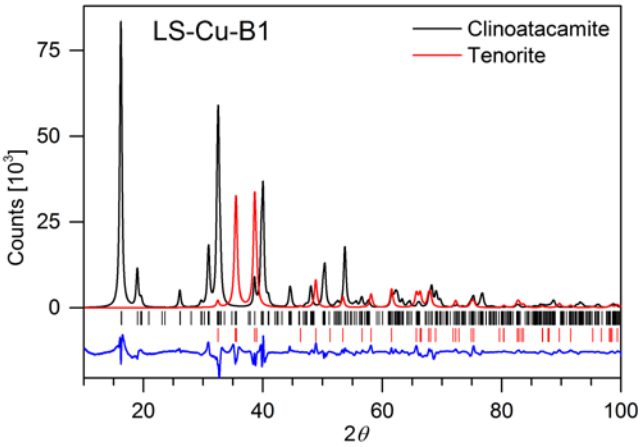

App. fig. 53. Rietveld refinement of XRPD patterns of LS-Cu-B1 having contributions from both clinoatacamite (black) and tenorite (red). Bragg positions are indicated with the bars and the blue curve shows the difference between recorded and fitted data. Refinements were carried out by PhD student Jonas Andersen at DTU Chemistry.

App. table 2. Crystallographic data and refinement summary for Rietveld refinement of XRPD patterns of reference samples of $Cu_2(OH)_3Cl$.

Sample name	**Natural atacamite**		**Synthesized mixture**	
Mineral name	Atacamite	Quartz	Clinoatacamite	Atacamite
Formula	$Cu_2(OH)_3Cl$	SiO_2	$Cu_2(OH)_3Cl$	$Cu_2(OH)_3Cl$
F_M (g/mol)	213.57	60.84	213.57	213.57
System	Orthorhombic	Trigonal	Monoclinic	Orthorhombic
Space group	P N M A	P 3_2 2 1	P 1 21/n 1	P N M A
***a* (Å)**	6.0211(5)	4.9055(4)	6.1543(3)	6.0521(5)
***b* (Å)**	6.8566(6)	4.9055(4)	6.8233(3)	6.8524(5)
***c* (Å)**	9.10257)	5.3927(4)	9.1325(3)	9.1030(7)
α (°)	90	90	90	90
β (°)	90	90	99.682(3)	90
γ (°)	90	120	90	90
***V* (Å^3)**	375.79(1)	112.39(3)	378.03(5)	377.51(9)
Z	4	3	4	4
ρ (g/cm^3)	3.774	2.663	3.752	3.757
Size (Å)	2720(30)	2700(200)	571(7)	479(8)
wt%	92.4(4)	7.6(1)	68.4(5)	31.6(4)
Parameters	26		29	
R_{wp} (%)	11.34		2.51	
χ^2	13.47		1.13	
R_p (%)	7.61		1.91	
Bragg refl.	210	60	427	213
R_B (%)	5.94	5.61	1.93	1.51

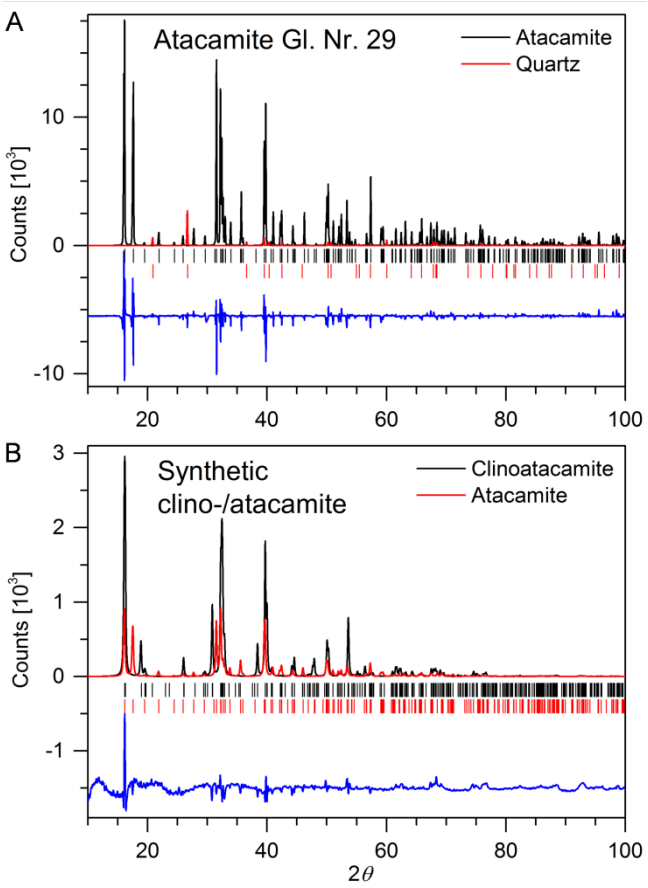

App. fig. 54. Rietveld refinement of XRPD patterns of (A) natural atacamite with contributions from atacamite (black) and quartz (red) and (B) synthesized mixture with contributions from clinoatacamite (black) and atacamite (red). Bragg positions are indicated with the bars and the blue curve shows the difference between recorded and fitted data. Refinements were carried out by PhD student Jonas Andersen at DTU Chemistry.

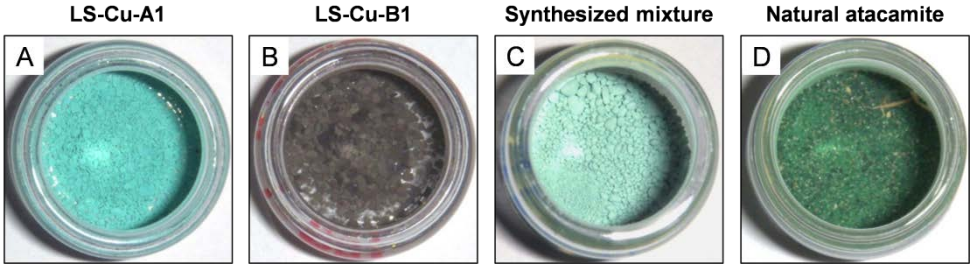

App. fig. 55. Photographs of (A-C) synthesized, purified and dried NPs and (D) natural atacamite.

App. fig. 56. Visible-light microscope image of (A) natural atacamite crystals with impurities and (B-C) natural anatacamite crystals.

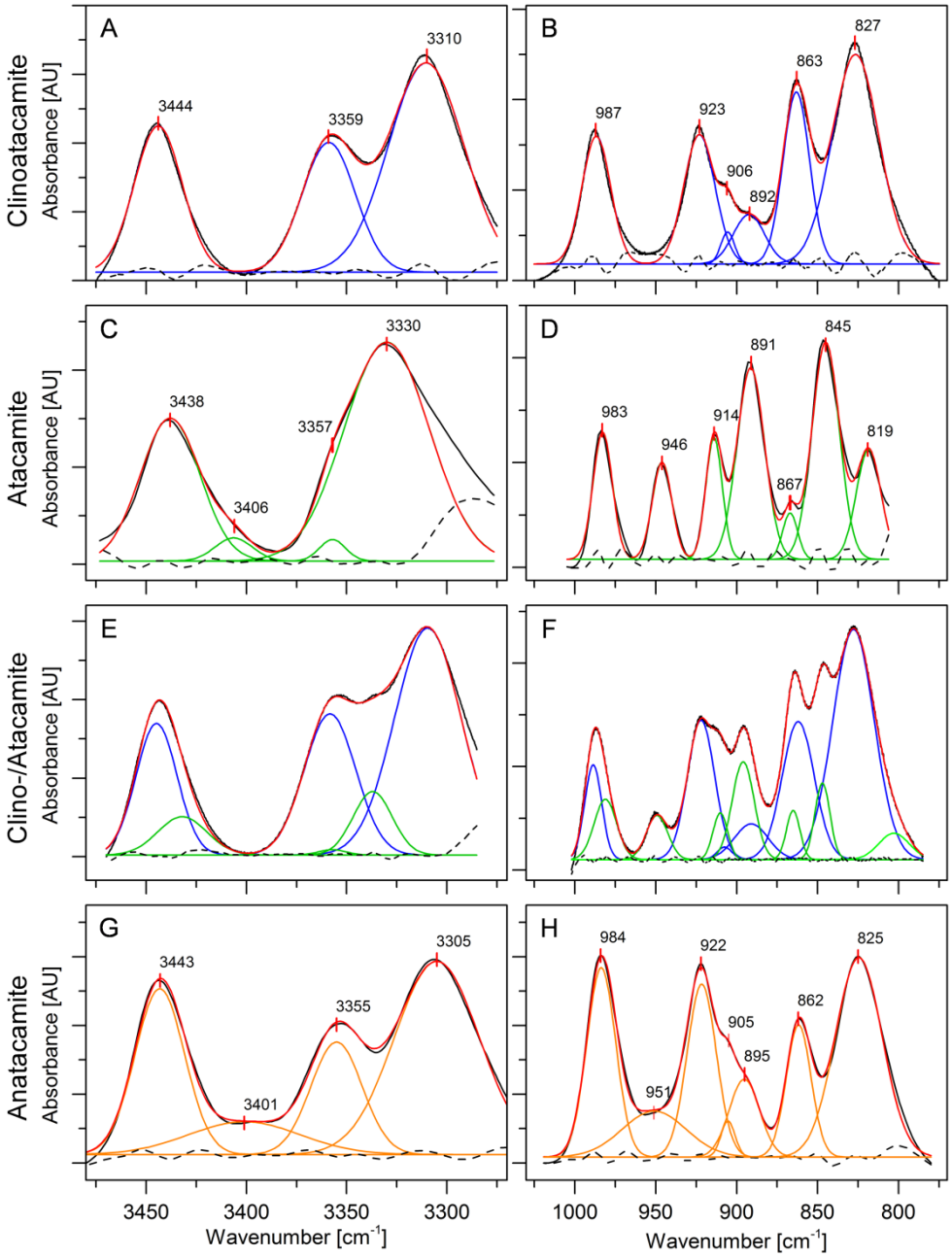

App. fig. 57. Gaussian fits of ATR-FTIR data of (A-B) LS-Cu-A1, (C-D) natural atacamite, (E-F) synthesized mixture and (G-H) natural anatacamite. Each panel contains raw data (black), sum of fit (red), difference between raw data and fit (dotted) and individual peaks of clino- (blue), ana- (orange) and atacamite (green).

Benzyl alcohol oxidation by CuO (4.3)

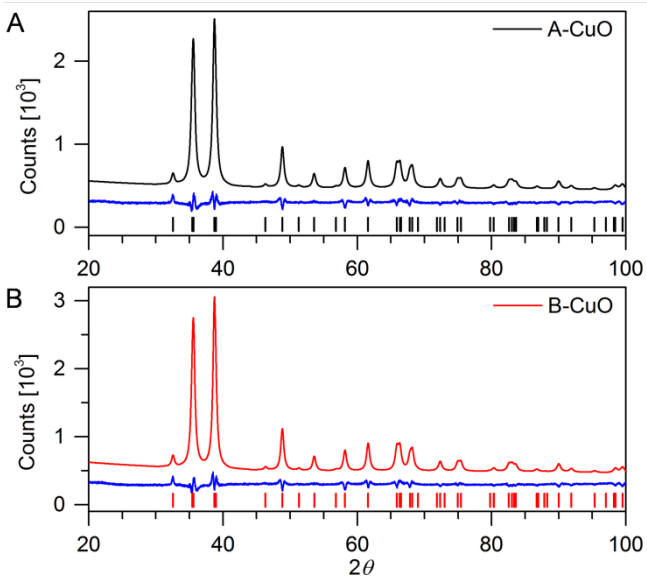

App. fig. 58. Rietveld refinement of XRPD patterns of as-synthesized (A) A-CuO (black) and (B) B-CuO (red). Bragg positions are indicated with the bars and the blue curves show the difference between recorded and fitted data. Refinements were carried out with PhD student Jonas Andersen at DTU Chemistry.

App. table 3. Crystallographic data and refinement summary for Rietveld refinement of XRPD patterns of as-synthesized CuO catalysts.

Sample name	A-CuO (as- synthesized)	B-CuO (as-synthesized)
Formula	CuO	CuO
F_M (g/mol)	79.55	79.55
System	Monoclinic	Monoclinic
Space group	C 1 c 1	C 1 c 1
***a* (Å)**	4.6817(2)	4.6833(2)
***b* (Å)**	3.4175(2)	3.4170(2)
***c* (Å)**	5.1317(3)	5.1302(3)
***α* (°)**	90	90
***β* (°)**	99.266(2)	99.275(2)
***γ* (°)**	90	90
***V* (Å^3)**	81.04(1)	81.03(1)
Z	4	4
***ρ* (g/cm^3)**	6.519	6.520
Size (Å)	175(0)	188(1)
Parameters	12	12
R_{wp} (%)	2.49	2.81
χ^2	0.35	0.48
R_p (%)	1.80	2.08
Bragg refl.	46	46
R_B (%)	1.25	1.51

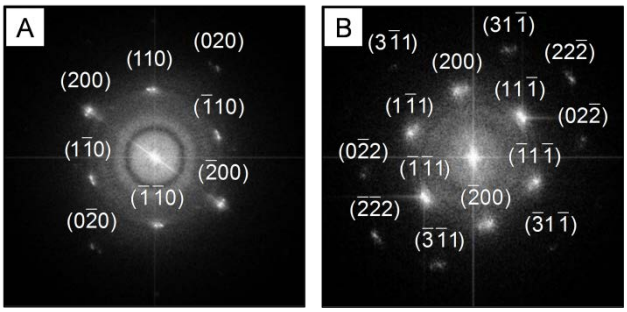

App. fig. 59. Indexed FFTs of the HR-TEM images shown in (A) Figure 113A and (B) Figure 113B.

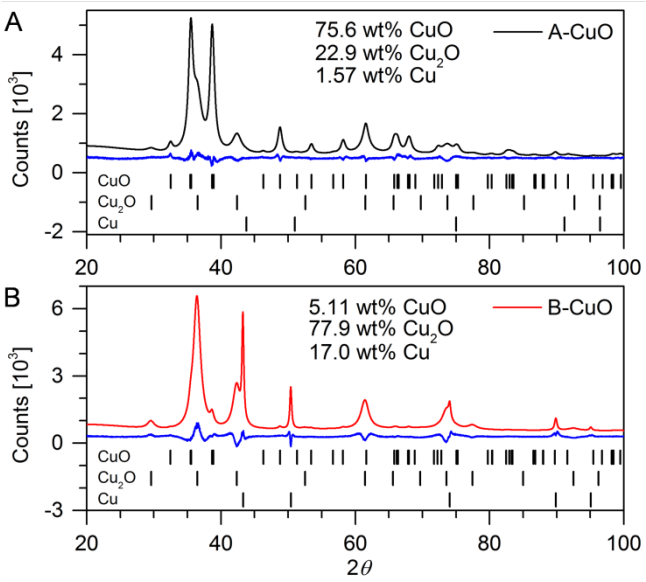

App. fig. 60. Rietveld refinement of XRPD patterns of spent (A) A-CuO (black) and (B) B-CuO (red). Bragg positions are indicated with the bars and the blue curves show the difference between recorded and fitted data. Refinements were carried out with PhD student Jonas Andersen at DTU Chemistry.

App. table 4. Crystallographic data and refinement summary for Rietveld refinement of XRPD patterns of spent CuO catalysts.

Sample name	**A-CuO (spent)**			**B-CuO (spent)**		
Formula	CuO	Cu_2O	Cu	CuO	Cu_2O	Cu
F_M (g/mol)	79.55	143.1	63.55	79.55	143.1	63.55
System	Monoclinic	Cubic	Cubic	Monoclinic	Cubic	Cubic
Space group	C 1 c 1	P n -3 m Z	F m -3 m	C 1 c 1	P n -3 m Z	F m -3 m
***a* (Å)**	4.6930(4)	4.2596(3)	3.5938(1)	4.730(2)	4.2631(2)	3.6151(1)
***b* (Å)**	3.4260(3)	4.2596(3)	3.5938(1)	3.415(1)	4.2631(2)	3.6151(1)
***c* (Å)**	5.1240(5)	4.2596(3)	3.5938(1)	5.022(2)	4.2631(2)	3.6151(1)
α (°)	90	90	90	90	90	90
β (°)	99.332(5)	90	90	99.39(2)	90	90
γ (°)	90	90	90	90	90	90
***V* (Å^3)**	81.29(2)	77.29(2)	46.42(5)	80.04(9)	77.48(1)	47.245(5)
Z	4	2	4	4	2	4
ρ (g/cm^3)	6.498	6.148	9.092	6.600	6.133	8.933
Size (Å)	-	-	-	-	-	-
wt%	77.6(3)	21.1(1)	1.29(4)	6.8(1)	77.6(3)	15.60(8)
Parameters		27			24	
R_{wp} (%)		4.93			5.50	
χ^2		2.30			2.82	
R_p (%)		3.50			4.14	
Bragg refl.	46	12	5	42	12	5
R_B (%)	2.49	1.54	0.83	1.54	1.70	1.79

Plasmonic photocatalysis (4.4)

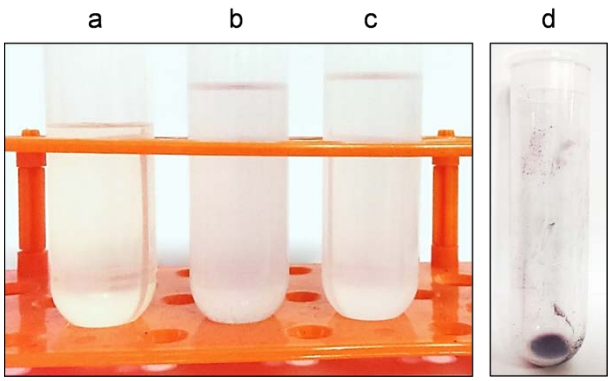

App. fig. 61. Photograph of centrifugation tubes with the supernatant from the first, second and third centrifugation treatments (a to c, respectively) and the sediment left after the third (d).

App. table 5. Centrifugation parameters for AuNP isolation from synthesis mixture.

Step	Condition	Speed	Time	
1	2:3, AuNP solution to ethanol	12k rpm	30 min	App. fig. 61a
2	Redispersed in ethanol	8k rpm	5 min	App. fig. 61a
3	Redispersed in ethanol	8k rpm	5 min	App. fig. 61c and -d

App. fig. 62. Photograph of TiO_2 paste applied to piece of 0.5 mm Ti sheet. The tape is still attached on either side of the paste strip.

App. table 6. Centrifugation parameters for AuNP isolation for composite paste, CP2, preparation.

Step	Repeat	Condition	Speed	Time	Fractions
1	-	2:3, AuNP solution to ethanol	12k rpm	30 min	6
2	4	2:3, water to ethanol	8k rpm	5 min	6
3	2	Ethanol	8k rpm	5 min	1

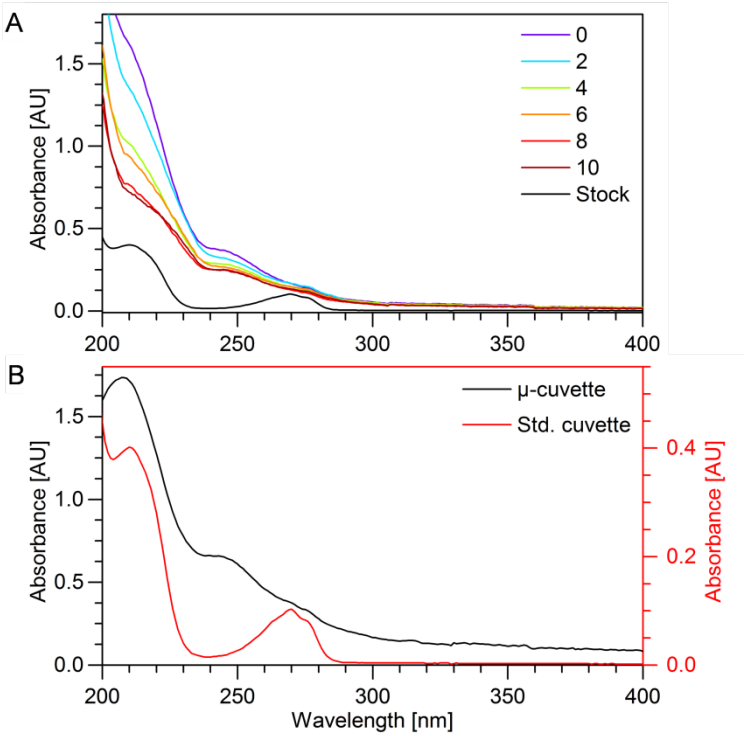

App. fig. 63. (A) UV-vis spectra recorded during phenol degradation experiment with visible lightusing the low-volume cuvette (dil: 1). The stock spectrum is recorded in a standard cuvette. Numbers refers to h after “light on”. (B) UV-vis spectra of phenol recorded in the low-volume cuvette (black) and standard cuvette (red) (dil: 1).

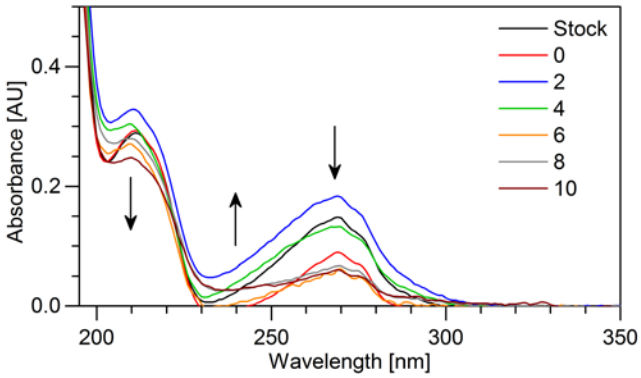

App. fig. 64. UV-vis spectra recorded during 2. phenol degradation experiment with visible light (dil: 1). Numbers refer to h after “light on”.